AD-A283 450

ATION PAGE

Form Approved
OMB No. 0704-0188

1. AGENCY USE ONLY (Leave blank)	2. REPORT DATE	3. REPORT TYPE AND DATES COVERED
	Aug 94	

4. TITLE AND SUBTITLE
Impingement Flow Heat Transfer Measurements of Turbine Blades Using Heat Array

5. FUNDING NUMBERS

6. AUTHOR(S)
Kenneth W Van Treuren

7. PERFORMING ORGANIZATION NAME(S) AND ADDRESS(ES)
AFIT Students Attending:
University of Oxford

8. PERFORMING ORGANIZATION REPORT NUMBER
AFIT/CI/CIA
94-030D

9. SPONSORING/MONITORING AGENCY NAME(S) AND ADDRESS(ES)
DEPRTMENT OF THE AIR FORCE
AFIT/CI
2950 P STREET
WRIGHT-PATTERSON AFB OH 45433-7765

10. SPONSORING/MONITORING AGENCY REPORT NUMBER

11. SUPPLEMENTARY NOTES

12a. DISTRIBUTION/AVAILABILITY STATEMENT
Approved for Public Release IAW 190-1
Distribution Unlimited
MICHAEL M. BRICKER, SMSgt, USAF
Chief Administration

12b. DISTRIBUTION CODE

13. ABSTRACT (Maximum 200 words)

"Original contains color plates: All DTIC reproductions will be in black and white"

14. SUBJECT TERMS	15. NUMBER OF PAGES 250
	16. PRICE CODE

17. SECURITY CLASSIFICATION OF REPORT	18. SECURITY CLASSIFICATION OF THIS PAGE	19. SECURITY CLASSIFICATION OF ABSTRACT	20. LIMITATION OF ABSTRACT

94-0300

ABSTRACT

A thesis submitted in partial fulfilment of the requirements of the degree of Doctor of Philosophy at the University of Oxford, Trinity Term 1994.

Kenneth W. Van Treuren
Merton College

Impingement Flow Heat Transfer Measurements
Of Turbine Blades Using a Jet Array

The requirement for increased gas turbine engine performance has led to the use of much higher turbine entry temperature (TET). The higher temperatures require active cooling of the turbine blade using compressor bleed air. Arrays of impinging jets are one method currently used to reduce the blade temperature on the midspan and leading edge. Air flows through small holes in a blade insert and is directed on the inside surface of a turbine blade to reduce local surface temperature. The engine situation was represented by a 10-20 times scale model tested in the internal cooling transient facility at the University of Oxford. The geometry chosen was for a widely spaced array with a jet spacing of $8d$ and a plate thickness to jet diameter of 1.2. Experiments were accomplished for a range of impingement plate to target surface spacings, z/d, (1, 2 and 4) and jet Reynolds numbers, Re_j, (10,000 - 40,000) with both staggered and inline array hole configurations. The transient liquid crystal technique, both peak intensity narrowband and hue temperature history wideband, enabled the determination of heat transfer coefficient and adiabatic wall temperature. For the first time, local detail of heat transfer on the target surface as well as observation of the crossflow influence on the jet at the target surface are possible. A large variation in heat transfer exists between the stagnation point and channel passage between jets (2 - 4 times) which was unknown in previous experiments. Insights gained from this local detail provide the basis for correlations of stagnation point and area averaged Nusselt number which are compared with other reported values. Also, the present work is the first to quantify the contribution of the array impingement plate to the target surface heat transfer by controlling the impingement plate temperature throughout the test. In regions away from the stagnation point, the impingement plate can contribute as much as 50% of the heat transfer at the target surface.

IMPINGEMENT FLOW HEAT TRANSFER MEASUREMENTS OF TURBINE BLADES USING A JET ARRAY

A thesis submitted for the degree of Doctor of Philosophy

at the University of Oxford.

June 1994

Kenneth W. Van Treuren

Merton College, Oxford

University of Oxford

Department of Engineering Science,

Parks Road,

Oxford OX1 3PJ

Tel (0865) 246561

ABSTRACT

A thesis submitted in partial fulfilment of the requirements of the degree of Doctor of Philosophy at the University of Oxford, Trinity Term 1994.

Kenneth W. Van Treuren
Merton College

Impingement Flow Heat Transfer Measurements
Of Turbine Blades Using a Jet Array

The requirement for increased gas turbine engine performance has led to the use of much higher turbine entry temperature (TET). The higher temperatures require active cooling of the turbine blade using compressor bleed air. Arrays of impinging jets are one method currently used to reduce the blade temperature on the midspan and leading edge. Air flows through small holes in a blade insert and is directed on the inside surface of a turbine blade to reduce local surface temperature. The engine situation was represented by a 10-20 times scale model tested in the internal cooling transient facility at the University of Oxford. The geometry chosen was for a widely spaced array with a jet spacing of $8d$ and a plate thickness to jet diameter of 1.2. Experiments were accomplished for a range of impingement plate to target surface spacings, z/d, (1, 2 and 4) and jet Reynolds numbers, Re_j, (10,000 - 40,000) with both staggered and inline array hole configurations. The transient liquid crystal technique, both peak intensity narrowband and hue temperature history wideband, enabled the determination of heat transfer coefficient and adiabatic wall temperature. For the first time, local detail of heat transfer on the target surface as well as observation of the crossflow influence on the jet at the target surface are possible. A large variation in heat transfer exists between the stagnation point and channel passage between jets (2 - 4 times) which was unknown in previous experiments. Insights gained from this local detail provide the basis for correlations of stagnation point and area averaged Nusselt number which are compared with other reported values. Also, the present work is the first to quantify the contribution of the array impingement plate to the target surface heat transfer by controlling the impingement plate temperature throughout the test. In regions away from the stagnation point, the impingement plate can contribute as much as 50% of the heat transfer at the target surface.

ACKNOWLEDGEMENTS

Having walked the "hallowed halls" of the University of Oxford the past three years, I now know the satisfaction and relief of seeing my research come to a conclusion. As I use the word my, I am fully aware that reaching this point is due to the help and encouragement of the many people I have had the privilege of knowing during my stay in Oxford.

First, I must thank Professor Terry Jones for the opportunity to study at Oxford and his willingness to take on a "mature" student. His approach to tackling the "challenges" faced in life (and research) has left a lasting impression on me. I am forever grateful to Dr. Peter Ireland for his insight and encouragement while accomplishing this thesis. He has a genuine interest and excitement about the research done at Oxford that is infectious. He was directly responsible for keeping me focused on the project and his many discussions on heat transfer as well as life in England provided a wealth of information. I would like to thank Dr. Zoulan Wang for his technical expertise and the use of his image processing software. In addition, Mike Lucas, David Gillespie and Victor Kuk, my fellow students in the lab, provided a sounding board for ideas and an opportunity to vent frustrations encountered along the way, a necessary part of any research project.

Any research project done at Oxney uses the skill and expertise of the technicions, without whom it seems nothing would get done (or at a minimum things would take much longer). In particular, my thanks go to Mr Pat Timms who took my drawings and made them reality. His confidence in my ability far exceeded my own at times. Having seen many people through the D.Phil process, his advice was invaluable. Mr. Terry Baker and Mr Tony Sims also provided valuable technical assistance in the development of the rig and for that I am grateful. Miss Sarah Harrison provided the needed insight into the maze of University workings and on many occasions provided the miracle of cutting through the red tape. Mr. Jon Mooney and Miss Janet Hovard provided the photographic work and made my poor photographic technique look good in the final product.

I wish to thank Rolls-Royce for the interest and funding in this area of impinging jets, in particular Mr. S. Toby Kohler for his management of the project The helpful insight gained from seminars and discussions is appreciated. In addition, I am grateful for to Col Michael L. Smith, the United States Air Force Academy and the United States Air Force Institute of Technology for the opportunity to study at Oxford.

I leave to last the appreciation and love I have for my wife, Renée, and children, Sherry, Jeffrey, and Timothy, who endured much over the last three years, not the least of which was being uprooted and taken to a different country. Their understanding and patience enabled me to concentrate and ultimately accomplish the task.

TABLE OF CONTENTS

LIST OF FIGURES

LIST OF TABLES

LIST OF SYMBOLS

A	constant [**Florschuetz et al. (1981)**]
$A_{crossflow}$	percent crossflow area of influence
A_{jet}	percent jet area of influence
A_o	total jet hole area
A_o^*, A_f	ratio of jet hole area to opposing target surface area
$b(\lambda)$	camera blue filter transmissivity
B	constant [**Florschuetz et al. (1981, 1982)**], blue video signal
C	constant [**Florschuetz et al. (1982)**]
C_D	jet plate discharge coefficient
c_p,c	constant pressure specific heat
d	jet hole diameter
$e(\lambda)$	normalized spectral distribution
$E(\lambda)$	illumination spectrum
f	friction factor $\tau/(\frac{1}{2}\rho u^2)$
$g(\lambda)$	camera green filter transmissivity
G	green video signal
G_c	crossflow mass velocity based on channel cross section area
$\bar{G}_c$	G_c normalized by channel exit mass velocity
G_j	jet mass velocity based on jet hole area
$G_\perp^*$	superficial jet mass velocity based on jet plate area
$\bar{G}_j$	average G_j
h	heat transfer coefficient
h_c	crossflow heat transfer coefficient
h_j	jet heat transfer coefficient
h_p	impingement plate heat transfer coefficent
H	hue signal
I	illumination level, intensity signal
k	thermal conductivity
k_{solid}	solid thermal conductivity
ℓ	thickness of jet plate, calorimeter thickness
L	streamwise length of impingement surface
L_c	characteristic length
m	constant [**Kercher and Tabakoff (1970), Florschuetz et al. (1981)**]
m_c	initial crossflow rate
m_j	total jet flow rate
M	initial crossflow-to-total jet flow ratio
n	constant [**Kercher and Tabakoff (1970), Florschuetz et al. (1981)**], number of points used in determination of hue history uncertainty
Nu	Nusselt number
P	local channel pressure
P_c	upstream channel pressure

P_{exit}	exit manifold pressure (from rig)
P_o	jet plenum pressure
Pr	Prandtl number
q	heat flux
$r(\lambda)$	camera red filter transmissivity
R	ideal gas constant, red video signal
$R(\lambda)$	reflectance spectrum
Re_c	crossflow/channel Reynolds number (using z)
Re_j	jet Reynolds number (using d)
S	saturation signal
t	time
T_{aw}	adiabatic wall temperature
T_c	temperature of coolant flow or crossflow
T_g	temperature of the gas
T_i	initial temperature of target surface
T_j	temperature of jet flow
T_m	temperature of metal
T_o, T_{plen}	jet plenum temperature
T_p	impingement plate temperature
T_s	temperature of surface
Tu	turbulence intensity
u	velocity
w	width or span of channel
x	streamwise distance, distance
$\bar{x}$	non-dimensional streamwise distance
x_n	streamwise jet hole spacing
y_n	spanwise jet hole spacing
Y	monochromatic intensity signal
z	channel height

Greek symbols

$\eta_{crossflow}$	crossflow cooling effectiveness
η_{jet}	jet effectiveness
γ	ratio of specific heats
μ	dynamic viscosity
ρ	fluid or material density
τ	channel wall shear stress
α	thermal diffusivity
ϕ	turbine cooling effectiveness
ϕ_1	constant [Kercher and Tabakoff (1970)]
ϕ_2	constant [Kercher and Tabakoff (1970)]
β	$h\sqrt{t}/\sqrt{\rho ck}$
σ	standard deviation
σ_T	standard deviation of data point in hue calibration
θ	fundamental unit of T in dimensional analysis

CHAPTER 1 - INTRODUCTION

Applications of impinging jets to promote mass and heat convective transfer include paper drying, spot-cooling of electronic components, glass tempering and the heat treatment of metals. The work reported in the literature that is of most interest to the current experiments involves impingement cooling of turbine blades. This thesis reports on an experimental investigation of the distributions of convective heat transfer coefficient, h, on a flat surface beneath different configurations of impinging jets. A transient heat transfer method has been developed by the author to yield local values of h and adiabatic wall temperature, T_{aw}.

1.1 Gas Turbine Engine Performance

The goals of Integrated High Performance Turbine Engine Technology (IHPTET) are pushing military low bypass gas turbine engine technology to achieve an engine thrust to weight ratio of 20:1, a figure that is double a typical present day value [Dix and Petty (1990) and Petty and Henderson (1989)]. At the same time, a significant improvement in fuel economy will benefit civil engines as well. These engines will use a variety of new technologies. Fifty percent of the improvement will result from advancements in materials. Ceramics and composites would allow stoichiometric TETs (turbine entry temperature). However, problems with brittleness and oxidation make manned applications currently impossible. Advanced alloys will extend the current metal temperature limitations slightly but required levels of TET for IHPTET show the need to improve turbine blade cooling. The dilemma facing an engine designer is to increase the specific thrust of an engine, which increases the

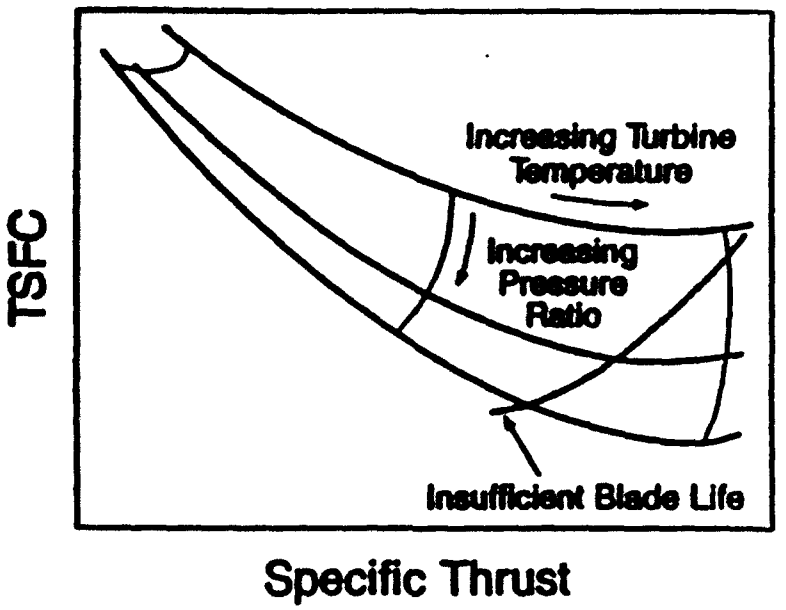

Figure 1.1 Thermodynamic tradeoffs [**Borns (1989)**].

engine thrust to weight, while reducing the specific fuel consumption (see Figure 1.1). A higher TET provides a greater specific thrust which can decrease engine diameter for a given thrust requirement, decreasing drag, or increase thrust for a given diameter, increasing payload capability. Today's higher engine compression ratios (approaching 30:1) can increase TET and improve thermal efficiency, greatly reducing fuel consumption. Higher TETs required for increased performance will cause higher thermal fatigue and higher stress problems for the designer. With hot section design life requirements now 50% of the airframe life, users are demanding reliable, long-life performance. A reduction of blade metal temperature of 40°C can improve blade life 10 fold [**Cowie (1990)**]. Increasing cooling air to lower the blade metal temperature reduces the amount of air available to produce thrust and consequently the cycle

efficiency decreases. The use of film cooling on the external surfaces of the turbine blade also decreases the aerodynamic efficiency of the turbine blading.

1.2 Performance Improvements

1.2.1 Materials

Monolithic ceramics have a good high temperature strength in the 1900 K range and a resistance to oxidation in the combustion environment. The drawbacks associated with their use are brittleness and low reliability. Ceramic matrix composites show the same high strength at high temperature but, in addition, have increased toughness. However, they are difficult to fabricate. Another promising material is the carbon/carbon composite. This class of composites has good strength at very high temperature, high toughness, and low density. They can operate at the 2480 K environment but are subject to oxidation as well as fabrication problems.

The new nickel superalloys are extending current metal technology and, coupled with manufacturing techniques such as the single grain crystal and rapid solidification rate alloys, are increasing allowable blade temperatures. With these alloys there is still a need to employ turbine cooling using the relatively cool air bled from the compressor.

1.2.2 Cooling Techniques

There are four basic methods of utilizing cooling air in a turbine which are

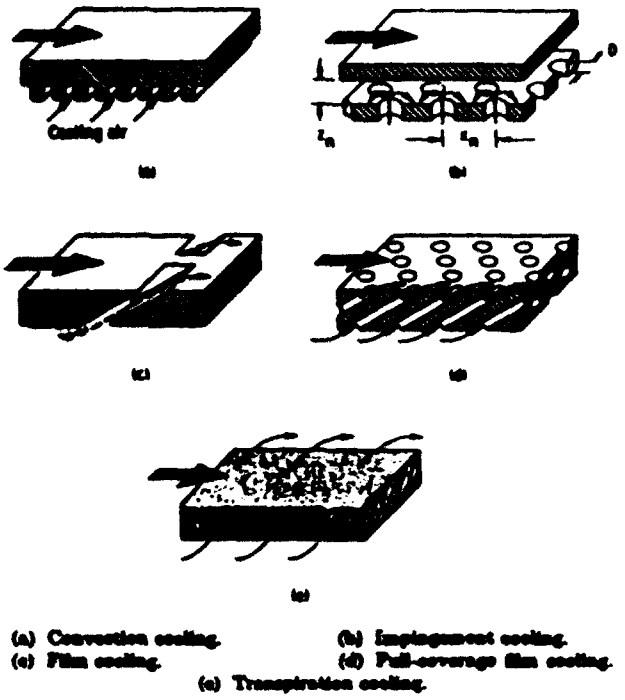

(a) Convection cooling. (b) Impingement cooling.
(c) Film cooling. (d) Full-coverage film cooling.
(e) Transpiration cooling.

Figure 1.2 Internal cooling methods [**Collady (1975)**].

illustrated in Figure 1.2:

Passage Convection - Air flows through internal passages machined or cast into the turbine blade. Convection is often enhanced with ribs or pedestals cast into the passage to increase turbulence, wetted surface area and hence, heat transfer.

Impingement - Air flows through small holes in a blade insert. These form impinging jets on the inside surface of a turbine blade to reduce local blade surface temperatures.

Film - Air flows through holes to the blade external surface to provide a layer of cooler air between the combustor exit gases and the blade surface.

Transpiration - A porous material allows air to "weep" through and provide protection for the blade. There are considerable problems associated with structure and deposition.

Turbine cooling effectiveness is defined as:

$$\phi = \frac{T_g - T_m}{T_g - T_c} \tag{1.1}$$

where T_m, T_g and T_c are the temperatures of the metal, gas and coolant. Figure 1.3 shows the effectiveness of various cooling combinations. Film cooling in combination with crossflow impingement is extremely effective. Increasing the amount of cooling airflow also improves cooling effectiveness for all cooling methods and combinations. The challenge facing the turbine blade designer is to choose the cooling methods to produce a blade that achieves the required permissible TET and that uses the minimum amount of cooling air.

1.3 Aim of Present Study

The present study experimentally modelled arrays of impinging jets which are commonly used in the midchord region of a turbine blade (see Figure 1.4). Exit temperature profiles from the combustor are not uniform. There is usually a region of high temperature at the passage midspan. The turbine designer often uses an array of jets impinging on the inner blade surface to reduce the effect on metal temperature of this temperature spike. Two items are of interest to achieve this result and optimize the turbine blade design.

The first item is the local patterns of heat transfer on the target surface produced by different arrays of impinging jets. This gives an indication of where hot spots or problem areas might occur on the blade. The heat transfer or cooling would

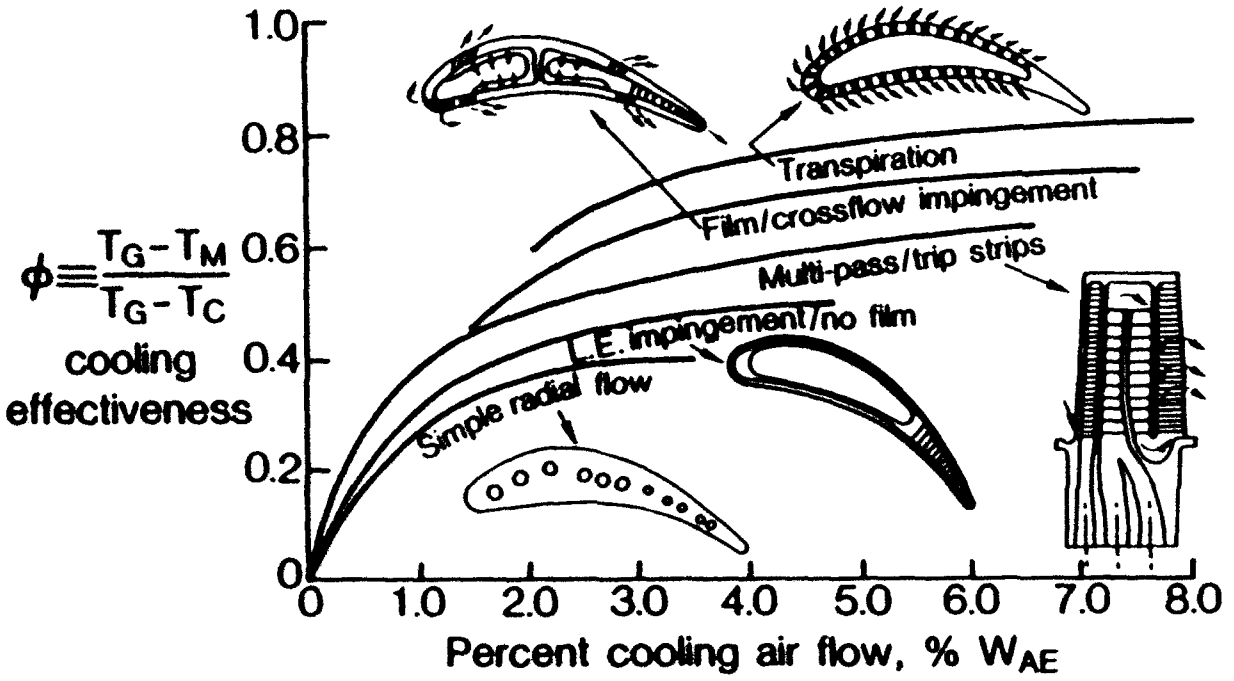

Figure 1.3 Turbine cooling effectiveness [Clevenger and Pickett (1990)].

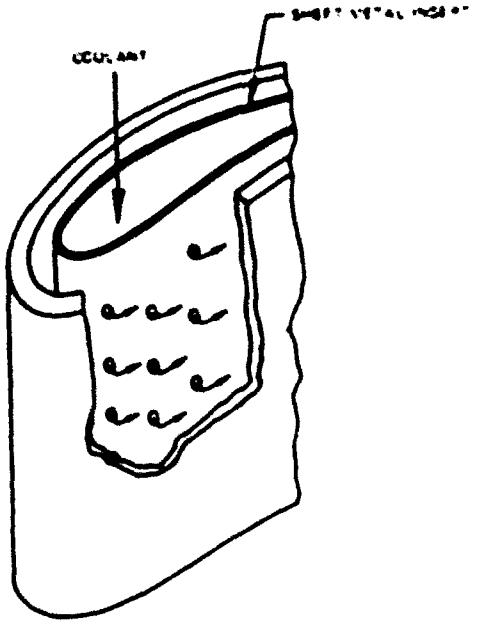

Figure 1.4 Midspan impingement cooling [Oates (1985)].

be highest under the jet and decline moving away from the jet impingement zone. Earlier experimental work has looked at spanwise averaged heat transfer values but, until the present work, the local surface features were unknown. The present work details local values of Nusselt number, Nu, and T_{aw} distributions for both staggered and inline arrays. By developing a transient liquid crystal technique which can experimentally determine the local T_{aw}, the heat transfer can be defined using the true local driving gas temperature giving a more accurate representation of Nu. Previous experimenters have mostly used the jet temperature, T_j, to define heat transfer which produces different results.

The second item of interest to the turbine designer is an average value of heat transfer for an area affected by a given jet. This is particularly important when considering the cooling capacity of a given configuration of an array of jets. Knowing how average heat transfer behaves with changes in geometry and flow rates allows the designer to choose a configuration which can effectively cool the region of interest and at the same time minimize cooling airflow requirements. Other studies have been done on arrays of impinging jets which produced design correlations but the present study is the first to use insights of impinging jet structure gained from experimental observation of liquid crystal colour play and average the true local values for this purpose.

Examination of the literature showed that the influence of the impingement plate, the plate through which the cooling air passes, on the heat transfer at the target surface is not well understood. The impingement plate thermal boundary conditions are not usually reported in the literature. The temperature of this plate must be

different from both the cooling gas temperature and the target plate temperature and is significantly affected by lateral conduction at impingement insert attachment points. Also, transient engine operation alters the cooling gas and blade surface temperature. The time constant of the impingement plate is such that, during the transient, the dimensionless plate temperature will change significantly. For the first time, an experimental technique has been developed and data reported on the influence of the impingement plate temperature on the target surface for an array of impinging jets.

1.4 Scope of the Thesis

The work of this thesis developed the transient experimental technique which enabled the determination of the first true local *Nu* values under an array of impinging jets, giving insight to the turbine designer. In addition, controlling the thermal boundary condition of the impingement plate allowed its contribution to the heat transfer at the target surface to be quantified for the first time beneath an array of impinging jets. Chapter 2 surveys the literature and describes work previously done in the field of impinging jets. The single impinging jet is well represented with supporting research. However, the complex flow field and its contributions to target surface heat transfer are not clearly understood. Some local values of *Nu* are reported but these vary depending on jet hole geometry and experimental technique. The added flow field complexity of crossflow in an array of impinging jets makes the problem much more difficult. Spanwise averaged data for arrays of impinging jets are reported but no true local values. Chapter 3 describes the flow zones of an impinging jet and details the crossflow model used for the current experiments. Also presented are the

transient liquid crystal techniques used to determine h and T_{aw}. Using superposition, the individual contributions of the jet and impingement plate to the overall target surface heat transfer can be quantified. Chapter 4 details the design process used for the present set of experiments and Chapter 5 deals with the experimental procedure and validation of the testing technique. Chapter 6 explains the two data processing methods used to obtain the data, the first being the double crystal technique with three narrow band liquid crystals and the second being the hue history technique with a single wide band liquid crystal. Chapter 7 uses liquid crystal colour play from the video testing, along with dust deposits and static pressure measurements, to discuss qualitatively the influence of the flow field on target surface heat transfer for both the inline and staggered arrays. Chapter 8 uses stagnation zone data to determine a prediction for Nu under the jets for the geometries and flow conditions tested. Chapter 9 presents representative local maps of Nu and jet effectiveness, η_{jet}, showing local variations over the target surface. These values are averaged and compared with correlations found using the current data.

1.5 Publications

The experimental work of the present study has been favourably received by the professional community. A paper entitled "Detailed Measurements of Local Heat Transfer Coefficient and Adiabatic Wall Temperature Beneath an Array of Impinging Jets" was presented at the American Society of Mechanical Engineers (ASME) International Gas Turbine and Aeroengine Congress and Exposition in Cincinnati, OH in May 1993. This work detailed the initial rig design and basic theory behind the

present study. Early data was presented which demonstrated the detail achievable with the experimental method as well as the significance of the influence of the impingement plate temperature. This paper will be published in the ASME Journal of Turbomachinery in the near future. A second paper entitled "Application of the Transient Liquid Crystal Technique to Measure Heat Transfer and Adiabatic Wall Temperature Beneath an Array of Impinging Jets" was presented at Eurotherm 32 in July 1993. This paper detailed the experimental technique and, for the first time, presented local area maps for entire arrays of jets. A third paper entitled "Local Heat Transfer Coefficient and Adiabatic Wall Temperature Measurement Beneath Arrays of Staggered and Inline Impinging Jets" will be presented at the American Society of Mechanical Engineers International Gas Turbine and Aeroengine Congress and Exposition in the Hague, the Netherlands in June 1994. This paper details results from the inline array data as well as introducing a method of processing hue history data comparing an inline and staggered jet configuration. The present work has also provided numerous examples of liquid crystal applications for lectures given by the University of Oxford research staff world wide.

CHAPTER 2 - LITERATURE SURVEY

There have been many experiments involving impinging jets which are usually aimed at specific applications. In convective devices for drying paper, textiles, and film materials, or for tempering glass or annealing metal, slot jets are frequently used. These slot jet studies [**Gardon and Akfirat (1966)**, **Martin (1977)** and **Saad et al. (1992)**], though giving insight into a two-dimensional jet behaviour, are not applicable to gas turbine geometries. Free circular jets, like those used by VTOL aircraft [**Knowles et al. (1991)**] or in spot cooling of electronic components [**Mudwar and Wadsworth (1991)**, **Ma et al. (1992)** and **Hollworth and Durbin (1992)**] also provide some insight to jet structure and interaction with the target surface but do not accurately model the turbine situation. There are comprehensive surveys of turbine cooling [**Metzger (1985)** and **Holland and Thake (1980)**] and more specifically that of impingement cooling by **Gauntner et al. (1974)**, **Downs and James (1987)**, **Yeh and Stepka (1984)** and **Jambunathan et al. (1992)**. **Downs and James** note that all experiments to this date have used steady state heat transfer measurement techniques. Several authors, such as **Goldstein and Franchett (1988)** and **Baughn and Shimizu (1989)**, use a steady technique with thermochromic liquid crystals as surface thermometers to measure single jet local heat transfer values. More recently, **Yan et al. (1992)** used a preheated wall insertion technique to measure transiently local heat transfer values under a single free jet with fully-developed pipe flow. **Abdul Hussain and Andrews (1990)** employed a transient cooling technique in a combustion simulation rig; however, no local measurements were possible. **Hippensteele et al. (1983)** report a qualitative study of an impinging array using liquid crystals while **Li**

et al. (1988) use a liquid crystal coated heater pad to determine local heat transfer coefficient for flow at low jet Reynolds number, Re_j, over staggered and inline arrays.

2.1 Single Jet

Single jet impingement is of interest to the present work. Jets at the start of an impingement array (with no initial crossflow) are least influenced by crossflow and their behaviour would be similar to a single impinging jet. A literature review of single circular jet impingement heat transfer has been made by **Jambunathan et al. (1992)**. Their summary covers parameters of interest in single jet impingement and serves to highlight the many differences between experiments that can have significant impact on the resultant heat transfer.

Obot et al. (1979) and **Popiel and Boguslawski (1986)** have suggested that nozzle geometry plays an important role in determining jet turbulence levels that could be responsible for the variations in measured heat transfer and optimum nozzle exit to target plate spacing, z/d, for maximum heat transfer especially in the stagnation region. Nozzles with contoured inlets would have approximately 25% decrease in heat transfer when compared to a sharp edged orifice at the same Re_j.

Lichtarowicz et al.(1965), **Hay and Spencer (1992)**, **Deckker and Chang (1965)** and **McGreehan and Schotsch (1988)** have suggested that the jet hole discharge coefficient, C_D, is not well defined for ratios of orifice thickness to hole diameter, ℓ/d, typical of engines between 0.5 and 2.0. Above this value the jet reattaches inside the jet hole and, if the ℓ/d is long enough, a fully developed pipe flow can occur with correspondingly increased turbulence levels and different exit

velocity profile.

Single jets can be either free or confined. With the free jet, air from the surroundings can be entrained into the jet, and, under some conditions this can significantly affect heat transfer [**Goldstein et al. (1990)** and **Striegl and Diller (1984a, 1984b)**]. **Bouchez and Goldstein (1975)** studied this effect for a single jet using an impingement cooling effectiveness parameter to characterize the adiabatic wall temperature, T_{aw}, for a fully developed, confined jet in crossflow. **Goldstein et al. (1990)** conclude that the heat transfer coefficient is independent of the jet temperature and the ambient temperature if the adiabatic wall temperature is used as a reference in the definition of heat transfer coefficient. The definition temperature used to determine the heat transfer coefficient varies in the literature. **Andrews and Hussain (1984)** recognized the influence of this variation on design correlation coefficients and suggested the use of a log mean temperature difference between impingement plate temperature and jet plenum temperature. **Jones (1991)** and **Kim et al. (1993)**, among others, suggest the use of a recovery temperature, representative of T_{aw}, to standardize this problem throughout the turbine industry.

Gardon and Akfirat (1965, 1966) studied the influence of turbulence in determining the heat transfer characteristics of an impinging slot and round jet. They showed the peak heat transfer in the stagnation region occurs at plate to jet spacing of 6-8*d*. This was accounted for by the arrival of turbulence from the expanding shear layers at the stagnation point. After 6-8*d*, the turbulence level in the shear layer would be expected to reduce with distance. Artificially increasing turbulence in the jet using a wire mesh also increased stagnation heat transfer by approximately 40%

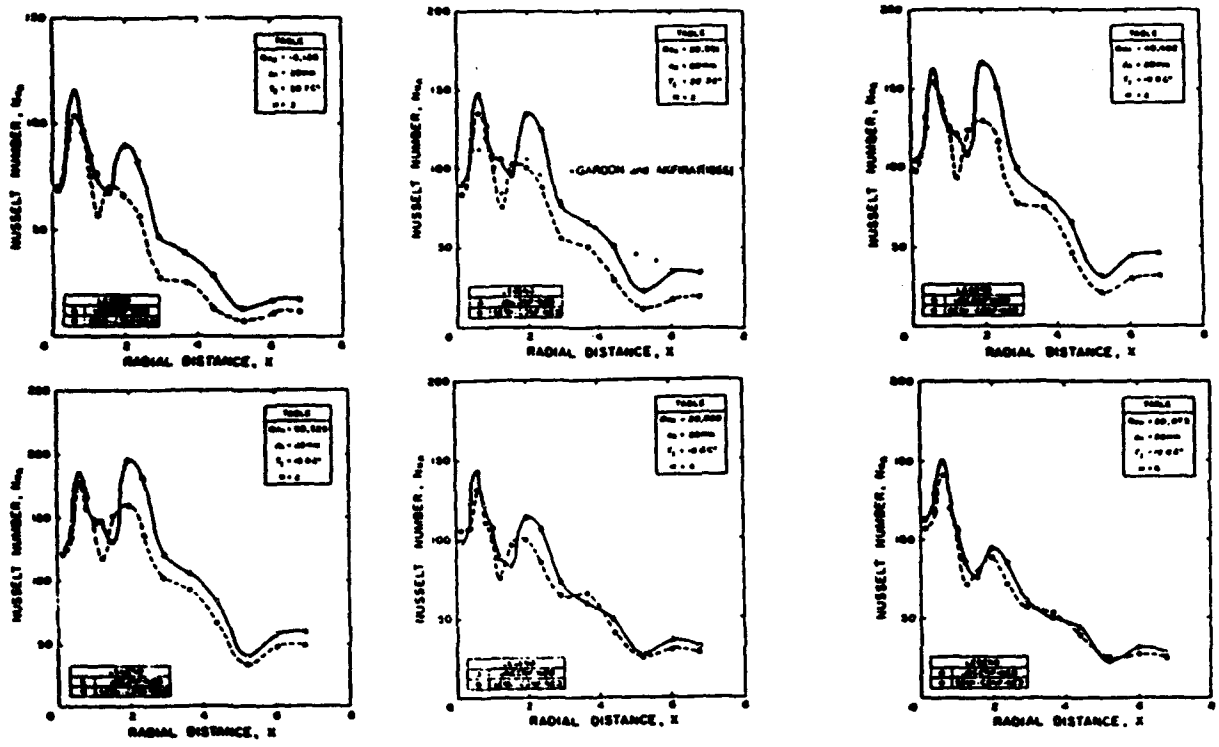

Figure 2.1 Local maximum of Nusselt Number located 0.5*d* from the stagnation point [**Obot et al. (1982)**].

for close nozzle to target plate spacings.

A *maximum in local heat transfer* which occurs at a distance of 0.5*d* radially outward from the stagnation point has been frequently reported in the literature for sharp-edged, low *l/d* jet holes at low *z/d* values (below the maximum stagnation heat transfer *z/d* referred to previously) (see Figure 2.1). The existence and size of this local peak in heat transfer are functions of Re_j and *z/d*. Some researchers attribute this local peak to a minimum in the boundary-layer thickness of the wall jet which is caused by a local acceleration of the flow [**Gardon and Akfirat (1965), Koopman and Sparrow (1976)** and **Obot et al. (1979)**]. **Pamadi and Belov (1980)** have theoretically shown this increase is due to the interaction of the jet with the quiescent air in the shear layer which is highly turbulent and impinges on the heat transfer

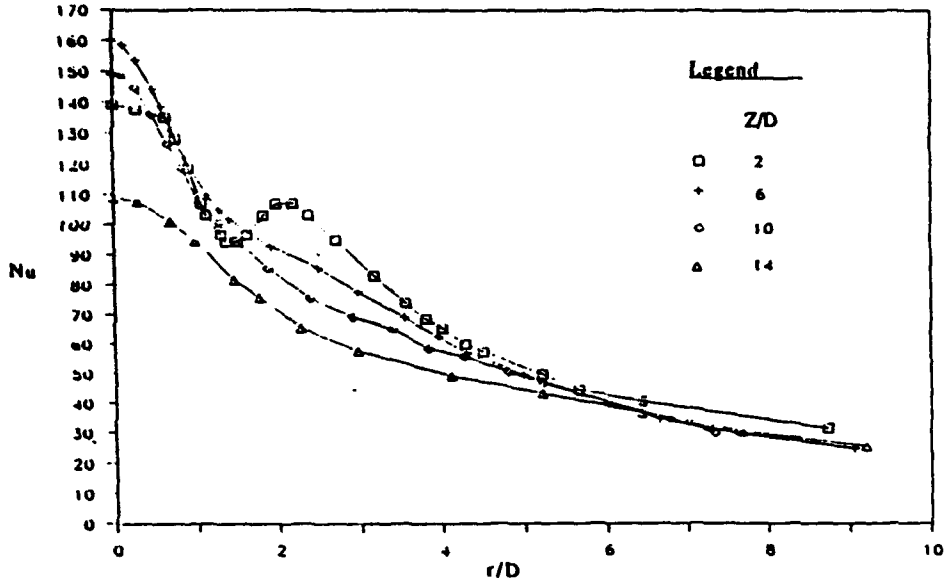

Figure 2.2 Influence of *z/d* on secondary peak in Nusselt Number **[Baughn and Shimizu (1989)]**.

surface. A fully developed jet exit profile is more uniform in turbulence intensity and velocity and does not display this particular characteristic, as seen in Figure 2.2. Also discussed in the literature are secondary heat transfer coefficient peaks that occur further from the stagnation region. Both **Obot et al. (1979)** and **Baughn and Shimizu (1989)** find that a peak occurs at a radial position of about two jet diameters from the stagnation point for an unconfined impinging jet (see Figure 2.2). Confinement of jet flow with a top plate causes significant reductions in impingement heat transfer, with the largest effect occurring at small *z/d* as shown in Figure 2.1 **[Obot et al. (1982)]**. Confinement also shifts the secondary peak slightly toward the stagnation region. **Lucas et al. (1992)**, have produced the only sharp-edged, confined single jet data which reveals a second peak at a 1.5*d* distance from the stagnation

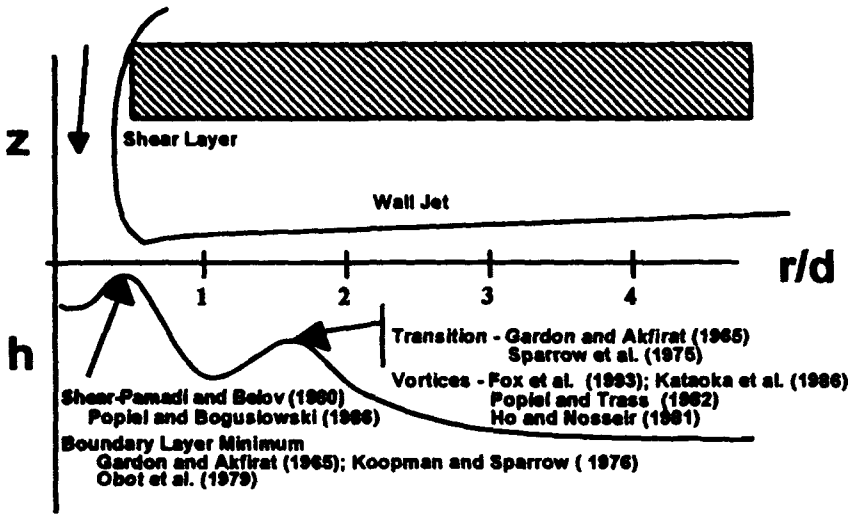

Figure 2.3 Jet profile and peak heat transfer locations under an impinging jet.

point for $z/d = 1$ and Re_j greater than or equal to 15,000. **Gardon and Akfirat (1965)** supposed these secondary peaks mark the transition of the boundary layer from laminar to turbulent which enhances heat transfer coefficient. **Popiel and Trass (1982)** visually show this position also coincides with the point at which toroidal vortices, formed in the shear region of a jet, strike the target surface suggesting this is responsible for the increase in heat transfer. Many other flow visualization experiments also document these vortices [**Fox et al. (1993), Kataoka et al. (1982) and Ho and Nosseir (1981)**]. Figure 2.3 summarizes the regions of peak heat transfer under an impinging jet. Most researchers attempt to correlate Nusselt number, Nu, based on jet diameter to jet Reynolds number, Re_j, Prandtl number, Pr, and some function of geometry. Others present graphs of Nu against distance from the jet centre line resolved to the capability of the experimental test rig. The work of **den Ouden**

and Hoogendoorn (1974) is typical, using a jet produced by a long tube not subject to crossflow. Plots of *Nu* against radial distance from the jet are presented for different conditions. The correlation in Equation 2.1 from these authors is the result of one of the earliest uses of liquid crystals for temperature measurement. This correlation for jet stagnation point *Nu* recognizes the importance of and includes the effect of turbulence intensity, *Tu*, measured at the jet exit.

$$\frac{Nu_D}{Re_D^{0.5}} = .497 + 3.48\left(\frac{Tu\ Re_D^{0.5}}{100}\right) - 3.99\left(\frac{Tu\ Re_D^{0.5}}{100}\right)^2 \qquad (2.1)$$

Popiel et al. (1980) also present a correlation for stagnation point Nusselt number. Here the influences of z/d and Re_j are modeled for a fully developed, unconfined jet with $2 < z/d < 5$.

$$Nu = \left[0.65 + 0.084\left(\frac{z}{d}\right)\right] Re_j^{0.5}\ Pr^{0.4} \qquad (2.2)$$

The stagnation point value can be seen to increase continuously with z in this range. These correlations do not apply to the inlet geometry and jet confinement of the current experiments. Their experimental geometry and flow conditions lead to correspondingly higher predictions of stagnation point heat transfer. Some researchers provide correlations to predict empirically the local value of *Nu* as a function of radial distance from the stagnation point. The form of the correlations is often similar to Equation 2.2 with the exponent of *Re* increasing from approximately 0.5 under the stagnation region to between 0.7 and 0.8 away from the jet.

2.2 Multiple Jet

In comparison to single jets, a study of the heat transfer performance of arrays of impinging jets involves many more experimental parameters. Test and boundary conditions investigated differ greatly through the literature and some sources do not precisely specify all conditions. **Obot and Trabold (1987)** point out that the treatment of spent flow from a confined array in different studies have ranged from unrestricted outflow on all sides to restriction of flow such that it leaves from one side of a rectangularly bounded impingement surface. **Kercher and Tabakoff (1970)** presented some early work on impingement cooling. Using a steady state technique, they tested the effects of jet diameter, jet spacing and jet-to-surface spacing and presented the following empirical correlation for average *Nu*:

$$Nu = \phi_1 \, \phi_2 \, Re_j^{m} \, Pr^{\frac{1}{3}} \left(\frac{z}{d}\right)^{0.091} \tag{2.3}$$

where m, ϕ_1 and ϕ_2 are determined from graphs derived from their data. The parameter ϕ_2 highlights one of the major differences between arrays and single jets. This parameter is a function of crossflow to jet mass velocity ratio, G_c/G_j. Increasing G_c/G_j decreases the value of ϕ_2 and hence the average *Nu*.

Much of the research on impinging jets is centred around the influence of crossflow, both from spent flow within the array or from an initial source upstream of the array, on the jet structure and reduction in cooling effectiveness of the jet as it strikes the target surface [**Bouchez and Goldstein (1975)**, **Catalano et al. (1989)**,

Stoy and Ben-haim (1973), Sherif and Pletcher (1989) and **Scherer et al.(1991)**]. Jet interaction, which depends on the spacing of the jet array in both the streamwise and spanwise direction, can also significantly affect the target surface heat transfer. As a result, the jet structure observed for the isolated jets is significantly changed in the presence of crossflow. Moving through an array, for an array with low *z/d* and with the spent flow exhausting in one direction, the crossflow at the start of the array decreases the average *Nu* [**Florshcuetz et al. (1980)**]. Row resolved average *Nu* exhibits a minimum value early in the array until downstream, towards the flow outlet, the contribution of the increased crossflow to the total heat transfer can increase the average *Nu* for $z/d = 1$. The average *Nu* decreases through the array for larger *z/d* values. Increasing *z/d* always decreases G_c/G_j for a given average Re_j and so the streamwise distribution of average *Nu* tends to be more uniform. For widely spaced jets, the array average *Nu* increases as *z/d* increases to 2. The average *Nu* reaches a maximum level and then decreases as *z/d* is increased further.

Hole geometry is again important and influences the stagnation point region and, to a lesser extent, the turbulence level in the other areas of the jet array. It is interesting to note that the crossflow does have an influence on the jet stagnation heat transfer. Increasing crossflow tends to deflect the jet stagnation position in the downstream direction. At G_c/G_j values of about 0.4, even the jet exit velocity profile can be significantly altered [**Crabb et al. (1981)** and **Andreopoulos (1982)**]. Also critical to the influence of crossflow is the arrangement of the jet holes, which can be either in an inline or staggered configuration.

The University of Arizona and the University of Leeds provide more recent

work on impinging arrays. **Florschuetz et al. (1980-1985)** from the University of Arizona conducted extensive tests on both inline and staggered hole geometries for use in turbine cooling. Early tests focused mainly on flow fields without initial crossflow and produced the following correlation for row resolved average Nusselt number:

$$Nu = A\ Re_j^m \left(1 - B\left(\left(\frac{z}{d}\right)\left(\frac{G_c}{G_j}\right)\right)^n\right) Pr^{\left(\frac{1}{3}\right)} \qquad (2.4)$$

The constants were determined from best fits to the experimental data. The average heat transfer levels predicted by this correlation are dependent on local Re_j, G_c/G_j and array geometry. Separate sets of constants exist for both inline and staggered hole geometries. Further tests by this group produced results for the effects of crossflow at the entrance to the array, nonuniform array geometry and different initial crossflow temperature. The heat transfer data presented are limited by the experimental method to spanwise averaged, streamwise resolved values. The presented data give a very comprehensive indication of the heat transfer characteristics for many different impingement arrays. The correlation, derived for the case of no initial crossflow, can be applied to any array geometry, within specified limits, as the constants A, B, m, and n depend on the hole spacing and channel height. **Andrews et al. (1983-1992)** and **Abdul Hussain and Andrews (1990, 1991)** at the University of Leeds also systematically considered the jet impingement problem but the applications they considered were targeted at combustor wall cooling systems. Initial work used an apparatus which allowed spent flow to exit on all four sides of the array, but later

work looked at the effect of crossflow for a single exit plane array. Several correlations have been presented some, of which are applicable to the turbine situation.

Experiments by **Saad et al. (1980)** increased the resolution of heat transfer measurements for a staggered array. Though spanwise averaged, their results clearly define the peaks of heat transfer beneath the impinging jet and show the downstream displacement of the peak in h beneath the jet due to crossflow. **Hollworth and Cole (1987)** achieved an even better resolution ($0.3d$) with geometries similar to those chosen for the present experiments. Their data was also spanwise averaged. A summary of some of the literature in the field of arrays of impinging jets is given in Table 2.1. In the table, pitch is reported as either x/d and y/d distance between jets or the open area ratio, A_f. A_f is the ratio of the jet hole area to the opposing target surface area. With the higher resolution possible by the use of liquid crystals, it is hoped that the present work will provide a better basis for understanding the heat transfer behaviour of arrays of impinging jets. Presently, the spanwise jet to jet interaction, as well as crossflow influences, are not well understood. The experiments reported in this thesis provide insight into both areas.

Florschuetz et al. (1982) and **Andrews et al.(1983, 1985)** concluded that the influence of the impingement plate temperature on target plate heat transfer levels needed to be quantified. In the current work, attention was paid to the careful control of the impingement plate temperature. Most other research does not report this temperature. The contribution of this thermal boundary condition to the overall heat transfer coefficient at the target plate was recently measured by **Lucas et al. (1992)**. They concluded that beneath a single confined jet at large hole to target plate spacing

Table 2.1 Comparison of Impinging Array Literature.

author	date	nozzle	dia mm	Re_j	z/d	pitch	data	other	type	technique
Chance	1974	sharp *l/d=1*	3.175-15.545	3k-20k	2-4	*x/d, y/d* 7,12	$NuPr^{-1/3}$	correlation	inline	heated plate
Galant & Martinez	1982	sharp	3-13	6k-65k	3.3-8	*x/d, y/d* 8	$NuPr^{-1/3}$	correlation	inline	heated plate transient
Goldstein & Timmers	1982	sharp *l/d*=1	10	40k	2,6	*y/d* 4	*Nu*		line circle	liquid crystal heated plate
Hollworth & Berry	1978	sharp *l/d*=1	2.5,5.5	3k-35k	1-10	*x/d, y/d* 10-25	*Nu*	local & average	inline	heated plate; heat flux sensor
Huang	1963	sharp *l/d*=1,2	3.175, 6.35	1k-10k	1-21.36	A_r .0075-.003	*Nu, h*	correlation	inline	heated plate
Kercher & Tabakoff	1970	sharp *l/d*=.263-1.18	.254-2.032	.332k-3.71k	1-4.8	*x/d, y/d* 3.17-12.5	$NuPr^{-1/3}$	correlation	inline	heated plate
Koopman & Sparrow	1976	jet orifice	6.35	2.47k-10k	2-10	*y/d* 4,6.67	*Sh*	single row	line	naphthalene
Li et al.	1988	sharp *l/d*=1	2.4	880	1,2,3	*x/d* 5 *y/d* 6.77	*h*	crossflow (init)	inline stag	liquid crystal heated plate
Obot & Trabold	1987	sharp *l/d*=3.02	3.175	1k-20k	2-16	*x/d* 4-10 *y/d* 8-4	*Nu*	outflow condition	inline	heated plate
Florschuetz et al.	1980-85	sharp *l/d*=1	0.635-7.62	5k-50k	1,2,3	*x/d* 5-15 *y/d* 4-8	*Nu*	correlation crossflow	inline stag	heated plate
Andrews et al.	1984-92	sharp *l/d*=2.43-9.92	0.71-8.18	1k-24k	0.5-13.5	*x/d, y/d* 1.86-21.46	*Nu*	correlation crossflow	inline	heated plate

and high Re_j, the impingement plate heat transfer coefficient can locally exceed the plenum temperature heat transfer coefficient. The effect is caused by a large recirculation vortex that encircles the jet and draws air back to the jet flow along the impingement plate. Significant heat transfer between the plate and the recirculating gas is responsible for the impingement plate temperature influence on target plate heat transfer. The present work has succeeded in measuring the impingement plate effect in an engine representative array of impinging jets.

There are very few computational investigations of the flow field and heat transfer performance of impinging jets. Recently, **Cooper et al. (1993)** have done experiments using a fully developed, unconfined pipe jet, similar to **Baughn and Shimizu (1989)**, with particular attention to flow details needed to do computational modelling. **Craft et al. (1993)** predicted flow field and heat transfer results for this case using four different turbulence models with encouraging agreement. **Kim and Benson (1992,1993)** and **Claus and Vanka (1992)** both used numerical procedures to describe the flow field of a jet in crossflow. The results are sufficient to gain insight into distortion of the jet structure. A recent **AGARD Conference 534**, "Computational and Experimental Assessment of Jets in Cross Flow," focused primarily on the analysis and prediction of V/STOL jets.

CHAPTER 3 - THEORY

This chapter describes the impinging jet flow field and presents a simplified crossflow model which allows determination of local Re_j. Next, the target surface heat transfer model used, to include the influence of the impingement plate, is described. Lastly, a discussion of the liquid crystal theory, with an introduction to the particular the techniques used in the current experiments to measure surface temperature, is given.

3.1 Description of the Impinging Jet

The single impinging jet flow can be divided into four distinct regions as shown in Figure 3.1. The first region, or free jet region, is a developing flow zone where surrounding fluid is entrained into the jet. This entrainment causes a mixing or shear region around the jet core which locally reduces the jet velocity and increases the turbulence level. Initially, the fluid velocity on the jet centreline remains approximately equal to the nozzle exit velocity and is usually referred to as the jet potential core. Mixing eventually causes a decay in centreline velocity until the velocity falls to 0.95 of the nozzle exit velocity, defining the end point of the potential core. In the case of unconfined, free jets this point usually occurs approximately six jet diameters from the nozzle exit **[Baughn and Shimizu (1989)]**. For the confined jet, issuing from a sharp-edged orifice and under the influence of crossflow, this occurs at less than three jet diameters **[Sparrow et al. (1975)]**. The jet formed by the sharp edged impingement plate is very different to that from a long tube supplying a free jet. One major effect in the former case is the presence of separation which may

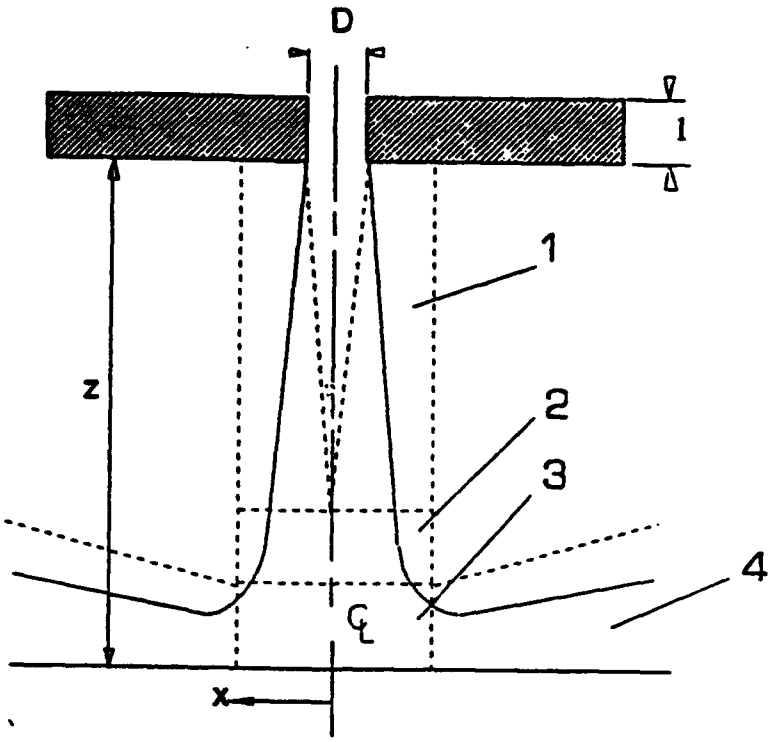

Figure 3.1 Regions of the impinging jet flow field [**Jambunathan et al. (1992)**].

mean that the jet diameter is considerably less than the hole size if the flow does not reattach. This effect would mean that the shear layer would encroach on the potential core within a shorter distance than in the case of the free jet referred to above. Other differences between the two cases are initial flow state in the jet and the different wall geometries.

If the target plate is further from the orifice exit than the end of the jet potential core, the region labelled 2 in Figure 3.1 exists. Here, after the end of the potential core, the axial velocity decreases with increasing distance from the nozzle exit. **Schlichting (1979)** reports the fall of the centreline velocity and the jet half width (width where the axial velocity equals half the centreline velocity) is directly proportional to the distance from the end of the potential core.

The third region (3) is known as the deflection or stagnation zone. It is characterized by a rapid decrease in axial velocity and a corresponding rise in static pressure. Since local total pressure is conserved in this region outside the boundary layer, the vertical velocity component is transformed into a radial velocity. The stagnation zone extends from the jet centreline to a radial distance where the radial velocity is a maximum. **Martin (1977)** has shown that the boundary layer thickness under the jet is inversely proportional to $Re_j^{0.5}$ and is essentially constant. The boundary layer reaches approximately one-hundredth of the jet diameter for the Reynolds number range of these studies.

The last region, (4) in Figure 3.1, is termed the wall jet region. Moving out from the stagnation point through region (3), the flow accelerates close to the target wall. This acceleration cannot continue as the velocity distribution between the plates develops since increasing overall velocity at increasing radius would violate volume continuity. Through region (4) the flow near the wall decelerates. The positive pressure gradient keeps the boundary layer laminar in region (3) and transition to turbulence occurs shortly after entering the deceleration zone, region (4). The wall jet and free jet boundary layer together form a typical wall jet profile. The wall jet is associated with higher levels of heat transfer coefficient than are found beneath normal developing flow on account of the turbulence generated by the shear between the wall jet and the surrounding air. This turbulence is transported to the boundary layer at the heat transfer surface.

Arrays of jets, produced from a plate as shown in Figure 3.2, have the same zones as discussed previously but the interaction of adjacent jets and the pressure of

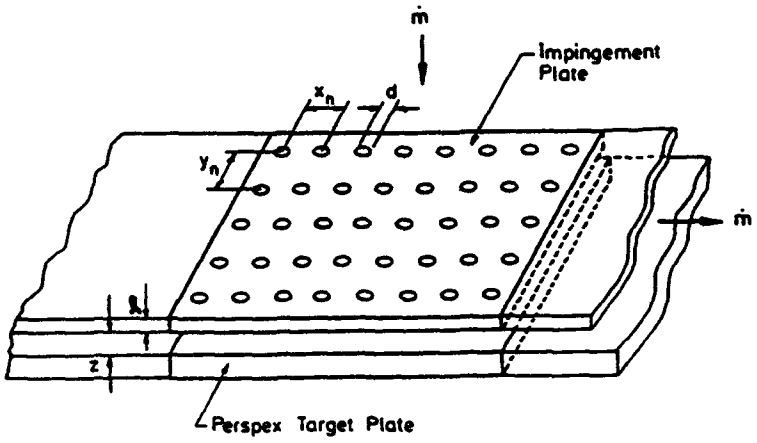

Figure 3.2 Schematic diagram of the inline array **[Van Treuren et al. (1993)]**.

crossflow can alter the jet structure at the surface. A crossflow region would exist, Figure 3.3, upstream and around the previously mentioned regions (1)-(4). As stated earlier, the wall jet region will still experience higher heat transfer at the target surface than channel flow in part due to the high level of turbulence whether the flow remains laminar or becomes turbulent. Increased heat transfer will also occur between spanwise jets which exhaust in one direction as the crossflow in this area is accelerated. The actual wall jet surface coverage will be limited in the upstream and spanwise direction by crossflow. Behind the jet, separation and vortices occur further influencing the jet and heat transfer values. Upstream, horseshoe vortices from jet/crossflow interaction create separation lines which are swept downstream by the crossflow. Clearly the flow field and heat transfer coefficient distribution under an impinging jet are extremely complex. Certain simplifying assumptions must be made

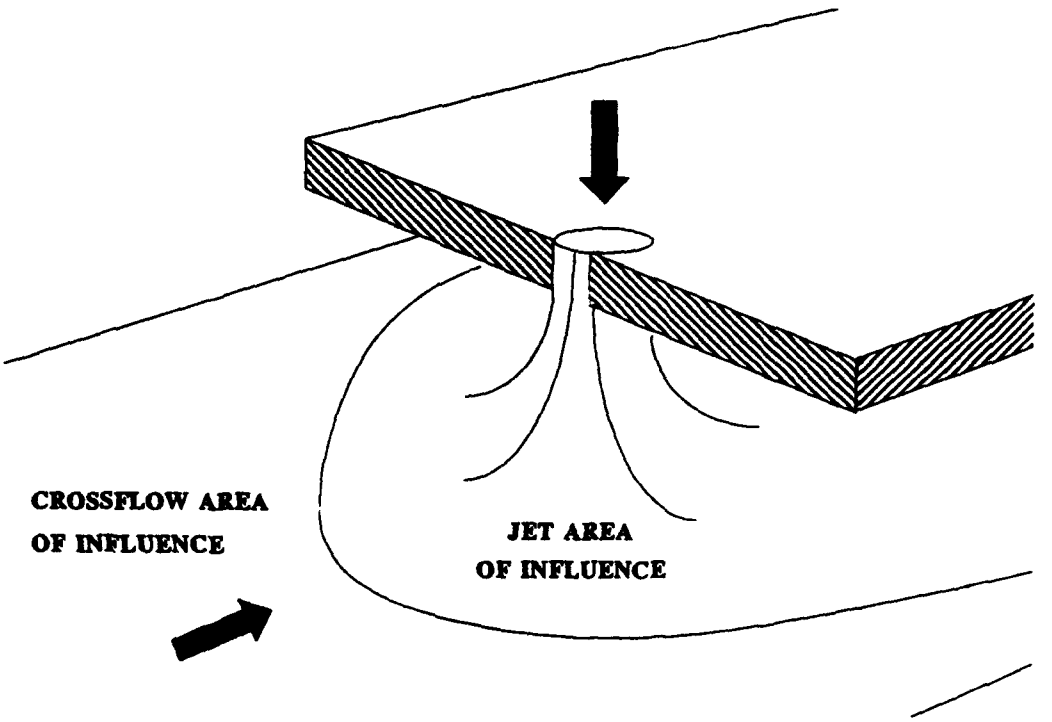

Figure 3.3 Influence of crossflow on impinging jet structure.

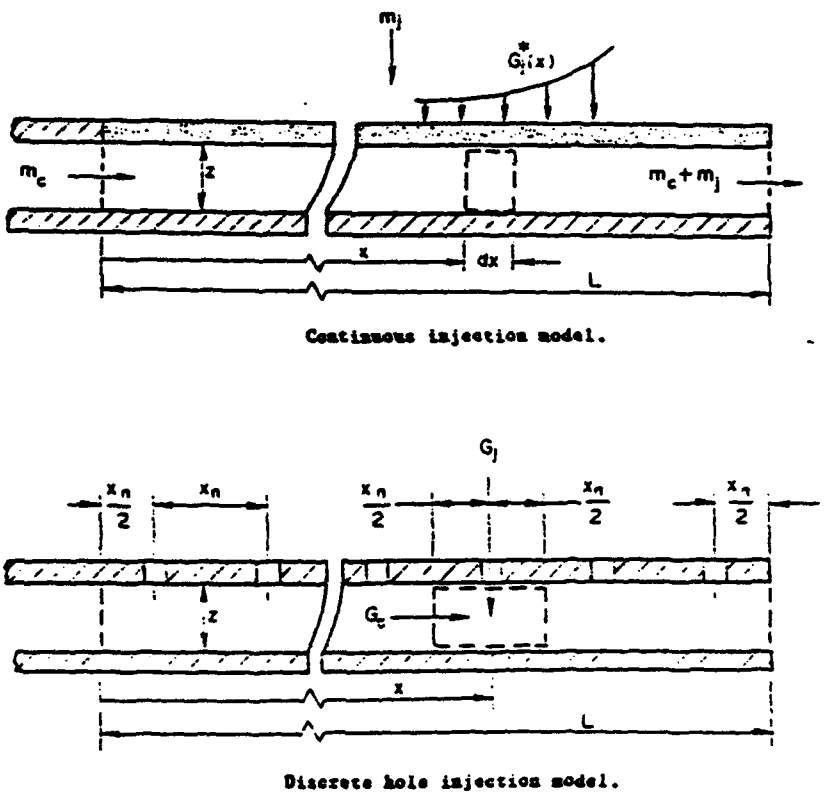

Figure 3.4 Continuous injection model used in the analysis of the flow field **[Florschuetz et al. (1982)]**.

to analyze the influence of crossflow on an array of impinging jets.

3.2 Flow Field Analytic Model

This particular analysis follows the analytic model presented first by **Martin (1977)** and then **Florschuetz et. al. (1982)**, which replaced the discrete hole array with a surface over which the flow is uniformly injected (Figure 3.4). The jet velocity, G_j, is related to the continuously distributed injection velocity, G_j^*, by the open area ratio, A_o^*, in the equation $G_j^* = G_j A_o^*$. A_o^* is the jet hole area divided by the area of the impingement plate covered by a single jet. By initially assuming incompressible flow, the distributed injection velocity may be written:

$$G_j^* = A_o^* C_D \sqrt{2 \rho (P_o - P)} \tag{3.1}$$

where C_D is discharge coefficient, P_o is the jet supply total pressure, ρ is the density and P is the static pressure. A force momentum balance on the control volume results in:

$$dP = - \frac{2 G_c \, dG_c}{\rho} - \frac{2 \tau \, dx}{z} \tag{3.2}$$

where τ is the channel wall shear stress. In practice the second term on the right hand side of Equation 3.2 is small compared to the other terms in the equation for the test conditions considered. Hence, it was felt adequate to estimate this term using standard channel correlations. This was borne out by the close agreement between prediction and experiment (see Chapter 7). A mass balance gives:

$$G_j^* = \frac{z\, dG_c}{dx} \tag{3.3}$$

Defining the non-dimensional crossflow velocity $\tilde{G}_c = \dfrac{G_c}{\left(\dfrac{m_c + m_j}{wz}\right)}$ and the non-dimensional streamwise distance, $\tilde{x} = x/L$, the boundary conditions for the case with initial crossflow become:

$$\tilde{G}_c = \frac{M}{(1 + M)} \qquad \text{at} \qquad \tilde{x} = 0 \tag{3.4}$$

$$\tilde{G}_c = 1 \qquad \text{at} \qquad \tilde{x} = 1 \tag{3.5}$$

where M is the initial crossflow to total jet mass flow ratio. The differential equation which determines the flow is obtained by combining equations 3.1, 3.2 and 3.3:

$$\frac{d^2 \tilde{G}_c}{d \tilde{x}^2} = \frac{B^2 \tilde{G}_c \left[1 + f\left(\frac{L}{2z}\right) \frac{\tilde{G}_c}{\left(\frac{d \tilde{G}_c}{d \tilde{x}}\right)} \right] + C \left(\frac{d \tilde{G}c}{d \tilde{x}}\right)}{1 + C \frac{\tilde{G}_c}{\left(\frac{d \tilde{G}_c}{d \tilde{x}}\right)}} \tag{3.6}$$

where:

$$B = \frac{\sqrt{2}\, A_o^*\, C_D\, L}{z} \tag{3.7}$$

and:

$$C = \left(\frac{A_o^* L}{z} \right) \left(\frac{1}{C_D} \right) \left(\frac{d C_D}{d\left(\frac{G_c}{G_j} \right)} \right) \tag{3.8}$$

For the case of no shear and constant C_D and P_o, eliminating G_j^* and P from the previous equations gives the streamwise jet velocity distribution:

$$\frac{G_j}{\bar{G}_j} = B \frac{(1 + M)\, \cosh B\tilde{x} - M \cosh B(1 - \tilde{x})}{\sinh B} \tag{3.9}$$

and the crossflow to jet mass velocity ratio:

$$\frac{G_c}{G_j} = \left(\frac{1}{\sqrt{2}\, C_D} \right) \frac{(1 + M)\, \sinh B\tilde{x}' + M \sinh B(1 - \tilde{x}')}{(1 + M)\, \cosh B\tilde{x} - M \cosh B(1 - \tilde{x})} \tag{3.10}$$

where $\tilde{x}' = \tilde{x} - (1/2)(x_n/L)$. The case is solved numerically when C_D is not constant but is a function of G_c/G_j and/or the wall shear term. The friction factor, f, can be approximated according to **Kays and Crawford (1986)** using the channel Reynolds number, Re_c, with Re_c regions suggested by **Florschuetz et al. (1982)**:

$$f = \begin{bmatrix} 24/Re_c & Re_c < 2{,}000 \\ 0.079/Re_c^{0.25} & 2{,}000 < Re_c < 30{,}000 \\ 0.46/Re_c^{0.20} & 30{,}000 < Re_c \end{bmatrix} \tag{3.11}$$

For G_c/G_j values greater than approximately 0.5, an appropriate empirical model of C_D is required otherwise, C_D is considered constant **[Florschuetz et al. (1982)]**. Solutions to the differential equation can be obtained by the shooting method using a fourth order Runge-Kutta method. Provided that the continuous injection model results in

an injection velocity distribution which is linear over the length of all streamwise pitches, a very small error is introduced in calculating the discrete injection velocity from the value of the continuous function evaluated at the jet row centre line, having taken account of the area ratio. Computer codes were written by the author in Fortran for the cases with and without friction. Considerable insight was gained into the flow at test conditions using these computer codes. Agreement between measured and model predicted static pressure distributions in the present work was excellent as reported in Chapter 7. This enabled the local Re_j to be calculated using this model for all of the heat transfer experiments.

3.3 Definition of Heat Transfer Model

For the case where initial crossflow is present, most researchers treat the impingement jet with crossflow as a three temperature problem. These temperatures are the surface or wall temperature, T_s, the jet temperature, T_j, and the crossflow temperature, T_c. Effectiveness, $\eta_{crossflow}$, is defined as:

$$\eta_{crossflow} = \frac{T_{aw} - T_j}{T_c - T_j} \tag{3.12}$$

where T_{aw} is the adiabatic wall temperature. The heat flux at the target surface is given by:

$$q = h\,[\,(\,1 - \eta_{crossflow}\,)\,(\,T_j - T_s\,) + \eta_{crossflow}\,(\,T_c - T_s\,)] \tag{3.13}$$

Thus, $\eta_{crossflow}$ can be thought of as a temperature difference weighting factor which quantifies the relative contributions of both the jet and crossflow to the target surface

heat flow.

Noticeably missing from Equations 3.12 and 3.13 is the influence of the impingement or array plate temperature on the heat transfer system. In the actual engine situation, during steady operation this plate would be at a temperature between the coolant flow and the target surface temperature. Two researchers, namely **Florschuetz et al. (1982)** and **Andrews et al. (1983, 1985)**, suggest that the impingement or array plate temperature, T_p, needs to be included amongst the experimentally matched parameters. **Florschuetz et al.** initially conducted experiments with resistance heater wires heating an aluminium array plate. They observed that varying power levels had no measurable effect on the results. Later tests with an acrylic resin array plate holder, essentially uncoupling the array plate from the test rig, showed an effect of the plate temperature on $\eta_{crossflow}$ at small values of $\eta_{crossflow}$ where jet flows dominate. **Florschuetz et al.** concluded that the plate temperature had a secondary effect on the overall heat transfer coefficient and recommended that, in future studies, more attention be paid to the carefully controlling the thermal boundary condition at the exit plane of the impingement jet plate. Later tests **[Florschuetz and Su (1985)]** compare results from experiments using an aluminum and acrylic resin array plates and concluded, within the uncertainties of the experimental technique, the possible effects of heat leak through the jet plate and lateral conduction within the plate to be insignificant. Therefore, **Florschuetz et al.** do not account for this boundary condition and the effects are discounted. **Andrews et al.** note that any heating of the array plate can affect the heat transfer processes at the target wall and cause a significant reduction in coolant flow for a constant pressure

loss. They also advise controlling the jet exit thermal boundary condition but further experiments conducted are vague about impingement plate conditions. A careful set of experiments performed at Oxford University by **Lucas et al. (1992)** with a single impinging jet clearly demonstrated the influence of the impingement plate temperature on the target surface heat transfer. Recirculation regions mapped out with flow visualization showed convective conditions can exist where heat lost to the impingement plate can account for as much as 50% of the total target plate heat transfer. For this reason the present study includes the plate temperature as a controlled thermal boundary condition.

Due to linearity of the energy equation, if properties and flowfield are considered to be independent of temperature boundary conditions, superposition may be used to determine temperature fields and heat transfer to surfaces. Thus, solution for many boundary conditions may be added to arrive at the solution for the desired boundary conditions. For the situation considered here a uniform jet inlet temperature and uniform target plate temperature and impingement plate temperature were used. This gives three defining temperatures which enables a solution to be found from superposition given in Equation 3.14. It should be added that uniform temperatures are not necessarily required for superposition to apply. A non-uniform wall temperature develops during the transient experiment. However, the local heat transfer is determined as though the target wall was uniform at the local temperature. This is obviously an approximation. At the start of the experiment the wall is at a uniform temperature whereas at long times the wall will reach the local recovery temperature. Thus, the analysis will be exact at the early times in the experiment for the wall

temperature variations will be small compared to the driving temperature potentials. Two methods may be used to determine the influence of wall temperature variations on the measurement; firstly, superposition may be employed in a theoretical estimate as performed by **Dunne (1983)** and **Ireland (1987)** for particular cases; secondly, the heat transfer coefficient may be measured at different times in the experiment, all with different surface temperature profile histories, and its consistency checked. Figure 5.11 shows a plot of channel heat flux against surface temperature for a location where an upstream wall effect would be expected. The constant slope shows h is sensibly unchanged throughout the test. In experiments reported here the stagnation region will be necessarily independent of upstream surface temperature variation effects. The three temperature superposition equation for the current experiments is:

$$q = h_j (T_j - T_s) + h_c (T_c - T_s) + h_p (T_p - T_s) \qquad (3.14)$$

Rearranging:

$$q = (h_j + h_c + h_p) \left(\frac{(h_j T_j + h_c T_c + h_p T_p)}{(h_j + h_c + h_p)} - T_s \right) . \qquad (3.15)$$

or simply:

$$q = h (T_{aw} - T_s) \qquad (3.16)$$

Both the total heat transfer coefficient, h, and the adiabatic wall temperature can be found in a transient test using the double crystal method of measuring heat transfer (see Section 3.6.1). For a particular test the following two equations can be written:

$$h_j + h_c + h_p = h \tag{3.17}$$

$$h_j T_{j_1} + h_c T_c + h_p T_p = T_{aw_1} h \tag{3.18}$$

A third equation is required and is obtained by altering the jet temperature:

$$h_j T_{j_2} + h_c T_c + h_p T_p = T_{aw_2} h \tag{3.19}$$

In the case of no initial crossflow, these equations can be simplified. Local heat flux to the target plate can be described in terms of two heat transfer coefficients.

$$q = h_j(T_j - T_s) + h_p(T_p - T_s) \tag{3.20}$$

Rearranging:

$$q = (h_j + h_p)\left(\frac{(h_j T_j + h_p T_p)}{(h_j + h_p)} - T_s\right) \tag{3.21}$$

or simply:

$$q = h\,(T_{aw} - T_s) \tag{3.22}$$

as before. For the transient techniques used in the current experiments both h and T_{aw} will be evaluated. Thus, for the case with no initial crossflow, only one test is required to determine the h_j and h_p using the following equations:

$$h_j + h_p = h \tag{3.23}$$

$$h_j T_j + h_p T_p = h T_{aw} \tag{3.24}$$

The present work for which initial crossflow was absent gives the results in terms of Nusselt number

$$Nu = \frac{h\,d}{k} \tag{3.25}$$

and the jet effectiveness

$$\eta_{jet} = \frac{T_{aw} - T_p}{T_j - T_p} \tag{3.26}$$

It is easily shown that the jet effectiveness is the jet heat transfer coefficient, h_j, divided by the total heat transfer coefficient, $h_j + h_p$. In regions where the jet effectiveness is unity, the adiabatic wall temperature is the same as the jet temperature.

3.4 Liquid Crystal Theory

Encapsulated thermochromic liquid crystals have been used in heat transfer analysis for quite some time [**den Ouden and Hoogendoorn (1974)**, **Ireland (1987)** and **Wang (1991)**]. Essentially, the transient technique takes advantage of the temperature response of the pitch of the liquid crystal helical structure in the cholesteric mesophase [**Bonnett (1989)**]. As the temperature of the crystal is increased, it selectively reflects light and typically the wavelength of the reflected light passes through the visible spectrum. This characteristic can be used to accurately measure surface temperature over entire areas of the experimental apparatus. The colour response is calibrated to temperature using a thin foil thermocouple mounted on the test surface. The encapsulated chiral-nematic material performance is degraded by chemical contamination and ultra-violet light though it is insensitive to pressure

and shear changes occurring during a heat transfer experiment. The encapsulation of the liquid crystal material helps protect it from the effects of applied stresses. The crystal is encapsulated in small polymer shells with diameters of approximately 10 μm. The shell is thin, corresponding to only 10% of the capsule weight, and thus, does not significantly reduce the usefulness of the temperature response. A typical crystal response time of 3ms has been found, **Ireland and Jones (1987)**, for materials which have colour plays close to room temperature. An aqueous slurry of these capsules can be mixed with a binder and sprayed onto a test surface. A monolayer 20 to 30 μm thick reflects sufficient light for the heat transfer experiments. The brightness of the colour response under fixed lighting does not significantly increase for thicker layers **[Bonnett (1989)]**.

Under the thermal conditions of a heat transfer experiment, heat conducted laterally can be neglected compared to heat convected from the airflow. The temperature rise of the perspex can be found by solving the one dimensional Fourier equation:

$$\rho\, c_p \frac{\partial T}{\partial t} = k \frac{\partial^2 T}{\partial x^2} \qquad (3.27)$$

where ρ is the density, c_p is specific heat and k the conductivity of the substrate. The left hand side of the equation then quantifies the rate of change of thermal energy per unit volume within the material while the right hand side is equal to the net accumulation of heat per unit volume due to conduction. It is convenient to define the thermal diffusivity, α, as:

$$\alpha = \frac{k}{\rho\, c_p} \tag{3.28}$$

Thermal diffusivity is a measure of the thermal conductivity in comparison to the material thermal capacity. The boundary condition at the surface, $x = 0$, is:

$$q = h\,(T_{aw} - T_s) \tag{3.29}$$

where T_{aw} is the fluid temperature, T_s is the surface temperature, and h is the convective heat transfer coefficient. The initial condition is that $T(x,0) = T_i$. The solution is for a semi-infinite domain for which $T = T_i$ at $x = \infty$. Solving the Fourier equation by using Laplace transforms yields:

$$\frac{T_s - T_i}{T_{aw} - T_i} = 1 - e^{\beta^2}\, erfc(\beta) \tag{3.30}$$

with:

$$\beta = \frac{h\sqrt{t}}{\sqrt{\rho\, c_p\, k}} \tag{3.31}$$

where T_i is the surface initial temperature and t is the time. Thus, using a liquid crystal technique, the surface temperature at a particular time enables the convective heat transfer coefficient to be evaluated provided all other terms in Equations 3.30 and 3.31 are known. The assumption has been made in this analysis that a uniform material temperature prevails initially and that the material is sufficiently thick that the thermal pulse does not travel to the model outer surface within the test time. Lateral conduction was shown analytically and experimentally to be negligible by

Dunne (1983). Both **Dunne** and **Ireland and Jones (1985)** state errors in lateral conduction will be unimportant provided that the second derivative of heat transfer coefficient with respect to distance along the surface is small compared to the value of heat transfer coefficient divided by the square of the thermal diffusion depth. For heat transfer distributions which change rapidly with distance the test time must be short to minimize the thermal diffusion length. In the present experiments the stagnation zone is the region most influenced by lateral conduction. Estimates of the second derivative of heat transfer coefficient with respect to distance along the surface show lateral conduction is negligible at this point.

3.5 Steady State Technique with Uniform Wall Heat Flux

One of the most common methods for measuring array heat transfer coefficient described in the literature is a steady state technique which uses a uniform wall heat flux **[Florschuetz et al. (1980), Andrews et al. (1987), Obot et al. (1979)** and **Saad et al. (1980)]**. Since this technique is the most widely used, it is important to understand this technique when comparing steady state experimental data with the current transient experimental data. This steady state method generally consists of an air supply, a flow metering section for determining the jet Reynolds number, interchangeable jet impingement plates for investigating various geometries and a heated target plate. A single instrumented target plate usually consists of multiple segment heater strips with the longest dimension perpendicular to the exhaust flow direction. The heater strips are insulated to minimize lateral conduction as well as heat lost from the apparatus. Radiated heat transfer is either accounted for or shown

to be negligible. The power level into each heater is monitored allowing the thermal boundary condition (heat flux) at each pad to be known. The target plate surface temperature is monitored using thermocouples. Knowledge of the heat flux, the jet temperature and the wall temperature allow the heat transfer coefficient to be calculated. A limitation of this technique, however, is that heat transfer coefficients are averaged over the heater pad. Spanwise average results from jet arrays show trends in heat transfer coefficient in the major flow direction only. The measurement resolution can vary depending on the jet diameter and width of the heater pad. A low resolution experiment obscures local variations due to the complex flow field. There are reports of problems which can occur in accounting for heat conduction through the interfaces between heater strips. Most importantly, it is typical for the test rig to require a substantial amount of time to achieve thermal equilibrium before data can be obtained.

More recently several steady state experiments have used liquid crystal technology to measure surface temperature [**Baughn and Shimizu (1989), Li et al. (1988), Lucas et al. (1992)** and **Goldstein and Franchett (1988)**]. In these experiments, a thin metallic coated heater is used to provide a continuous uniform heat flux. The heater coating is chosen to be sufficiently thin to render lateral heat conduction negligible. The experimental technique is similar to that discussed in the previous paragraph. By setting a power level on the crystal coated heater, an isotherm appears on the target plate. A series of local heat transfer coefficient conditions are obtained over the target surface by using several power settings. The contours provide a better understanding of the impinging jet flow field than average results discussed

previously. Since only one isotherm at a time can be seen using a single liquid crystal material, in order to get meaningful data for a particular jet Reynolds number many tests must be performed. Each test can take tens of minutes of settling time and this seriously restricts the data rate. As for the transient method, discussed in Section 3.6, care must be taken in the use of liquid crystals. The crystals must be correctly calibrated, and, since the crystals are sensitive to ultraviolet light, their calibration and response must be checked over the duration of the test series. Since liquid crystals operate by reflecting light, the light intensity from the coated surface is directly proportional to the illumination intensity. The resulting patterns must be recorded optically. An image processing system can help simplify data acquisition and reduce the time necessary to process the data [**Baughn and Yan (1991)**]. The transient liquid crystal technique was applied to the current experiments since it has a significantly higher data rate than steady state methods.

3.6 Transient Liquid Crystal Technique

The transient technique allows the local heat transfer coefficients over the entire surface of the target plate to be found in a single, short duration experiment. Initially, room temperature air flows through the test section, Figure 3.5, and the flow rate is adjusted to match flow during the heat transfer experiment. Flow is then diverted through the bypass and the electrical heaters switched on. The heat transfer experiment starts when air is rapidly diverted back through the test section, thus achieving a necessary step change in gas temperature. As the air passes over the test model surface, the surface heats up and passes through the liquid crystal colour

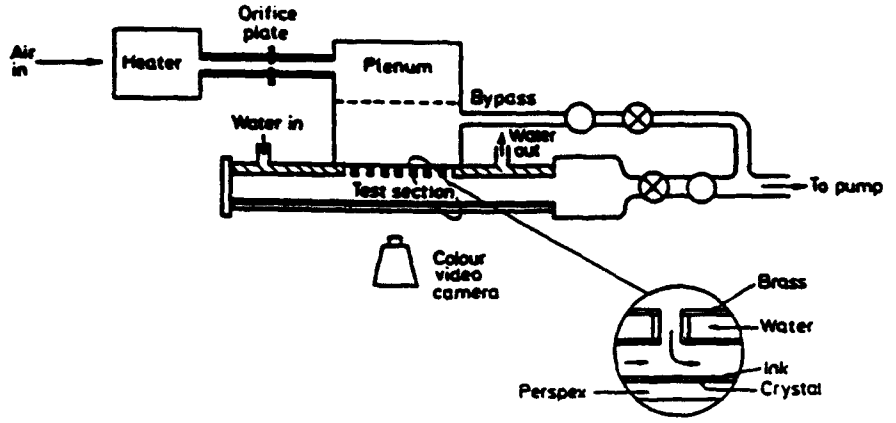

Figure 3.5 Experimental apparatus **[Van Treuren et al. (1993)]**.

display temperature. As the surface temperature increases, isotherms (which are seen as contours of constant colour) move over the surface. The time taken for the surface temperature to reach the colour display temperature enables the local heat transfer coefficient to be calculated. The areas that change colour soonest represent the areas of highest heat transfer (for example, directly beneath an impinging jet). Throughout each experiment, the contours move from areas of high heat transfer to regions of lower heat transfer. The test is recorded on video tape using a standard domestic video system. The time necessary for the colour to change at a given point, together with a knowledge of experimental temperatures, enables the local heat transfer coefficient to be calculated. Certain conditions are met to simplify the thermal analysis. Firstly, before the test begins, the complete perspex model must be at a

uniform temperature. Obviously, room temperature variations could affect the initial target plate temperature and care is taken to ensure that the room temperature remains uniform. One factor which limits the duration of the experiment is the time taken for the thermal pulse to travel through the target plate material. A 12mm perspex plate has a characteristic time, ℓ^2/α, [see **Schultz and Jones (1973)**] which permits test times of up to two minutes. It is also important to ensure that the change in gas temperature at the start of the test is close to a step change. In order for this to be achieved, flow establishment times must be short compared to the time for the liquid crystal to change colour. In the design of the present experimental apparatus the inclusion of an independently controlled plate temperature added another challenge. Since the jet plenum and impingement plate are at different temperatures, the adiabatic wall temperature and the heat transfer coefficient are unknowns. To solve this system requires a special application of the transient liquid crystal technique.

3.6.1 Double Crystal Technique for Intensity History

The double crystal technique uses the peak value of intensity or brightness reflected from the liquid crystal surface. This intensity peak, occurring at a measured test time and previously calibrated to a known temperature, uses the analytic solution given in Equation 3.30 to determine both the unknown heat transfer coefficient and unknown T_{aw}. It was originally used to account for surface temperature non-uniformity in a heated model, **Jones and Hippensteele (1987)**, and the technique has been adapted in the case of impinging jets to measure driving gas temperature. A coating which is a combination of two separate liquid crystal materials is used to

indicate two temperatures. Equation 3.30 can be written twice and the two simultaneous equations solved for h and T_{aw}. **Ireland and Jones (1987)** found that the technique is sensitive to experimental uncertainties and requires accurate temperature measurements and precise determination of the colour change times. Video image processing introduced by **Wang et al. (1993)** greatly improved accuracy of the later measurement. Care must be taken in choosing the crystal temperatures to minimise experimental uncertainty. Crystal temperatures must be sufficiently separated and the difference between the gas and crystal temperatures must be large enough to minimize errors.

3.6.2 Analytic Solution for Hue History

The near complete surface temperature history, provided by the variation in hue (colour) with temperature, in a sense, over specifies the problem by having more information than necessary to determine h and T_{aw}. It can be easily seen that only two temperature time coordinates need to be selected and processed using the procedure outlined previously. A better processing method uses a regression procedure to chose values of h and T_{aw} to produce the best fit of T_s calculated using Equation 3.30 to the measured temperature history. The technique is discussed in detail in Chapter 5 and the uncertainty, as has been described in **Wang et al. (1994)** and reported in **Van Treuren et al. (1994)**, in Chapter 6.

CHAPTER 4 - EXPERIMENTAL DESIGN

This chapter details the experimental design and modifications required to the Oxford University internal cooling test facility to accommodate an array of impinging jets. Engine representative conditions gave initial constraints to the experiments. Once final design parameters were decided, the actual impingement plates were built and installed. Modification to the test rig included design of a new orifice plate, water circulation system, and control panel. Finally, the selection of appropriate liquid crystals enabled the collection of accurate data to begin. For clarification, use of the term "jet row" generally refers to a line of jets perpendicular to the crossflow.

4.1 Initial Design Constraints

Impinging jets of air have been widely used in the cooling of turbine blades for many years. A survey of some array geometries, both inline and staggered, and

Table 4.1 Summary of engine array geometries and conditions.

Parameter	Engine	Rolls-Royce	Model
z/d	1.5 - 4.2	1.2 - 6.6	1, 2, 4
x/d	4 - 14	1.1 - 15.6	8
y/d	4 - 12	3.4 - 12.2	8
ℓ/d	.31 - 1.2	.5 - 1.2	1.2
Re_j	3600 - 17,800	3500 - 42,000	3500 - 40,000
d (mm)	.25 - .66		5
u_j (m/s)	46 - 208		
ρ (kg/m**3)	12		
M	.23 - .55		

conditions for existing engine designs are given in Table 1. Shown are some engine data from the literature survey, Rolls-Royce data, and the eventual values selected for the test model. The choice of diameter fixes the actual physical size of the test rig and massflow requirements and its selection will be discussed below. The chosen channel height to jet diameter ratios, z/d, are representative of the range found in actual engines with the most common z/d being 3.0. The choice of the ratio of streamwise distance between holes to jet diameter, x/d, and the ratio of spanwise distance between holes to jet diameter, y/d, are representative of a widely spaced array. For the present design, the array jet spacings were x/d and y/d ratios, or pitch, of 8 and 8 respectively. The impingement plate thickness to jet diameter ratio, t/d, in engines is mostly on the order of 1 and a value of 1.2 was chosen for the present work. The range of Re_j is quite large and it was planned to develop a test rig which would encompass the range 3,500 - 40,000. Many impinging array designs have initial crossflow to jet mass velocity ratios, G_c/G_j, of 0 indicating no crossflow is present at streamwise jet row number one. Other designs have spent flow from upstream impingement zones influencing the first streamwise jet row. The present apparatus was designed to be capable of obtaining an initial crossflow G_c/G_j of up to 1.0 at streamwise jet row number one.

4.2 Impingement Hole Geometry

The exact geometry of the hole edge at the entrance to the impingement jet hole is of importance to the impingement array thermal performance. **Benedict et al. (1974)** and **Hay et al. (1987)** both show that changing from a sharp edged inlet to

a rounded inlet increases the discharge coefficient. **Obot et al. (1979)** showed that, for short nozzles (ℓ/d = 1), a sharp-edged nozzle gives at least 20% higher *Nu* averaged over the target surface than a rounded nozzle for a $z/d = 4$. This effect was shown to be due to the influence of inlet geometry on the mean velocity and turbulence profiles at the nozzle exit and resulted in the sharp edged nozzle yielding a higher average *Nu* for values of z/d up to 8. The smaller the value of z/d the more pronounced the difference. They point out that most researchers do not report the type of edge used in testing. Jet hole edges can greatly influence both the turbulence intensity and velocity at the jet exit. Both **Gardon and Akfirat (1965)** and **den Ouden and Hoogendoorn (1974)** also show increases in *Nu* with increasing turbulence intensity. The selection of an inlet hole geometry for the current experiments was then predicated by the type in use in current engines. Three sample blade inserts, supplied by Rolls-Royce, were examined using a Scanning Electron Microscope (SEM) to determine the geometry of the hole inlet. The results are shown in Figures 4.1, 4.2, and 4.3. All of the holes were laser drilled and the blade inserts themselves were from operational engines.

Sample blade insert A, in Figure 4.1, has a inline array on the blade suction surface with each streamwise jet hole offset slightly toward the trailing edge with outward blade radial position. At the suction surface, the impingement insert has a jet hole diameter of 0.48mm and a thickness of 0.36mm which gives an $\ell/d = 0.75$. The streamwise and spanwise spacing of the array is $7d$ and $5d$ respectively and the number of holes in the streamwise direction varies from 2 to 6, with the maximum occurring at the midspan region. On the pressure surface, the jet hole diameter is

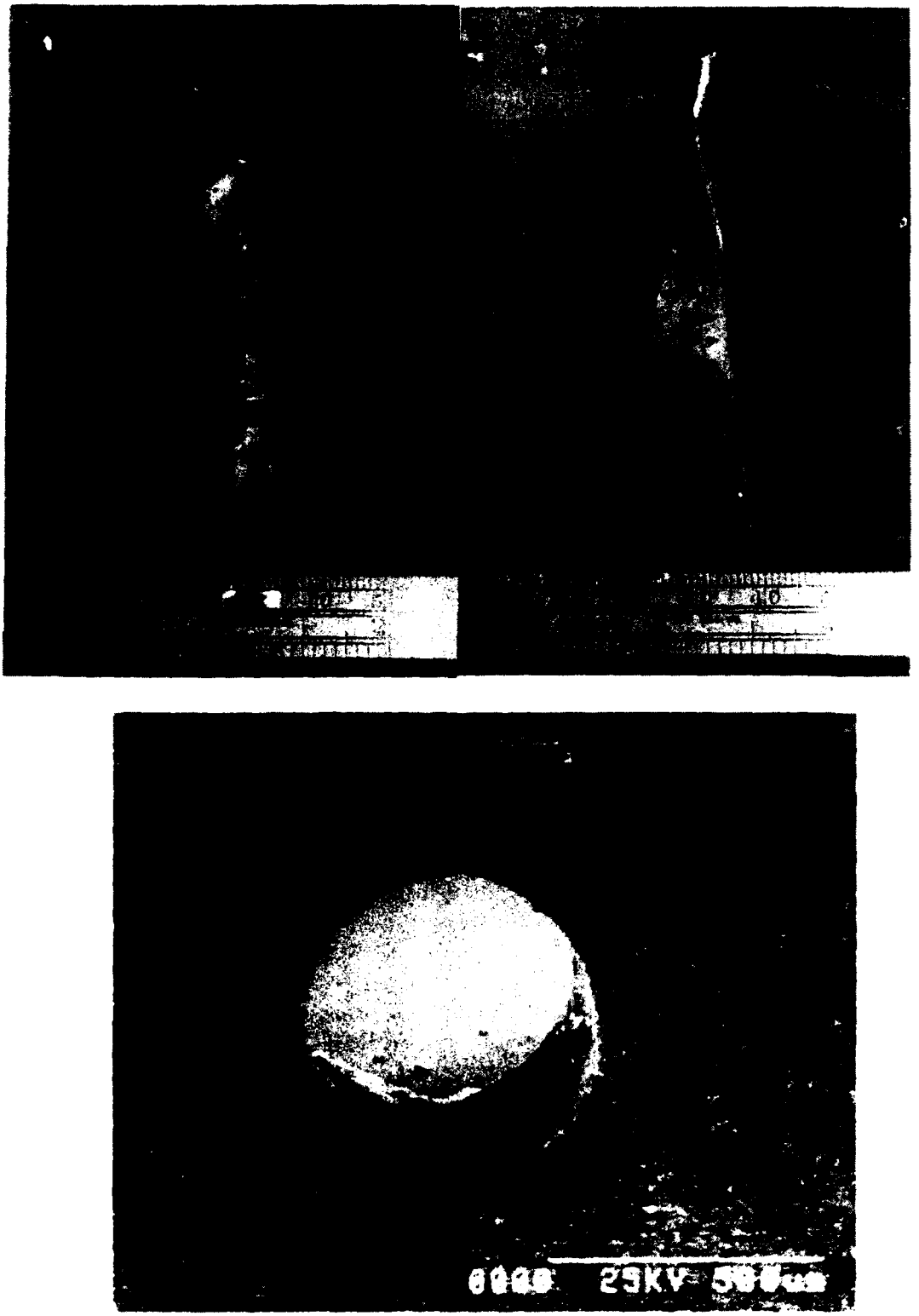

Figure 4.1 Sample blade insert A: suction surface, pressure surface and jet hole (jet hole image from Scanning Electron Microscope).

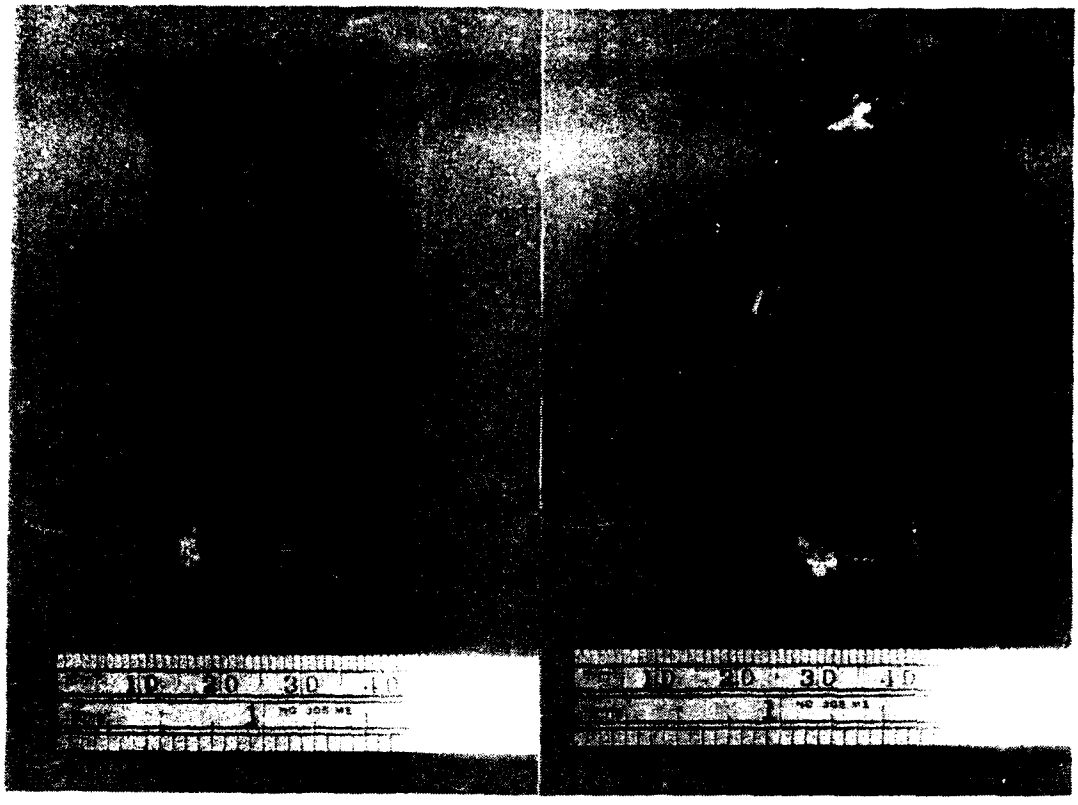

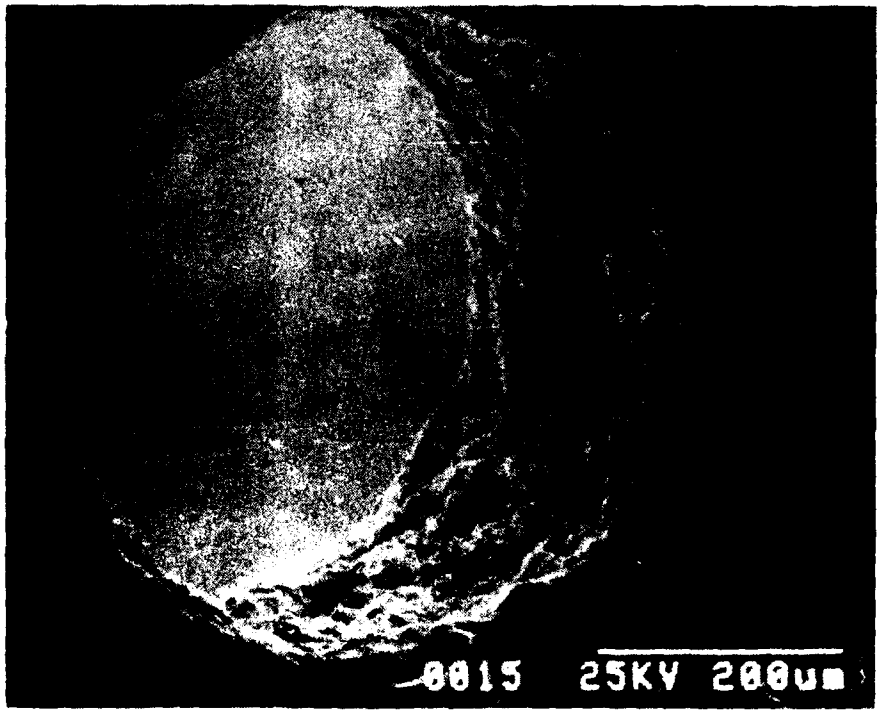

Figure 4.2 Sample blade insert B: suction surface, pressure surface and jet hole (jet hole image from Scanning Electron Microscope).

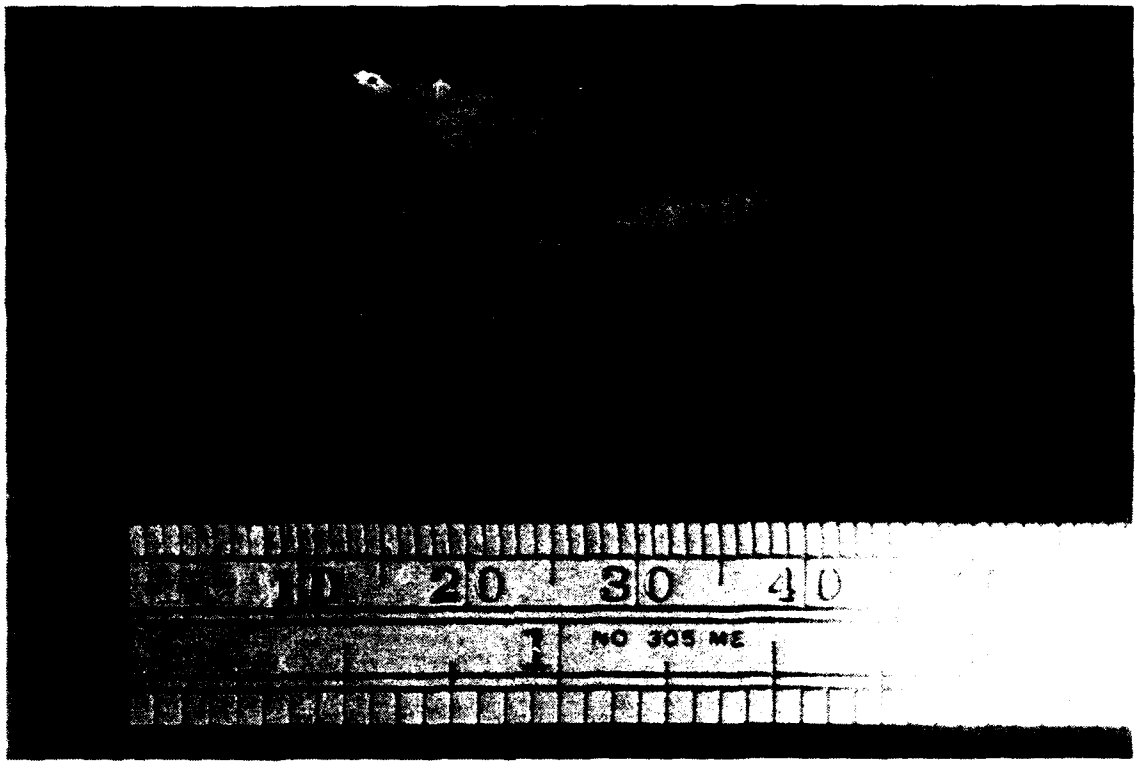

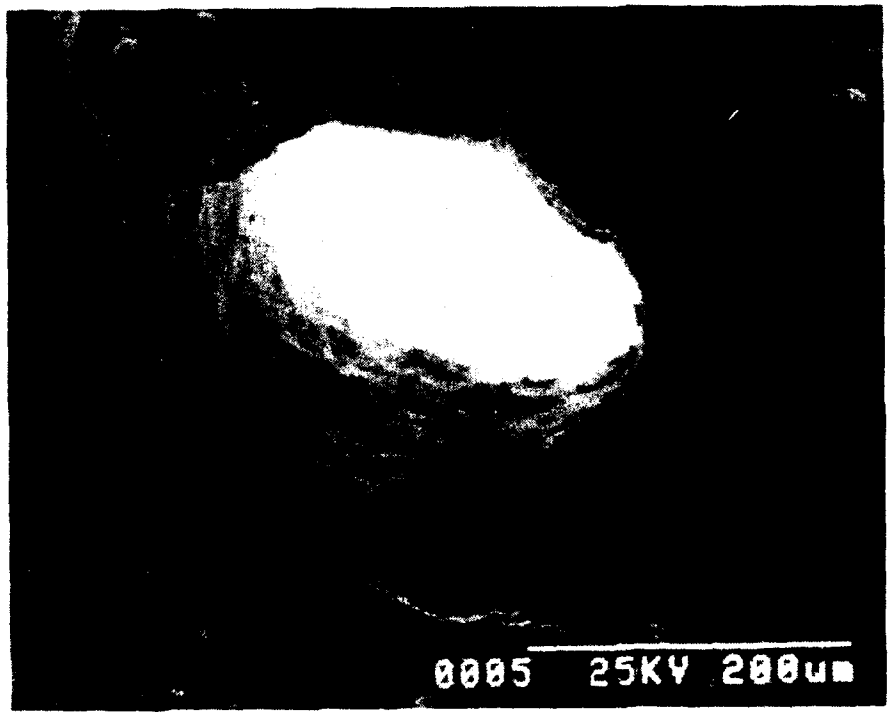

Figure 4.3 Sample blade insert C: planview and jet hole (jet hole image from Scanning Electron Microscope).

0.95mm and the holes are arranged in an inline array with three jet rows at the midspan region. The first two jet rows have a spacing of 2x3 and the third is located 4*d* downstream. Examination of the inlet edge of a suction surface jet hole, representative of laser drilled holes on the blade, reveals the edges to be sharp and the shape circular.

Sample blade insert B, in Figure 4.2, has a jet hole diameter on the suction surface of approximately 0.42mm and thickness of 0.46mm giving an $\ell/d = 1.1$. The arrays are arranged in a staggered configuration. The surface has a maximum of six jet rows in the midspan region that have a spacing which ranges from 6x6 to 3x3 at the hub and tip. The last jet row is located approximately 14*d* downstream of the previous jet row. This last row of jets begins a new impingement zone which the spent flow exhausts out the blade trailing edge. The upstream array flow exhausts through film cooling holes and thus, would never influence the last streamwise jet row. The pressure surface spacing is 3x3 in the midspan region with a maximum of 7 jet holes at this location having a diameter of 0.48mm. This number of jet holes decreases to three at the tip. Near the blade hub, the spacing increases to 6x6 decreasing the number of jet holes to three and four depending on the row. Again, a gap (in this case 11*d*) exists between the fourth and fifth jet rows at the midspan region that extends over the entire insert in the radial direction. The inlet in this sample also appears circular and sharp-edged.

The last sample blade insert, C in Figure 4.3, is an inline configuration with a jet hole diameter of 0.3mm and thickness of 0.32mm giving an $\ell/d = 1.06$. This section had a spacing (larger dimension to smaller) of 3x4 with at least 22 holes in

LASER ACOUSTIC

Figure 4.4 Laser and acoustically drilled hole comparison [**DeMeis (1991)**].

the larger dimension and 10 in the smaller dimension. Of the three samples, this insert had the most irregular inlet edge where small portions of the material had flaked off. Based on the samples, a circular jet hole with sharp edges was chosen for the current experiments as representative of current manufacturing technology. This type jet hole inlet also allows comparison with data from other work found in the literature. In the future, the use of acoustic methods would produce a very well defined edge (Figure 4.4). Alternatively, investment casting of impingement holes could be used to produce a radiused corner.

4.3 Similarity Considerations

Similarity analysis is used to ensure that the experiment accurately models the engine conditions. The first step in the dimensional analysis is to identify the

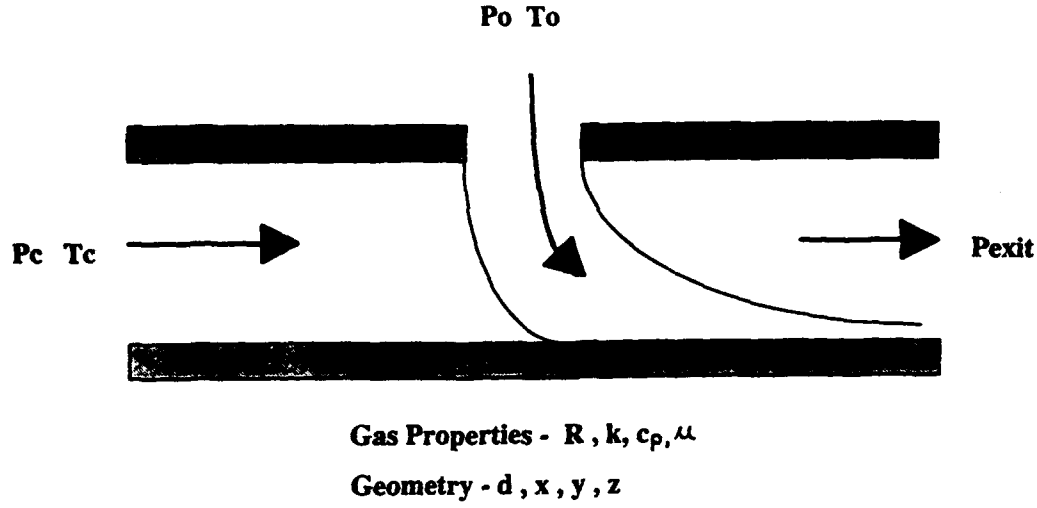

Figure 4.5 Significant parameters for determining heat transfer coefficient which were used in the similarity analysis.

parameters which determine the flow field and the temperature field for the jet array. The significant parameters which determine the heat transfer coefficient, Figure 4.5, are:

$$h = h\,(P_c, T_c, P_o, T_o, R, c_p, \mu, k, d, P_{exit}, z, x, y) \quad (4.1)$$

Given these 14 parameters, Buckingham's Pi theorem can be used with the fundamental units chosen as M, L, t and θ, to show that the 10 independent dimensionless groups may conveniently be chosen as:

$$\frac{h\,d}{k} = \frac{h\,d}{k}\left(\frac{P_o}{P_{exit}}, \frac{P_o}{P_c}, \frac{T_o}{T_c}, \frac{c_p\,\mu}{k}, \frac{T_c\,k\,\mu}{d^2\,P_{exit}^{\,2}}, \frac{c_p}{R}, \frac{z}{d}, \frac{x}{d}, \frac{y}{d} \right) \quad (4.2)$$

This relationship can be thought of as:

$$Nu = Nu\ (Exit\ Mach,\ Inlet\ Mach,\ Temperature\ Ratio,\ Pr,\ Re,\ \gamma,\ Geometry) \quad (4.3)$$

Matching geometry is achieved by scaling existing engine configurations. The ratio of specific heats, γ, is matched because cooling air usually comes from the latter stages of the compressor prior to combustion and has the same value of γ as atmospheric air. The Prandtl number, *Pr*, varies little with temperature and pressure and is sensibly the same at the atmospheric conditions used in the apparatus as it is in the engine. Representative engine temperatures would be approximately 925 K for the jet plenum and 1050 K for the target surface (inside surface of the turbine blade) temperature. When initial crossflow is present in the array, it would have a temperature, after leaving the plenum, between these two temperatures. This is because it would have picked up some energy in cooling locations upstream of the array under consideration. It was planned to approximate the absolute temperature ratio of jet plenum to initial channel crossflow by using a T_c higher than T_o. Absolute temperature ratios, T_c/T_o, T_f/T_o and T_p/T_o, are close to unity for both the engine and experiment. In order to estimate the effect of not matching temperatures, the approach of **Kays and Crawford (1980)** was used. They suggest a property ratio scheme to account for the effect of the variation of the transport properties with temperature

on Nusselt number. This scheme corrects the constant property value by multiplying by a ratio of surface to freestream temperature raised to an exponent. This exponent depends on the type of flow considered. For this experiment, the freestream to surface temperature ratio is furthest from unity at the start of the test. The difference between Nusselt number correction factors for the engine and experiment is always less than 2% for the turbulent boundary layer. Under a stagnation point the difference is less than 1%. Thus, the influence of the absolute temperature ratios is small. The present apparatus will be adapted to investigate the influence of initial crossflow in future experiments.

Assuming that air behaves as a perfect gas (constant γ and R) and that viscosity is proportional to the square root of temperature, it can be shown that if both Mach number and Reynolds number are matched then:

$$\rho_{model}\, d_{model} = \rho_{engine}\, d_{engine} \tag{4.4}$$

where d is the jet diameter and ρ is the density of the coolant at stagnation (or supply) conditions. Using an engine representative density of 12 kg/m^3 and engine diameters between 0.25-0.5mm yields model diameters of 3.0-6.0mm for a model density of 1 kg/m^3. For conditions with high Re_j and large channel height ($z/d > 1$), the pressure drop through the array is mainly across the jet holes rather than along the channel. At sufficiently low exit pressure, choked flow occurs at certain jet holes. For engine conditions with high Re_j and small channel height ($z/d = 1$), the channel itself can choke. Compressibility was encountered but, for the present range of average Re_j and

jet hole diameter, choked flow did not occur across the jet holes.

One parameter missing from the similarity considerations is the Biot number defined below as:

$$Bi = \frac{h\, L_c}{k_{solid}} \tag{4.5}$$

This is a parameter which provides a measure of the temperature drop in a solid material relative to the temperature difference between the surface and the fluid. A Biot number, Bi, $<<$ 1.0 would mean the material is at a uniform temperature for the characteristic dimension of thickness. A large Biot number would indicate the material has a temperature gradient across its thickness. In the current experiments the scaled Biot number would still be sufficiently small not to be a factor. In addition, one of the boundary requirements for the experiment is holding the temperature of the impingement plate constant which, in a sense, forces the Biot number to be small and therefore not something which needed to be matched between the engine and experiment.

4.4 Array Geometry Selection

Specification of the array geometry consisted of determining the number of streamwise jet rows, spanwise jet rows and jet hole diameter. These parameters fix the physical dimensions of the test section. An acceptable solution had to be found within the limitations of the flow capacity and heater capacity of the existing system. The most recent uses of the transient test rig have been described by **Wang (1991)**

and **Byerley (1989)**. The existing hardware consists of an inlet containing electric heaters rated at 36 kW connected to a heater plenum. The maximum possible dimensions of the test section are 2.2 metres long and 0.6 metres wide. The test section can accommodate various depths up to 0.12 metres connecting to an exhaust outlet. Air is pulled through the transient rig from atmospheric pressure to 0.1 bar absolute with a water ring pump which is capable of a volumetric flow rate of 0.471 m^3/sec. Massflow through the system then depends on the density present at the water ring pump making it necessary to limit pressure loss in the system. A bypass system is connected between the heater plenum and pump to enable the heaters to reach thermal equilibrium before the transient test starts. A system of gate valves control the actual flow conditions during the run and bypass phases. Fast acting valves, which operate within 0.1-0.2 seconds, switch between conditions. The present experiments required that extensive modifications were made to this rig to study several different impingement arrays with adjustable initial crossflow to jet mass velocity ratios. In addition, it was intended that the jet temperature could be adjusted relative to the crossflow temperature and that there be a means of keeping the jet impingement plate temperature constant.

With these constraints in mind, a series of spreadsheets was written to explore various designs in an analysis of the flow which included compressibility and viscus pressure loss. Given the engine representative parameters previously discussed, various array geometries were investigated which sought to maximize hole diameter using available massflow. With the combined maximum values of Re_j, initial G_c/G_j, and z/d, the airflow requirements were used to determine the maximum jet hole

diameter possible within the design constraints. The analysis showed that, at the very highest Re_j and lowest z/d, the tunnel exit would choke. This condition required a larger scale to achieve Re_j without choking the tunnel exit. At the larger scale, the apparatus required a high massflow which would encounter a pump capacity limitation. More rows of holes in an array configuration also requires more massflow. The array would not be engine representative if too few rows of holes were used.

The first step in determining the final array geometry was to decide the number of streamwise and spanwise rows. The chosen inline array configuration had five spanwise rows and eight streamwise rows giving a total of 40 jets. Five spanwise holes ensured that the centre streamwise row would be free from wall influences. The eight streamwise holes were engine representative and allowed sufficient streamwise distance to observe the effect of crossflow influencing the jets as noted in the literature. The staggered array had four fewer holes as the even numbered streamwise jet rows were offset half a pitch in the spanwise direction. **Florschuetz et al. (1980)** experimented with staggered arrays and concluded it was not necessary to include half jet holes at the sidewall to make the flow field insensitive to edge effects. For this reason, half holes were not included in the current experiments.

Fixing the number of holes then enabled the jet hole diameter to be determined. A value of $G_c/G_j = 1$ at the first streamwise row and a $z/d = 4$ and $Re_j = 40{,}000$ corresponds to the condition requiring maximum massflow. A jet hole diameter of 5mm allowed most test conditions to be covered. It was anticipated that rig limitations would be encountered at the low z/d and high Re_j conditions depending on the channel friction factors. In addition, it would prove difficult to cover the high

Re_j high z/d experiments because of pump capacity limitations. The array plates used are shown in Figure 4.6 for the inline array and Figure 4.7 for the staggered. The diameter chosen gives the model an approximate scale of 10-20 times actual engine size. Having chosen the pitch, the widely spaced jet array plate (8x8 pitch) then required manufacture of a 1.5m long, 0.2m wide array plate with a 0.7m section ahead of the array of impingement holes which connects to the heater plenum. The array itself is midway along the plate to allow fully developed flow to be achieved ahead of the array and sufficient downstream channel for future studies of impingement with other methods of heat transfer enhancement.

4.5 Orifice Plate Design

The jet plenum feed, orifice, insulation, and water circulation system are shown in Figure 4.8. To minimize pressure loss through the rig and ensure sufficient massflow, 4 inch diameter pipework was used to supply heated air to the jet plenum. The air passed from the heater plenum through a gate valve which will be able to regulate the amount of air from the heater box during future tests with initial crossflow. This valve was always fully open during tests with no crossflow initially. Downstream of this valve the air enters a 4 inch tee section which included another 4 inch gate valve to allow cooler room temperature air to be mixed with the heater air. In this way a plenum temperature which is lower than the initial crossflow temperature can be achieved. For tests without initial crossflow, this valve was fully closed. Downstream from where the two flows combine in the tee is another 4 inch gate valve which will be used to control the total flow to the jet plenum in tests with initial

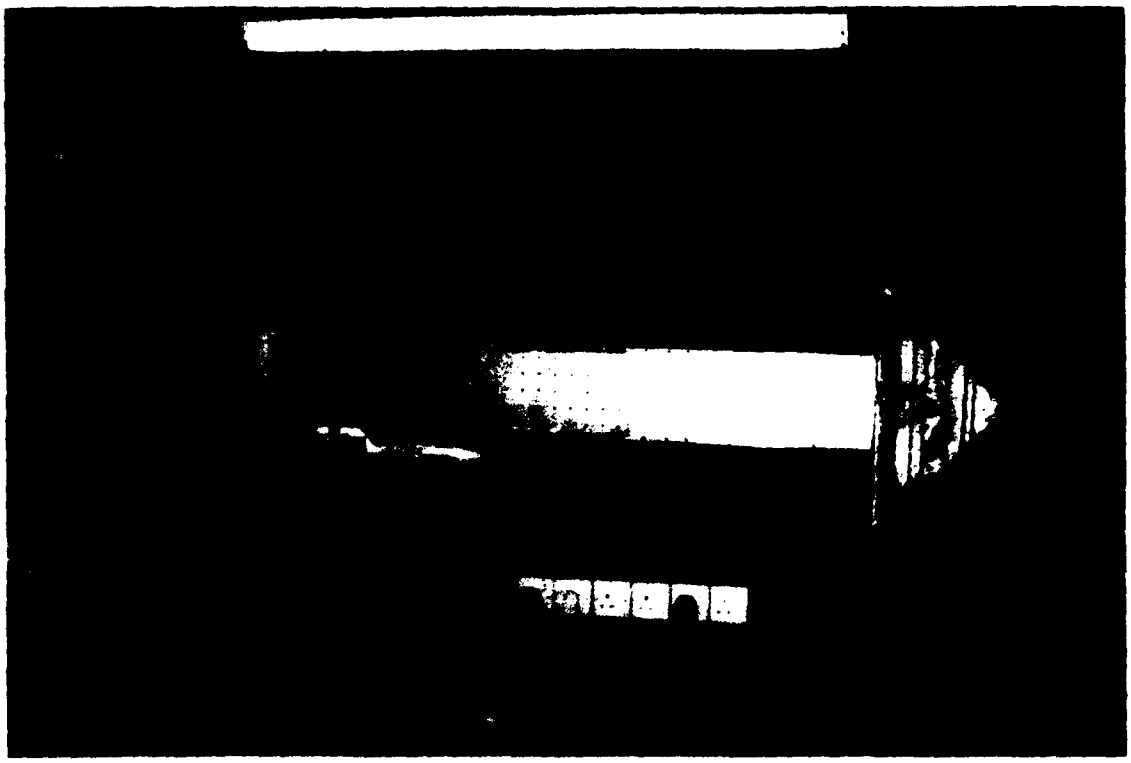

Figure 4.6 The inline array plate connected to the exhaust pipe.

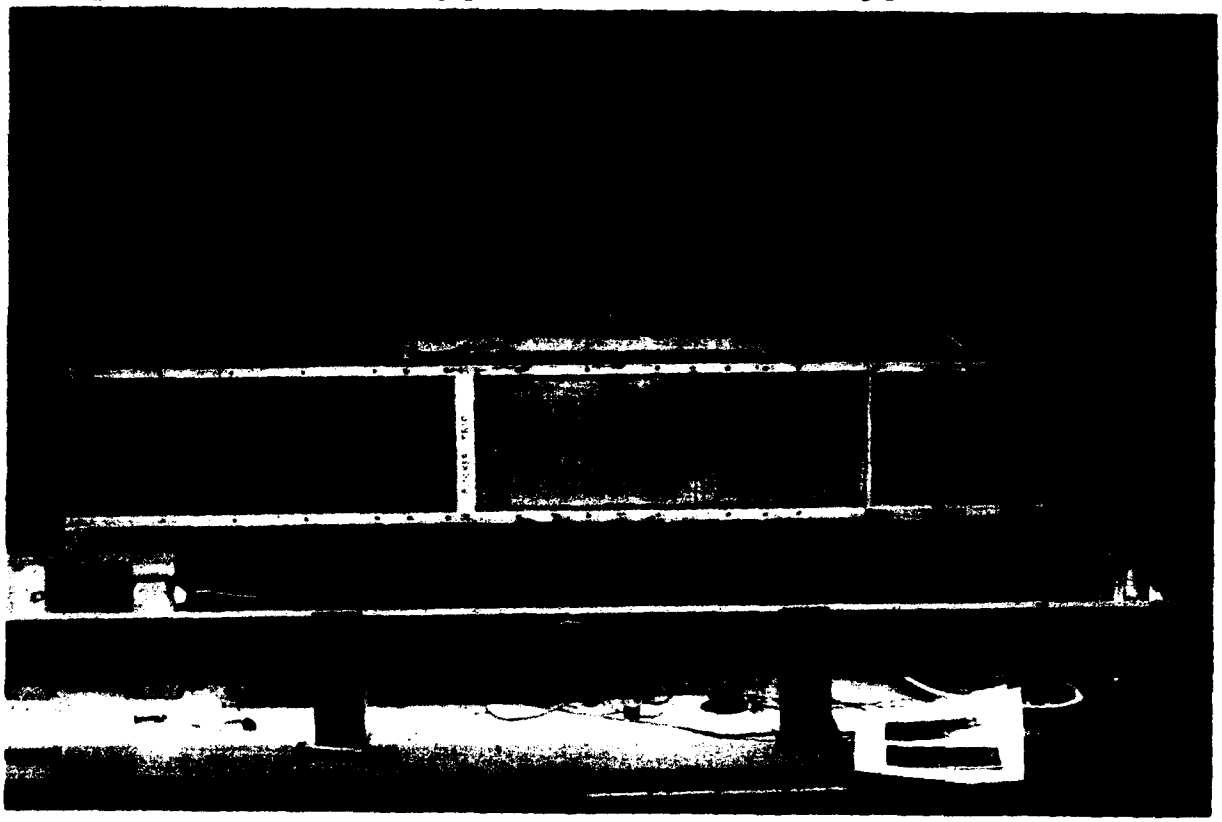

Figure 4.7 The staggered array plate connected to the exhaust pipe.

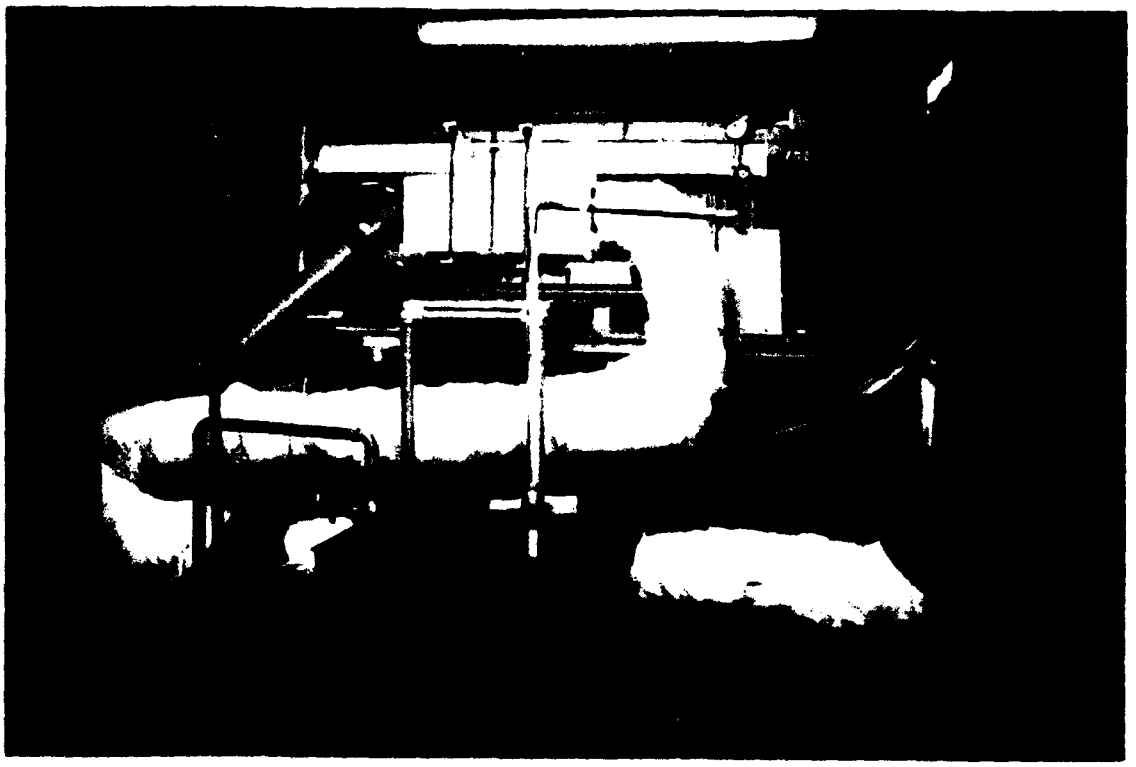

Figure 4.8 Rearview of the experimental apparatus showing orifice, insulated pipework, jet plenum and water circulation system.

Figure 4.9 Detail of the inlet to the jet plenum box.

crossflow. For tests without initial crossflow this valve was fully open. From this point, 4 inch diameter PVC pipe was used to route the heated air to the plenum. The PVC pipe has an upper temperature limit of about 70°C which is above the required jet temperature. A gate valve downstream of the test section set the flow required for the actual test. Another gate valve in the bypass controlled the flow during the heater warm up phase for the tests with no initial crossflow. An orifice plate meter designed to BS1042 was included in the 4 inch pipe. To minimize pressure loss in the jet plenum feed pipework a different orifice plate was used for each required Re_j. The internal diameter of orifice holes used caused a pressure loss of less than 4 inches water gauge at the jet impingement hole. All piping was covered with 2 inches of fibreglass insulation to minimize heat loss to the test room (which could influence initial reference temperatures for the target surface) and to decrease the time required to achieve a steady pipework temperature upstream of the plenum.

4.6 Array Plate Manufacture and Water Circulation System

The requirement to hold the array plate temperature constant during the test run meant that the test plate had to be actively cooled. Since the plate thickness to jet diameter ratio was fixed at 1.2, this engine geometry was reproduced with a hole diameter of 5mm using a thickness of only 6mm.

Brass plates 1.5mm thick were chosen for the inline array as the outer panels leaving a 3 mm wide interior channel. The selection of brass as the plate material allowed the impingement plate to be soldered together. Even limiting the maximum design gauge pressure to 1 bar, meant that internal supports were needed to reduce

plate deflections to an acceptable level. Analysis from **Young (1991)** led to the inclusion internally of 1cm wide strips at 5cm pitch on centre line in a streamwise direction. The jet holes were formed from brass tubes reamed to 5mm internal diameter and machined to include a shoulder at each end to enable the tube to be soldered to the brass plates. Estimates of convective heat transfer to the plate based on reasonable estimates of the channel velocity showed that a limit of 1°C temperature change through the plate required 3.8 kg/sec of water. The pressure difference required to achieve this flow rate, including frictional losses in the channel and piping, was 2.5 bar which was too high for structural reasons. Dropping the flow rate by 50% increased the plate temperature difference to 2°C and dropped the required pressure difference to 0.6 bar. The actual water temperature change across the array test section would be much less. Slight bowing of the array plate which developed during manufacture was alleviated by a system of levered clamps which bent the array test section back to the flat condition. External plate stiffeners were used elsewhere. Once built, the array plate was pressure tested to check integrity. At around 8 psi several pinhole leaks occurred at the array holes. Heating up and cooling down of the plate along with stresses induced in handling the plate were sufficient to cause cracking of some of the soldered joints. A technique for sealing these leaks was developed using **Locktite Engineering Adhesive 290** with an internal vacuum. The first system installation used positive pressure water circulation and consisted of a water storage tank, pressure gauge, associated pipework and valves and a pressure relief valve set at 0.5 bar as a safety measure. When operated, the plate temperature would increase slightly over a period of tens of minutes but during the short duration

of the transient test its temperature could be taken to be constant. Since the purpose of the water cooling system was to maintain a constant plate temperature during the test, no attempt was made to regulate the temperature other than putting ice into the main water storage tank to maintain a water temperature close to the perspex initial temperature and avoid the jet plenum influencing the target surface during the bypass phase.

When the rig was first operated, the subatmospheric tunnel channel pressure increased the pressure differential between the plate and channel which caused leaks to develop. A decision was made to use the pump to pull the water through the array plate and operate the water channel at subatmospheric pressure. This met with great success and all the water leaks were stopped. The pressure relief valve was removed and a vacuum gage included upstream of the array plate. This gage indicated the water driving pressure difference and allowed leaks to be detected when the vacuum level dropped. Figure 4.8 shows the water circulation system used.

The staggered array used a different method of construction. To avoid the buckling problem caused by localized heating of the plate during soldering, a bonding adhesive, **Locktite 580**, was used to glue the plate together. This material was similar to the material used to fix leaks for the inline plate though more viscous and with a much higher strength. The plate material was **Dural** and bracing and hole manufacture was essentially the same as for the inline case. Two small leaks occurred initially on end seams. These were quickly fixed by applying the viscous adhesive to the seam. The standard system vacuum was used to draw the material into the leak and, when the vacuum gauge had achieved its normal (sealed) operating value, the rig

was shut down and left overnight. No further problems were noted. The glue technique was found to be quite robust and the glue not affected by the water flow.

4.7 Plenum/Bypass Design

The plenum was designed to provide a uniform flow of heated air to the jet array. The final plenum configuration consisted of a 0.5 m x 0.5 m x 0.2 m box made of 1 mm thick galvanized steel (see Figure 4.9). It was bolted to the outside of the brass array plate and centred over the array itself. The plenum acted as a large stilling chamber and produced a feed geometry which is representative of that used in engines. Between the air entrance to the plenum and the jet impingement plate was a flow straightener, a perforated metal which includes 4.5mm diameter holes of $A_{hole}/A_{surface}$ = .39761. The perforated sheet was sufficiently far from the jet inlets to allow the multiple jets formed enough distance to mix out prior to entering the jet holes.

Heating the plenum during the bypass phase to an equilibrium condition also proved to be a challenge. Consideration of the plenum velocities expected during testing showed that buoyancy forces were significant at low Re_j. Care was taken to select the correct plenum material to minimize heating times. A study was done to calculate insulation heating times and equilibrium temperatures. By using 1 mm steel with 1 inch exterior polystyrene, the Biot number of the plenum wall was kept low. Plenum heating times were on the order of 45 minutes to one hour for low flow rates.

At the start of the design process there was concern that heated jet plenum air during the bypass phase might disturb the initial temperature uniformity of the target

plate. A shutter system was designed to effectively isolate the jet plate from the plenum. This shutter proved hard to seal and its operation was somewhat difficult in practice. During tunnel commissioning, it was found that the shutters were not needed because a subatmospheric plenum pressure during the bypass phase ensured a small amount of room temperature air from the exhaust pipe flowed through the jet holes from the target surface to the jet plenum. In addition, the water circulation system operating during the bypass phase also helped to eliminate convective heating of the target plate.

It was also necessary to design a bypass from the jet plenum to allow the jet plenum and heaters to reach a thermal equilibrium prior to testing. A pipe downstream of the flow straightener but before the array plate ducted airflow to the water ring pump. A gate valve downstream controlled the massflow during the bypass phase and a fast acting valve isolated the vacuum pump from the plenum chamber. This fast acting valve was expressly designed for the system (see Figure 4.10). It was gravity driven and the plunger is held in place by an electromagnet when the valve was open. Switching the flow through the test section interrupted the electric current to the electromagnet and caused the plunger to fall. The time required for the plunger to fall was approximately 0.15 seconds. During the switching, which initiated the transient test, it was noticed the plenum would undergo fluctuations in pressure which delayed the onset of steady conditions. To minimize the pressure excursions, a rig controller was designed and built which used timing circuits to sequence the above plunger valve and the electrically activated solenoid valves. It was then possible to tune the timer delays to minimize the flow startup time. A new controller box was

designed that sequenced the valves, triggered data acquisition and started an elapsed time signal displayed on the recorded video signal. The switching between rig and bypass operation was achieved by push button control. Lights were included to indicate the position of all system valves. A photograph of the control box is given in Figure 4.11 and a schematic of the control circuit in Figure 4.12. Figures 4.13 to 4.15 show a sample sequence of plenum pressure records taken using a fast response transducer with three different electric solenoid valve delay times. The delay time is adjusted by changing a potentiometer setting.

4.8 Crystal Selection and Array Reference Marking

Narrow band liquid crystals were used for the inline array cases. The colour play temperatures were determined by an iterative procedure which identified different constraints at different zones under the impinging jet. The heat transfer coefficient was expected to be highest under the jet and lowest in the channel remote from the array holes. Times for liquid crystal colour change were calculated using estimates of heat transfer coefficients and achievable jet plenum temperatures. This study confirmed the need for three liquid crystal materials to be used in a composite coating. The higher temperature pair would be used for the relatively short change times under the jet where heat transfer coefficient and driving gas temperature would be calculated using the double crystal technique described in Chapter 3, Section 3.6.1. The lower temperature pair would be used for heat transfer coefficients occurring in the channel. Crystal temperatures of 25°C, 30°C and 36°C were selected. A spreadsheet was used to calculate the local adiabatic wall temperature and heat transfer coefficient. The

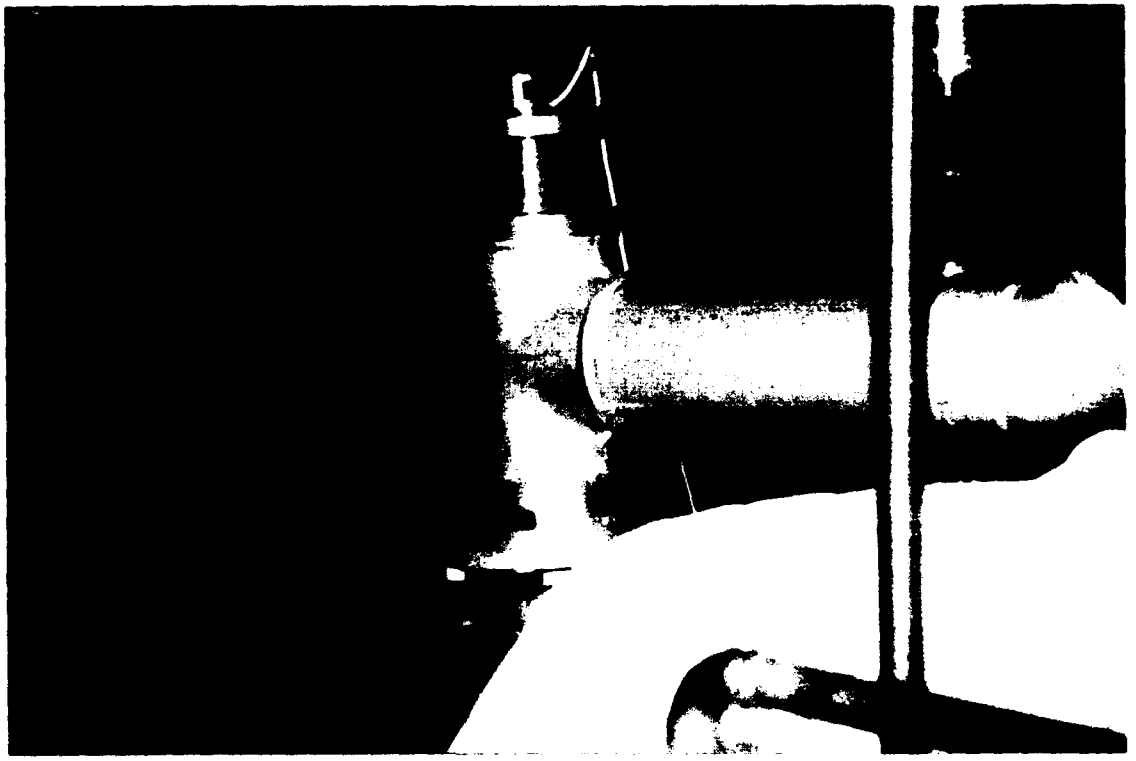

Figure 4.10 The gravity actuated fast acting valve designed to isolate the plenum exhaust during bypass.

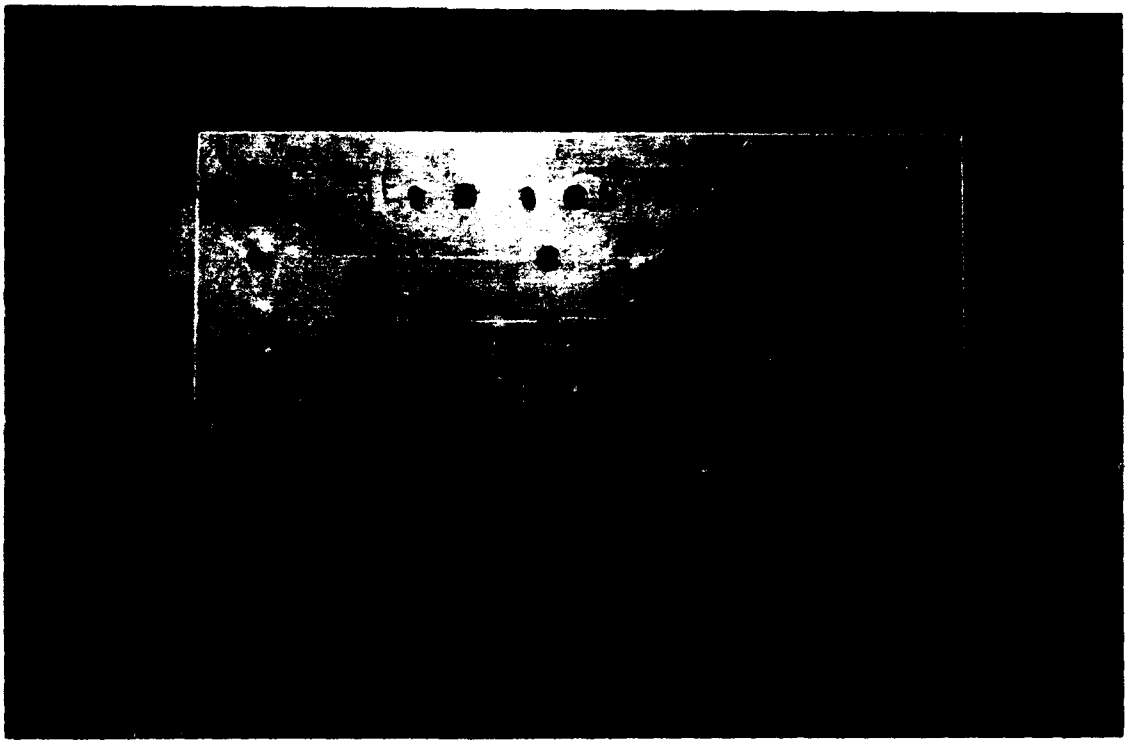

Figure 4.11 Photograph of control box.

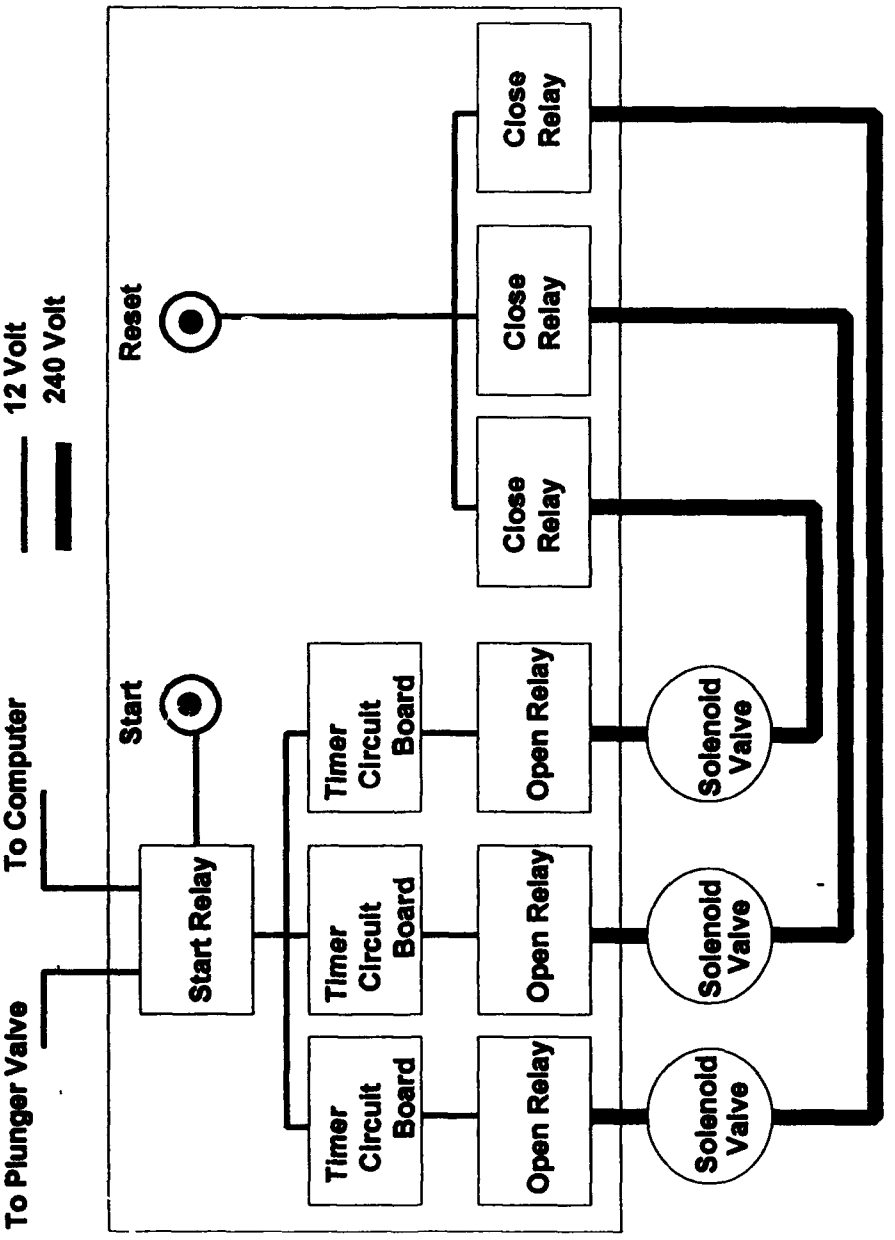

Figure 4.12 Schematic of the control circuit.

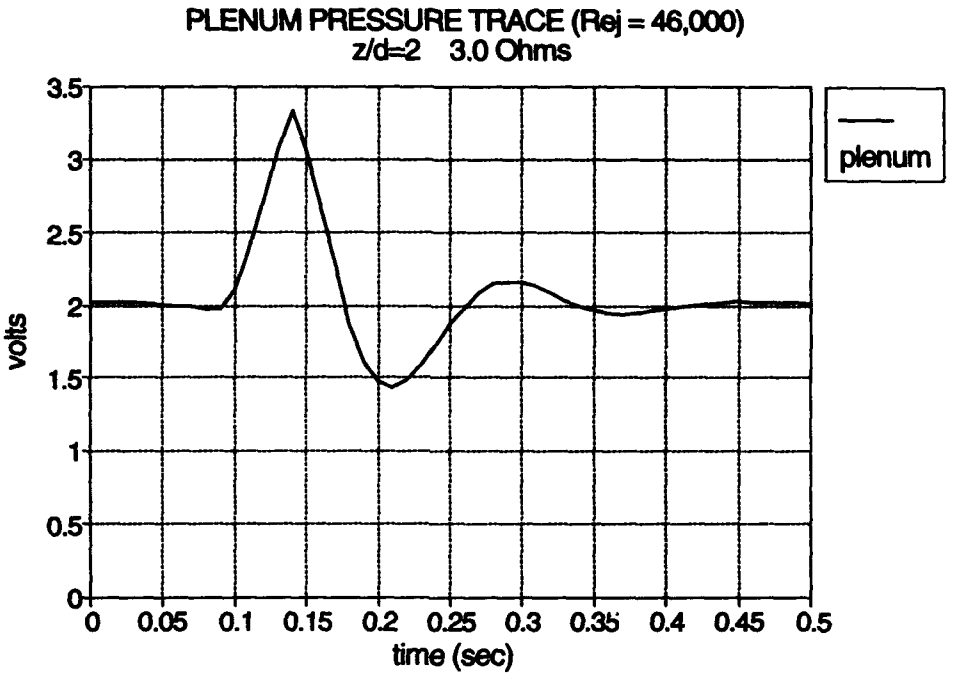

Figure 4.13 Plenum pressure record with a short time delay.

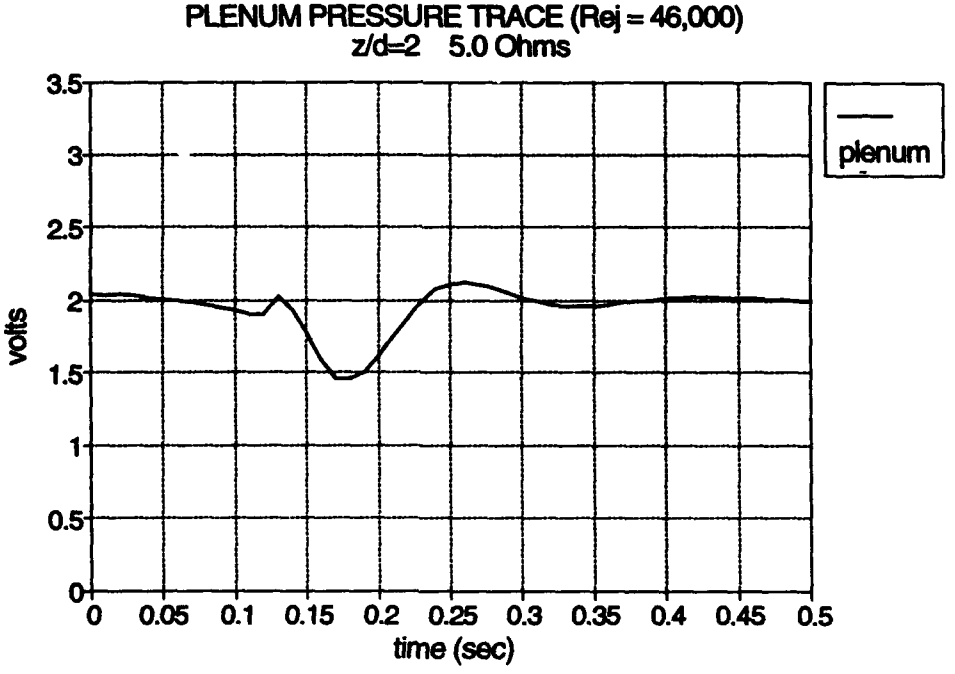

Figure 4.14 Plenum pressure record with a balanced time delay.

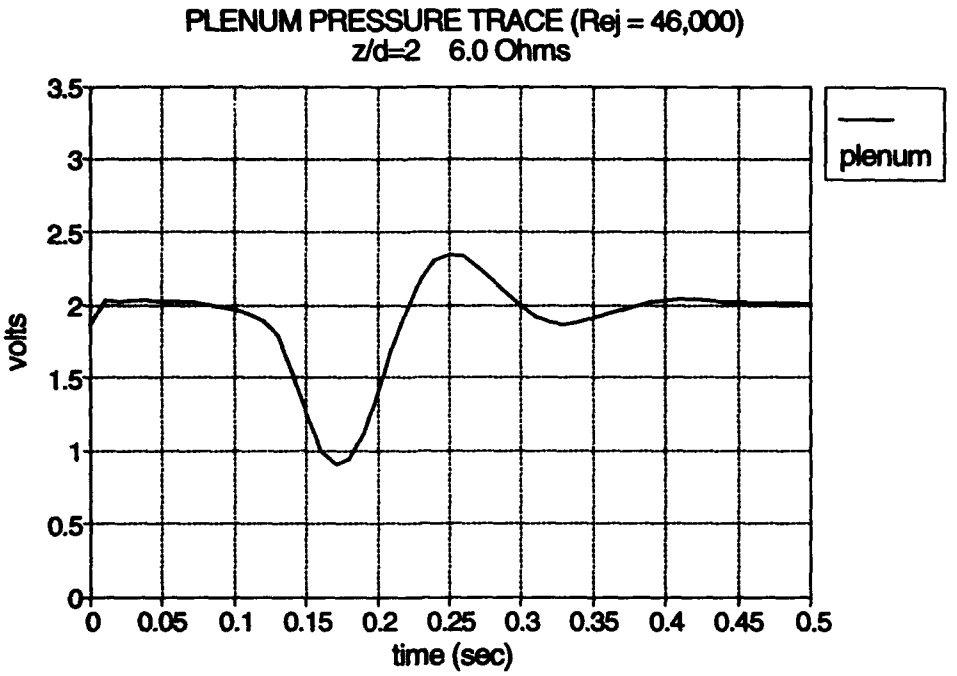

Figure 4.15 Plenum pressure record with a long time delay.

same solution procedure was used to investigate the overall uncertainty in these quantities for measured quantity uncertainties.

A different approach to liquid crystal thermometry was applied to the data acquired for the staggered array of impinging jets. A wideband liquid crystal was used to measure the surface temperature variation throughout most of each experiment. The hue signal was calibrated to surface temperature, as described in Chapter 5. Because of the nature of the information given by a wideband crystal, it was desired that the temperature spread be sufficient to span the projected surface temperature range. With a jet plenum temperature around 40°C it was desirable to use a liquid crystal within a temperature range which extended from the initial perspex temperature to the plenum temperature. The first experiments for z/d = 1 used a crystal with a calibrated range of 30°C to 40°C. A second wide band crystal with a calibrated range

of approximately 25°C to 40°C was used for subsequent tests.

Marks on the target surface were used to provide visible reference locations for image processing. In the past, the surface was scribed which produced lines which were visible in the video image. For the current experiments, the target surface was marked with an acrylic water-soluble white paint manufactured by **Polly-S**. The paint was thinned and applied with a **Rapidograph** pen with nib diameter 0.35mm. Since the paint is water soluble, it has no effect on the crystal and provides an easily visible mark. The inline array tests have small "x" marks located midway between jets in both the spanwise and streamwise directions. For the staggered array, a small dot of approximately the pen diameter was sufficient to be visible on the video frame. The dots were placed on each streamwise jet row line at half jet pitches. The smaller size obscured less of the target surface and smaller pitch improved accuracy.

CHAPTER 5 - EXPERIMENTAL PROCEDURE

This chapter describes the operation and commissioning of the Oxford University internal cooling transient test rig which was modified by the author for the current series of experiments. Although the capability exists to conduct experiments with initial crossflow, only tests without initial crossflow were accomplished and are discussed in this chapter. The potential of the apparatus to investigate the effects of initial crossflow will be used in future research.

5.1 System Description

The experimental apparatus is shown in Figure 5.1 and 5.2. The existing hardware consisted of an inlet chamber which housed a 36 kW bank of electrical heaters connected to a plenum. The heated air travelled through 4 inch diameter pipe containing an orifice meter to a second plenum which directly fed the impingement array. This jet plenum, which had dimensions 0.5x0.5x0.2m, included a flow straightener set parallel to the impingement plate. The impingement plate thickness to hole diameter ratio was 1.2 and the perspex target plate set at 1, 2, and 4 hole diameters from the impingement plate. The jet hole spacing was $8d$ in both the streamwise and spanwise directions. The array plates were manufactured from sheet metal and included a water channel which was used to hold the impingement plate temperature constant throughout each transient experiment. The inline array had eight rows of 5mm diameter holes in the streamwise direction and five rows spanned the channel. The staggered configuration had alternate rows offset by half a pitch which resulted in a one hole difference between alternate rows. The plate was 1.5m in

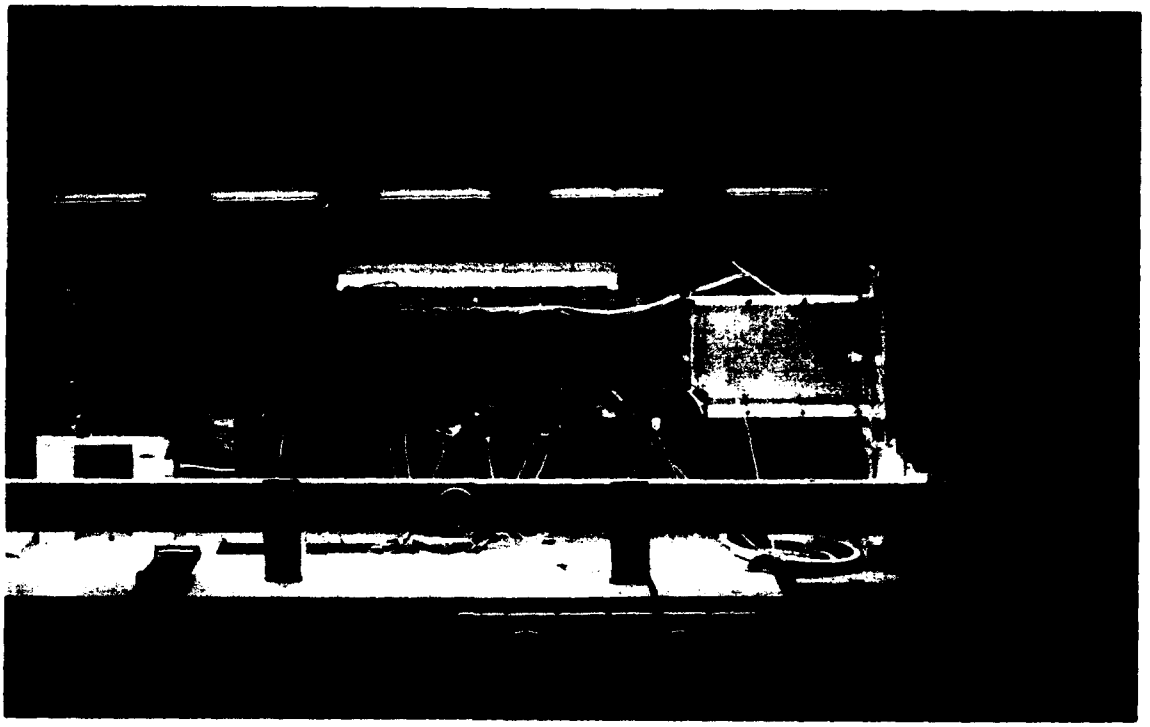

Figure 5.1 Transient test facility with impingement array plate.

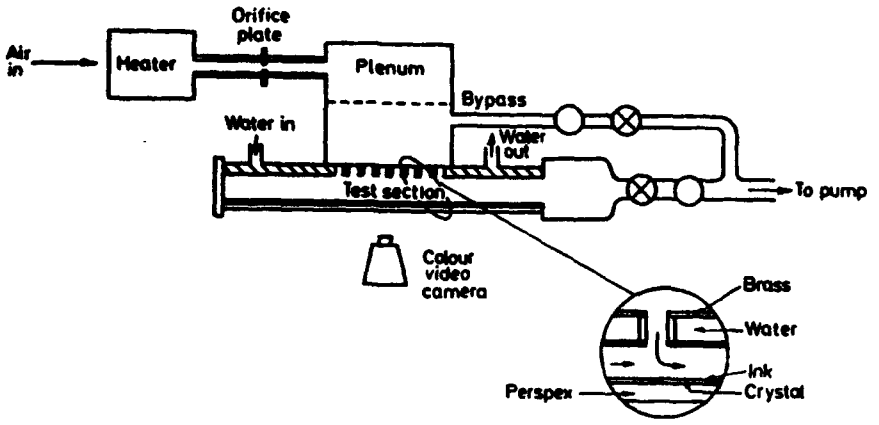

Figure 5.2 Schematic of the transient test facility used for impingement array experiments.

length and 0.2m in width. A perspex blocker plate was located 4*d*, or half a pitch, upstream of the first jet row. This plate spanned the channel and ensured no initial crossflow was present. Measurements of temperature and differential pressure 210mm downstream of the last row on the array centreline permitted the massflow to be compared to that measured at the orifice plate upstream of the jet plenum. Agreement was usually between 1-3%. In addition, static pressure was measured in the channel close to each jet hole. This static pressure was used to calculate individual flow rates at all of the jet row locations. Summing these values and comparing with the value from the orifice plate yielded agreement better than 1%. A bypass system allowed heated flow to preheat the pipework and jet plenum to a steady temperature prior to the test initiation. Surface temperatures of the impingement plate and target surface were measured using type T thin foil thermocouples. Gas temperatures were measured using type T 0.003 inch diameter wire thermocouples housed in stems 1mm in diameter. Gate valves set the experimental flow rate and fast acting valves were used to start the transient test. For the inline array, a coating which combined three different encapsulated liquid crystals was used to measure the surface temperature of the perspex target surface. Developments in the image processing approach meant that, for the staggered array experiments, a single wideband liquid crystal was used. The liquid crystal response was recorded using CCD video cameras positioned outside the tunnel that viewed through the 12mm thick perspex wall. Light transmitted through the crystal was eliminated by a coating of thermally thin black ink. The liquid crystal was calibrated in place using thin surface mounted thermocouples fixed to the surface on top of the black ink. The coating was illuminated by fluorescent

tubes positioned above and beneath the test section. A frame grabber and associated software, written by **Wang et al. (1993, 1994)**, were used to determine the peak intensities in the case of the triple crystal or the hue history in the case of the wide band crystal.

5.2 Instrumentation

The double crystal method is sensitive to errors in the measured quantities and a great deal of attention was paid to improving the accuracy of the instrumentation and to the procedure used to acquire data. At the heart of the data acquisition system was a **DTR 1500 Transient Recorder** made by CIL. It was a high speed, 16 channel A to D converter connected to an **IBM PC/AT**. A C-language program, DTRGO.EXE, controlled the interface between the computer and the DTR. Fourteen thermocouple channels were sampled and these were cold junction compensated to an accuracy of 0.1°C. A simple ice bath was used which was checked by a calibrated mercury in glass thermometer. Initially, the static pressure inside the heater plenum was measured by a **Furness Controls FCO44 Differential Pressure Transducer**. This pressure was used to match the flow between the bypass and experimental phases. It was later found that matching the jet plenum pressure or orifice plate differential pressure provided a satisfactory means of balancing the two flow phases. These two readings were used to set the flow through the heater during the bypass phase to be the same as that through the test section during the experiment. Two **SENSYM 142SC01D Differential Pressure Transducers** measured both the channel flow differential pressure downstream of the array and jet plenum pressure. Because

the transducer response time is very short (0.1 msec), the transducers were used to determine the onset of initial jet and channel flow and thus test initiation. These transducers had an output voltage between 1-5V and were directly logged onto the DTR 1500. For the present experiments, two DTR 1500 channels logged the pressure transducer voltages while other channels monitored various surface and gas temperatures. Surface temperatures were obtained by rapid response thin foil 0.05mm thick type T thermocouples. Gas temperatures were taken using 0.003 inch diameter wire type T thermocouples in 0.9mm or 1mm stems. The heater box and ice bath temperatures were monitored using **Omega Microprocessor Thermometers** (Models CL23 and HH21). The channel static pressure was sampled using a **Furness Controls 10 Channel Controller** (which switched the transducer between static ports) connected to an **Air-Neotronics Pressure Meter** (Model PDM210) having a range of 0-140 inches water. An additional pressure meter (Model PDM204) with a range of 0-19.99 inches water was used to measure orifice pressures. Video images were recorded by four **Panasonic F-10 CCD Cameras** on standard **Panasonic VHS recorders**. Processing was done on a standard IBM PC/AT computer by operating a computer controlled **Panasonic AG-7330 VHS recorder**.

5.3 Experimental Procedure

The actual operation of the internal cooling transient rig proved very complex and care was taken with each test to ensure the data quality. The test procedure was as follows:

1. Prepare the ice bath and check that the 0°C reference temperature is obtained

with the mercury in glass thermometer. Insert the thermocouple reference junctions into the ice bath and monitor the ice bath temperature during all phases of testing with a hand held microprocessor thermometer.

2. Check the pressure transducer connections to the power supply and ensure that the correct voltage is displayed (8V). Check the pressure transducers ports are connected correctly (jet plenum and downstream array). Check the Furness Controls 10 Channel Scanner has all the static pressure taps correctly connected.

3. Check that the handheld instruments are in place. The 0-19.99 inches water gauge range pressure meter measures orifice pressures and the 0-140 inches water gauge range meter measures the jet plenum/static pressure during the test. The ice bath and heater temperatures are monitored with the microprocessor thermometers.

4. Check the video system. All four cameras must be focused and the field of view set. Check the that video tapes are set to the proper place and the video timers operating properly. Set appropriate date and start time on the video timers. Make a run card for visually marking the test run number on the video tape.

5. Check the DTR operation. First, ensure that the 14 thermocouples are in their proper channels. Take the amplifier zero settings for the DTR using DTRGO.EXE. Sample all channels to get the initial temperature and pressure transducer levels. A spreadsheet was used to view data files from DTRGO.EXE.

6. Balancing the fast acting valves begins by using the orifice spreadsheet program to determine the orifice pressure required for the desired average Re_j and desired jet plenum temperature. Next, operate all the fast acting valves three times to ensure unhindered operation. Check that the heater is off. Start the water circulation system noting system pressure (10.5 inches Hg vacuum). With the fast acting valves in the operate condition, turn on the water ring pump and set the gate valve downstream of the array to the proper orifice pressure. Stop the water ring pump, set the fast acting valves to bypass and restart the water ring pump. The gate valve downstream of the bypass fast acting valve sets the orifice pressure to the required level. Set a resistance corresponding to a delay time on the control panel and then transiently operate the system, logging data for approximately 1 second. During transient operation, check the video timer function and test initiation LED in video display for camera 3. Using the spreadsheet, determine if DTR and all channels functioned properly by reviewing the data. Check whether the valve sequencing time delay is optimised to minimise the pressure disturbance caused by switching. If the jet plenum pressure is not sufficiently balanced repeat the process using another delay time.

7. With valves sequenced and the required flow set, position the fast acting valves for bypass, start the water ring pump and turn on the heaters. The bypass flow rate can be increased to decrease preheating time however, prior to test initiation, a settling time at the desired orifice pressure is required. The usual preheat time varied from 20 to 40 minutes. During this bypass phase,

sample the DTR periodically to monitor plate temperatures and system pressures. Adjust the heater and bypass flow rates. Once the required jet plenum temperature is reached (or slightly exceeded) check the final flow rate is correct. Sample all the channels to gain pre-test values. Turn on the video recorders, display the test card in all camera views momentarily, turn on the array fluorescent lights and set the computer to the data acquisition mode. Turn on all room lights with the exception of the fluorescent tube behind the cameras (to minimize camera reflection). Initiate the test by pressing the button on the control panel. Check that the video timers are operating and the DTR sampling data. Two different data sample rates are used. The first rate samples channels at 100Hz for 0.5 sec to monitor flow initiation and then the channels are sampled at 1 sec intervals for 2 minutes thereafter.

8. After 2 minutes, save the data file, stop the video tape recorders and turn off the array lights. Sample the DTR channels again to get the temperatures of the orifice and downstream channel at the start of pressure data collection and again at the conclusion of pressure data collection. Pressure measurements are taken at the orifice, downstream channel location, jet plenum, static channel pressure taps and finally the orifice again. Variation in the orifice measurement is never more than two to three percent from start to the conclusion of pressure data collection. The pressure measurement process takes approximately five minutes.

9. After all measurements are taken, turn off the heaters, water ring pump and water circulation system in that order.

10. Using the spreadsheets, determine if valves were properly sequenced and if data was logged properly. Determine the average Re_j, required temperatures and start initiation time for later processing. Run the array simulation program which uses the flow model to determine local Re_j, G_c, and G_j values.

5.4 Commissioning

An extensive commissioning exercise was performed on the rig prior to processing the video image data to obtain the heat transfer results presented in following chapters.

5.4.1 Massflow Determination

After assembly, the entire system was sealed using silicon sealant and leak checks performed. The orifice plate massflow, total flow predicted from the static pressure across the holes and the airflow from the downstream pitot static measurements were checked for agreement. If agreement was not satisfactory, smoke from incense sticks, which was found not to damage the liquid crystal, was used to detect air leaks and the apparatus was resealed. This procedure was repeated until satisfactory agreement was achieved. Agreement was usually 1-3% between the orifice plate and pitot static measurements and 1% between the orifice plate and the flow rate calculated using channel static pressure. The procedure had to be repeated each time a configuration change was made.

5.4.2 Plenum Temperature Uniformity/Water Circulation System

The original jet plenum contained a shutter system effectively to seal the plenum from the channel/array plate during the bypass phase. Eventually, the problems of rapid shutter operation prior to test as well as an inability to seal the shutter system during operation led to an alternate method of target surface isolation from the flow. By allowing a very small amount of bleed air to enter the array channel from the downstream area, a slightly higher pressure was maintained in the channel preventing hot plenum air from entering the test section and affecting the target surface temperature uniformity.

Heated air entered at the rear of the plenum through a perforated 4 inch pipe which spanned the jet plenum and contained outflow holes which distributed air uniformly. The air then passed through a flow straightener which ensured a uniform flow into the plenum just prior to the impingement jet holes. Figure 5.3 shows a traverse of normalized temperatures across the plenum. During operation, across the plenum, the temperature did not differ by more than 1°C from the average value. In the bypass phase, the plenum temperature profile could be significantly affected if too much air was allowed to bleed back into the plenum. A large temperature decrease occurred in the vicinity of the plenum bypass outflow as the bleed air entered the test section from a position downstream of the array. Minimizing this bleed air minimized its effect on bypass plenum temperature profiles. During testing three thermocouples located 50mm upstream of jet holes 1, 4 and 8 in the plenum were used to measure jet plenum temperature at midspan and usually agreed to within 0.5°C. The air

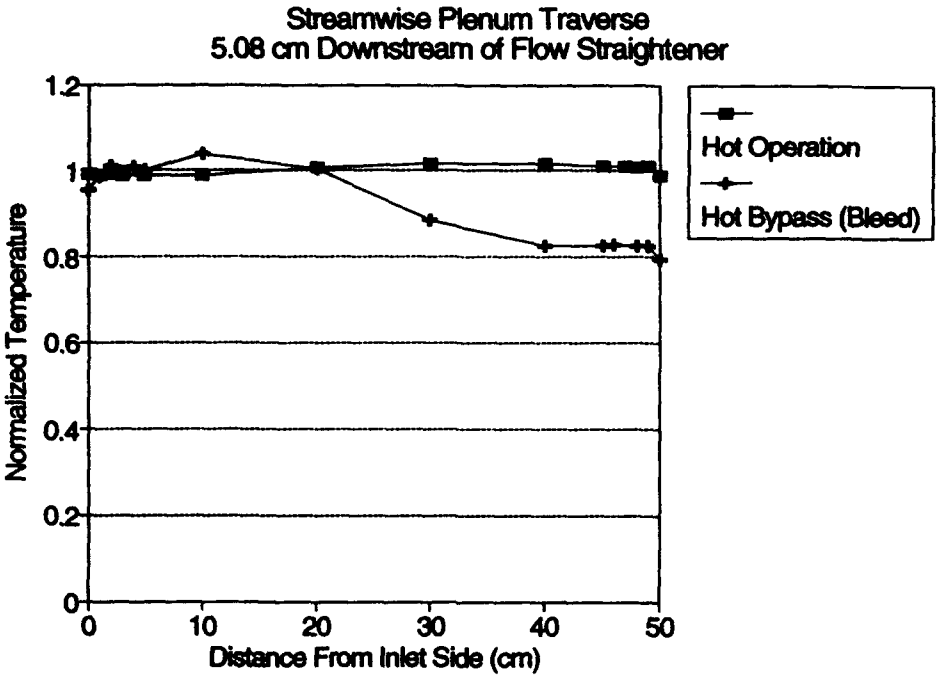

Figure 5.3 Streamwise temperature traverse of plenum centreline 5.08cm *downstream of flow straightener.*

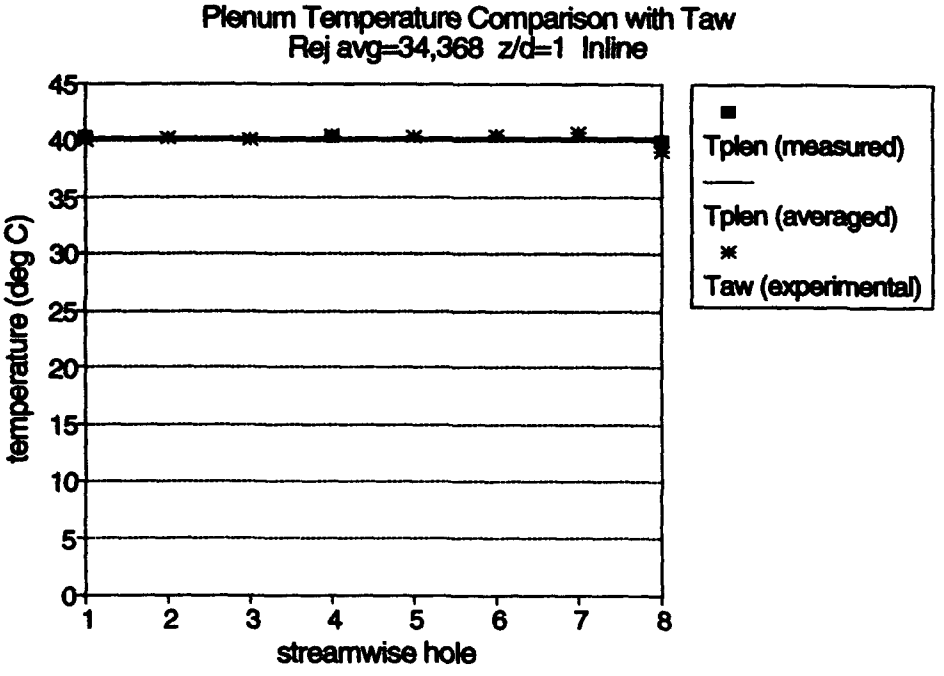

Figure 5.4 Measured plenum temperatures compared with experimentally predicted adiabatic wall temperatures.

temperature used to process the data was then an average of these three thermocouples. Figure 5.4 shows this agreement and compares these measured temperatures with calculated T_{aw} using the double crystal method in the stagnation region for each row of jets. Here the experimentally calculated temperatures at the stagnation point based on the intensity history are virtually the same as the measured plenum temperature as expected.

The water circulation system temperature was controlled by maintaining the temperature of the water tank with ice. This temperature control, along with reverse air flow through the impingement plate, was sufficient to maintain the target surface to within approximately 0.2°C uniformity. Initial tests showed evidence of vertical gas temperature gradient in the plenum as the bottom jets showed crystal colour play sooner than the top jets. This temperature variation was never more than 1°C. A survey of the box wall temperatures revealed two important points. Firstly, where the plenum contacted the impingement plate, the plenum wall was cooler than the gas. In other words, there was a plenum wall temperature gradient from the front to the rear of the plenum. Secondly, a plenum gas temperature gradient existed from top to bottom. The first situation was corrected by a rubber gasket which thermally uncoupled the metal surfaces of the impingement plate and plenum box. The second was remedied by increasing the external polystyrene insulation to a two inch thickness and by placing a thin sheet of expanded polystyrene on the inside surface. After these modifications, no vertical temperature gradient in the plenum gas temperature was noted. Since gas temperature measurements were taken on the plane of the holes of interest, the plenum temperature was accurately characterized for all tests.

5.4.3 Crystal Calibration

For the intensity processing approach applied to the inline configuration, three narrowband liquid crystals, R25C1W, R30C1W, and R36C1W, supplied by **Hallcrest**, were used to cover the desired experimental temperatures. The intensity method involved calibrating the three chosen liquid crystals for the peak intensity temperatures. After the target surface was prepared and installed, the calibration was performed in place under the heat transfer test lighting conditions. A surface mounted foil thermocouple, located in a region of uniform heat transfer was used for calibration. The surface was heated to the blue colour play temperature of the highest temperature crystal and then allowed to cool for an extended period until colour disappeared. This colour change was recorded on video at the same time the DTR logged the thermocouple temperature. The calibration test took about 6 minutes. This video was then processed to find the three intensity peaks corresponding to the three separate crystals. Once the times for the peak intensities were known, it was simply a matter of looking up the thermocouple temperature corresponding to the peak intensity time. The initial calibrations for the narrowband liquid crystals were 26.1, 30.6, and 35.1°C. Recalibration was performed six months later to check the calibration and no change was noted. Since monochromatic processing of the peak intensity signal from narrowband liquid crystals was being used, one calibration was sufficient for all cameras.

The hue calibration was more complicated. The hue values from crystals are not sensitive to intensity or illumination levels but are very dependent on angle of

illumination and observation. The calibration is also dependent on the camera colour performance. Thus, the calibration must not only be performed in place under experimental lighting, it must also be done for each camera. Two wideband liquid crystals, BM/R25C15W/S-40 spanning 15°C and BM/R20C20W/S-40 spanning 20°C, were supplied by **Hallcrest**. Again, thermocouples located in areas of uniform heat transfer were used and the tests repeated until a reliable calibration of hue against temperature was achieved. Typical hue, saturation and intensity plots are given in Figure 5.5 with actual calibration data shown in Figure 5.6. Two limits arise from the calibration between which the hue value increases monotonically with temperature. The calibrations were averaged and the result is the "cam4cal" curve presented in Figure 5.6.

As a final calibration check, the surface temperature variation predicted from the analytical solution to the diffusion equation using the experimentally determined h and T_{aw} is compared with the temperature signal taken directly from the hue history.

5.4.4 Verification of the Tunnel Transient

The one dimensional heat conduction equation assumes a step change in gas temperature. Thermocouple traces of the plenum temperature, shown in Figure 5.7, initially indicated a lag in gas temperature of tens of seconds at low average Re_j. The thermocouples used consisted of 0.003 inch diameter wire in 1mm OD steel tubing with thermocouple wires/junction protruding 3mm from the end. The wires were fixed in the tube with Superglue, which filled the tube length. It was thought that stem conduction could cause a problem and a thermocouple of wire diameter 0.001 inches

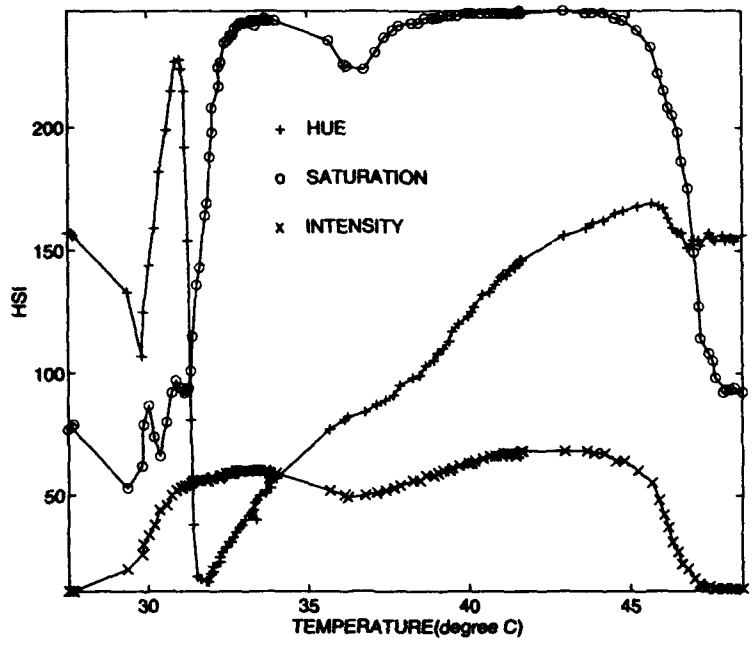

Figure 5.5 Typical hue, saturation and intensity plot **[Wang et al. (1994)]**.

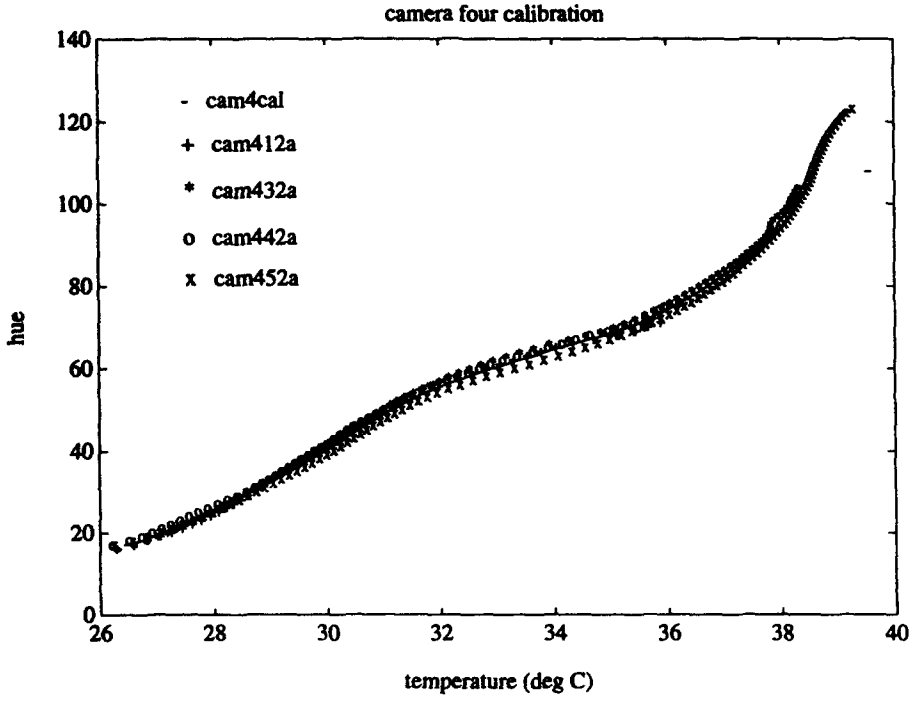

Figure 5.6 Calibration curve for BW/R20C20/s-40 from camera 4.

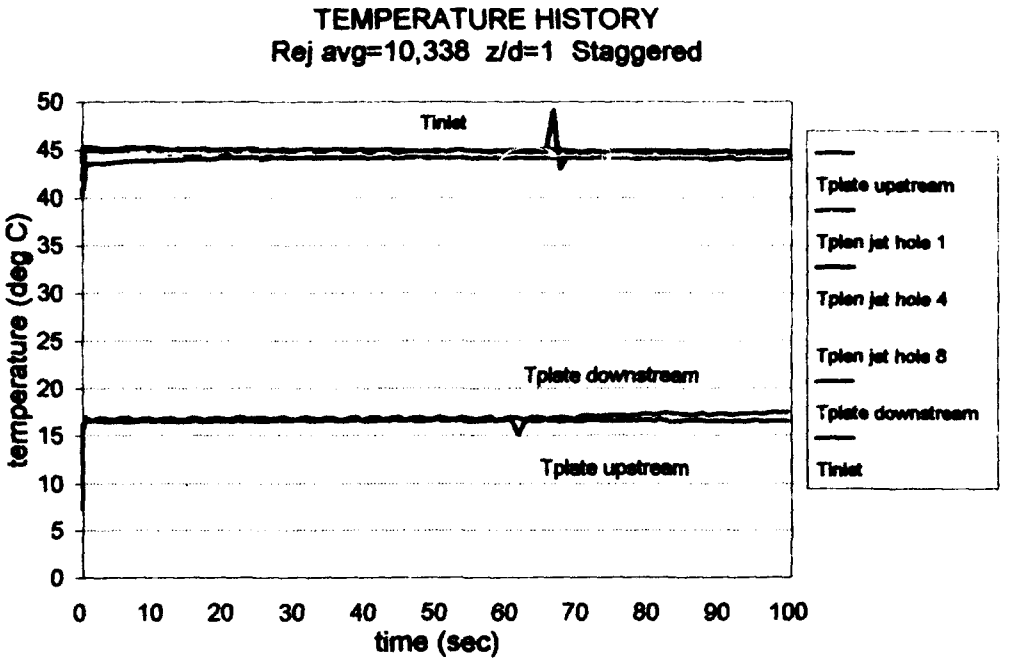

Figure 5.7 Typical temperature history of inlet, plenum and plate thermocouples.

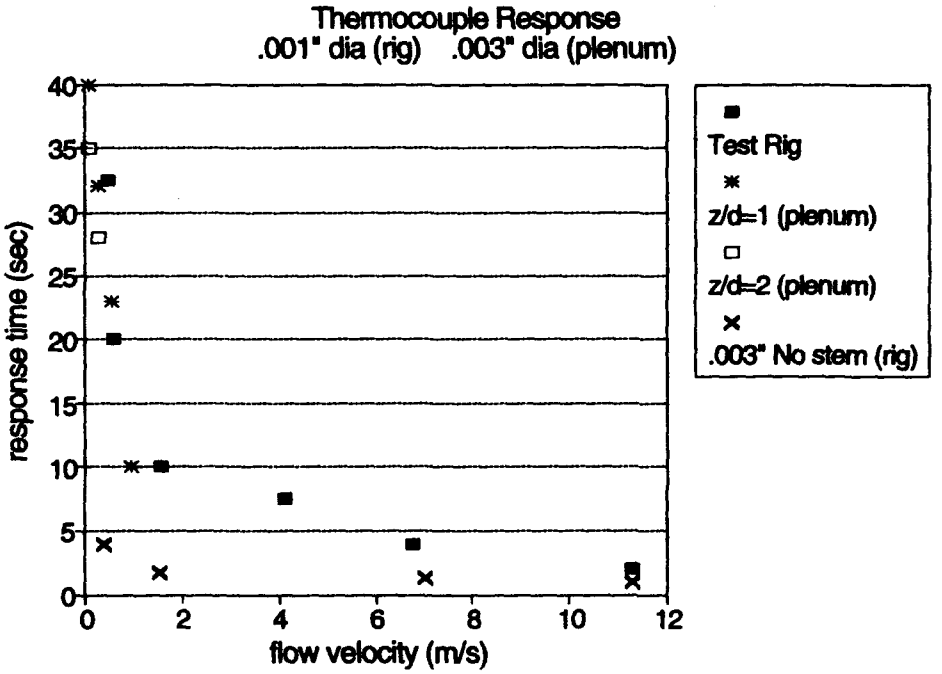

Figure 5.8 Thermocouple response to a step change in temperature for various flow rates.

in a ceramic stem was made and used in the jet plenum. This thermocouple was expected to have a faster response. Experimental studies conducted with 0.001 inch diameter wire in a ceramic stem on a test rig giving a known step change in gas temperature, results shown in Figure 5.8, indicated that, at the low velocities encountered in the plenum, the thermocouple time constant was too long to resolve the rig starting transient. Also plotted in Figure 5.8 are data from a 0.003 inch diameter wire without a stem showing a much faster response to the temperature change for all velocities tested. The plenum inlet temperature was monitored during the tests and found not to vary. During bypass phase, the plenum thermocouples were several degrees lower than the plenum inlet temperature due to the bleed back of air into the plenum from the cool test channel during the bypass phase. When the valves were switched to start the heat transfer experiment the plenum inlet temperature remained constant during the test. Thus, it was reasonable to assume that the actual air entering the jet hole was the temperature eventually reached by the plenum thermocouple during the test. Downstream of the array, as the velocity was quite high compared to the plenum, the channel gas thermocouple was a good indication of the actual channel gas temperature change with time.

Another check on whether a step change with time occurred was to examine a surface thermocouple response under a jet. The thermocouple response could be analyzed in two ways. Firstly, by inspection of the measured temperature with time, it is possible to determine whether the temperature trajectory does in fact follow one dimensional heat conduction prediction. Figure 5.9 shows an analytic solution to the thermocouple data with a value of h = 740 W/m^{2}K and T_{aw} = 41.5°C. In the second

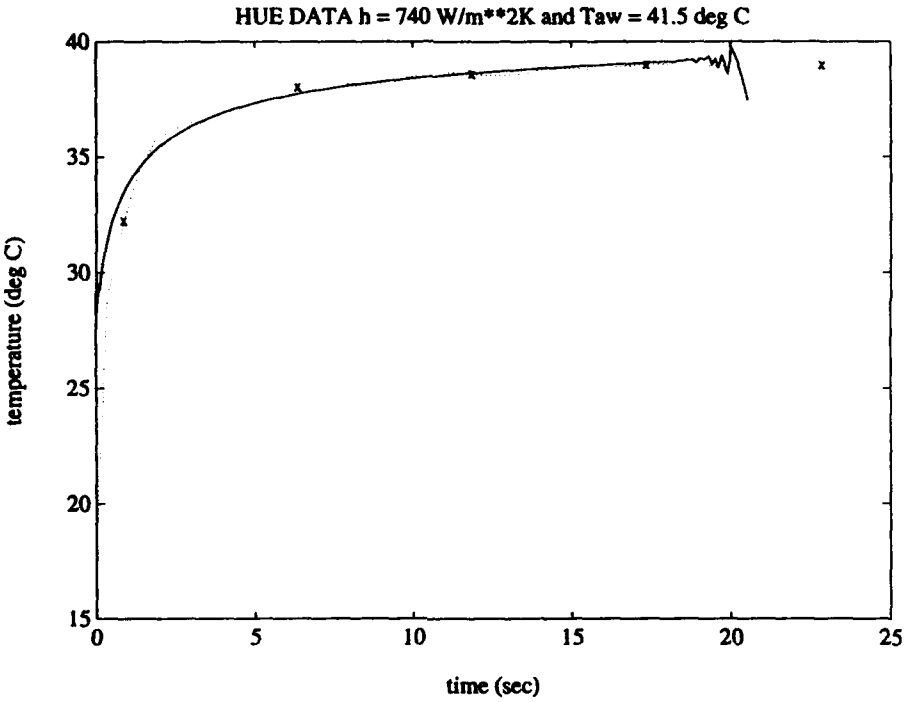

Figure 5.9 Analytic solution to thermocouple data under jet row one (Re_j avg = 41,727; z/d = 2; staggered).

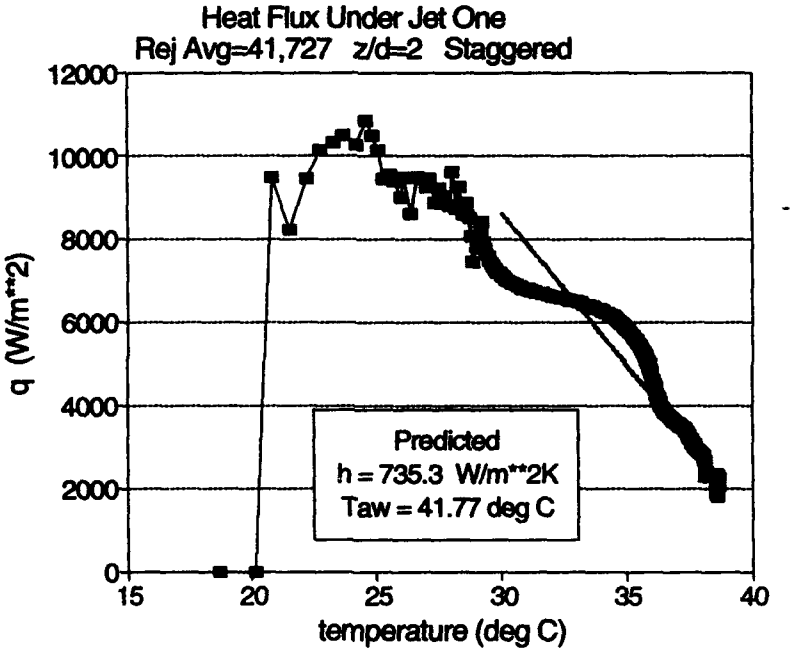

Figure 5.10 Heat flux under jet row one (Re_j avg = 41,727; z/d = 2; staggered).

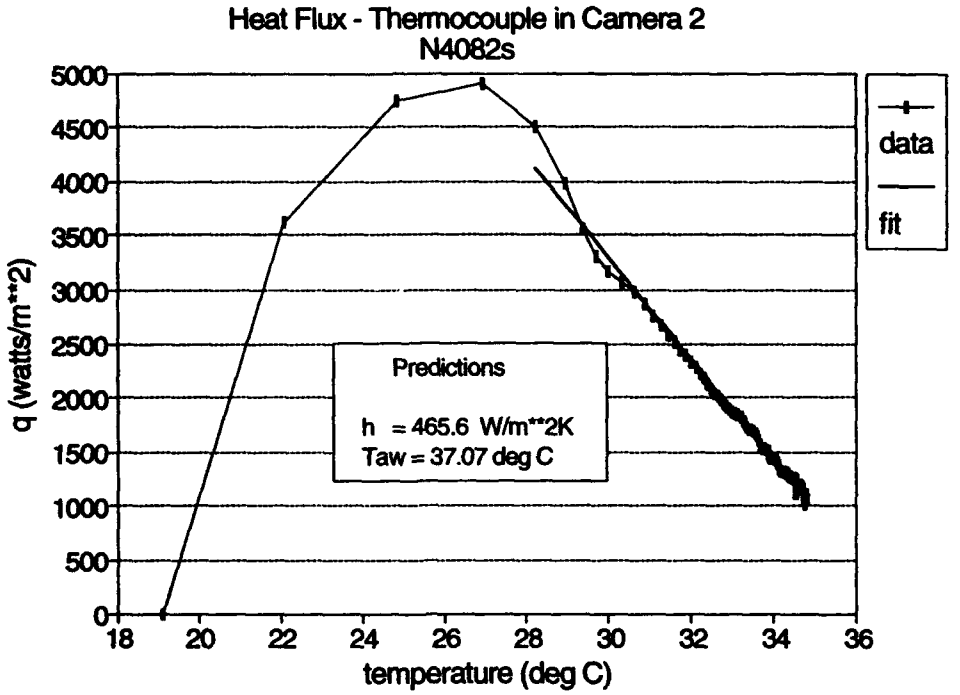

Figure 5.11 Channel heat flux from a surface thermocouple near jet row four (Re_j avg = 41,727; z/d = 2; staggered).

method, the same data could be used to produce a plot of heat flux against surface temperature. As the surface temperature approaches the adiabatic gas temperature, the heat flux falls to zero. Using the method developed by **Oldfield et al. (1978)**, the prediction of h = 735.3 W/m^{2}K and T_{aw} = 41.77°C under row one can be seen, Figure 5.10, to agree with the former solution and predicts very closely the measured jet plenum temperature of 41.58°C for this test. The hue history calculations at this same position yield values of h = 736.35 W/m^{2}K and T_{aw} = 42.41°C. Figure 5.11 shows the heat flux in a crossflow location near jet row four during the same test. Its prediction of h = 465.6 W/m^{2}K and T_{aw} = 37.07°C closely match the analytic solution to the thermocouple results of h = 461.6 W/m^{2}K and T_{aw} = 37.22°C and also the hue history values of h = 486 W/m^{2}K and T_{aw} = 37.0°C.

5.4.5 Jet Hole Discharge Coefficient

Florschuetz et al. (1982) determined that, with no initial crossflow and G_c/G_j less than 0.5, the hole discharge coefficient was uninfluenced by crossflow and was insensitive to variation in Re_j. The value of C_D was estimated in several ways:-

1. The plenum was pressurized and the flow determined by the orifice plate with the target surface removed and the holes exhausting to atmosphere. The flow from all 40 holes was found to be the same. A discharge coefficient of 0.82 was calculated.
2. This is very close to value of C_D (0.83) selected to match the predicted static pressure from **Florschuetz et al.** to the measured pressure distribution.
3. This value of C_D also falls within the range of values, 0.76-0.83, used by **Florschuetz et al.** with similarly widely spaced jet holes.
4. The result is also very close to an experimental measurement of 0.81-0.82 by **Hay et al. (1987)** for a thick, sharp-edged orifice with no crossflow.
5. **McGrehan and Schotsch (1988)** produced a model to predict discharge coefficients for sharp-edged and rounded inlet hole geometry. Their model predicts a discharge coefficient for the current conditions of 0.80. They also confirm the insensitivity of discharge coefficient to Re_j.
6. Proprietary data supplied by Rolls-Royce gave a value of C_D of 0.82 for the geometry and pressure ratios of the current experiment.

An uniform discharge coefficient of 0.82 was used in the present experiments for both the inline and staggered array. At higher values of G_c/G_j than used in the present

study, C_D decreases as shown by **Florschuetz et al. (1982)**.

5.4.6 Valve Sequencing

After the first few tests, it was noted that the valve time delay required to minimise the flow establishment time could be correlated against average Re_j. Figure 5.12 was used to provide an estimate of time delay resistance for subsequent tests.

5.4.7 Channel Velocity and Temperature Profiles

With the smaller scale of the current experimental test rig, channel temperature profile data are difficult to achieve. In the 4 inch plenum feed pipe, temperature profiles clearly showed the flow to be well mixed out, especially at the inlet to the plenum. In the channel, the profiles downstream of the array were fully developed. Turbulence generated from the jet/crossflow interaction was thought to hasten the onset of developed conditions.

5.4.8 Transient Start Time Determination

With the very short crystal change times occurring directly beneath the jets at the highest Reynolds numbers, it was necessary to assess the effect of the finite flow establishment time on experimental accuracy. Figure 5.13 shows the channel dynamic head signal and illustrates the time delay from valve switching to achievement of steady conditions. For these conditions, it can be seen that the transient lasts for approximately 130ms. A superposition approach was used to determine the correct

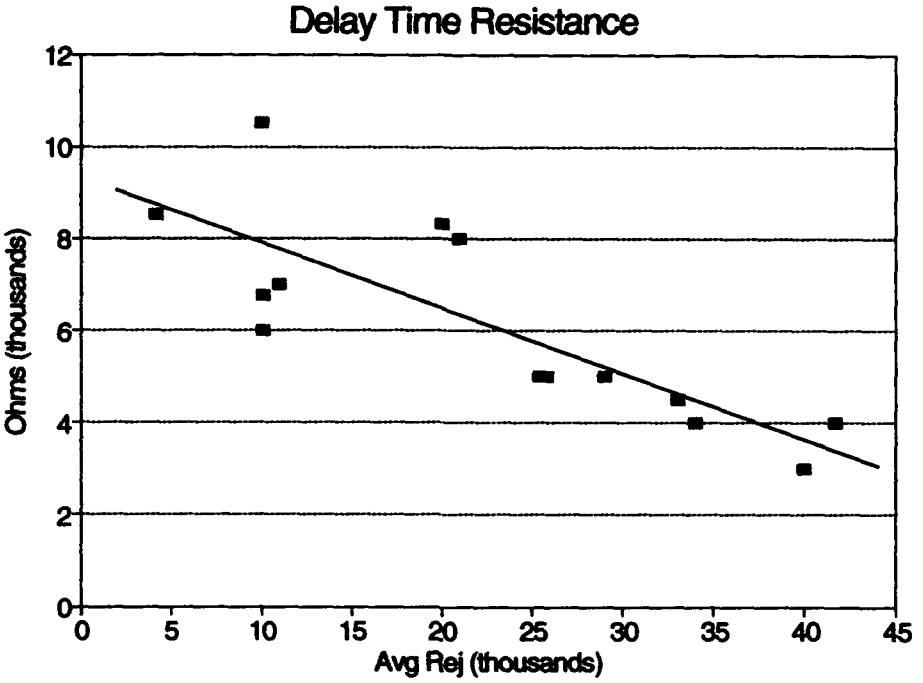

Figure 5.12 Time delay resistance settings for valve sequencing.

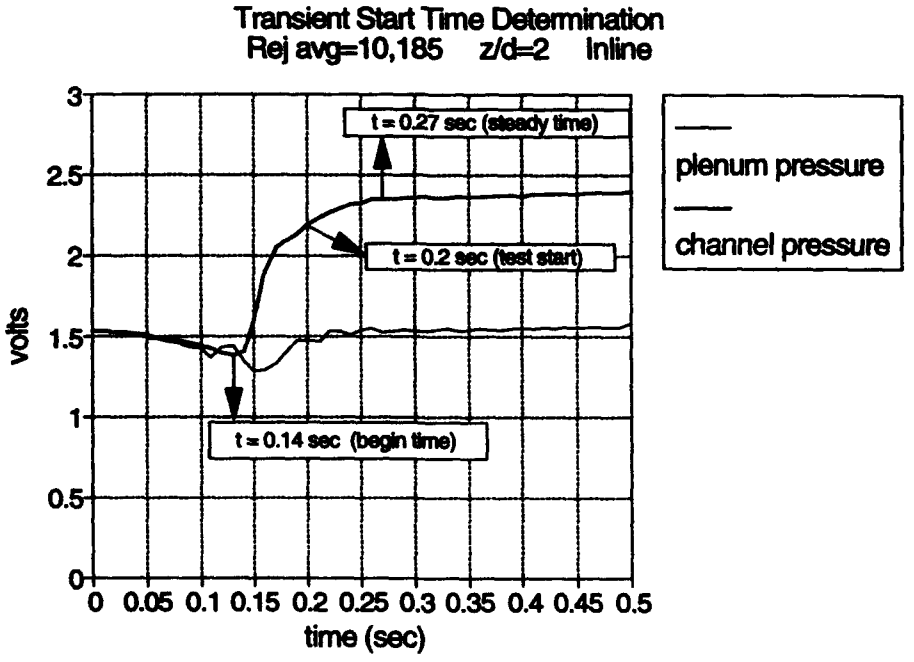

Figure 5.13 Pressure traces used to determine transient start time.

time delay to subtract from the liquid crystal data for heat transfer processing. By approximating the rising heat flux through the tunnel transient by a series of steps, it was estimated that the error in surface temperature increase, even for crystal change times as short as 800ms, was less than 5% when a delay of half the flow establishment time was subtracted from the crystal change times. The flow establishment time was determined from the logged pressure signals for all test conditions and one half of this delay (approximately 60ms) was subtracted from the times signals from the liquid crystal colour changes.

CHAPTER 6 - DATA REDUCTION

The two data processing techniques used to obtain heat transfer results are described in this chapter. The intensity history technique, used for the inline arrays, involved the use of a coating consisting of multiple narrow band liquid crystals for which the surface temperature was calibrated to the peak intensity of a monochromatic signal. A hue history technique was used for the arrays of staggered holes which employed a single wideband liquid crystal. For this latter method, a near continuous temperature history at all target surface locations was obtained by processing a colour attribute of the video recordings of the surface colour change.

6.1 Inline Array

All liquid crystal colour changes were recorded from a video camera on standard VHS video tape. Four cameras were used to achieve the necessary spatial resolution. The video tapes were then processed using software developed by Wang **[Wang et al. (1993)]**. The software used a frame grabber to digitize the video tape, frame by frame, over a specified window for the entire test. One minute of video tape was typically analyzed to cover most of the target surface. **Wang et al. (1993)** detail the equations used to process an intensity signal and a description of the definition of colour video signals is given here for the sake of completeness. A video signal can be considered to be composed of three signals. Those are the red, R, the green, G, and the blue, B, signals. R, G, and B signals can be calculated from the illumination spectrum, $E(\lambda)$, and reflectance spectrum, $R(\lambda)$, using the following integrals:

$$R = \int_{-\infty}^{\infty} E(\lambda)R(\lambda)r(\lambda)d\ \lambda \qquad (6.1)$$

$$G = \int_{-\infty}^{\infty} E(\lambda)R(\lambda)g(\lambda)d\ \lambda \qquad (6.2)$$

$$B = \int_{-\infty}^{\infty} E(\lambda)R(\lambda)b(\lambda)d\ \lambda \qquad (6.3)$$

where $r(\lambda)$, $g(\lambda)$, and $b(\lambda)$ are camera filter transmissivities. For a liquid crystal surface, the reflectance, $R(\lambda)$, is a function of temperature and thus, the surface reflectance is replaced by $R(\lambda,T)$. The PAL broadcasting standard uses three signals which are linearly related to R, G, and B. Y is the monochromatic intensity signal and is defined as:

$$Y = 0.229R + 0.587G + 0.114B \qquad (6.4)$$

Thus, Y is a function of the lighting, $E(\lambda)$, the liquid crystal reflectance, $R(\lambda,T)$, and the camera response. Assuming that the illumination at different locations on the liquid crystal surface varies only in total power and not in normalised spectral distribution $e(\lambda)$, defined as $E(\lambda)/I$, Y can be rewritten as

$$Y = I * \int_{-\infty}^{\infty} e(\lambda)R(\lambda,T)(0.299r(\lambda)+0.587g(\lambda)+0.114b(\lambda))d\ \lambda \qquad (6.5)$$

or alternatively

$$Y = I * C(T) \qquad (6.6)$$

The measured Y signal as the liquid crystal changes colour is a function of the surface temperature and the Y level is proportional to the local strength of illumination level. Figure 6.1 shows a typical intensity history for the mixture of three narrowband liquid crystals used in the current inline array experiments. Thus, for any given location, it is possible with an intensity history to locate the peak in intensity which can be calibrated to a specific temperature for any liquid crystal. Within the digitized window it is possible to take individual intensity histories at any target surface location. Figure 6.2 shows the 133 surface locations used to determine the heat transfer distributions over the target surface. A 9x9 regular grid covers the entire area of the target surface covered by one jet at equal intervals. A 6x6 higher resolution grid surrounds the jet impingement zone, and a very closely spaced 4x4 box of adjacent pixels is used to resolve the heat transfer level at the stagnation point. Finer features were resolved by increasing the grid density locally. The image processing software generated intensity histories for the selected grid spacing and placed them in

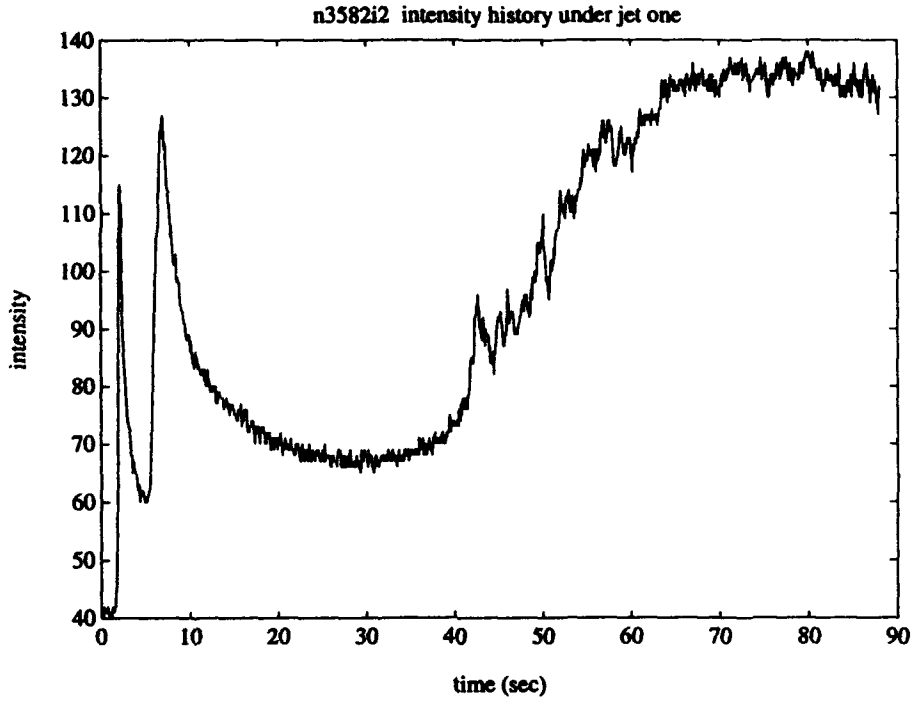

Figure 6.1 A typical intensity history for a coating comprising three narrow band liquid crystals.

a data file compatible with **MATLAB**[1], a mathematical data processing package. Software written in **MATLAB** determined the time for the intensity signal to peak. This program required input from the user since the number of intensity peaks could only be determined from inspection of the signal. This was because not all locations had a sufficiently high level of heat transfer to cause the perspex surface temperature to reach the peak intensity temperature of the highest temperature liquid crystal. The user determined time intervals which included each of the peaks. The program then found the peaks of the defined regions and wrote the times to a data file along with the grid point number, pixel location and number of crystals present. This data file

[1]**MATLAB**, The Math Works, Inc. Cochituate Place, 24 Prime Park Way, Natick, MA 01760, USA.

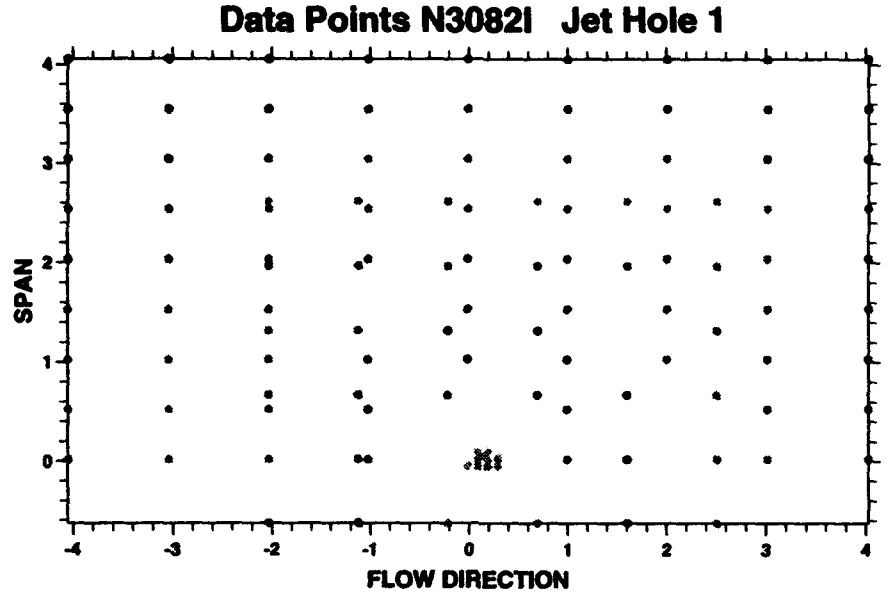

Figure 6.2 A typical data acquisition grid.

was then imported into a spreadsheet for producing heat transfer results. The master data spreadsheet was linked to three other spreadsheets. Each of the linked spreadsheets contained the crystal calibration temperatures as well as plenum, impingement plate and initial target surface temperatures. One spreadsheet used the two higher temperature crystals to calculate the local heat transfer coefficient and the adiabatic wall temperature. A separate spreadsheet used the lower two temperatures and a third spreadsheet employed only the lowest crystal temperature for situations where one peak occurred and the T_{aw} could be inferred from surrounding locations. Separate values of jet and impingement plate heat transfer coefficient were also calculated. The stagnation point data was averaged over the 16 pixel box and recorded. All local value results were written to a file containing heat transfer values

and pixel coordinates. This file was imported into a graphics package, **Unimap**[2] to obtain interpolated local maps of *Nu* and jet effectiveness, as well as area averaged data. **Unimap** imported irregularly spaced data and interpolated a surface between the points. This surface was then averaged over the target area salient to each row. All inline array heat transfer experiments were processed in this manner and both local and average results are given in Chapters 8 and 9. This process was repeated for all of the eight inline jet holes for each plate spacing and average Re_j tested. The average time to process one test condition from video acquisition to final data presentation is approximately four to four and a half weeks depending on the number of data points processed. Figure 6.3 shows the sequence of operation in the intensity history processing procedure.

The uncertainty analysis followed the perturbation method of **Moffat (1988)** to evaluate partial derivatives and used the experimental uncertainties given in Table 6.1 and 6.2. The uncertainty analysis was performed for the two extremes of heat transfer coefficient measured. First, in Table 6.1 is a typical value for the stagnation zone under a jet. The parameter which contributes most to the uncertainty is the first liquid crystal event time. For points furthest from the jet, shown in Table 6.2, uncertainty in the thermal product dominates the overall uncertainty.

6.2 Staggered Array

Hue history processing is described fully in **Wang et al. (1994)**. The process

[2]**Unimap**, Uniras, 376 Gladsaxevej, DK-2860, Sobørg, Denmark

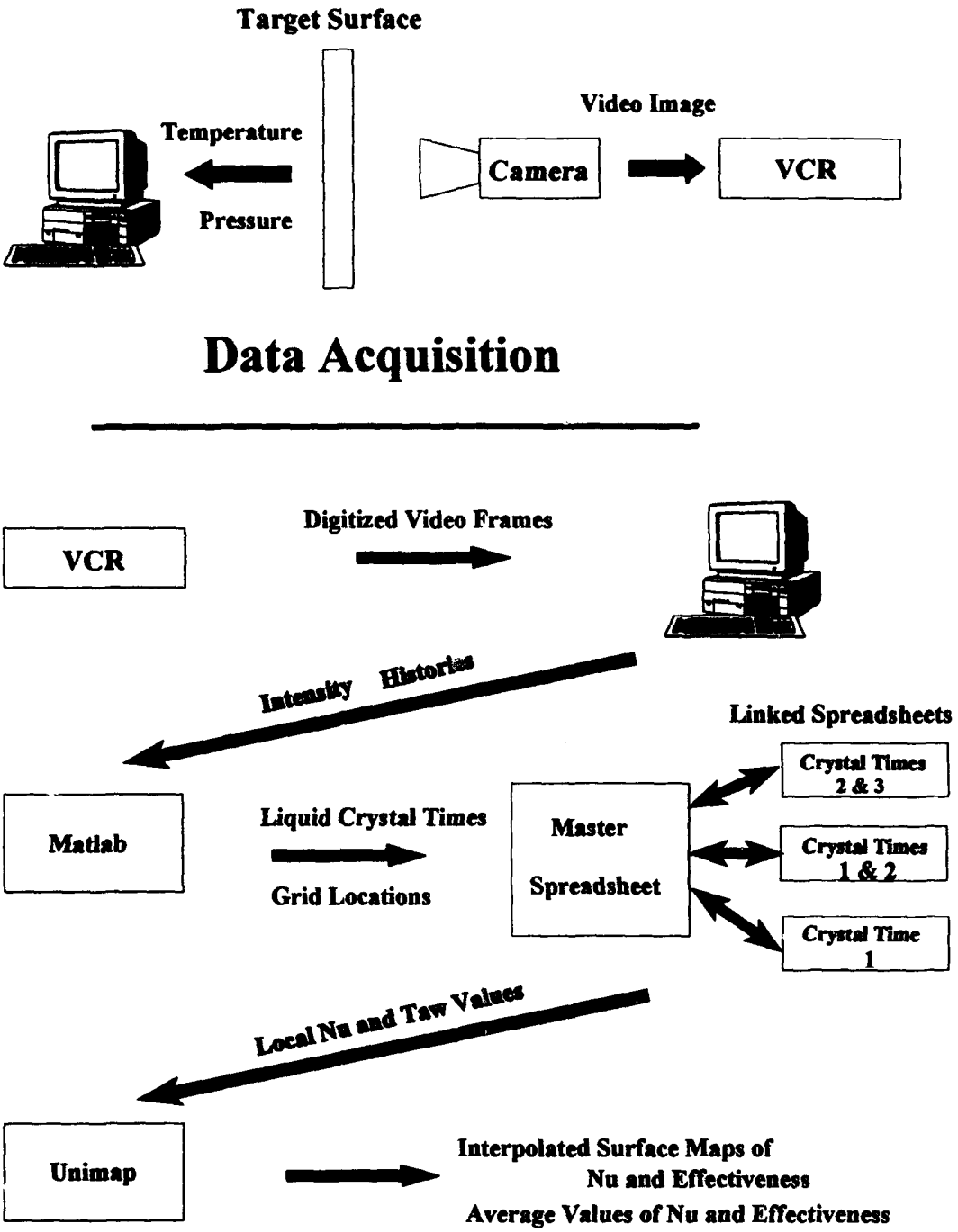

Figure 6.3 Flow diagram of intensity history processing.

Table 6.1 Parameters used in the uncertainty analysis for the double crystal method in the stagnation zone under a jet.

Parameter	Value	Delta	Jet % error in h	Jet % error in η
t_1 sec	1.05	+/- 0.077	8.02	2.42
t_2 sec	6.29	+/- 0.077	1.02	0.49
$\sqrt{\rho ck}$ $W\sqrt{sec}/m^2K$	569	+/- 29	5.1	0
T_{init} deg C	16.57	+/- 0.2	1.68	0.2
T_{cryl} deg C	30.6	+/- 0.1	3.52	0.94
T_{cry2} deg C	35.1	+/- 0.1	2.57	1.29
T_{jet} deg C	41.06	+/- 0.3	0	1.25
T_{plate} deg C	17.4	+/- 0.3	0	1.25
RSS-Const Odds			10.64	3.44
Worst Case			21.91	7.84

uses the *RGB* signals introduced in the description of the intensity based method. The values are mapped to hue, *H*, saturation, *S*, and intensity, *I* signals. They are defined as follows:

$$H = \frac{1}{360}\left[90 - \arctan\left(\frac{F}{\sqrt{3}}\right) + \begin{matrix} 0, G>B \\ 180, G<B \end{matrix}\right] \qquad (6.7)$$

Table 6.2 Parameters used in the uncertainty analysis for the double crystal method in the crossflow region.

Parameter	Value	Delta	Crossflow % error in h	Crossflow % error in η
t_1 sec	4.81	+/- 0.077	1.07	0.25
t_2 sec	54.05	+/- 0.077	0.05	0.03
$\sqrt{\rho ck}$ $W\sqrt{sec}/m^2K$	569	+/- 29	5.10	0
T_{init} deg C	16.57	+/- 0.2	2.34	0.25
T_{cryl} deg C	26.1	+/- 0.1	3.69	0.82
T_{cry2} deg C	30.6	+/- 0.1	2.43	1.33
T_{jet} deg C	41.06	+/- 0.3	0	1.25
T_{plate} deg C	17.4	+/- 0.3	0	1.25
RSS-Const Odds			7.22	2.10
Worst Case			14.68	4.45

where

$$F = \frac{2R-G-B}{G-B} \quad for \quad G \neq B \qquad (6.8)$$
$$F = R \quad for \quad G=B$$

$$I = \frac{R+G+B}{3} \tag{6.9}$$

$$S = 1 - \left[\frac{\min(R,G,B)}{I}\right] \tag{6.10}$$

It is desirable for processing to use a colour index which is a simple and monotonic function of the liquid crystal temperature and is independent of the local illumination strength. H satisfies these requirements as the hue signal from the liquid crystal coated surface illuminated by fluorescent strip lights changes smoothly and continuously from 0 to 240 as the temperature of the crystal is increased. H is also independent of illumination strength as inspection of the definition of F shows.

In the current experiments, video tape recordings were acquired in the same manner as for the inline array and the video tapes processed on the same equipment. The software used previously was modified to produce the hue histories for specified grid locations. A numerical procedure was used to determine the correct value of local heat transfer coefficient and adiabatic wall temperature. When these values are selected, the surface temperature variation calculated using Equation 3.30 should be the same as the variation determined from the hue signal.

$$\frac{T_s - T_i}{T_{aw} - T_i} = 1 - e^{\beta^2}\, erfc(\beta) \tag{3.30}$$

The known form of the surface temperature was used to enable T_{aw} to be determined first. For known values of T_i and T_s, Equation 3.30 can be inverted, for a guessed value of T_{aw} to determine the variation of β throughout the experiment. Since

$\beta = h\sqrt{t}/\sqrt{\rho ck}$, a plot of β^2/t versus time should be a horizontal straight line. An iterative bisector procedure was used to determine the value of T_{aw} which achieved this criterion. The value of h then followed as $\sqrt{\rho ck}$ times the β^2/t value. A **MATLAB** program was written to take the hue history, perform the hue to temperature transformation using a calibration lookup table and then use a least squares regression to determine the value of T_{aw} to give a zero slope β^2/t graph. Once the convergence criterion has been reached, the program calculates the heat transfer coefficient, h, based on the mean β^2/t of the best fit straight line. Figure 6.4 shows a sample β^2/t plot. To check the solution, the selected values of h and T_{aw} are then used to generate an analytic surface temperature solution which is plotted along with the original temperature history curve for surface temperature confirmation. Figure 6.5 shows an example. The hue software uses interlaced video frames (time resolution 0.02 seconds) and processing 3,000 temperature values covering one minute of test data takes approximately 12 minutes per grid data point to converge. By selecting only a finite number of regularly spaced points along the temperature history curve it is possible to characterize the time history trajectory and arrive at the same solution. Twenty temperature points along the curve converge in approximately 2 minutes without significantly sacrificing accuracy. The output from this program is read into a spreadsheet to convert the grid pixel locations to functions of diameter and ensure the data is in a format compatible with the **UNIMAP**. The data files are interpolated in **UNIMAP** and *Nu* and jet effectiveness values are averaged over the target surface. This data can then be correlated and compared with other experimental data. The process from video acquisition to final data format takes approximately three weeks.

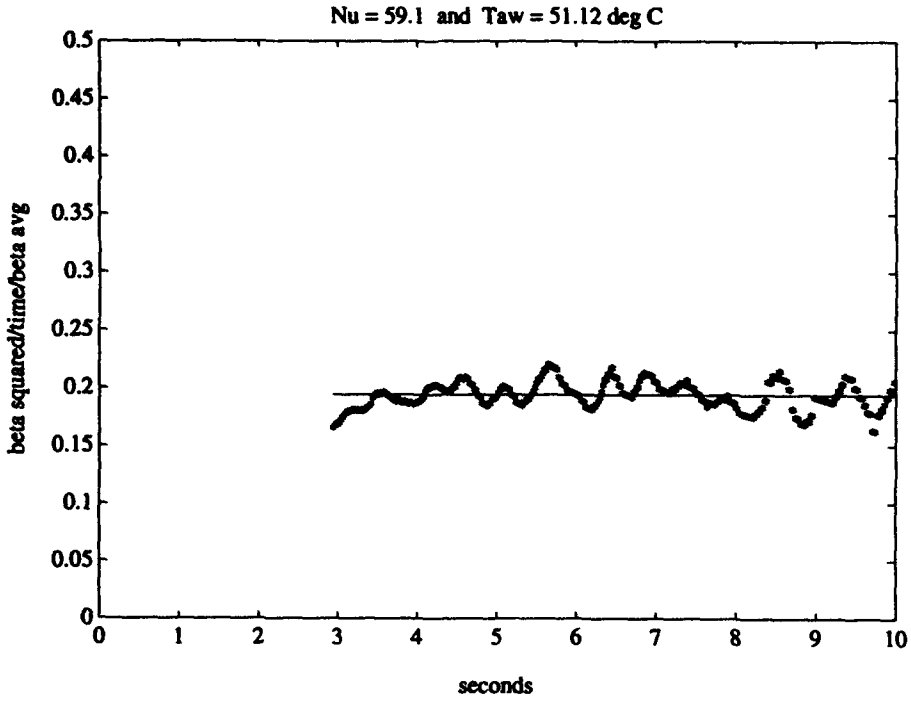

Figure 6.4 Hue temperature history data fit using least squares regression.

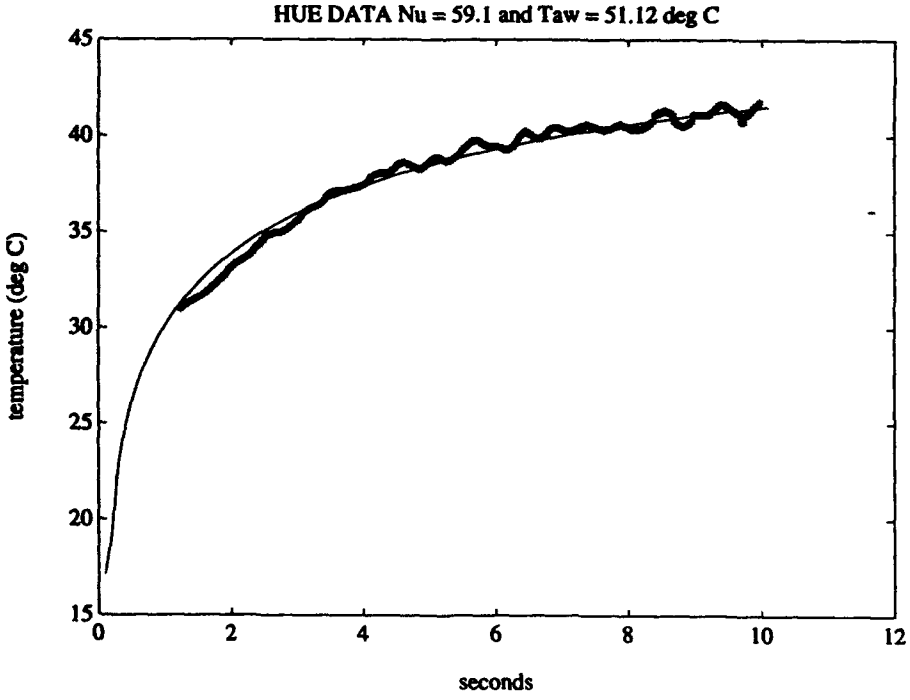

Figure 6.5 Analytic solution from least squares regression compared with hue temperature history data.

A portion of that time however is consumed by the automated procedure described above which allows the user time to accomplish other tasks. Figure 6.6 shows the sequence of operation in the hue history processing method.

The uncertainty in this temperature history method has been detailed in **Wang et al. (1994)**. Uncertainty in the hue-temperature calibration, brought about by instrumentation drift, changes in background lighting or illumination power, etc. may cause the calibration line to be different from the true liquid crystal performance. Repeat calibrations enable the uncertainty in the calibration curve to be less than 0.3°C. The effect of deviation in the calibration on experimental accuracy was found by dividing the temperature history range into n steps. The surface temperature history for a typical transient experiment was successively perturbed at each step by 1°C and the partial derivatives of h and T_{aw} determined numerically. The standard deviation, σ, in h caused by surface temperature uncertainty then follows from

$$\sigma^2 = \sum_{i=1}^{i=n} \left(\frac{\partial h}{\partial T_i} \sigma_T \right)^2 \qquad (6.11)$$

where σ_T, the standard deviation in the calibration, is taken to be the same at each step. Equation 6.11 can be extended to include the effects of errors in other measured quantities. Using estimated values for uncertainties in initial surface temperature of 0.2°C, thermal product of 5%, and surface temperature measurement of 0.3°C gave the estimates of uncertainty found in Table 6.3. If the number of steps chosen is large, the solution reverts to one representative of uncorrelated noise superimposed on the

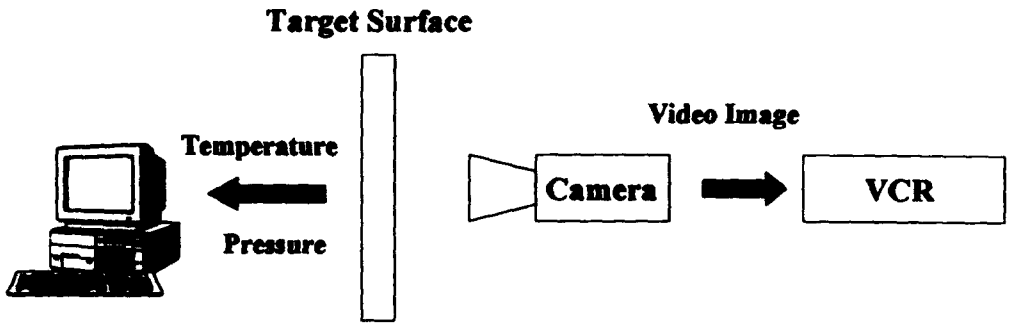

Data Acquisition

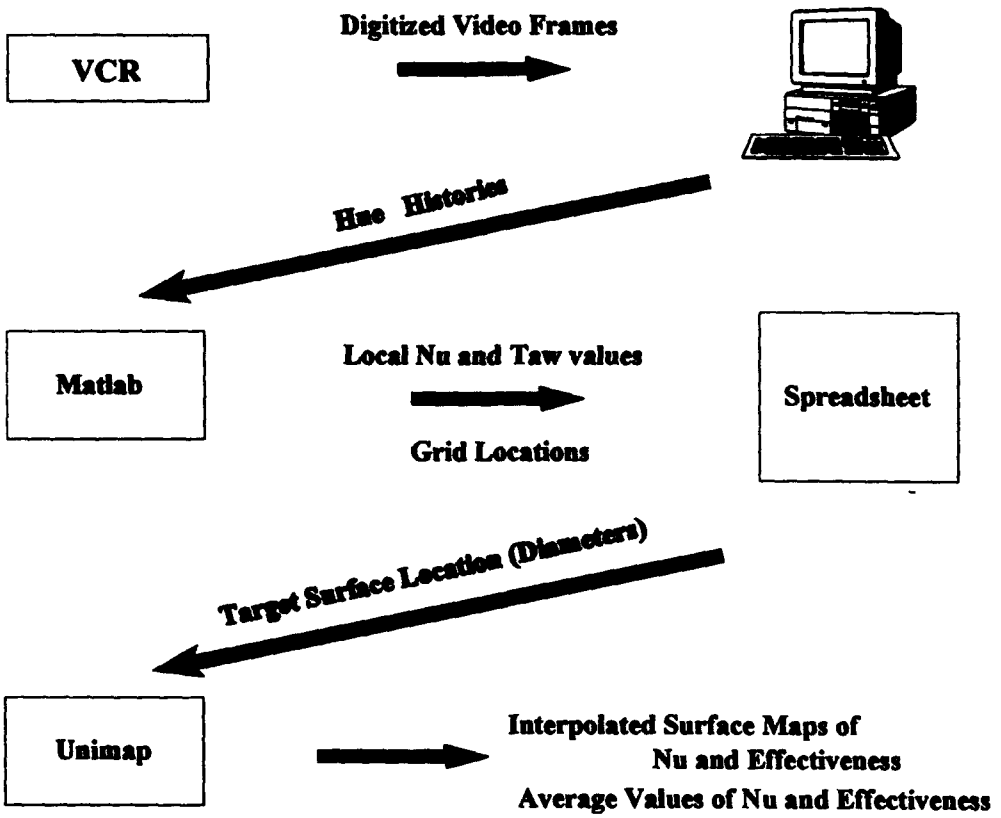

Data Processing

Figure 6.6 Flow diagram of hue temperature history processing.

Table 6.3 Uncertainty values for the hue temperature history matching method in percent.

Quantity	Uncertainty n = 5	Uncertainty n = 10
h	7.5	8.5
T_{aw}	1.5	2.1

temperature signal and the resulting uncertainties in h and T_{aw} become very small.

6.2.1 Perspex Internal Reflection Effects

It was surprising that the uniform coating of the same wideband liquid crystal material should behave differently at positions with close proximity. Figure 6.7 shows the location of three data points used for comparison. Point 23 is located in a region of higher heat transfer adjacent to a jet. Points 30 and 38 are located upstream of a jet hole in a crossflow region of uniform heat transfer. Figures 6.8, 6.9 and 6.10 show surface temperature during the test and the analytic solution using the h and T_{aw} determined from the method previously discussed. Point 23, in Figure 6.8, shows a slight departure from the form of the analytic solution between 31-34°C. This deviation from the expected solution was not observed at all processing points. The data from points 30 and 38, shown in Figures 6.9 and 6.10, do not show this deviation. The possibility of a shift in the hue to temperature calibration brought about by a change in the spectrum of the illumination was considered. The coating used had been calibrated using an essentially steady state experiment in which the hue response at a position adjacent to a foil thermocouple was examined under

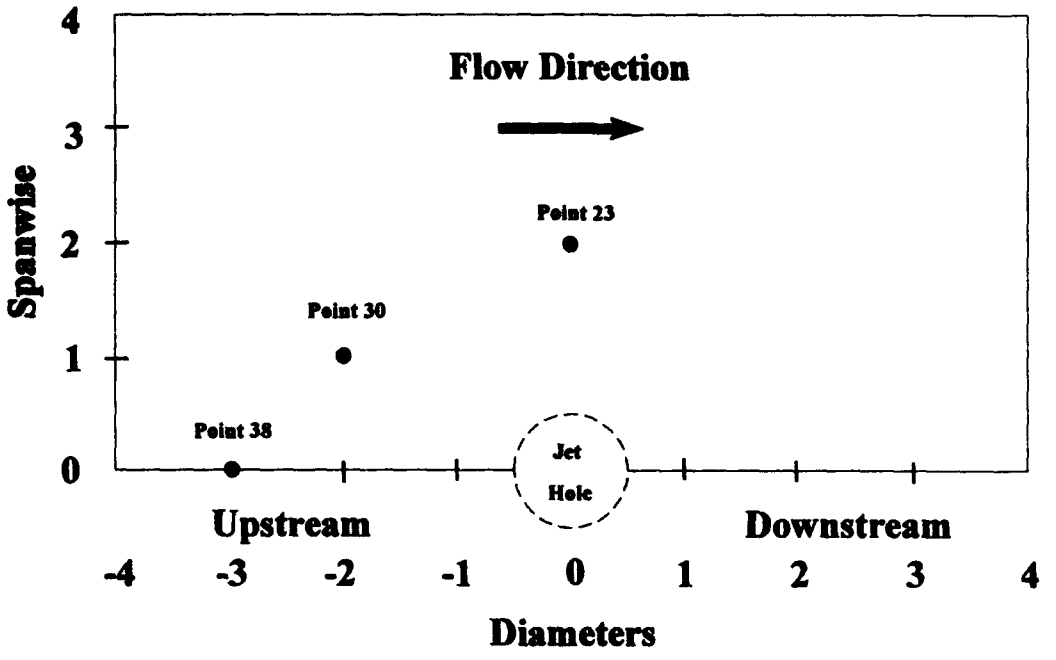

Figure 6.7 Target surface location of grid points used in comparison of hue and saturation signals (jet row 8; Re_j avg = 41,727; z/d = 2; staggered array).

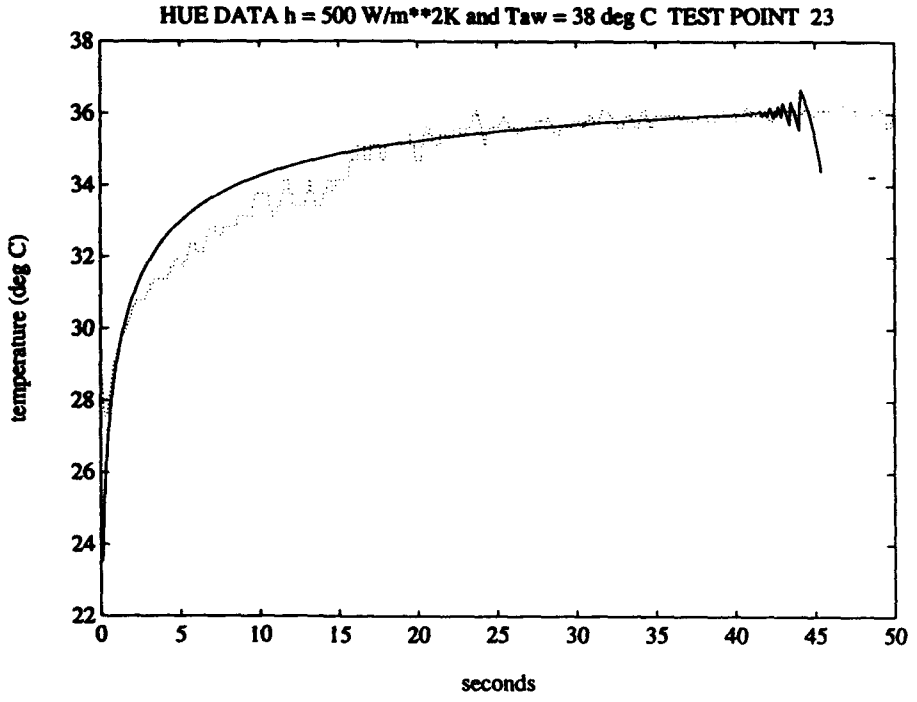

Figure 6.8 Analytic solution to grid point 23.

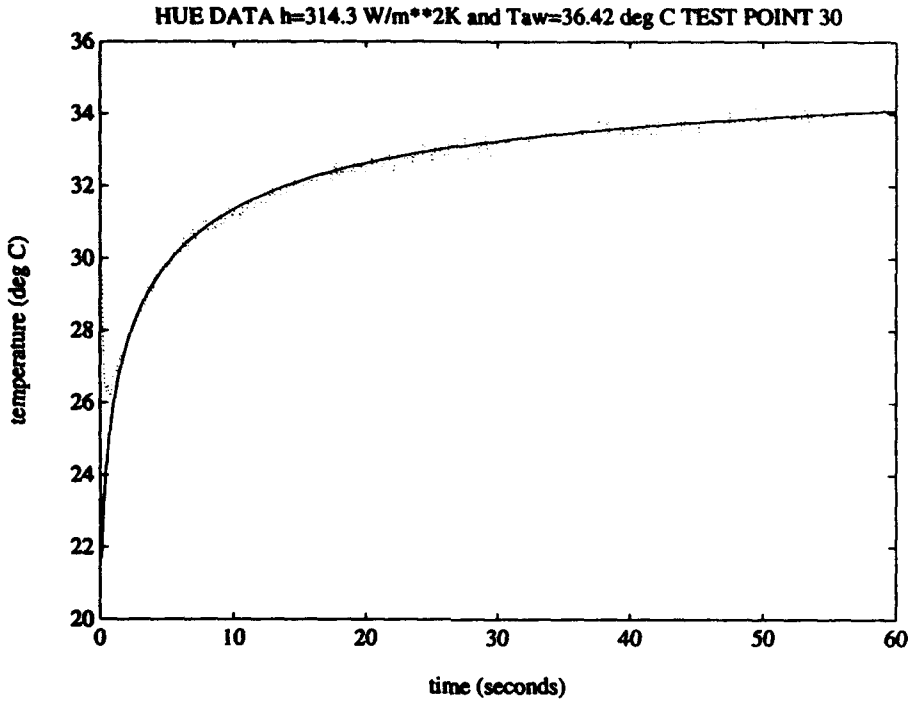

Figure 6.9 Analytic solution for grid point 30.

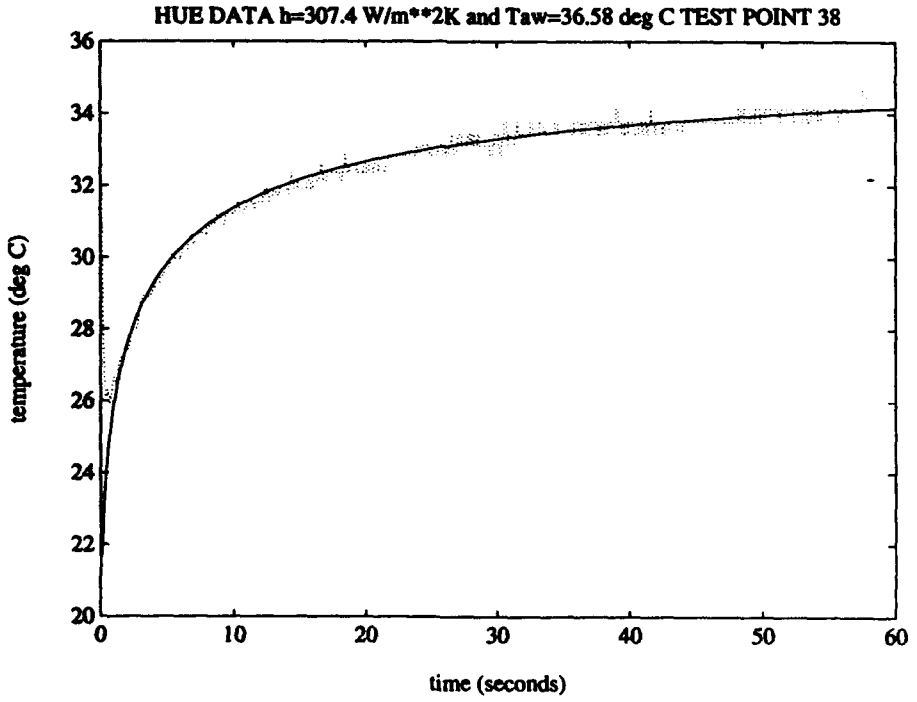

Figure 6.10 Analytic solution for grid point 38.

illumination from a fluorescent strip light. The low heating rate ensured that the coating temperature around the calibration point was sensibly uniform. The liquid crystal film is viewed through the perspex from the tunnel wall side away from the flow. The finite (12mm) perspex thickness means that some of the light incident on the crystal can arise from the coating remote from the measurement site. In other words, the local illumination spectrum is coupled to the colour play of the surrounding crystal. Subsequent wideband calibration experiments conducted by **Wang (1993)** reproduced a typical crystal colour play distribution under an impinging jet. He observed a similar deviation from the original hue to temperature calibration. This condition was corrected by cutting 6.5mm grooves into the side of the target surface away from the crystal at a 5x5mm spacing. The machined surface of each unpolished groove was a poor reflecting surface. This grid eliminated the internal reflection effects and reinstated the original calibration. As discussed in Chapter 3, the effects of lateral conduction and a nonuniform upstream wall temperature are expected to be small and not responsible for the deviation in the hue trajectory. If wall temperature non-uniformity were a factor, as the experiment progressed, the heat transfer coefficient would increase significantly and the surface temperature would be higher than that for a constant heat transfer coefficient. This deviation is in the opposite sense to that measured, as shown in Figure 6.8.

The possibility was investigated by examining the variation of the other colour signal, saturation, available from the video recording. The hue and saturation signals are both output from the frame grabber and, for the liquid crystal coating, vary with temperature. Both signals are independent of illumination strength and, for a constant

illumination spectrum, should be simply repeated. In other words, all hue-saturation coordinates should follow on a single curve irrespective of the crystal temperature. Figures 6.11 and 6.12 show the variation of hue and saturation values during the test for the three points considered. Figure 6.13 plots hue versus saturation for these three points. In this figure, temperature can be considered to be a parameter which increases in an anti-clockwise sense. Points 30 and 38 follow the same curve which is consistent with the high level of agreement between the temperature signal derived from the hue data and the selected analytic solution. The saturation trajectory from point 23 initially follows a similar hue-saturation curve but, the saturation starts to reduce and the data moves away from the curve discussed above for points 30 and 38. This is also the temperature (or elapsed time) at which the inferred temperature starts to depart from the analytical solution. The hue response is being influenced by a change in the illumination spectrum as the surrounding crystal changes colour. Thus, by obtaining a plot of hue-saturation for a calibration one can determine the quality of the hue data against this plot. Only data of high saturation, which match the calibration data, can be considered reliable. For a given optical system, including crystal, illumination and camera, hue can be plotted as a particular function of saturation, as shown in Figure 6.13. Temperature can be thought of as a parameter on the hue saturation locus. This means that, provided the optical system remained unchanged, the hue saturation trajectory during an experiment would not deviate even if the heat transfer coefficient were changing or if lateral conduction was influential. The significant deviation for the selected points illustrated in Figure 6.13 is evidence of an optical effect and is best explained by the total internal reflection phenomenon

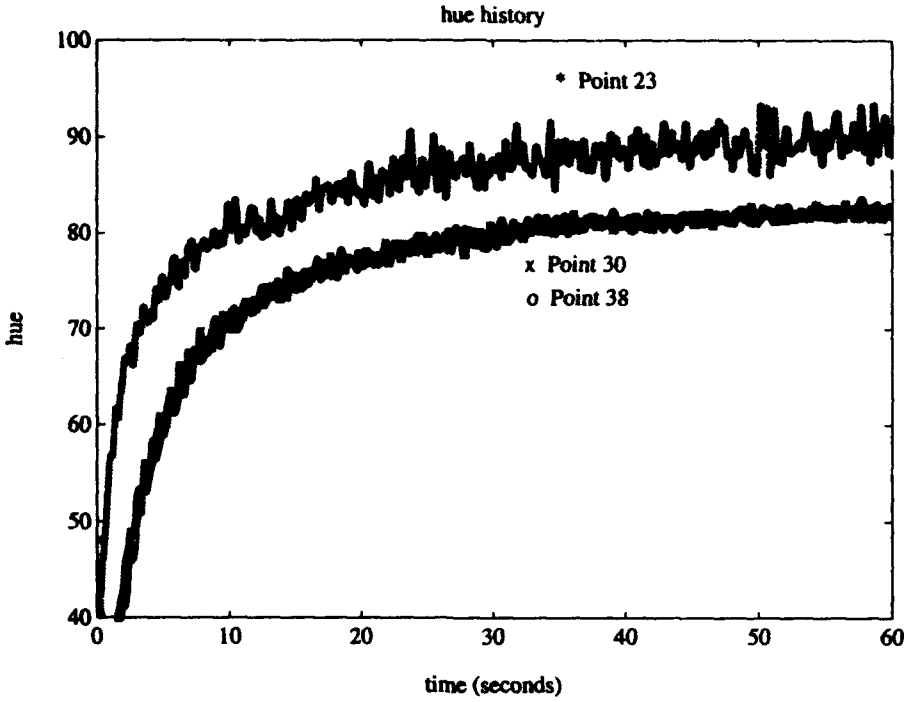

Figure 6.11 Hue histories for grid points 23, 30 and 38.

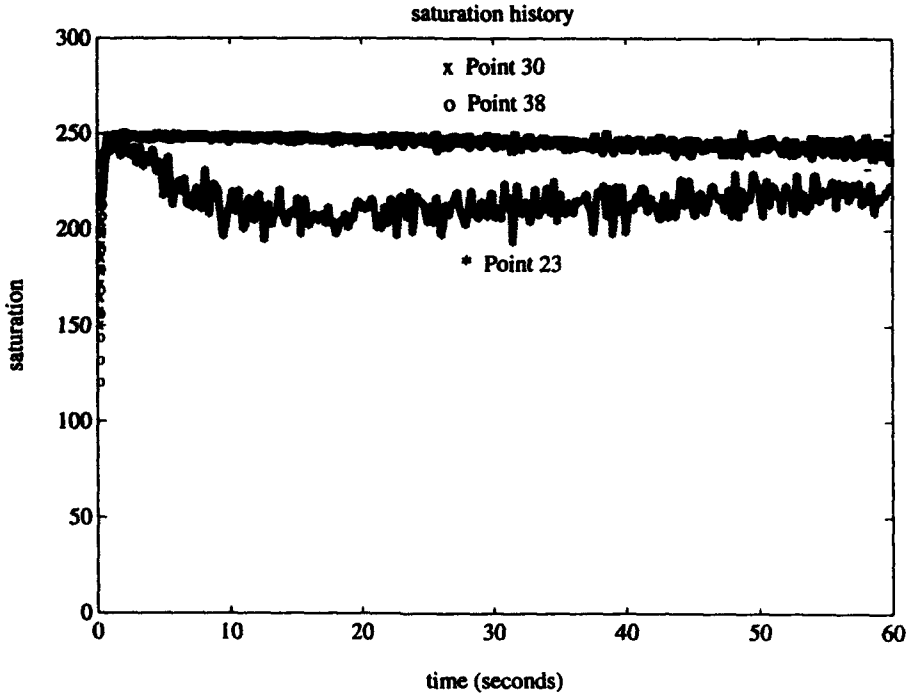

Figure 6.12 Saturation histories for grid points 23, 30 and 38.

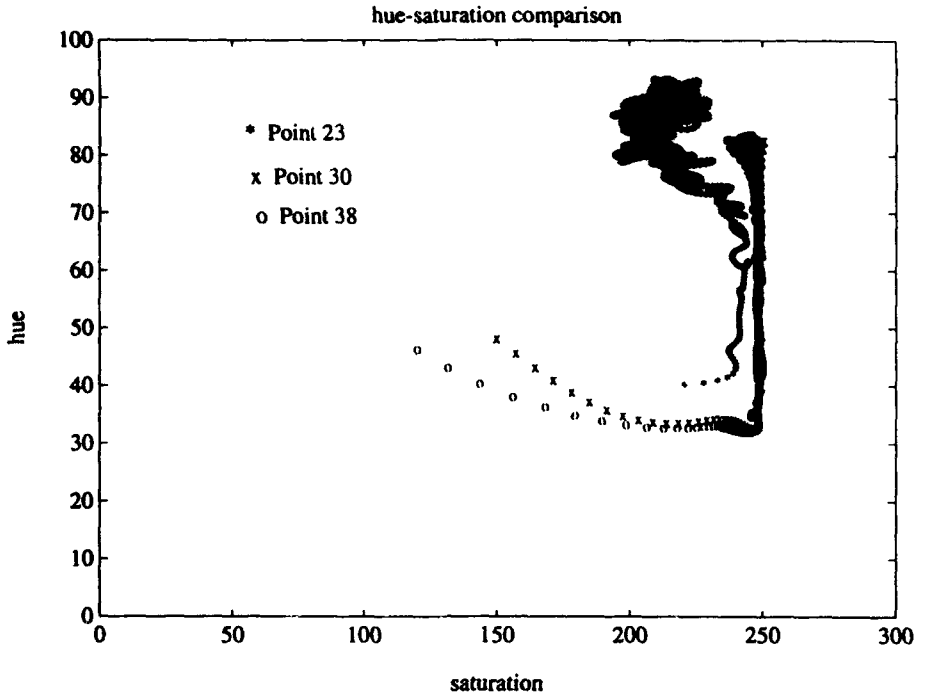

Figure 6.13 Hue-saturation comparison.

described above. It is interesting to note, however, that matching the first portion of data for point 23 results in the analytic solution also matching the data at the longer test times. From this result it can be inferred that, although some influence from surrounding locations is evident by the lower saturation values, the error introduced for these longer test times is small.

CHAPTER 7 - FLOW FIELD INTERPRETATION

This chapter uses the present experimental results to gain insight into flow field and local heat transfer features beneath arrays of inline and staggered impinging jets. The interpretation used three diagnostics. Firstly, the video tape recording of liquid crystal colour play of the transient tests shows the variation in heat transfer over the target surface. Second, static pressure measurements over the target plate give an indication of the effect of local crossflow on jet rows. Lastly, dust deposited on the target surface for two test configurations gives insight into the impingement process and surface shear variation which can be related to surface flow features.

7.1 Surface Crystal Colour Play

In addition to complete processing of the video data from a transient experiment to obtain accurate maps of local h and T_{aw}, an indication of relative heat transfer levels over the target surface can be obtained by inspecting the progress of liquid crystal colour play. The colour play appears first in areas of the highest heat transfer and, as the test progresses, the colour play moves towards areas of lower heat transfer. These isotherms, in the case of the narrow band liquid crystal, are in the form of a thin line and for the wide band liquid crystal, a hue variation. Inspection of video recordings of the liquid crystal colour play then indicates the variation of heat transfer level over the test surface. In the case of a heat transfer experiment with a uniform driving fluid temperature, the ratio of heat transfer coefficient between two points is inversely proportional to the square root of the ratio of the time from the flow initiation for colour play to occur. Simple scaling of h from measured time

ratios is not possible if T_{aw} is not uniform. Qualitative interpretation of video recordings is still possible for the present experiments since full processing showed that T_{aw} was a well behaved function of position.

7.1.1 Inline Array Colour Play

Representative time sequence images of the inline array for the extremes of z/d and average Re_j are shown in Figure 7.1 to 7.4. Figure 7.1 shows the time sequence for z/d = 1 and average Re_j = 10,170. Of interest is the circular nature of the colour change isotherms about the impingement point for the upstream jet rows. The influence of crossflow is minimal at the first jet row since the only crossflow present is that portion of spent flow from the first jet row which moves upstream to the closed end and is then channelled back between the first row of jets. To a certain extent, the jets must act as obstacles to the crossflow and would be expected to have circular cross sections. The area available to the crossflow would then be expected to reduce to a minimum close to the line between the jet centres. A local acceleration of the crossflow between adjacent jets could then be responsible for the slight increase in heat transfer in this region. Just downstream of this region, flow deceleration would explain the colour play lag. The first jet row then provides a flow that causes crossflow for the second row and this process accumulates for subsequent rows of jets. Inspection of the video data shows that the crossflow from upstream jets appears to be deflected to pass between jets within a row. The deflected flow can be seen to surround the following jets and build up along the channel. For each of the engine

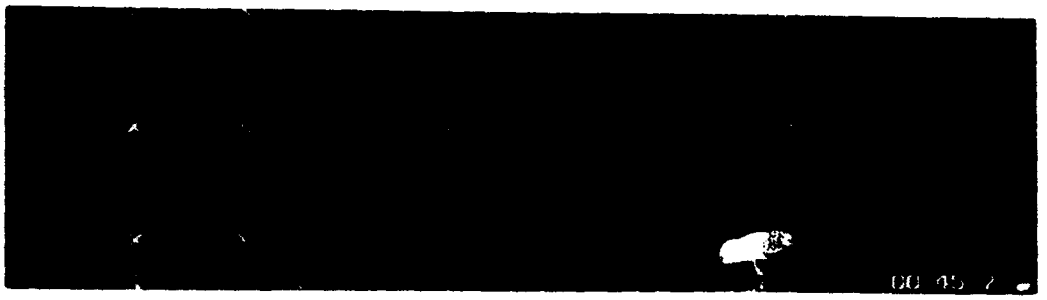

1.75 seconds

7.0 seconds

23.0 seconds

120.0 seconds

Figure 7.1. Time sequence for inline array (Re_j avg=10,170; z/d=1).

0.5 seconds

2.0 seconds

6.0 seconds

60.0 seconds

Figure 7.2 Time sequence for inline array (Re_j avg=34,368; z/d=1).

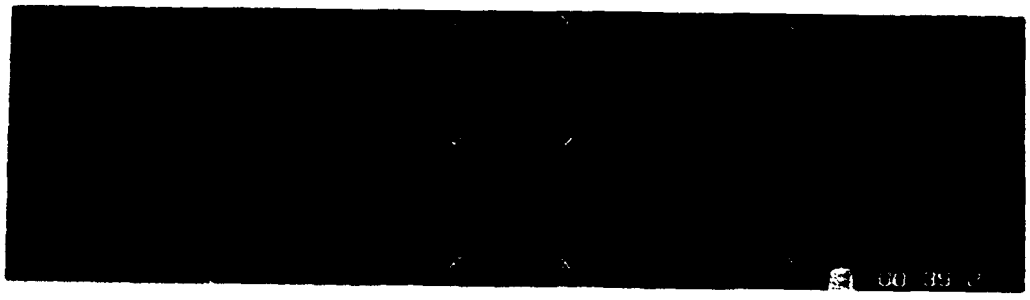

1.0 seconds

4.5 seconds

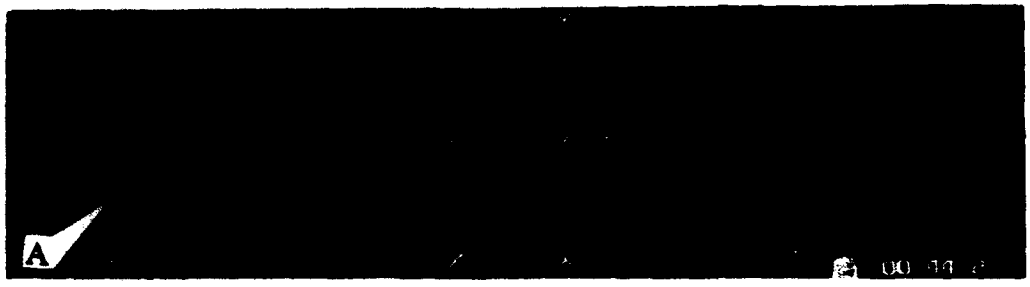

6.0 seconds

90 seconds

Figure 7.3 Time sequence for inline array (Re_j avg=10,161; z/d=4).

0.5 seconds

1.0 seconds

4.0 seconds

30.0 seconds

Figure 7.4 Time sequence for inline array (Re_j avg=39,559; z/d=4).

representative arrays tested, all of the jets reached the target surface and were surrounded by spent flow from upstream jets, referred to as the channel flow or crossflow below. The increasing crossflow progressively limits the spanwise spread of the jets as this moves downstream. Increasing crossflow also seems to limit the spread of the jet in the upstream direction. As this pattern is repeated for each streamwise jet row two things become obvious. Firstly, the upstream and spanwise influence of each jet diminishes through the array due to the effect of increasing crossflow. Secondly, as the accumulated channel flow accelerates, heat transfer increases and contributes significantly to the average value. With the addition of massflow at each successive jet row, the flow accelerates to give the highest velocity and channel heat transfer at the last row in the array. For this reason, the channel colour play occurs first at the rear of the array and moves upstream. The isotherms for the impinging jets change throughout the array from circular at the first streamwise jet row until, at the array end, the isotherms are distorted downstream from the stagnation point. The jet stagnation point heat transfer increases through the array as shown by the colour play progression. Colour play occurs first at the stagnation point beneath the jets in the downstream row.

The increases in channel and stagnation point heat transfer levels become more pronounced with an increase in average Re_j. Figure 7.2 shows the $z/d = 1$ array with an average $Re_j = 34{,}368$. At this higher average Re_j a number of new surface heat transfer features appear. Firstly, the stagnation point is not the region of highest heat transfer under the jet. For the first few jet rows, the region of highest heat transfer occurs in a ring with radius approximately $0.5d$ centred on the jet axis. The colour

play occurs first as a ring with colour play of the central stagnation point following closely thereafter. This region of highest heat transfer is thought to be the result of jet interaction with the quiescent channel air at the jet boundaries causing an increase in turbulence intensity with little reduction in gas cooling potential as discussed in Chapter 2 (Figure 2.3). The next feature to dominate is a ring of colour play with radius from approximately $1d$ to $1.5d$. This ring is populated with radial lines which begin at the stagnation region. This second region of enhanced heat transfer is probably influenced by two fluid dynamic mechanisms. The first is boundary layer transition since this is probably the region in which the boundary layer changes from its laminar to turbulent state beneath the jet. Secondly, vortices generated from the jet exiting the impingement plate have been shown to coalesce [**Fox et al. (1993)**] and strike the target surface to cause either transition or enhance heat transfer at the laminar boundary layer. This second ring is progressively swept downstream with each successive row until at the last jet row, the jet footprint is much reduced and the jet is little more than an obstacle in the flow.

The $z/d = 1$ array surface contours may be contrasted with those for the array with $z/d = 4$ shown in Figures 7.3 and 7.4. For the array with the larger channel height, the average Re_j is more uniform over the array length and the influence of crossflow on downstream jets is notably less. The more uniform distribution of stagnation point heat transfer level is the result of a more uniform flow from the jet holes because the flow accelerates less in the channel passage than in the $z/d = 1$ case. The $z/d = 4$ and $Re_j = 10{,}161$ test is shown in Figure 7.3. The jet isotherms are quite circular throughout the array. Still present are regions of local enhanced channel heat

transfer between spanwise jet rows. Another feature observed upstream of jet row two at 6 seconds (labelled "A" in Figure 7.3) is the appearance of possibly a horseshoe vortex ahead of the jet. This structure is not observed at the downstream locations. Isotherms remain circular upstream of the stagnation point at the array exit but downstream the isotherm trailing edge becomes flatter.

As Re_j is increased to 39,559 at $z/d = 4$, Figure 7.4, the nature of the overall variation in heat transfer over the surface remains the same as the $Re_j = 10{,}161$ case. However, at this z/d, the stagnation region does not show an increase in heat transfer at $0.5d$ from the jet axis. A similar effect was reported by **Goldstein and Timmers (1982)** and is thought to be due to the potential core not striking the target surface at this point. In other words, the shear layers have encroached to the jet axis.

7.1.2 Staggered Array Colour Play

Figures 7.5 to 7.8 show time sequences for the staggered array for the extremes of z/d and Re_j as already discussed for the inline arrays. A liquid crystal coating which displayed colour over a wide band of temperature was used for the staggered array experiments. Thus, a particular spatial temperature gradient through the crystal colour play produced a much wider band than would be observed for the narrow band crystal coating used for the inline array. The colour play contours are much wider than for the previous figures. As before, under conditions of uniform gas temperature, a constant colour line corresponds to a contour of constant h. Again, the first jet row in each of the series shows a very circular h pattern and the resultant flow structure

1.0 second

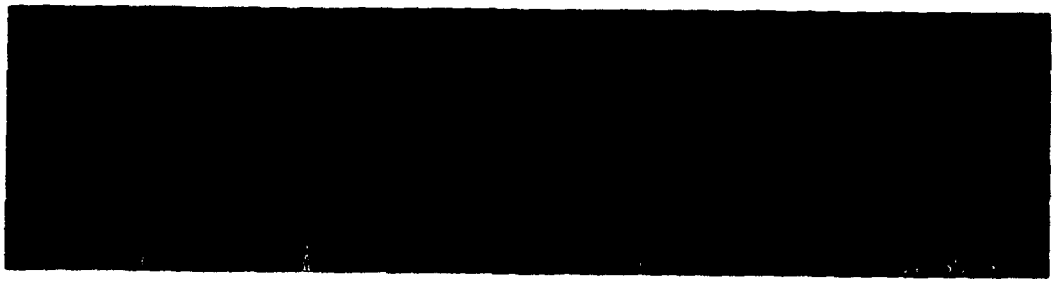

6.0 seconds

30.0 seconds

60.0 seconds

Figure 7.5 Time sequence for staggered array (Re_j avg=10,220; z/d=1).

0.44 seconds

1.5 seconds

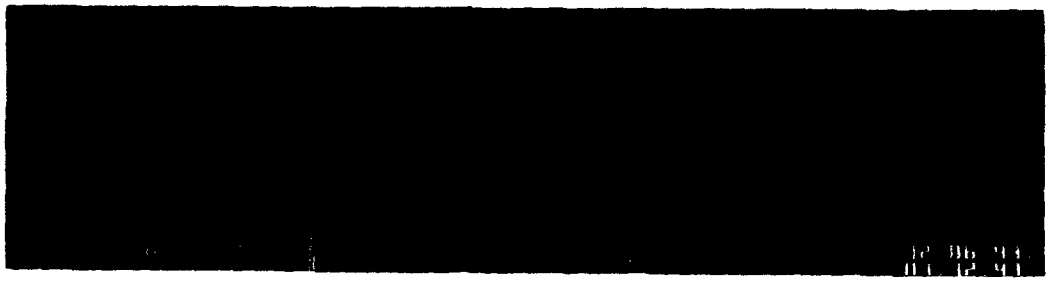

5.0 seconds

30.0 seconds

Figure 7.6 Time sequence for staggered array (Re_j avg=34,534; z/d=1).

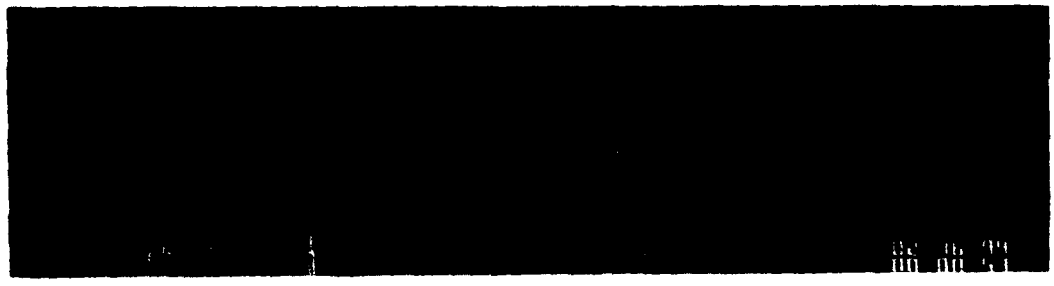

0.5 seconds

2.0 seconds

6.0 seconds

30.0 seconds

Figure 7.7 Time sequence for staggered array (Re_j avg=10,103; z/d=2).

0.2 seconds

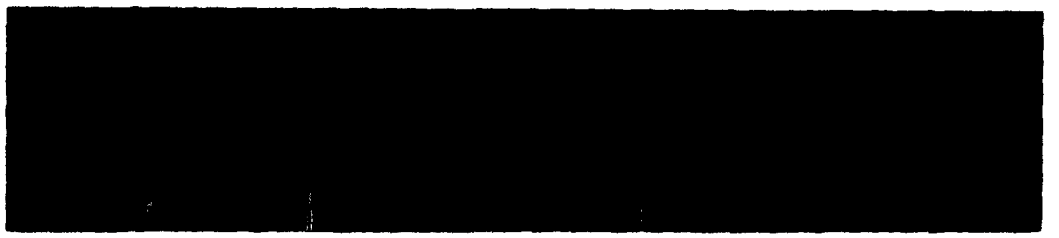

0.5 seconds

2.0 seconds

30.0 seconds

Figure 7.8 Time sequence for staggered array (Re_j avg=41,727; z/d=2).

is increasingly swept downstream on moving through the array. The staggered jets do not develop the long tails seen in the inline case. Instead, the upstream jet flow is channelled between jets in a particular row and is directed at the downstream jet where it is again deflected and channelled. This action confines the downstream portion of the jet and maintains the elliptical shape of the contours on the target area. Thus, the downstream influence of the jet is more limited than in the inline case. In Figure 7.5, the 1.0 second stagnation point colour play appearing at $0.5d$ is evidence of the first peak in heat transfer indicating a wideband liquid crystal colour is also able to visually detect fine surface heat transfer features. The ring of enhanced heat transfer at approximately $1d$ radius observed for the inline array is again apparent.

7.2 Target Surface Pressure

Pressure measurements were taken at various positions on the target surface, as shown in Figure 7.9. At locations away from the jet holes, these pressure tappings were used to measure the static pressure in the crossflow regions. The results of the measurements can be seen in Figures 7.10 to 7.13. For the various extremes in Re_j and z/d, actual measurements and predictions of static pressure using the **Florschuetz et al.** model, discussed in Chapter 3, for both the staggered and inline arrays agree very well. The uniformity of static pressure throughout the array in areas away from jet impingement points is noteworthy. Allowance was made in the analytic model for pressure drop caused by shear stress although, as mentioned in Chapter 3, this corresponded to a small component of the pressure drop for the case without initial

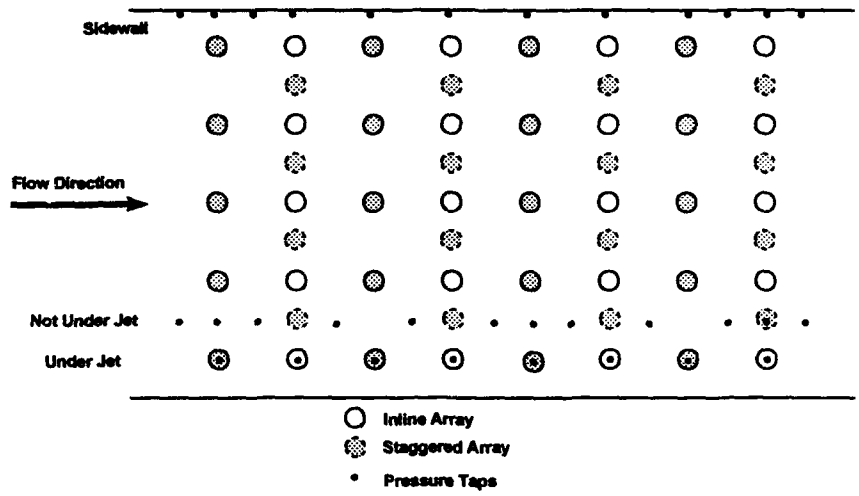

Figure 7.9 Target plate pressure tap locations from camera viewpoint.

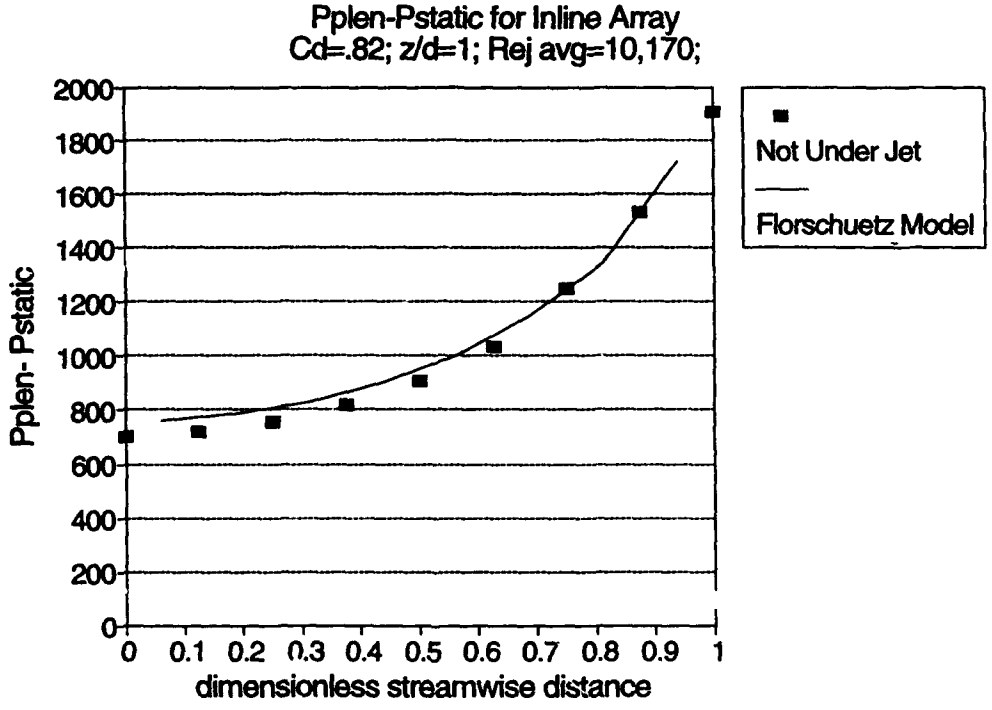

Figure 7.10 Model prediction of inline array static pressure for $z/d = 1$ and Re_j avg = 10,170.

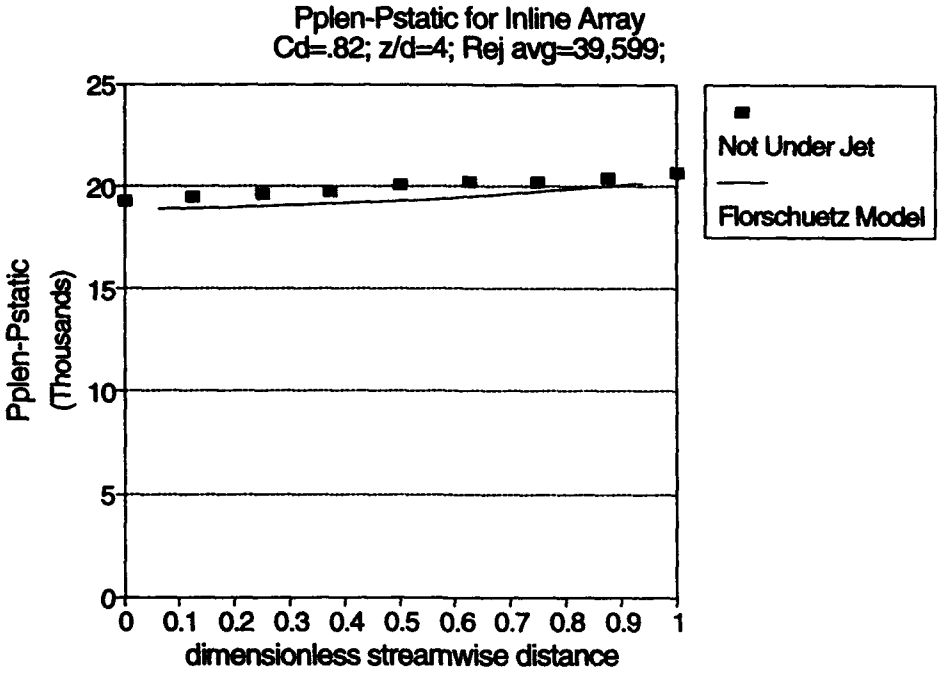

Figure 7.11 Model prediction of inline array static pressure for $z/d = 4$ and Re_j avg = 39,559.

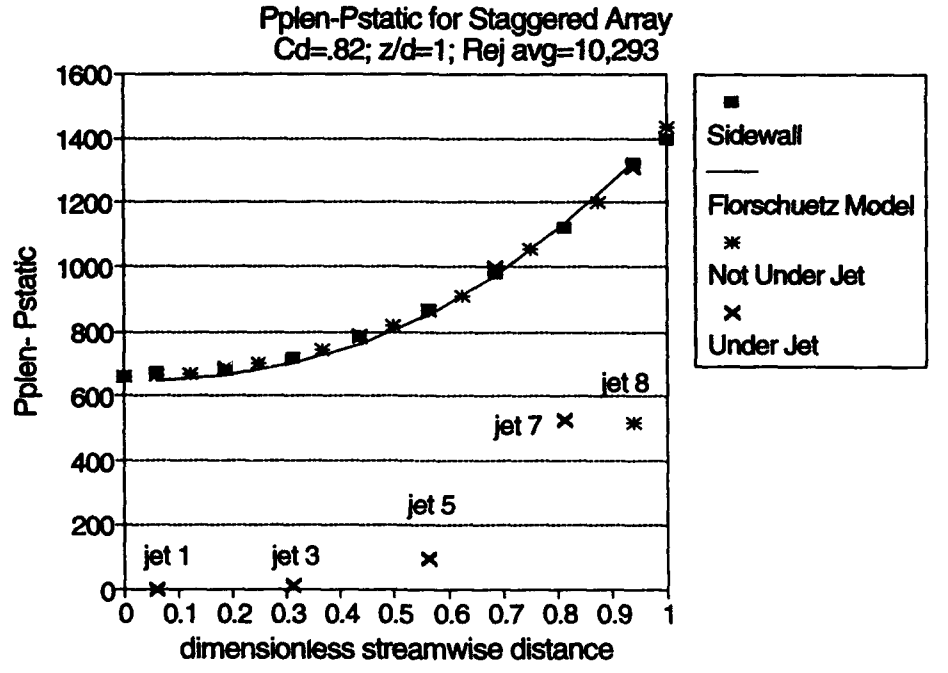

Figure 7.12 Model prediction of staggered array static pressure for $z/d = 1$ and Re_j avg = 10,293.

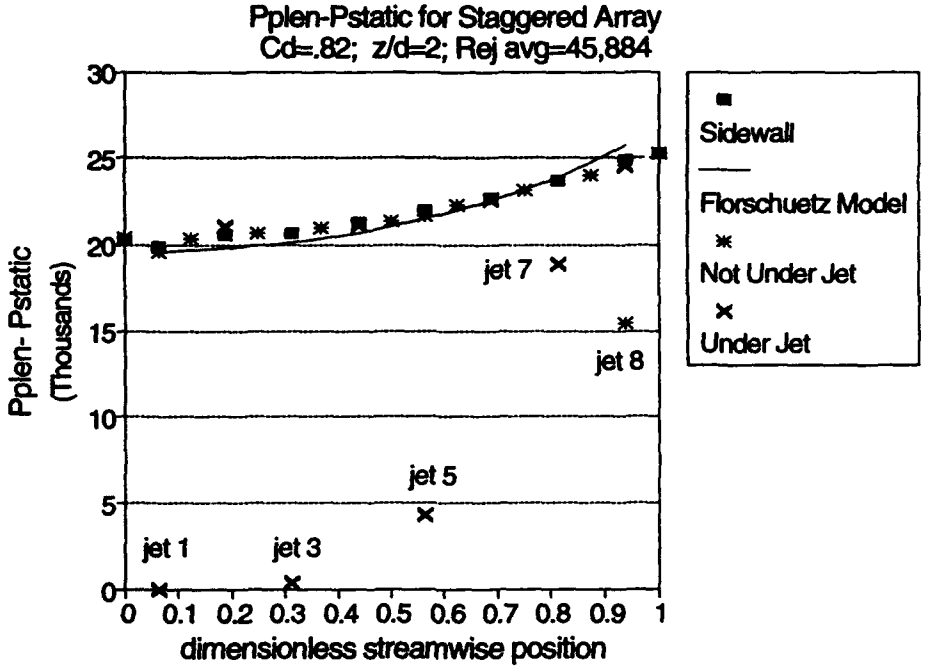

Figure 7.13 Model prediction of staggered array static pressure for $z/d = 2$ and Re_j avg = 41727.

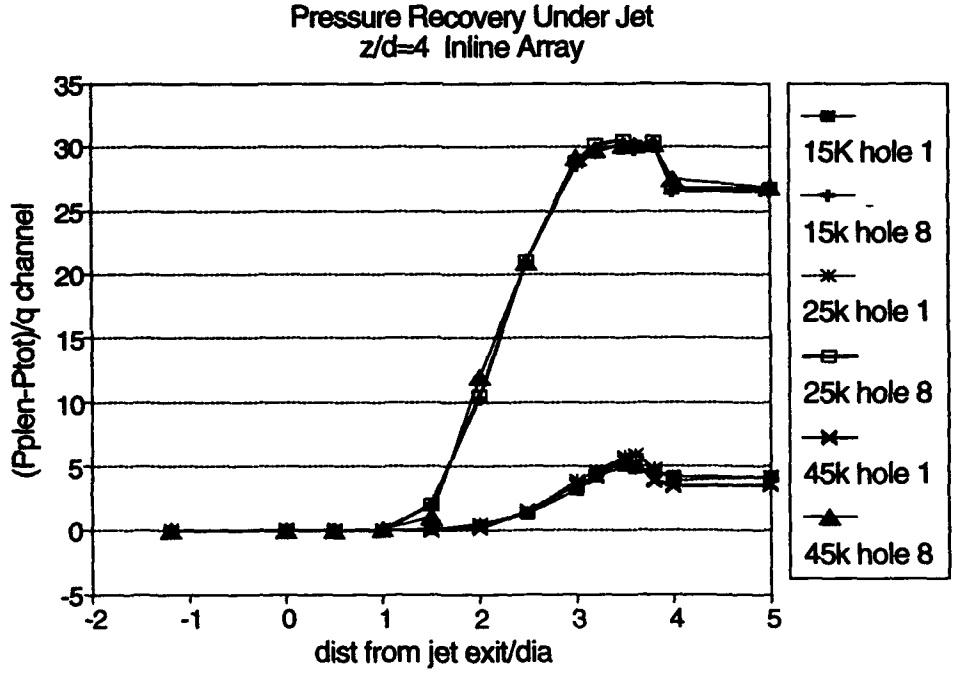

Figure 7.14 Pressure recovery under jet one and jet eight for an inline array as a function of position relative to the jet exit plane for $z/d = 4$.

Table 7.1 Crossflow to jet mass velocity ratios (G_c/G_j) predicted for all configurations tested.

	z/d	Jet 1	Jet 2	Jet 3	Jet 4	Jet 5	Jet 6	Jet 7	Jet 8
Inline	1	0.000	0.097	0.190	0.277	0.355	0.424	0.484	0.545
	2	0.000	0.049	0.097	0.145	0.192	0.237	0.280	0.321
	4	0.000	0.025	0.049	0.073	0.098	0.122	0.145	0.169
Staggered	1	0.000	0.097	0.190	0.277	0.355	0.424	0.484	0.546
	2	0.000	0.049	0.097	0.145	0.192	0.237	0.280	0.321

crossflow. The agreement measured and predicted static pressure was excellent and this analytic model was used to predict the variation of local Re_j throughout the array for both inline and static geometries. Model predictions of crossflow to jet mass velocity ratios are shown in Table 7.1. No differences were noted for a given *z/d* and jet configuration. No significant differences were noted between inline and staggered arrays at a specified *z/d* because the theory averages the crossflow over the channel area and does not account for hole alignment.

Several pressure tappings were positioned geometrically under jet holes as shown. Inspection of the static variation under the jets in Figures 7.12 and 7.13 shows that the plenum pressure is recovered up to the third streamwise jet row. Some small loss of total pressure is seen at the fifth jet row. At later rows, the stronger crossflow displaces the jet slightly downstream which results in a slightly lower pressure on the jet axis than the plenum pressure. Figure 7.14 shows recovery pressure under jet one and eight for a channel with *z/d* of 4. Three average Re_j were tested. A straight 0.9mm diameter probe was moved along the jet axis from the target surface to the

plenum. under both jets. The jet exit plane is at zero and four corresponds to the target surface plane. All pressure data are normalized by the downstream dynamic pressure. The plenum pressure is not recovered for the last jet location. This location has the greatest crossflow influence. The probe data indicates that the potential core at this position penetrates the channel flow approximately one diameter before being significantly deflected by crossflow. The first streamwise jet hole also does not recover the plenum pressure at the target surface. This location is the least affected by crossflow and indicates a penetration of the jet into the channel of up to two jet diameters before the pressure measured by the probe decreases from the plenum pressure. An influence of the upstream spent flow from jet row one is a possible reason for the pressure loss, but a more probable cause is that the potential core has mixed with entrained air and no longer extends as far as the surface for the $z/d = 4$ configuration. Figures 7.12 and 7.13 for the $z/d = 1$ and 2 staggered arrays show that the plenum pressure is recovered at the surface for the configurations for the first three jet rows. This indicates the jet potential core is in contact with the target surface for these configurations but not for $z/d = 4$.

7.3 Dust Deposits

Twice during configuration changes a very fine layer of dust was found deposited on the target surface. Calculations showed that the dust was thermally thin and did not affect the heat transfer results. The first occurrence, shown in Figure 7.15, was noticed during commissioning of the inline array configuration and the

second, shown in Figures 7.16 and 7.17, was after testing the $z/d = 1$ staggered array. These photographs give an indication of the influence of crossflow on the jet and the deposit patterns are related to the isotherms observed in the video time histories. The photographs also show the remarkable uniformity of the flow field between jets in a particular row and give insight to the flow field and showing a similarity to crystal colour play. Figure 7.15 shows the dust concentrations were highest in the stagnation region under the jet, the black spot surrounded by a lighter circular region, as well as along a line which is thought to mark the separation region between the jet and the crossflow. On moving downstream, this separation line moves closer to the jet impingement location. The dust also illustrates the deflection of the jet flow around the following jet and the spanwise extent of the jet limitation.

Figure 7.16 shows the dust concentrations on the target surface for a staggered configuration with a $z/d = 1$. The contrast of the dust with the black paint used for crystal colour enhancement proved adequate to determine dust position. Under jet one is a 3mm diameter circular region of higher dust concentration which is slightly less than the size of the jet diameter. Moving out radially, there is a region where no dust is found and then another circular region of less dense concentration beginning at about $0.6d$ and continuing to slightly over $1d$ where the dust disappears. The stagnation point dust concentration remains circular until after the fourth jet hole, where it begins to distort in the spanwise direction. The ring of dust around the stagnation point begins to distort with the second row, clearly showing the influence of crossflow on subsequent jets. Beginning with the second jet row is a region just upstream of the dust ring where the crossflow from the upstream jet and the jet itself

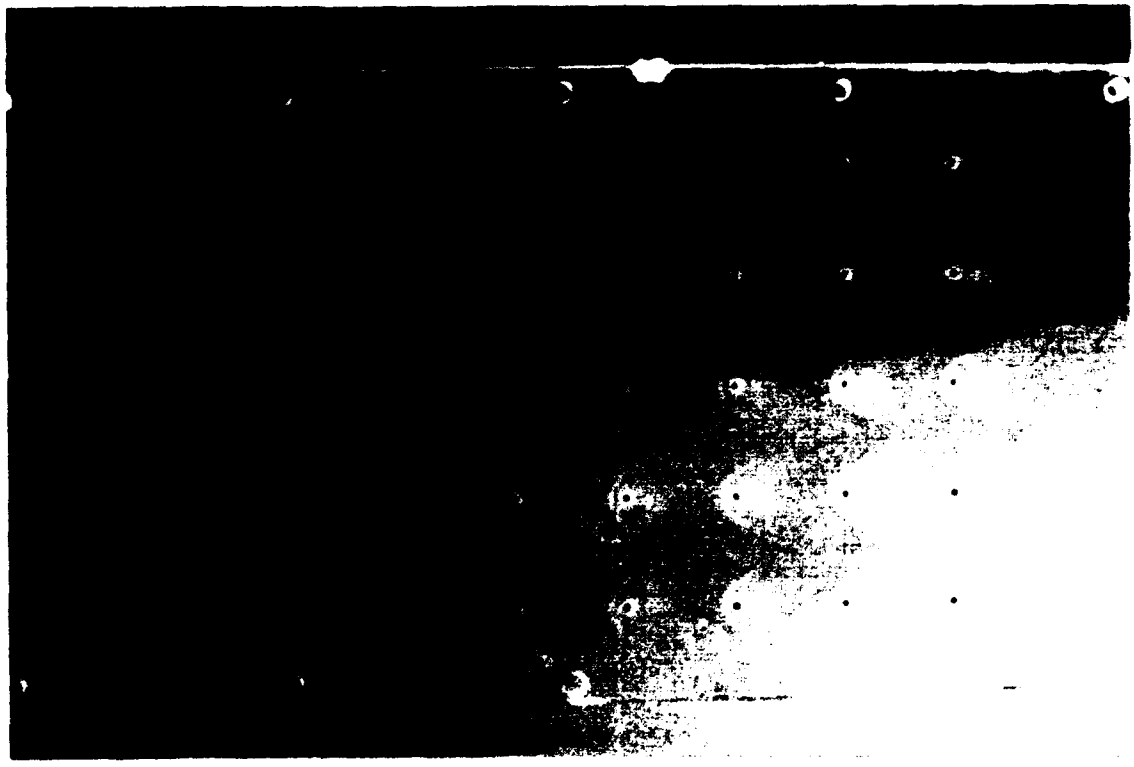

Figure 7.15 Dust concentrations on the target surface of the inline array at z/d=1.

Figure 7.16 Dust concentrations on the target surface for the staggered array at z/d=1.

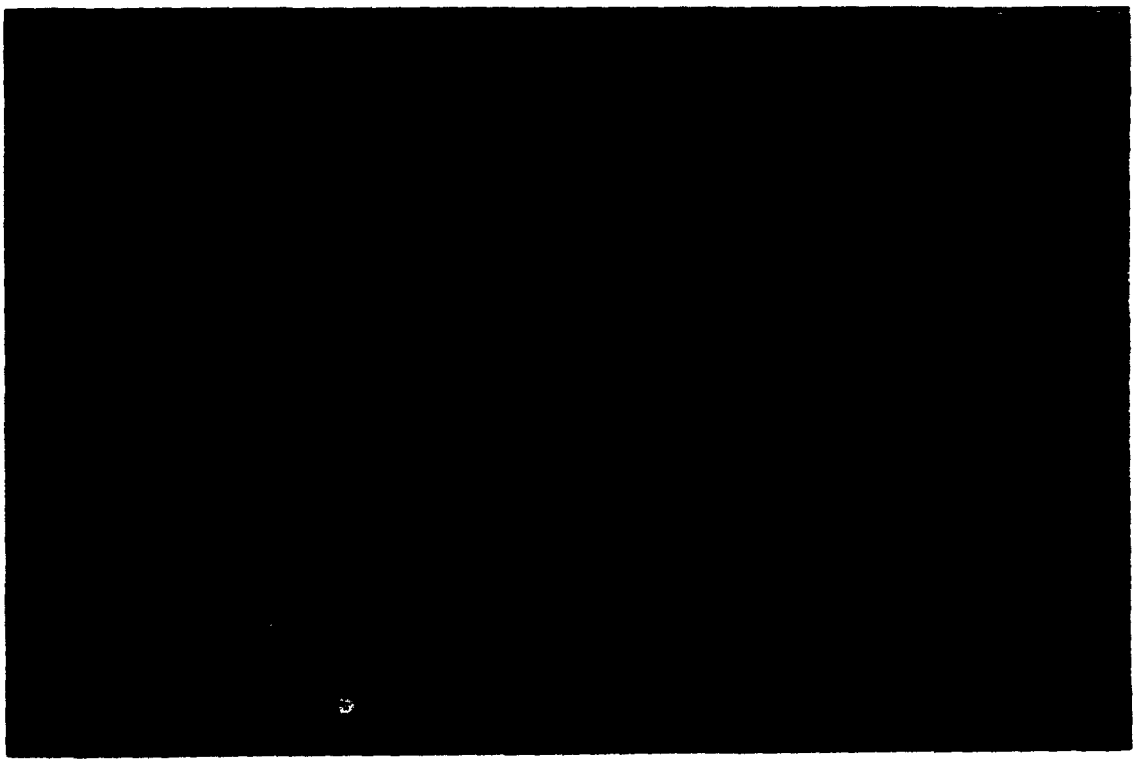

Figure 7.17 *Dust concentrations on the impingement plate for the staggered array at z/d=1.*

interact, forming a higher dust concentration in the form of a crescent. Initially, a small region between this crescent of dust and the circular dust pattern from the jet is clear. This gap disappears at the third jet row and by the fifth jet row, the crescent of dust is seen to be located at the clear region around the stagnation point. It is interesting to note the dust concentration positions immediately downstream of any jet hole position are essentially the same as the dust concentration positions downstream from the first jet stagnation point. It is easy to see the reduction of the jet effective target area with position through the array, showing the increasing importance of the channel flow at the exit of the array.

Of special interest for the staggered array with z/d = 1 were the dust concentrations on the impingement plate surface shown in Figure 7.17. The first

streamwise jet row shows no concentration. Moving downstream, a line of interaction between the jet and the crossflow shows the crossflow is deflected and passes between adjacent jets. Where the jet and crossflow interact is a region of low shear and dust is then deposited at this interface. By the fourth jet hole the deflection line has moved to the leading edge of the impingement jet hole. Jet flow recirculation to the impingement plate is not allowed to interact with the impingement plate upstream of the jet hole. The target surface dust deposits confirm this conclusion, as the deflected region at this point is almost touching the impingement region or region without any deposits.

Just downstream of the jet row 5 on the impingement plate is a double streak. This deflection region moves progressively downstream with distance through the array. At the same time, the double streaks become more intense and move toward each other. **Chiu et al. (1993)** present experimental oil streak data confirming this structure. The structure is consistent with the vortices generated by the crossflow around the jet striking the wake region behind the jet. They, as well as **Kim and Bensen (1993)**, have had a degree of success predicting surface streak lines for this flow field.

CHAPTER 8 - STAGNATION POINT DATA

In the region below each impinging jet, a zone of high heat transfer was observed, discussed in Chapter 7, and was identified as the stagnation point associated with the jet. However, when significant crossflow was present this stagnation point was swept downstream from the geometric centreline of the impingement hole. The stagnation point value of heat transfer was examined in some detail as much literature exists on the heat transfer levels of this phenomenon. In addition, the stagnation point heat transfer level is normally very close to the peak level for a particular row and its value affects the average heat transfer coefficient.

This chapter describes the variation of stagnation point heat transfer with row number, jet Reynolds number and crossflow. The stagnation point heat transfer measurement was taken in each case as follows. Firstly, the stagnation point location was identified on the test video tape. Next, a box extending four pixels by four pixels was chosen around this stagnation point and the intensity or hue history signals were transferred from the tape to computer for each of the 16 pixel locations. After processing, the heat transfer coefficients were found and the adiabatic wall temperature evaluated for these locations. The 16 values were then averaged to determine the stagnation point heat transfer coefficient and adiabatic wall temperature. At the beginning of the array, the stagnation point location corresponded closely with the hole axis. Towards the exit of the array, deflection of the stagnation point from the hole axis was noted of up to 1/2 of a jet diameter. In this chapter, detailed heat transfer results are presented for inline and staggered arrays and comparison is made between the results for the two configurations. Correlations are presented to cover the

range of average Re_j tested for all of the configurations tested with z/d = 1 and 2.

The significant conclusion from this part of the research is that the stagnation point Nusselt number is very close to that expected from consideration of isolated jet data. This is particularly true for the configurations with z/d values of 1 and 2 where the jet bounding shear layer does not reach the jet potential core. The dependence of stagnation point Nusselt number on Reynolds number is close to $Re^{0.5}$ which is consistent with the variation expected for a laminar boundary layer on the target surface. The absolute value is within the range of values reported in the literature for related impinging jet flow fields.

The adiabatic wall temperature was also determined at each stagnation point. These calculated temperatures agreed with the jet plenum temperature on the order of 0.5-1.0°C for most tests.

8.1 Inline Array

Stagnation point heat transfer data is presented in Figures 8.1 to 8.16 for the inline geometry and for the complete range of Reynolds numbers tested. For each channel spacing, the data are alternately presented in one of two forms in Figures 8.1 to 8.6. The first form, used in Figures 8.1, 8.3 and 8.5, is a comparison of stagnation point Nusselt number as a function of jet row location for different values of average Re_j at specified z/d. The second form of data presentation, used in Figures 8.2, 8.4 and 8.6, compares stagnation point Nu as a function of the corresponding impingement hole Re_j for a specified z/d. The steps in the analysis leading to the correlation (Equation 8.1) included in these figures are discussed below.

The two major influences on the stagnation point heat transfer level, other than the pressure difference between the plenum and the hole exit, are expected to be the strength of the local crossflow and the extent of the jet mixing. With this in mind, some general conclusions about the stagnation point data can be made for the inline case. For a given *z/d*, the stagnation point *Nu* always increases with an increase in average Re_j (see Figures 8.1, 8.3, and 8.5). The row by row increase in stagnation point heat transfer is evident from Figures 8.1, 8.3 and 8.5 and is, in the main, caused by the increase in local Re_j as the channel static pressure drops from array inlet to array exit. Graphs of stagnation point *Nu* as a function of local Re_j for the range of *z/d* tested are given in Figures 8.2, 8.4 and 8.6. In these plots, the results for each experiment appear as clusters where the variation in local Re_j is caused by the changing pressure difference across the holes through the array as discussed above. Thus, since the jet Reynolds number increases continuously through each array, the bottom left point for each cluster is for the first row of holes and the top right for the last row. The steps in Re_j between the clusters are due to the changes in total mass flow between experiments. It is interesting to note that the Nusselt numbers for each hole correlate well on the square root of Re_j as the total mass flow is increased. This is clear from Figure 8.2 where the stagnation point Nusselt numbers for the holes close to the start of the array follow the correlation. The correlation, which is discussed later, relates Nusselt number to local Re_j raised to an exponent of sensibly 0.5. The stagnation points downstream of the third row are not predicted by the correlation. In the case of *z/d=1*, the slope of each cluster is, however, greater than the slope of these lines and indicates that, through the array, the stagnation point

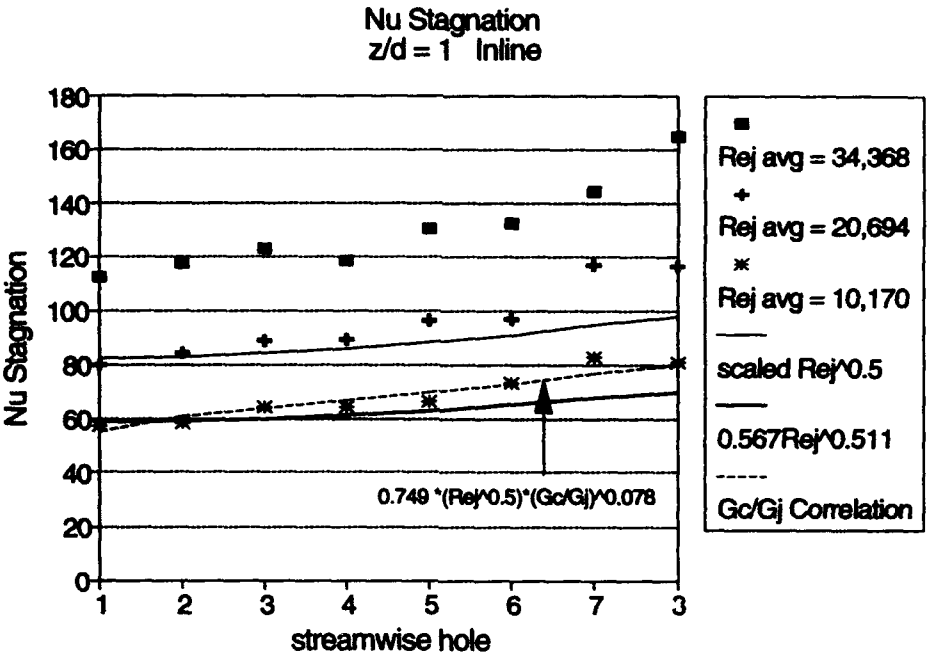

Figure 8.1 Stagnation point Nusselt numbers at streamwise locations for an inline array with $z/d = 1$.

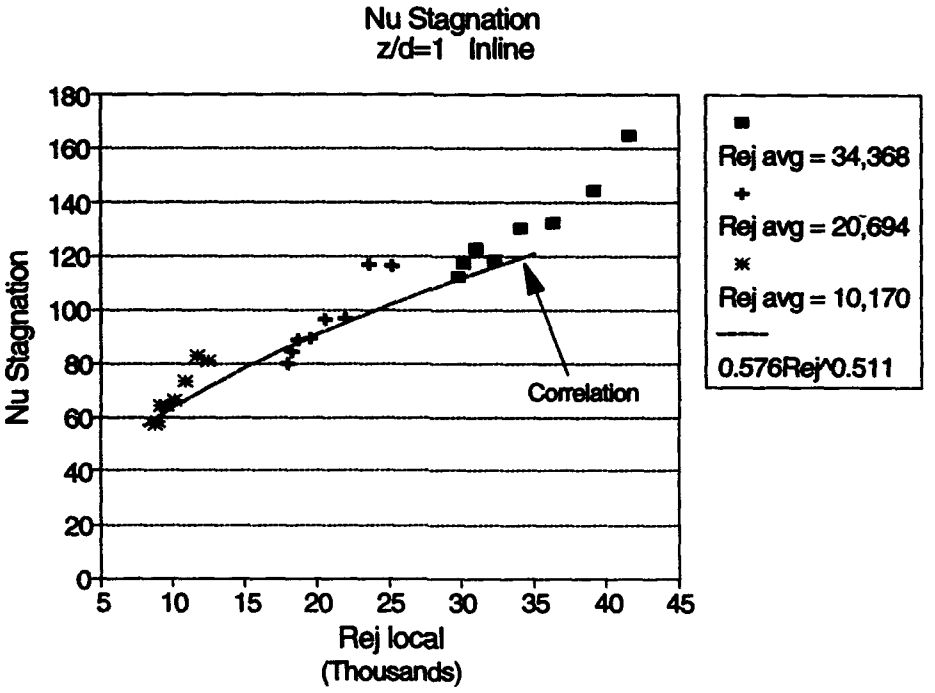

Figure 8.2 Inline array stagnation point Nusselt numbers for local Re_js and $z/d = 1$.

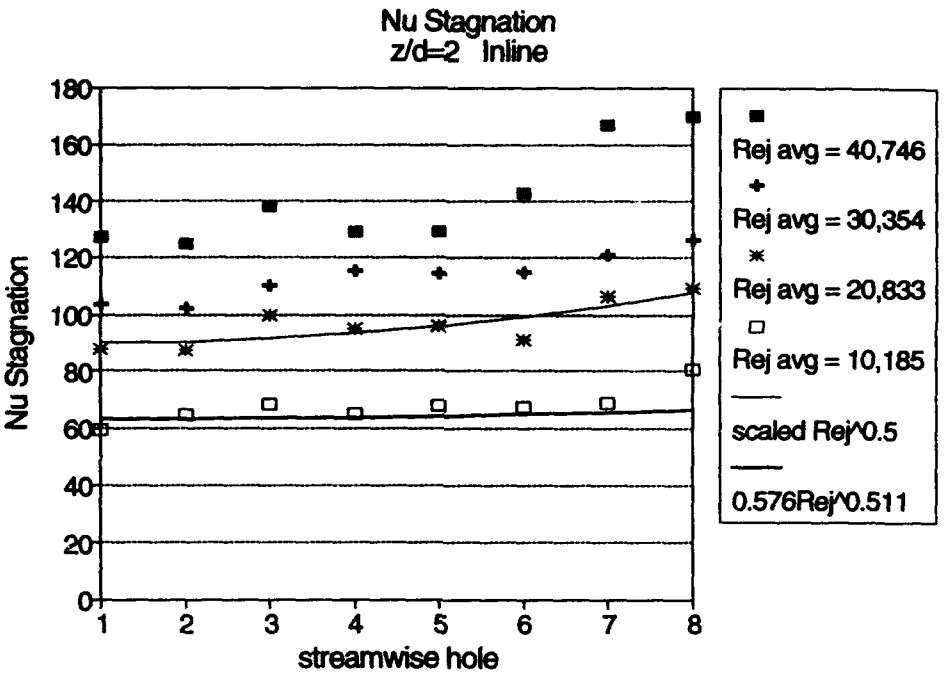

Figure 8.3 Stagnation point Nusselt numbers at streamwise locations for an inline array with $z/d = 2$.

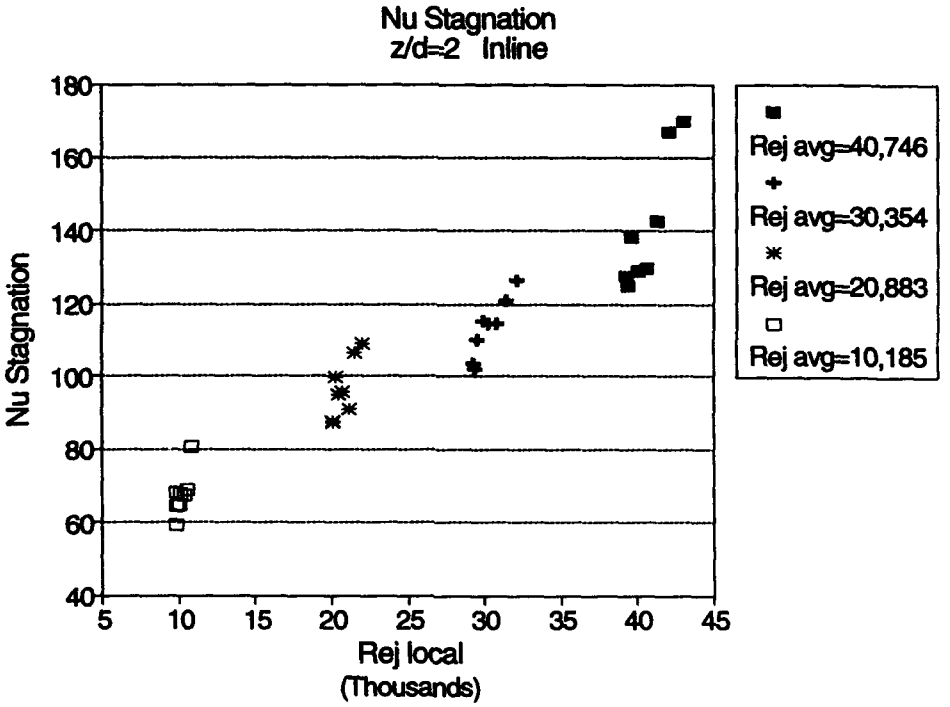

Figure 8.4 Inline array stagnation point Nusselt numbers for local Re_js and $z/d = 2$.

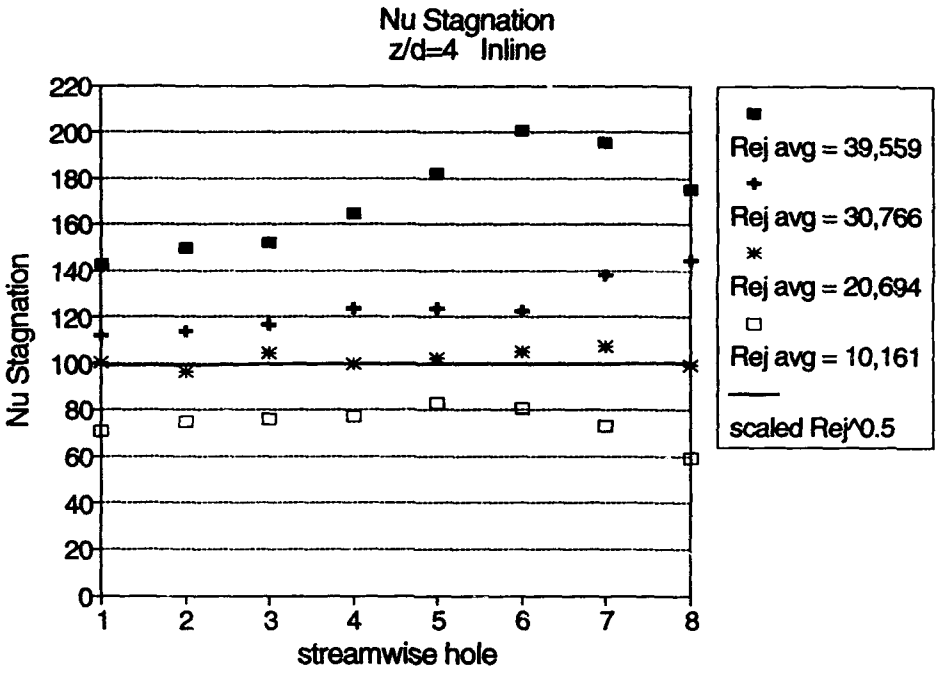

Figure 8.5 Stagnation point Nusselt numbers at streamwise locations for an inline array with $z/d = 4$.

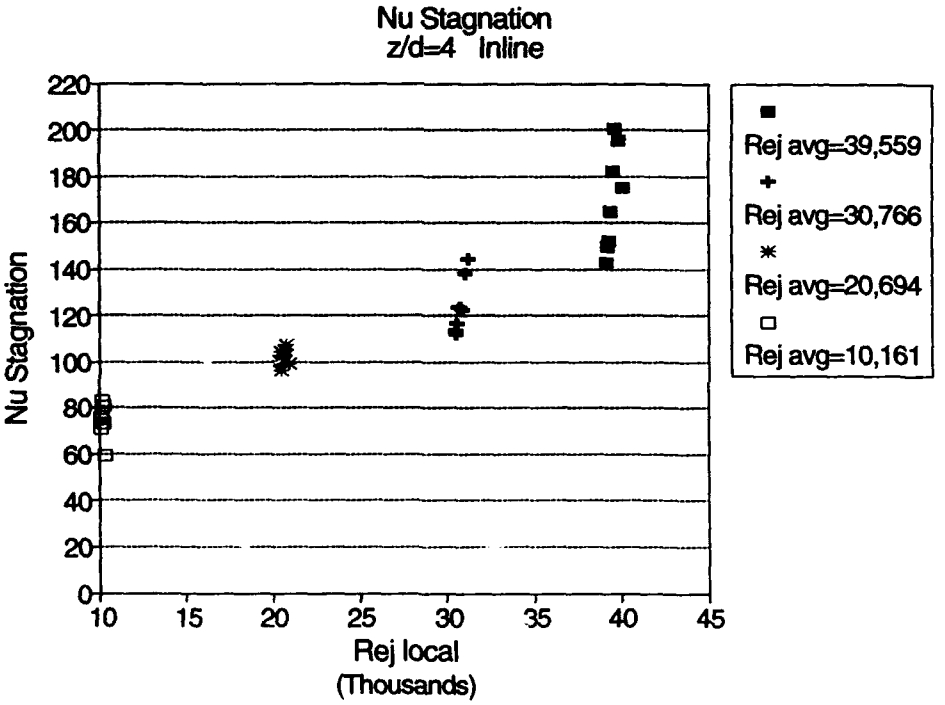

Figure 8.6 Inline array stagnation point Nusselt numbers for local Re_js and $z/d = 4$.

Nusselt number does not correlate simply on the square root of Re_j.

One possible explanation for the change in Reynolds number dependency is the influence of the crossflow on the jet velocity profile at the hole exit as reported by **Andreopoulos (1982)** and **Crabb (1981)**. At higher crossflows, the effective outlet area of the jet hole is reduced. Since the measured static pressure distribution agrees well with that predicted using the flow model developed by **Florschuetz**, the predicted air flow rate through these holes close to the array exit must be correct. This means that the reduction in area caused by the crossflow capping the hole exit will result in higher exit velocities than the velocity averaged across the hole geometric area. This higher outlet velocity is possibly the cause of the increase in stagnation point heat transfer above that predicted from the early array correlation. In other words, the flow model gets each jet massflow right but the heat transfer coefficients are increased by an effective reduction in the hole area. Complete correlation could only be attempted using Nusselt number and Reynolds numbers based on a changing hole diameter dependent on the hole effective area. It is also worth noting, as discussed in Chapter 7, that the surface isotherms of liquid crystal colour play indicate that the jet impingement zone near the array exit is no longer axisymmetric. This is further evidence of the effect of the crossflow on the jet.

At $z/d = 2$ (Figure 8.3), the streamwise dependence of Nu at stagnation points is closer to that predicted by laminar layer theory than that for a $z/d = 1$ array. The crossflow is less for the former case for the same average Re_j in the two cases. For example, the crossflow at the array exit for a $z/d = 2$ is approximately the same as the crossflow at row four for the $z/d = 1$ case. For $z/d = 4$ (Figure 8.5), the local Re_j

changes little through the array. The crossflow at the array exit for the $z/d = 4$ case is less than that at hole two for the $z/d = 1$ case.

For $z/d = 4$, a Re_j exponent of 0.5 is sufficient to characterize the increase in stagnation point *Nu* through the early portions of the array. The Re_j variation through the array is small and the crossflow at the array exit is minimal. The stagnation *Nu* increases through the array until approximately jet row six. After jet row six there is a slight drop in stagnation *Nu* not observed for other z/d values tested. Scaling between tests, where the Re_j changes were greater, indicates a greater Re_j exponent than 0.5 is required to characterize the Nusselt number dependence. One possible explanation for this drop is that the stagnation point at the array exit is being influenced by even the small amounts of crossflow present as the potential core no longer reaches the target surface.

The same data are also presented at a given average Re_j for the three values of channel height in Figures 8.7 to 8.14. Presented in this manner, the influence of channel height on stagnation point *Nu* for a given average Re_j, or flow rate, is apparent. The influence is small (Figures 8.7, 8.9, 8.11 and 8.13). For comparison of data at an average Re_j of 30,000 and 40,000, it was necessary to scale the $z/d = 1$ and average $Re_j = 34{,}368$ data to these values. Choking of the test channel flow for this z/d, discussed in Chapter 4, prevented data being taken above this average Re_j. For the first four jet holes, the data were scaled using local $Re_j^{0.5}$ as these positions were not influenced by crossflow. Rows five to eight were scaled using local $Re_j^{0.7}$ as this was found to be more representative for downstream holes under the influence of crossflow. It should be noted that these corrections were small. In general, for a

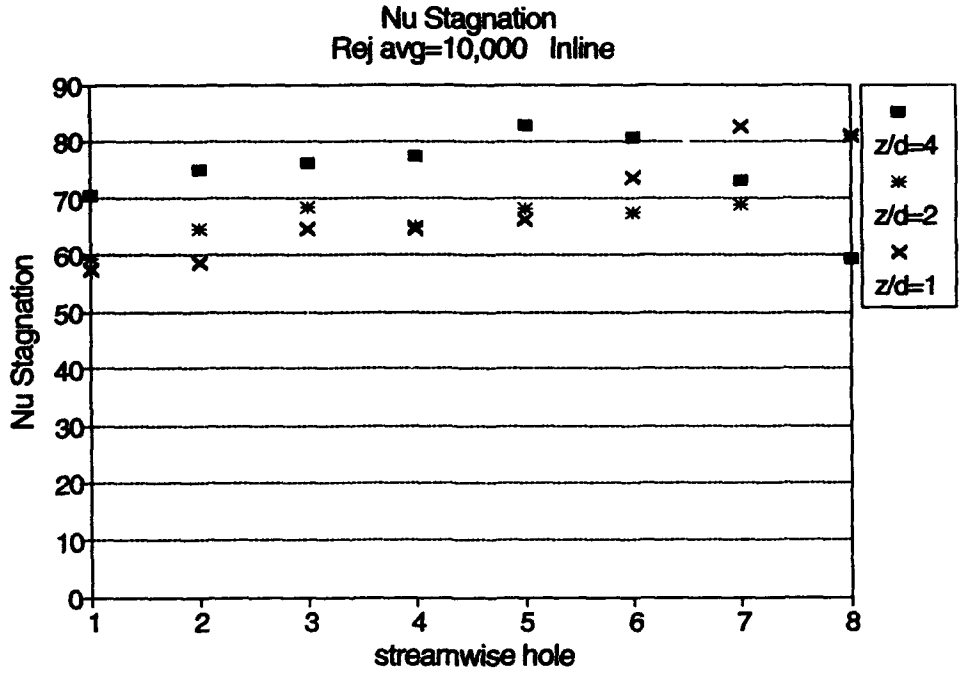

Figure 8.7 Inline - Re_j avg = 10,000 stagnation point Nusselt numbers at streamwise jet locations for z/d = 1, 2 and 4.

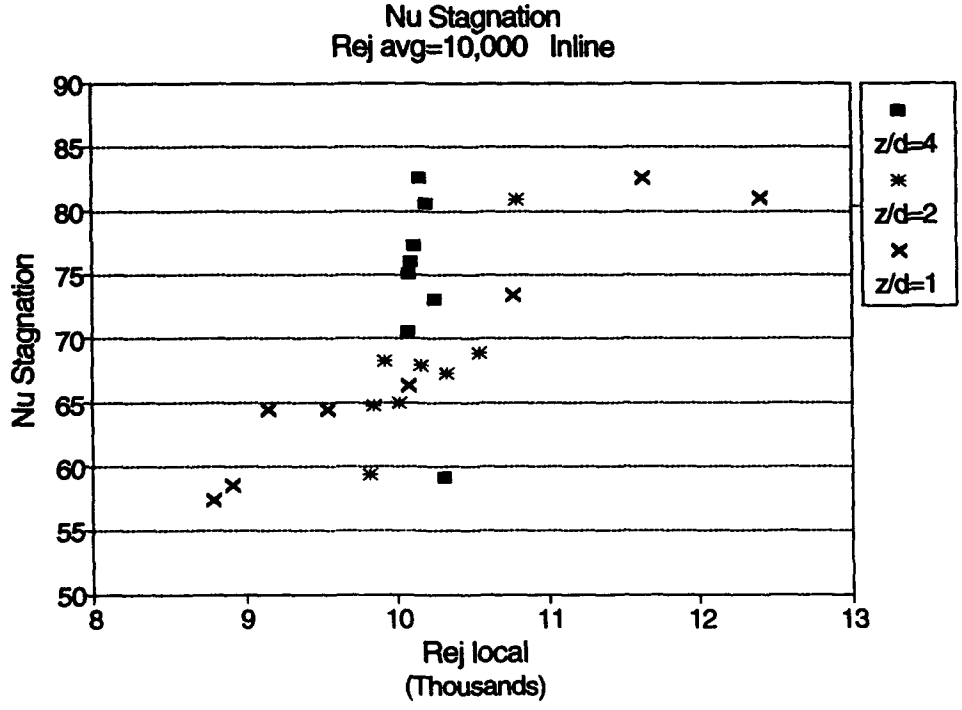

Figure 8.8 Inline - Re_j avg = 10,000 stagnation point Nusselt numbers for local Re_js at z/d = 1, 2 and 4.

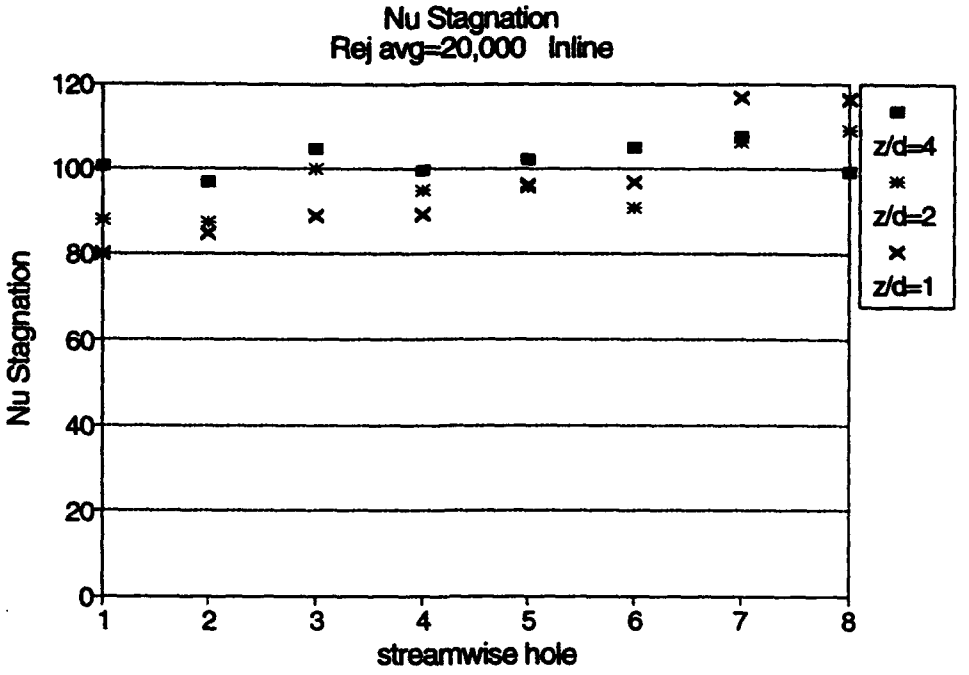

Figure 8.9 Inline - Re_j avg = 20,000 stagnation point Nusselt numbers at streamwise jet locations for z/d = 1, 2 and 4.

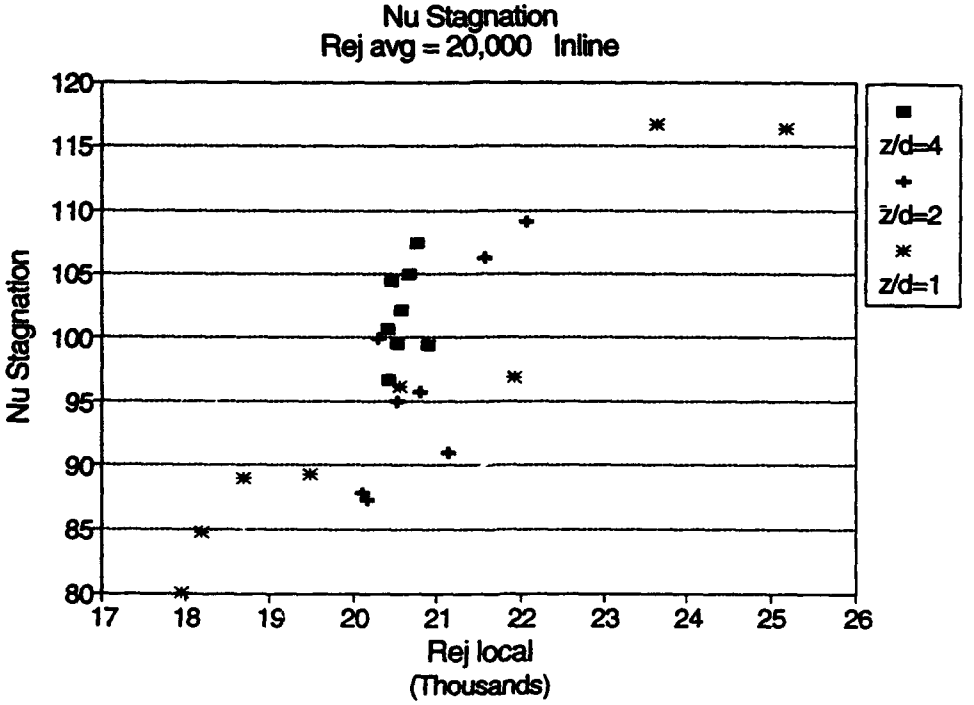

Figure 8.10 Inline - Re_j avg = 20,000 stagnation point Nusselt numbers for local Re_js at z/d = 1, 2 and 4.

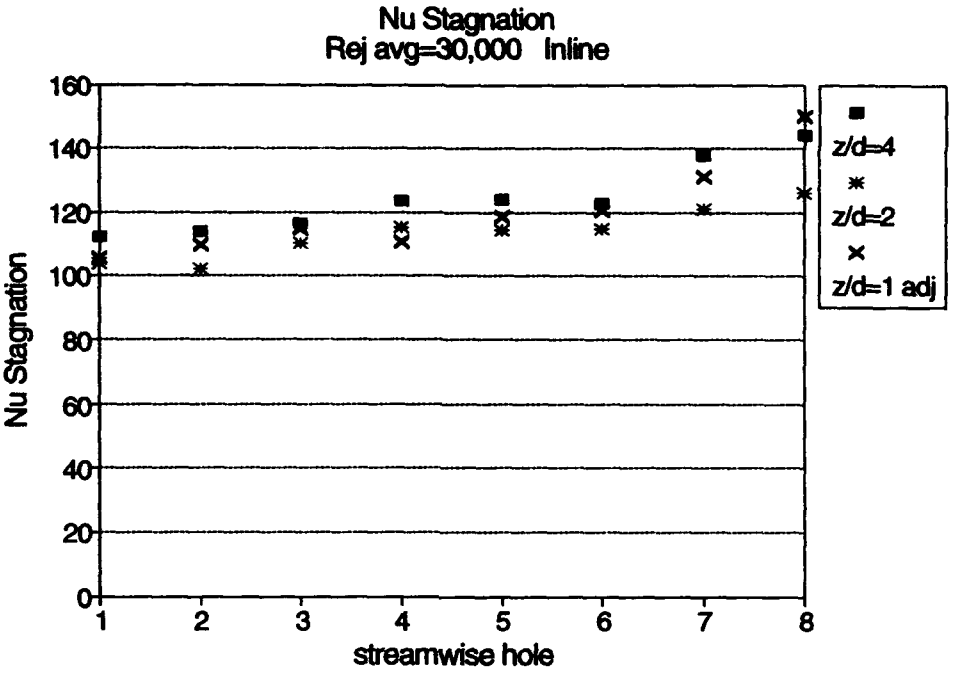

Figure 8.11 Inline - Re_j avg = 30,000 stagnation point Nusselt numbers at streamwise jet locations for z/d = 1, 2 and 4.

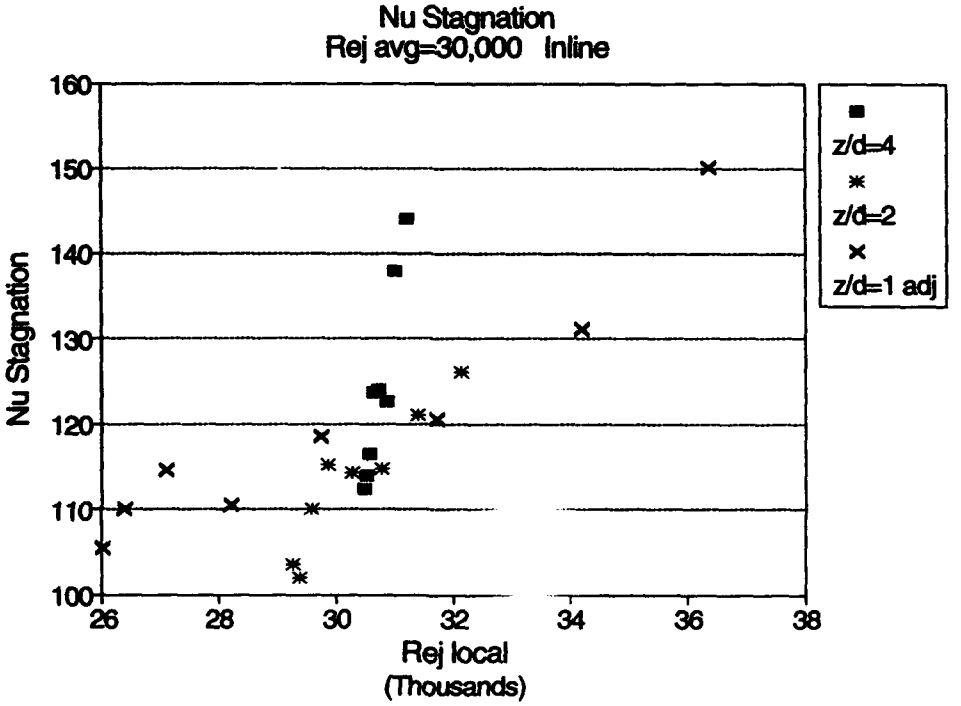

Figure 8.12 Inline - Re_j avg = 30,000 stagnation point Nusselt numbers for local Re_js at z/d = 1, 2 and 4.

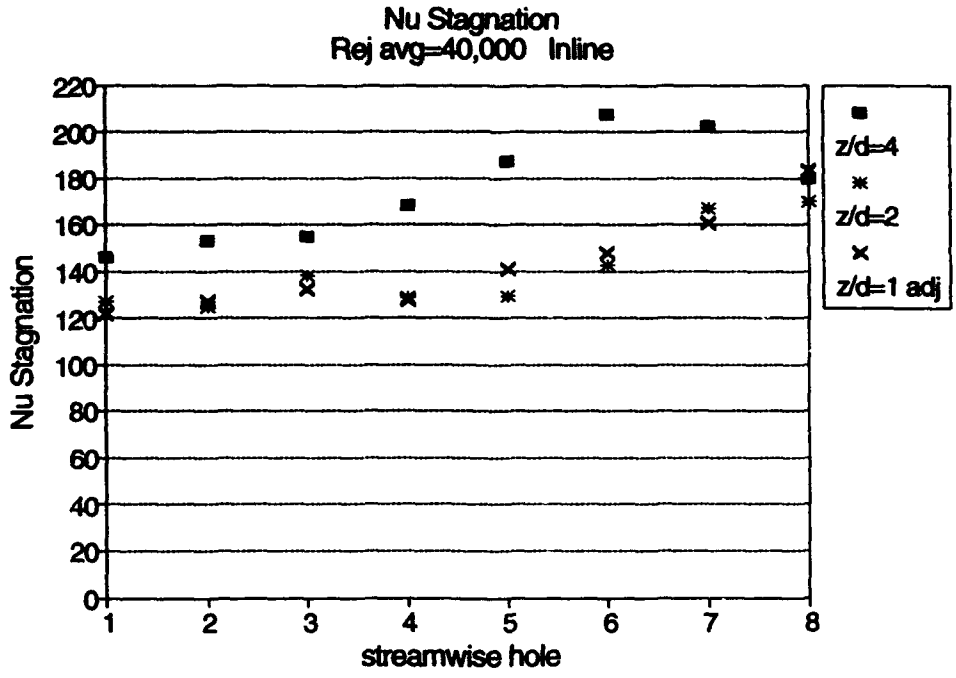

Figure 8.13 Inline - Re_j avg = 40,000 stagnation point Nusselt numbers at streamwise jet locations for z/d = 1, 2 and 4.

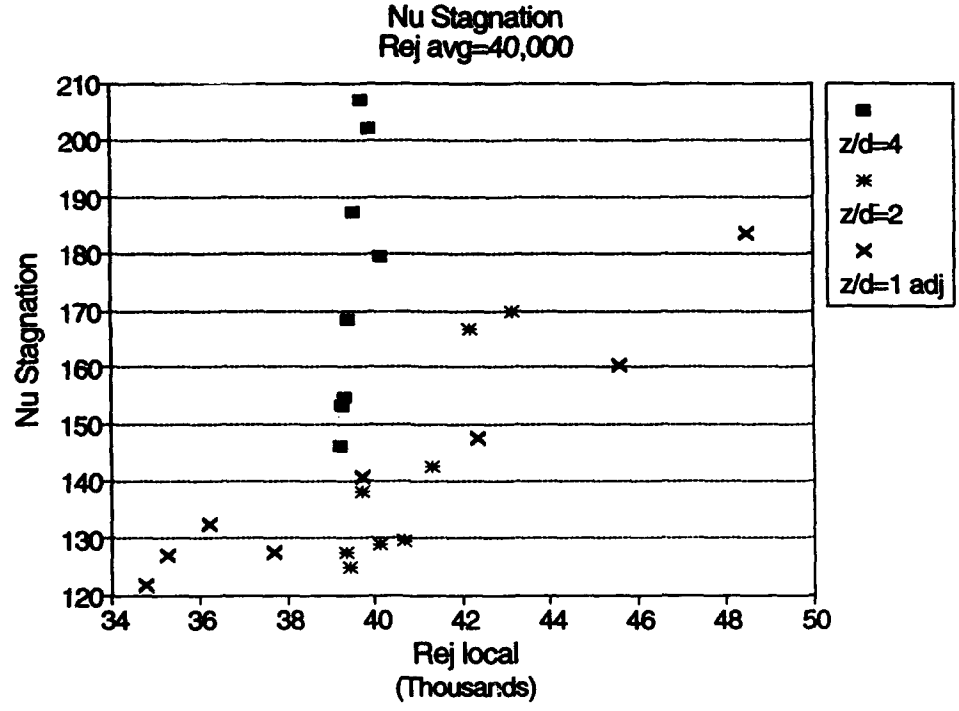

Figure 8.14 Inline - Re_j avg = 40,000 stagnation point Nusselt numbers for local Re_js at z/d = 1, 2 and 4.

given average Re_j, the heat transfer levels for a given row position are similar. Figure 8.9, however, illustrates that, for a given average Re_j, jets near the array inlet for the $z/d = 2$ case have higher local Re_j values which results in a slightly higher stagnation point Nu. Near the array exit, the order is reversed and the $z/d = 1$ configuration shows higher local Re_j with correspondingly higher heat transfer levels. The values for z/d =4 are generally higher throughout the array with the exception of the last row. These observations are consistent with the potential core striking the surface for the low z/d cases and the core being influenced by turbulence for $z/d = 4$. Plotting stagnation point Nu as a function of local Re_j shows this result (Figures 8.8, 8.10, 8.12, and 8.14). The z/d of 1 and 2 data are grouped around a common stagnation point Nu line while the z/d of 4 data are consistently higher and are best correlated with a different exponent.

Figures 8.15 to 8.19 show stagnation point Nu for all inline tests at given jet rows. Figures 8.15 displays data for the first row which would be expected to have a flow field resembling a single impinging jet in the absence of crossflow. Also shown on this graph is the data from **Lucas et al. (1992)** for an isolated confined impinging jet at z/d=1 and 2. Their data is close to the present data. The stagnation point Nu for the $z/d = 4$ data is consistently higher in the early row locations. By the seventh jet row, shown in Figure 8.19, the stagnation point Nu values are similar for all z/d values. Based on these observations and the measured recovery pressure discussed in Chapter 7, the stagnation point Nu for $z/d = 1$ and 2 are plotted in Figure 8.20 for the first four jet row locations. These locations are used in a least squares fit to the data which yielded the following equation:

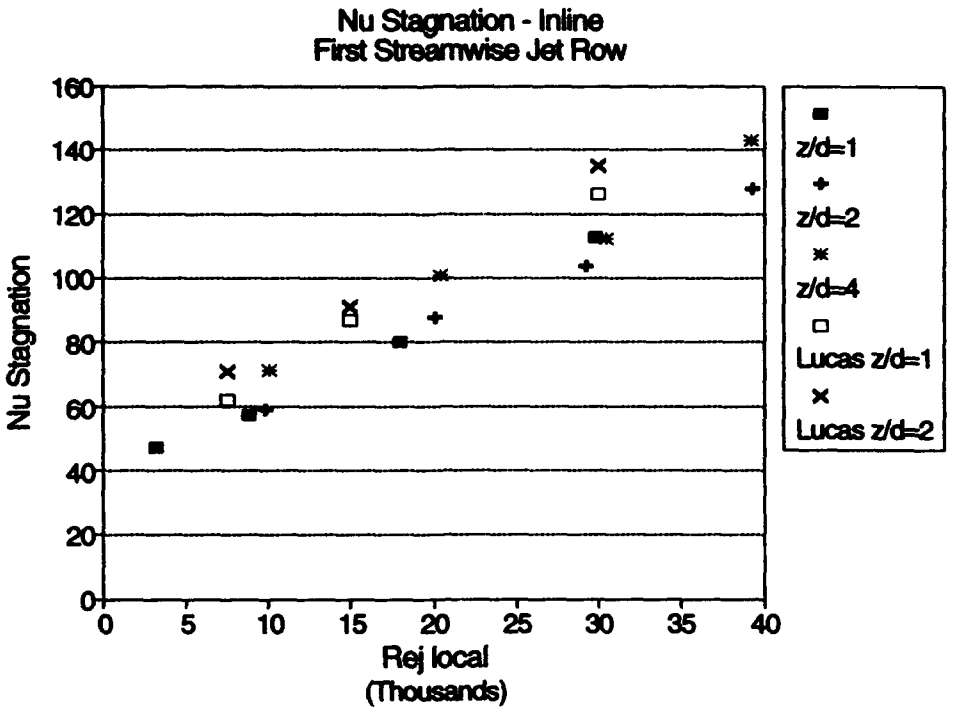

Figure 8.15 Stagnation Nusselt numbers at streamwise jet row one for all inline array tests.

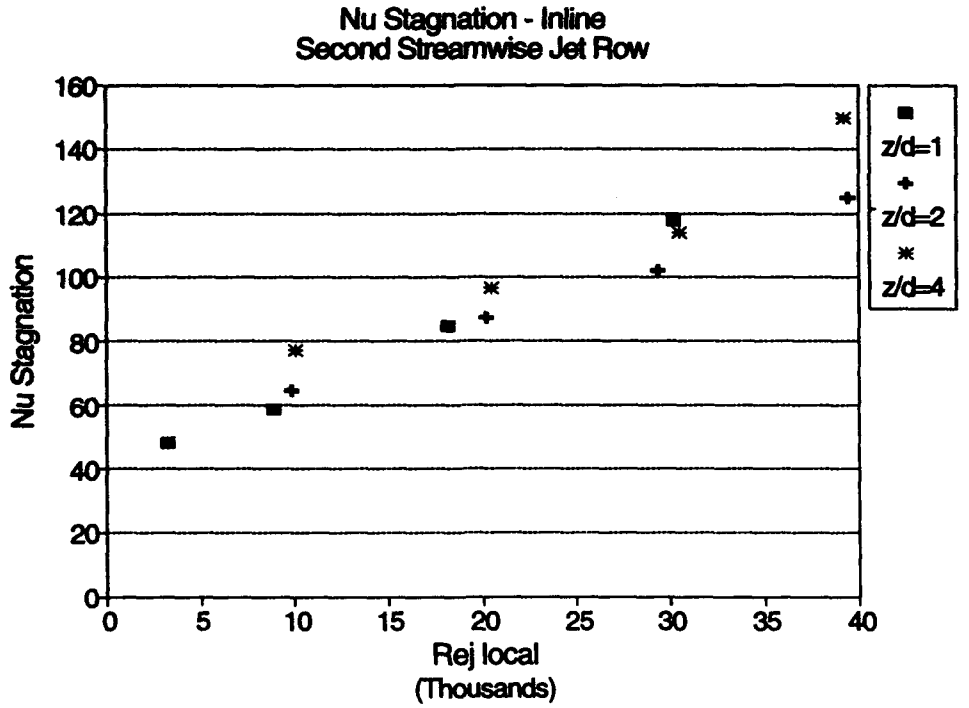

Figure 8.16 Stagnation point Nusselt numbers at streamwise jet row two for all inline array tests.

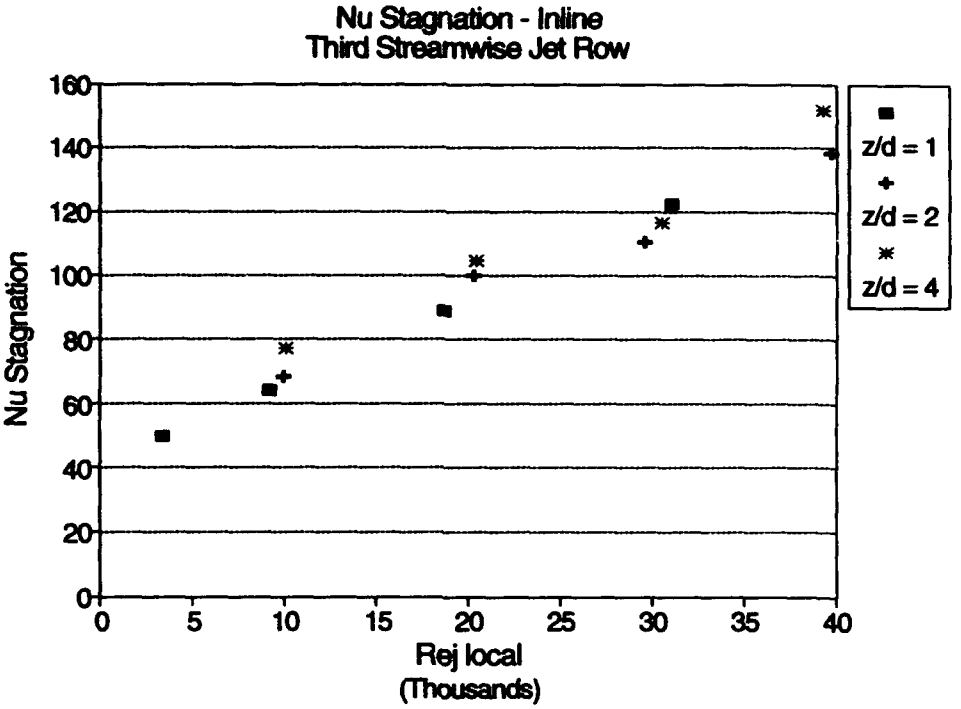

Figure 8.17 Stagnation point Nusselt numbers at streamwise jet row three for all inline array tests.

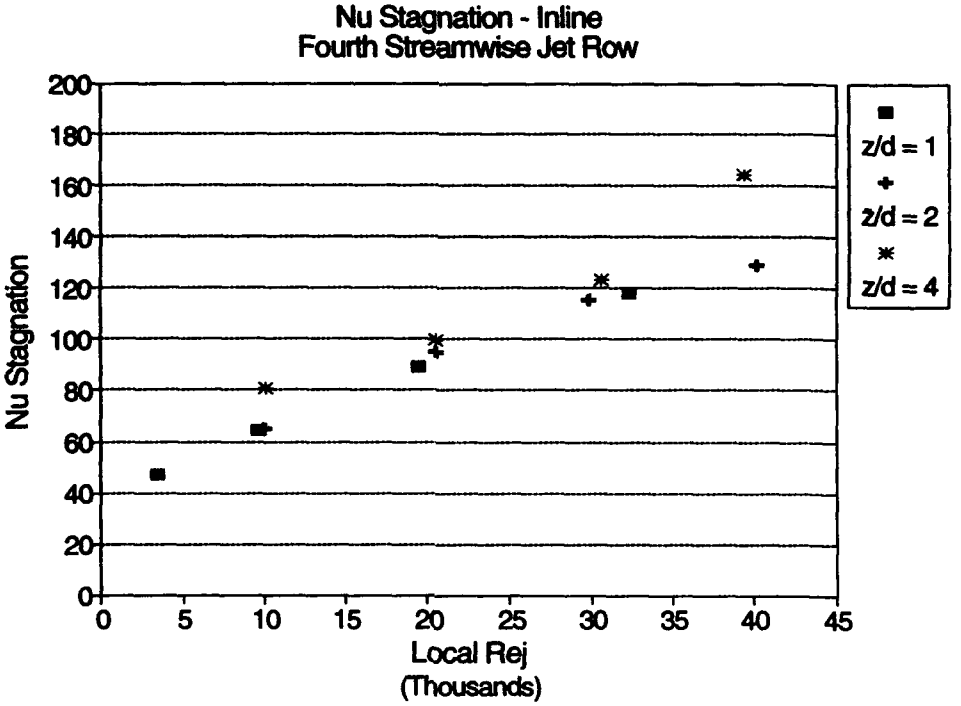

Figure 8.18 Stagnation point Nusselt numbers at streamwise jet row four for all inline array tests.

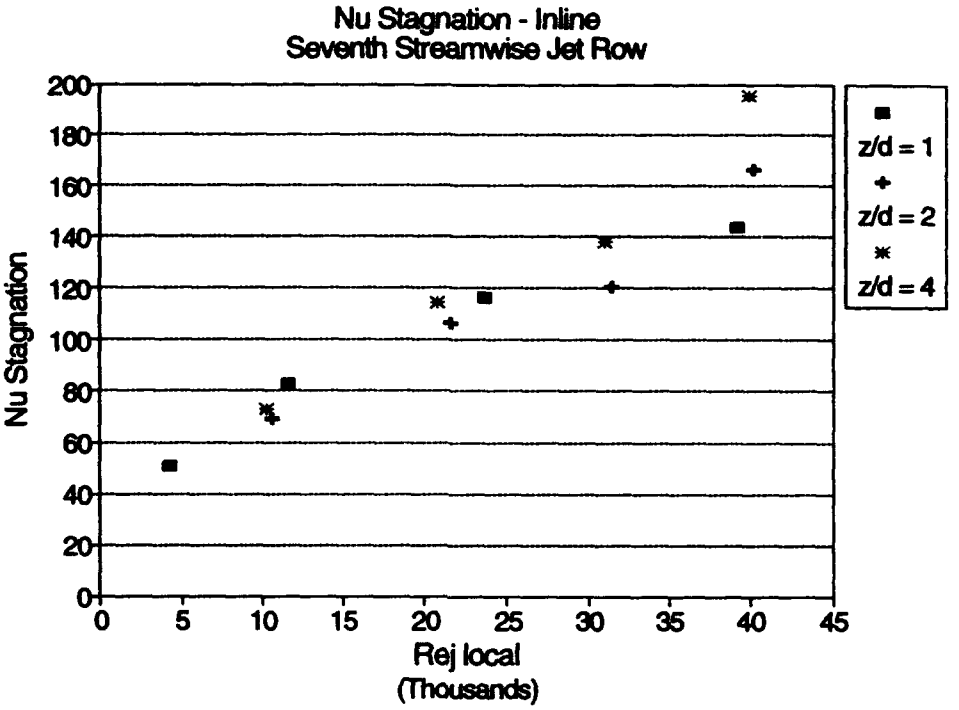

Figure 8.19 Stagnation point Nusselt numbers at streamwise jet row seven for all inline array tests.

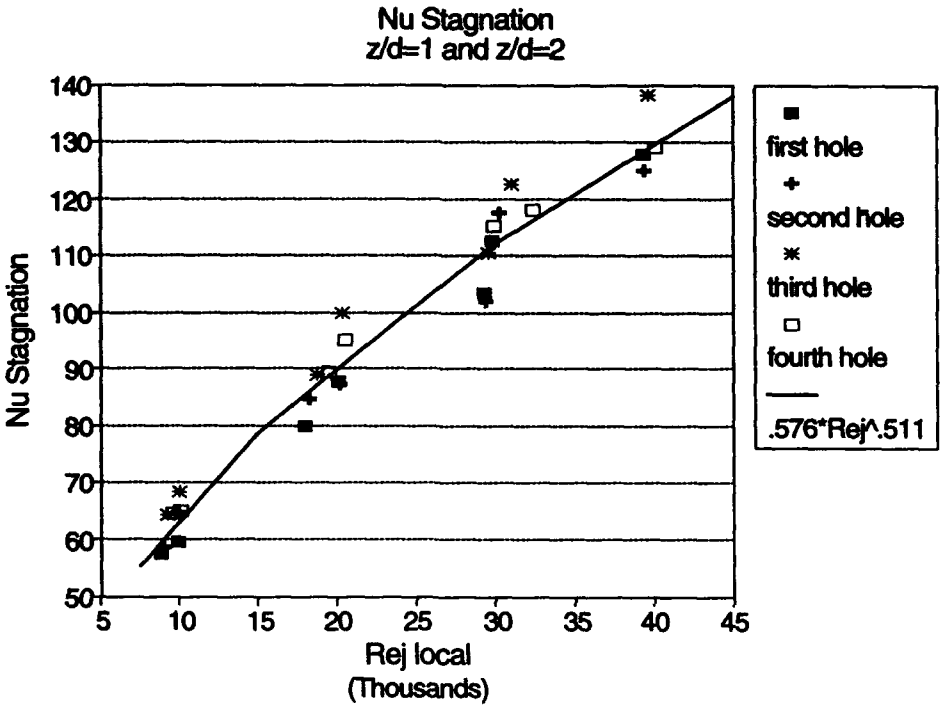

Figure 8.20 Reynolds number dependence of stagnation point Nusselt number for the first four streamwise jet rows at z/d = 1 and 2.

$$Nu = 0.567 * Re_j^{0.511} \quad (8.1)$$

A comparison of this equation with the experimental data can be seen in Figures 8.1, 8.2 and 8.3. It must be emphasized that this is a general equation for stagnation point *Nu* in the absence of crossflow for the conditions tested.

If one assumes a laminar boundary layer dependence on Re_j throughout the array, the influence of crossflow can be characterized in the following equation.

$$Nu = 0.749\ Re_j^{0.5} \left(\frac{G_c}{G_j}\right)^{0.078} \quad (8.2)$$

A comparison with experimental data is shown in Figure 8.1. Crossflow, G_c/G_j, is defined as the average crossflow between half a pitch upstream of the jet hole and half a pitch downstream. This equation would apply to the z/d = 1 and 2 geometries for the range of crossflow and Re_j tested.

8.2 Staggered Data

The results for the staggered array, presented in the same manner as the inline array data, are presented in Figures 8.21 through to 8.30. The general trends discussed for the inline array are also evident for the staggered array. Figures 8.21 and 8.23 for z/d = 1 and 2 show stagnation point *Nu* for all array positions. These figures illustrate a similar dependence of stagnation point *Nu* on $Re_j^{0.5}$ at all jet locations for the range of average Re_j tested. The values of stagnation point *Nu* through the array for a given

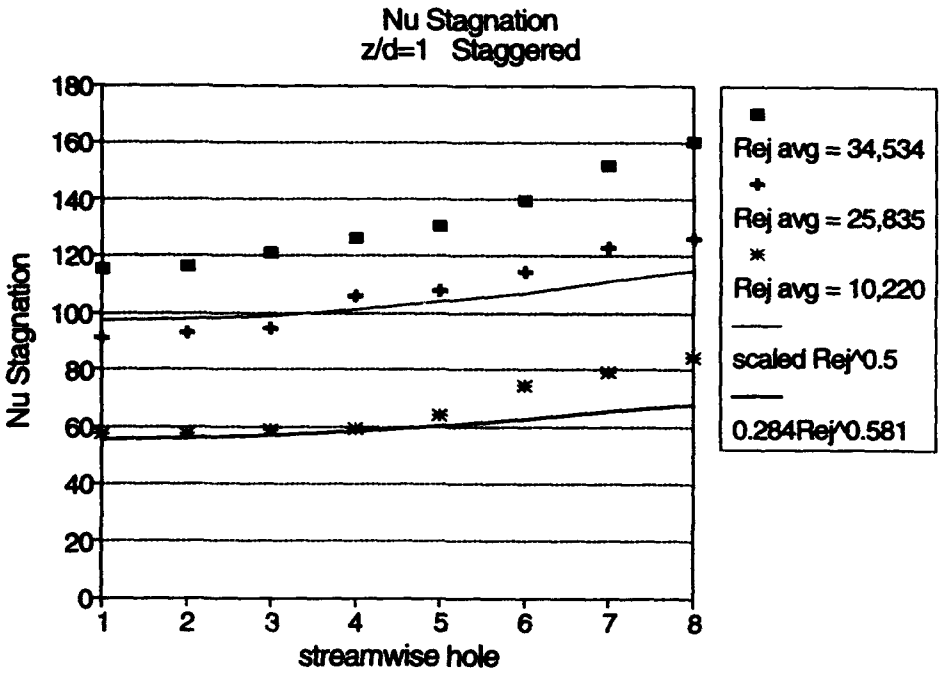

Figure 8.21 Stagnation point Nusselt numbers at streamwise locations for a staggered array with $z/d = 1$.

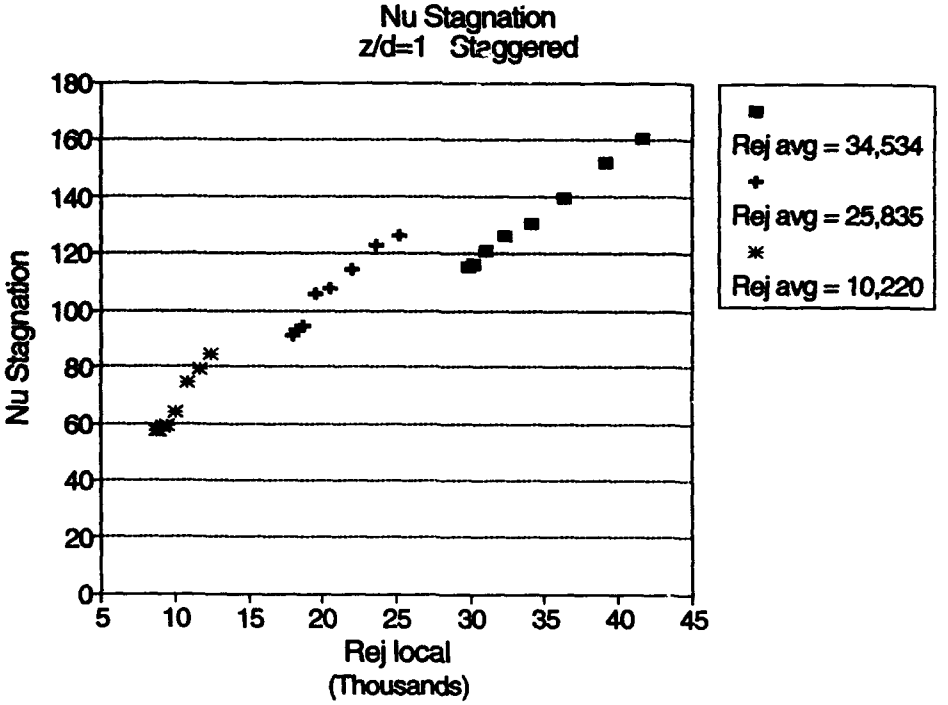

Figure 8.22 Stagnation point Nusselt numbers at local Re_js for a staggered array with $z/d = 1$.

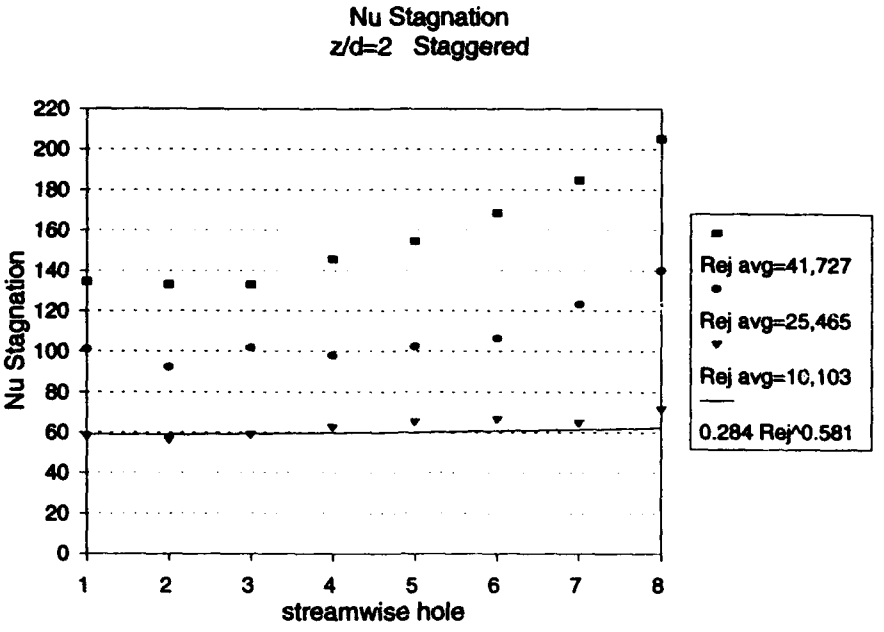

Figure 8.23 Stagnation point Nusselt numbers at streamwise jet locations for a staggered array with $z/d = 2$.

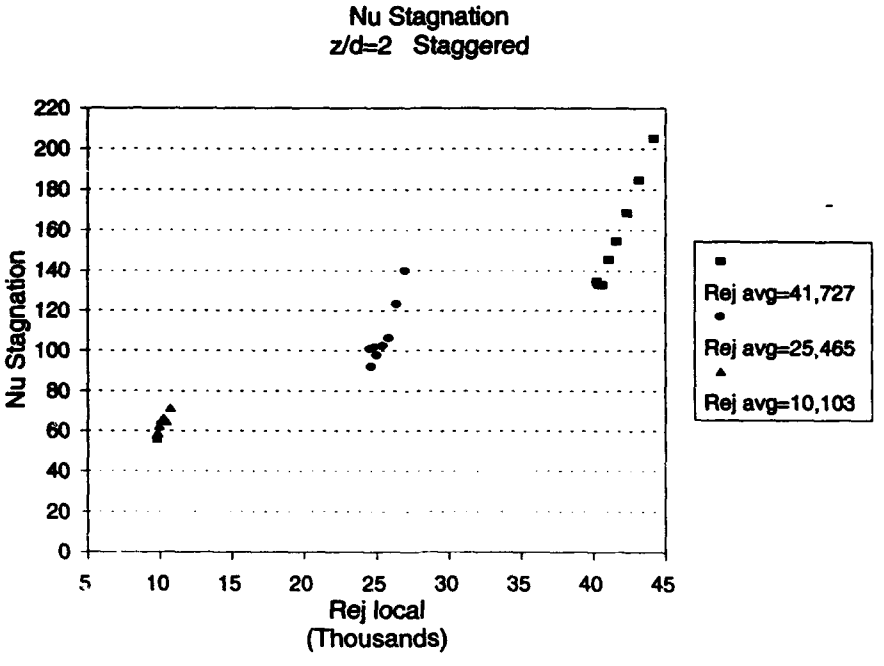

Figure 8.24 Stagnation point Nusselt numbers at local Re_js for a staggered array with $z/d = 2$.

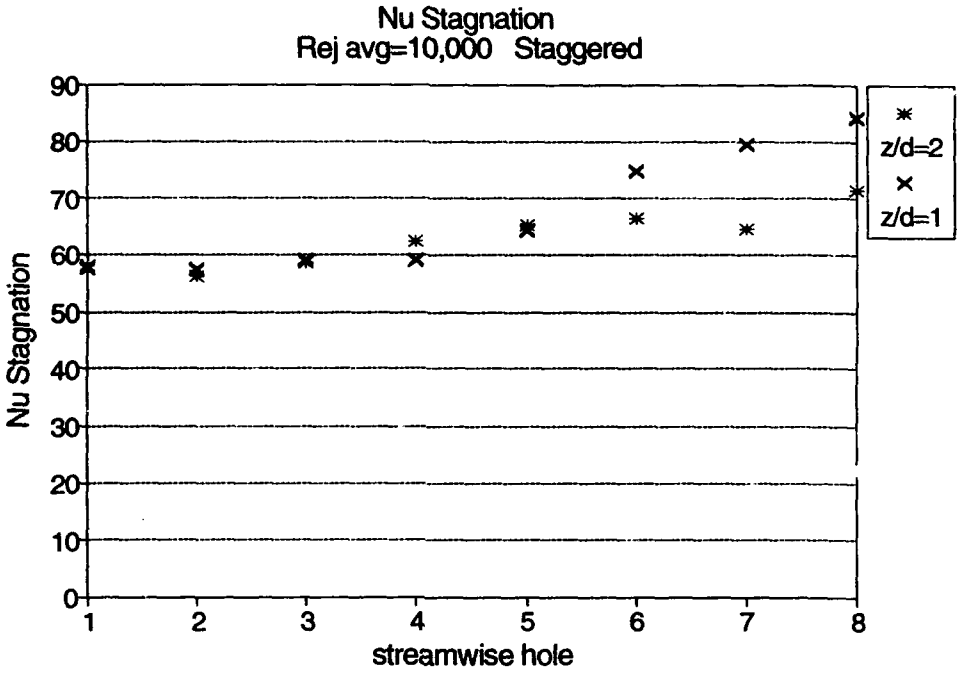

Figure 8.25 Staggered - Re_j avg = 10,000 stagnation point Nusselt numbers at streamwise jet locations with z/d = 1 and 2.

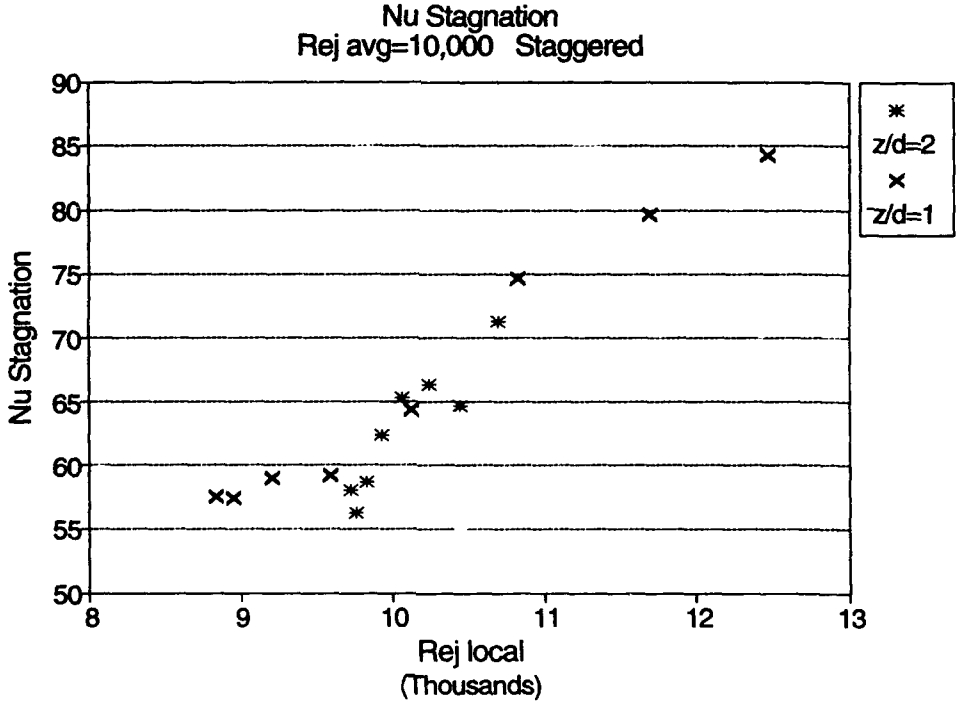

Figure 8.26 Staggered - Re_j avg = 10,000 stagnation point Nusselt numbers for local Re_js at z/d = 1 and 2.

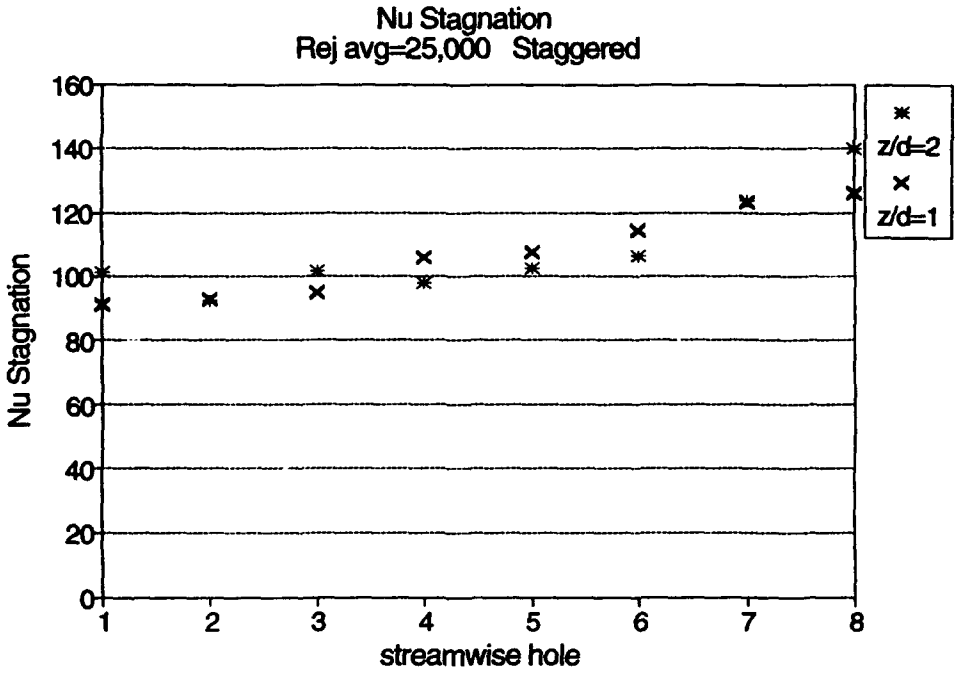

Figure 8.27 Staggered - Re_j avg = 25,000 stagnation point Nusselt numbers at streamwise jet locations for local Re_js with z/d = 1 and 2.

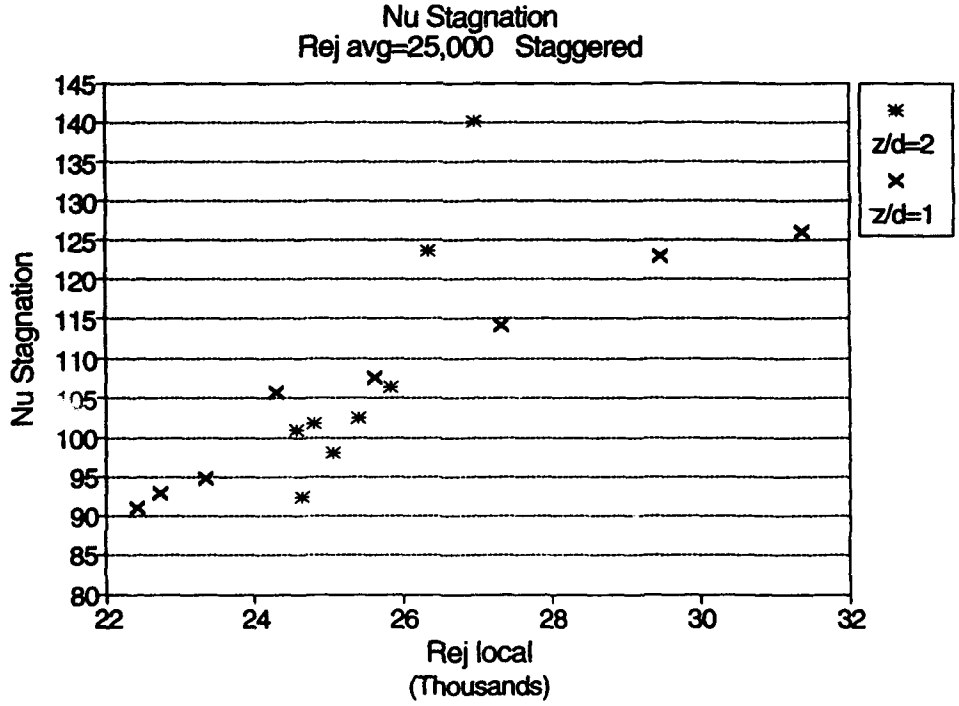

Figure 8.28 Staggered - Re_j avg = 25,000 stagnation point Nusselt numbers for local Re_js with z/d = 1 and 2.

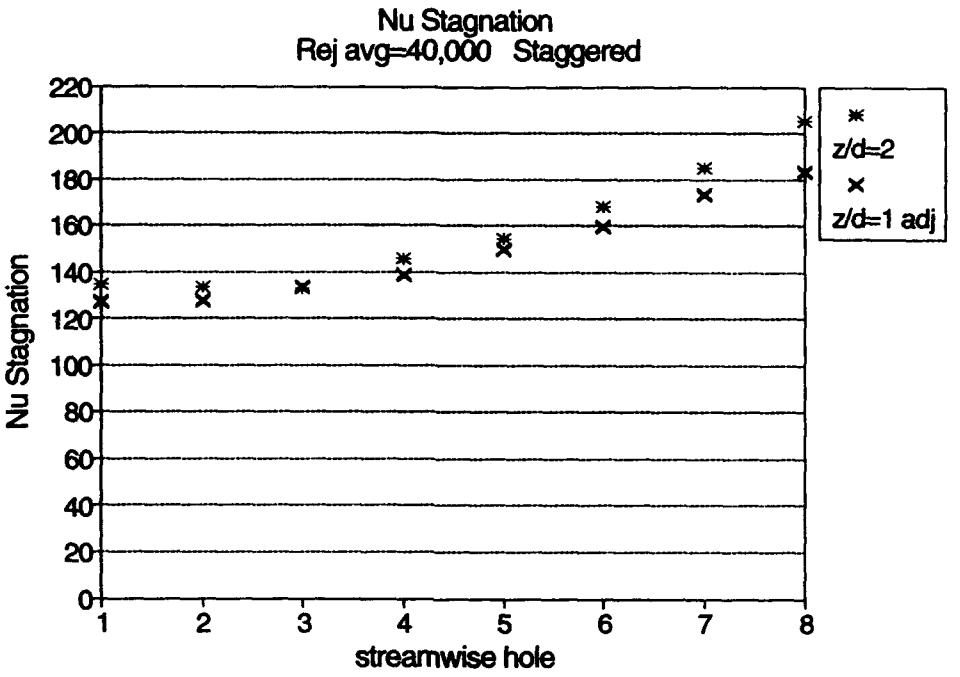

Figure 8.29 Staggered - Re_j avg = 40,000 stagnation point Nusselt numbers at streamwise jet locations for z/d = 1 and 2.

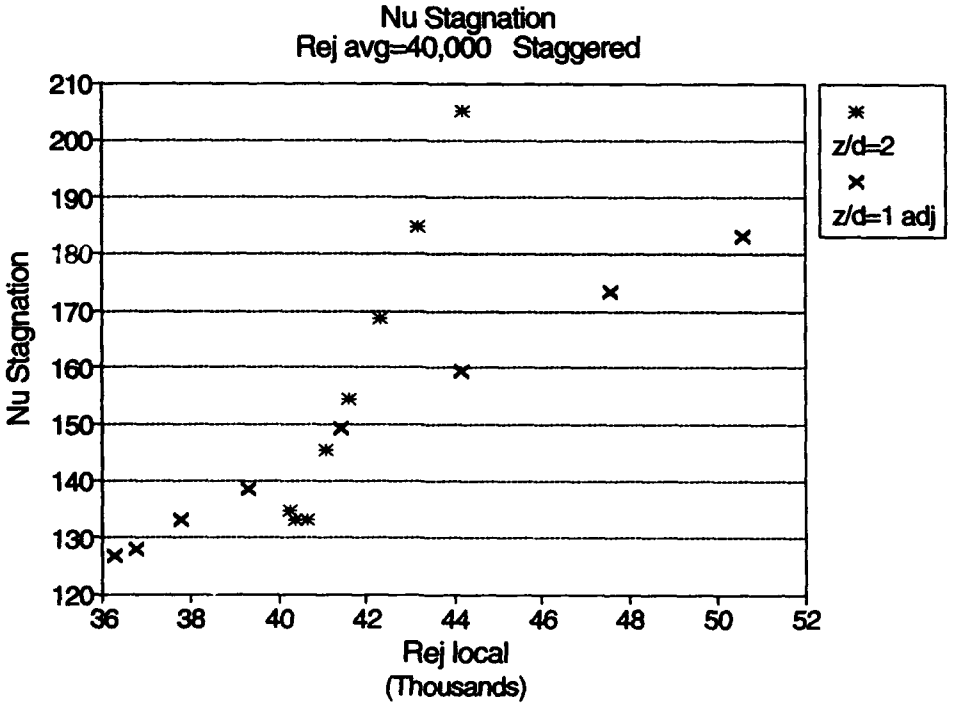

Figure 8.30 Staggered - Re_j avg = 40,000 stagnation point Nusselt numbers for local Re_js with z/d = 1 and 2.

average Re_j also follows approximately the square root dependence early in the array but towards the array exit experimental values are higher than would be predicted by this square root power. Again, the rise in stagnation point *Nu* through the array is partly the result of crossflow acceleration lowering the channel static pressure and increasing the massflow through the later holes. Stagnation point *Nu* does not increase as much through the array for $z/d = 2$ as the crossflow is lower than the $z/d = 1$ case and the local Re_j is more uniform. Figure 8.24 shows stagnation point *Nu* for local Re_j at a $z/d = 2$ and displays this result, with the stagnation point *Nu* more closely grouped. The exception is the average $Re_j = 40{,}000$ which shows a much stronger influence of crossflow on the stagnation point *Nu* with position through the array.

Figures 8.25, 8.27, and 8.29 display the stagnation point *Nu* at all jet locations for the range of average Re_j tested. The values for average $Re_j = 34{,}568$ were extrapolated to 40,000 a similar way to those for the inline case. Again the adjustment was small. As seen with the inline data, for a given average Re_j, the heat transfer levels for a given streamwise position are similar. Figure 8.27, however, illustrates that, for a given average Re_j, jets early on in the array for the $z/d = 2$ case have higher local Re_j values which result in a higher stagnation point *Nu*. Near the array exit, the order is reversed and $z/d = 1$ shows higher local Re_j with correspondingly higher heat transfer levels.

Figures 8.26, 8.28, and 8.30 show the $z/d = 1$ and 2 stagnation point *Nu* values ~~ local Re_j for the range of average Re_j tested. These results show the similarity between levels of heat transfer for all of the z/d values tested.

Figure 8.31 shows the stagnation point *Nu* for local Re_j at the first row for all

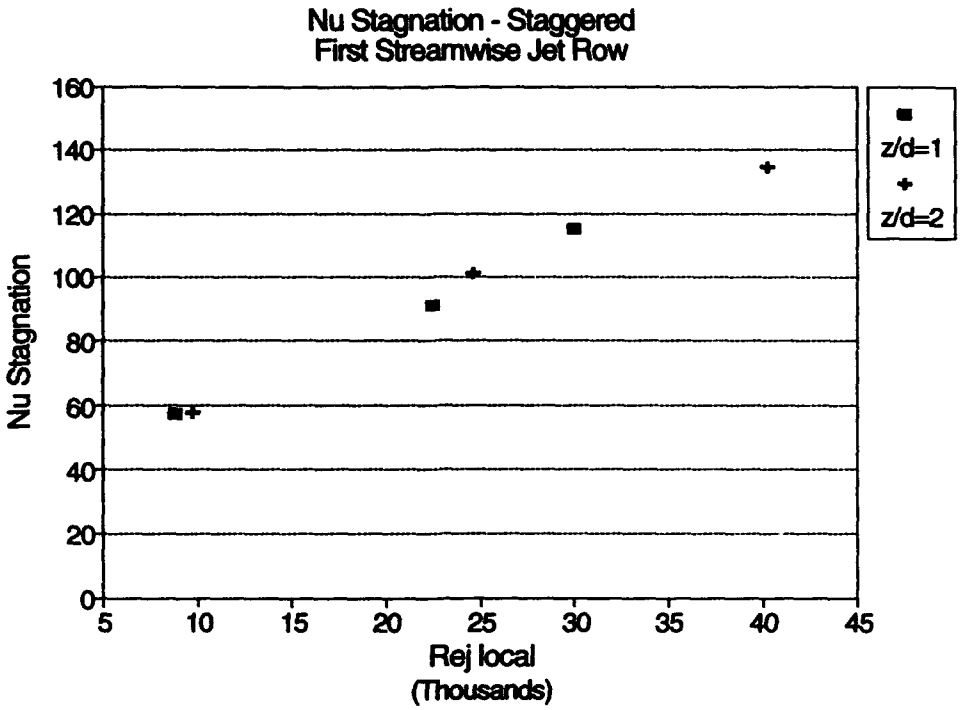

Figure 8.31 Stagnation point Nusselt numbers at streamwise jet row one for all staggered array tests.

staggered arrays tested. The values for z/d = 1 and 2 show excellent agreement. A similar plot for subsequent locations lead to the same conclusion. Regression of the first four jet rows for z/d=1 and 2 yields the following stagnation point Nu correlation for the conditions tested (see Figure 8.32).

$$Nu = 0.284 * Re_j^{0.581} \tag{8.3}$$

A comparison of this correlation with the experimental data can be seen in Figures 8.21 and 8.23. This equation shows a slightly higher Reynolds number dependence than the inline array case when fitting data for the first four holes and indicates a stronger influence of crossflow over these jet locations. Even though predicted crossflow values are similar between the inline and staggered array, in the staggered

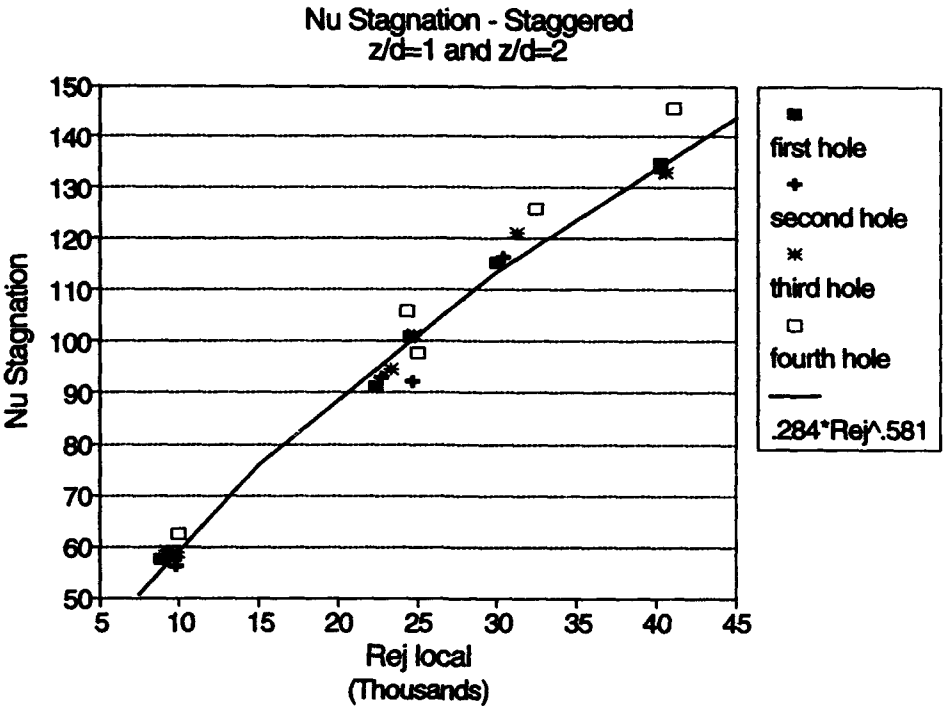

Figure 8.32 Staggered array Reynolds number dependence of stagnation point Nusselt number for the first four streamwise jet rows at z/d = 1 and 2.

array the full effect of the crossflow is channelled directly at each downstream impingement zone. For the inline case, the crossflow is deflected in the spanwise direction between the jets. When only the first two jets for all staggered conditions tested were considered (representative of staggered jets with small crossflow) the Re_j dependence of stagnation point Nu reduces to 0.53.

8.3 Comparison

Comparisons of stagnation point Nu between the staggered and inline arrays are presented in Figures 8.33 through 8.36. The agreement between the two geometries is excellent. This agreement indicates that the jets behave similarly for the two different configurations. The inline data used the intensity history method to

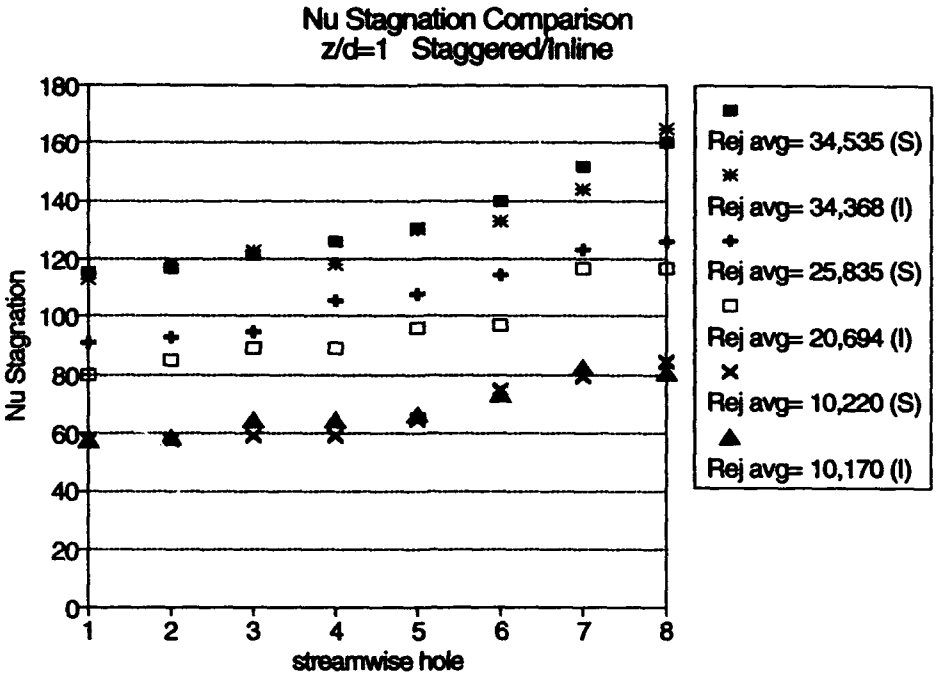

Figure 8.33 Comparison of stagnation point Nusselt numbers by streamwise jet locations for staggered and inline arrays at $z/d = 1$.

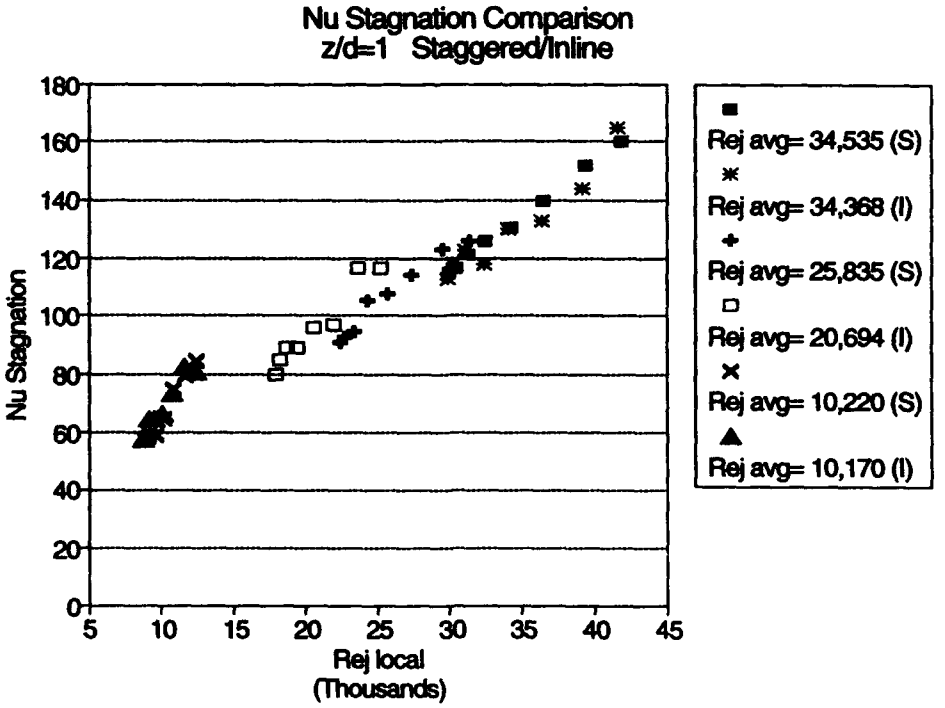

Figure 8.34 Comparison of stagnation point Nusselt numbers as a function of local Re_js for the staggered and inline arrays at $z/d = 1$.

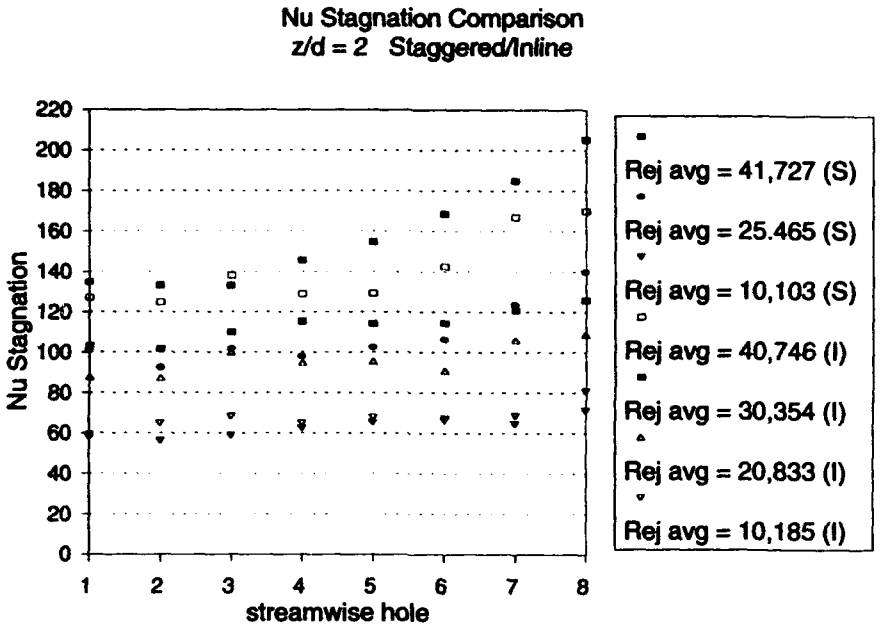

Figure 8.35 Comparison of stagnation point Nusselt numbers by streamwise jet locations for staggered and inline arrays at $z/d = 2$.

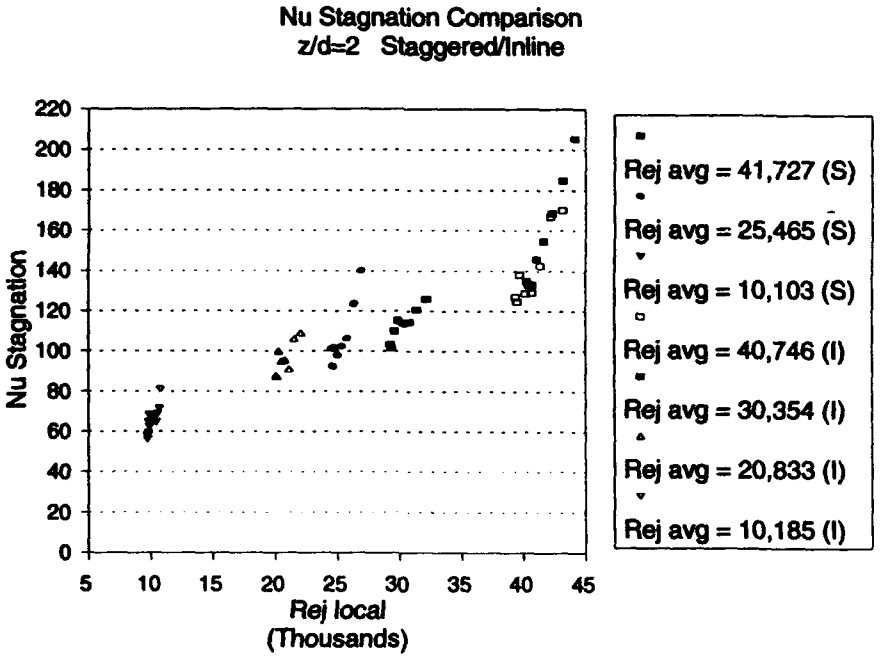

Figure 8.36 Comparison of stagnation point Nusselt numbers as a function of local Re_js for staggered and inline arrays at a $z/d = 2$.

process video tapes while the staggered data used the hue history method. The agreement between the two methods under similar flow conditions is seen to be excellent.

CHAPTER 9 - DETAILED HEAT TRANSFER MEASUREMENTS AND AVERAGED VALUES

This chapter details results of local Nusselt number measurements over the target surface. Presentations of experimental data, along with insights gained from the surface visualization, confirm the influence of crossflow and the *Nu* differences between the impingement area and the channel regions where the gas from upstream holes passes between jets at a certain location. Average values of Nusselt number over regions associated with each row of jets are also presented compared with the results of other workers and design correlations are given. In addition, measurement of T_{aw}, plotted as a jet effectiveness term, shows the effect of the impingement plate on target surface heat transfer. A region of high effectiveness means the jet dominates the heat transfer process while low effectiveness indicates entrainment of surrounding air has changed the local gas temperature. This chapter presents results for both staggered and inline arrays.

9.1 Inline Array Data

9.1.1 Local Measurements

As an example of measurements possible using the liquid crystal technique, Figures 9.1 to 9.10 show the variation with spanwise position at three jet rows for an average Re_j = 34,368 and a z/d = 1. At the first row of jets, as discussed in Chapter 7, the liquid crystal colour change contours advance in a circular manner up to about 3.0*d* from the stagnation point. This indicates that the heat transfer and flow field

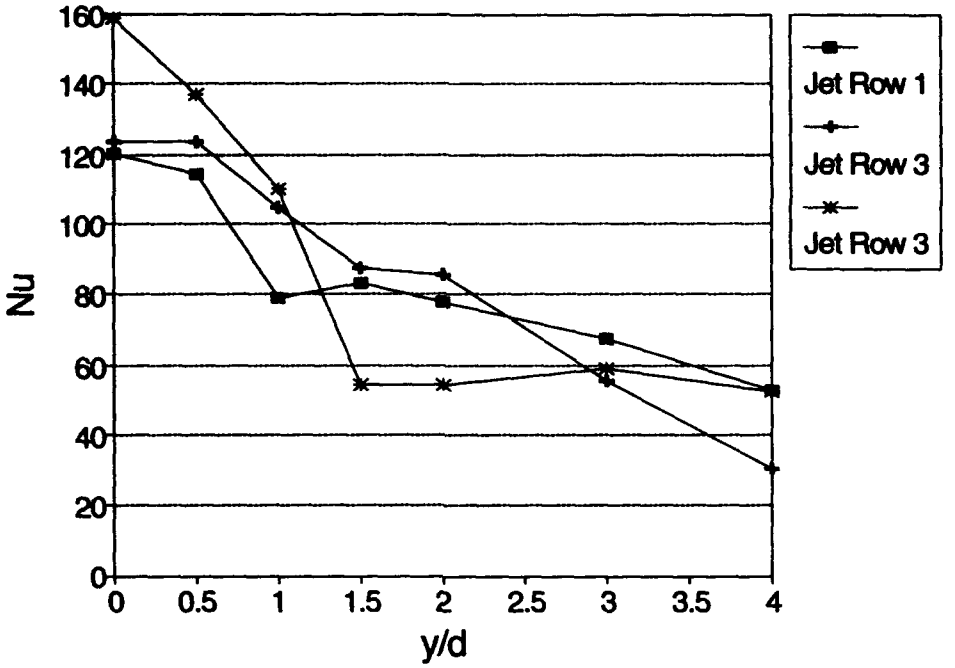

Figure 9.1 Spanwise variation of Nusselt number at three jet row locations (Re_j avg = 34,368; z/d = 1; inline).

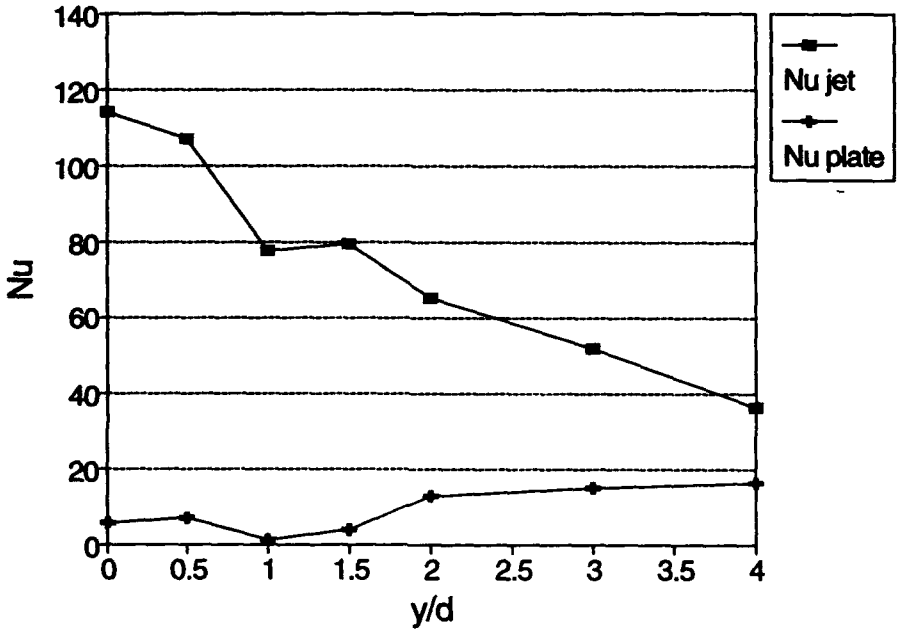

Figure 9.2 Spanwise variation of plate and jet Nusselt number at jet row one (Re_j avg = 34,368; Re_j local = 30,249; z/d = 1; inline).

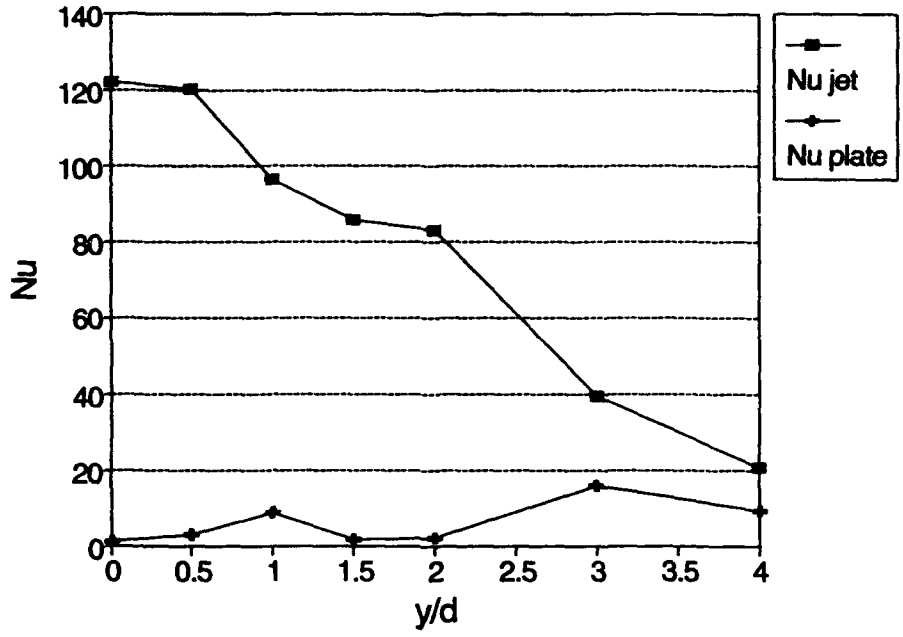

Figure 9.3 Spanwise variation of jet and plate Nusselt numbers at jet row three (Re_j avg = 34,368; Re_j local = 31,375; z/d = 1; inline).

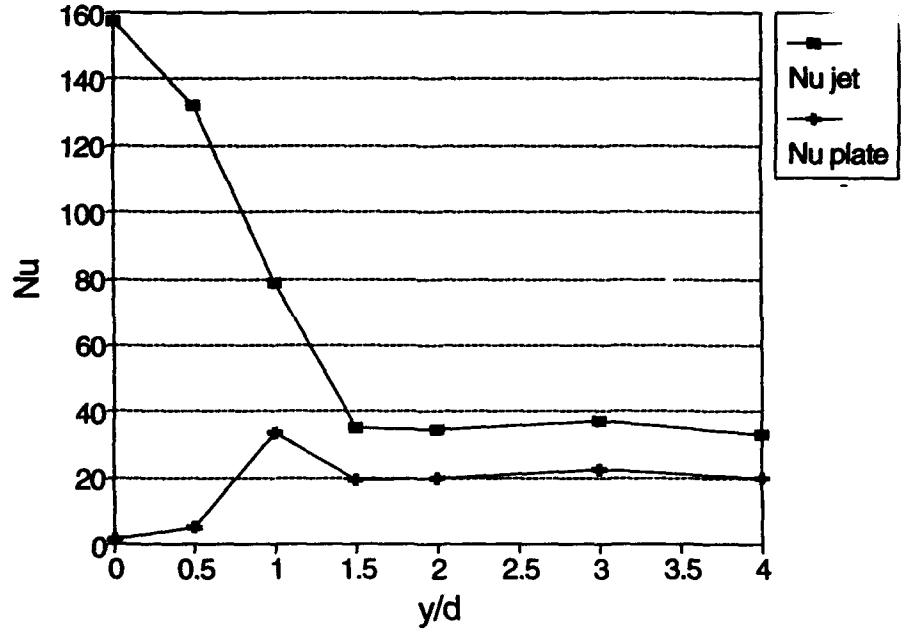

Figure 9.4 Spanwise variation of jet and plate Nusselt numbers at jet row eight (Re_j avg = 34,368; Re_j local = 41160; z/d = 1; inline).

local to the stagnation point should be comparable to that of a single jet. This circular shape is swept downstream as one moves through the array. Figure 9.1 shows the spanwise variation of Nu, comprised of both Nu_j and Nu_p as was previously defined in Chapter 3, for the first, third and eighth rows. It can be seen for the first jet row, local Re_j = 30,249 in Figure 9.1, that the heat transfer drops off rapidly up to one diameter from the centreline. A second peak exists at approximately 1.5 diameters. This peak has been observed at high Reynolds numbers under a single confined jet [**Lucas et al. (1992)**] and under a free jet [**Yan et al. (1992)**, **den Ouden and Hoogendorn (1974)**, **Obot et al. (1979)**]). Beyond this secondary peak the heat transfer decreases much more rapidly than for a single jet (**Lucas et al. (1992)**) due to the spent flow from the first jet exiting downstream between the jets. The second peak in heat transfer at jet row three, local Re_j = 31,375 in Figure 9.1, has been smoothed and shifted radially outward. Also noticeable is a 45% reduction in Nu at the four diameter point when compared with jet row one. The data for jet row eight, local Re_j = 41,160 in Figure 9.1, clearly shows the effect of crossflow on the local Nu. From the stagnation point, y/d = 0, the heat transfer decreases steadily to 1.5d and then remains relatively constant at a local Nu value similar in magnitude to the 4d level measured for jet row one. At jet row eight the jet is severely restricted and is mainly an obstacle to the crossflow. Figures 9.2 to 9.4 show the separate contributions of the jet and the impingement plate to the target plate heat transfer. Again, the second peak in Nu_j is apparent for jet rows one and three, shown in Figures 9.2 and 9.3. At downstream locations the impingement plate heat transfer coefficient becomes increasingly significant. Inspection of the jet row eight data, in Figure 9.4,

shows that the plate heat transfer accounts for as much as 40% of the overall value in the region of channel flow between the jets.

Nu distributions at the three different jet locations are given in Figures 9.5, 9.7 and 9.9 and illustrate the surface detail possible with the transient techniques used. Figures 9.6, 9.8 and 9.10 show the corresponding jet effectiveness plots. In these figures the jet hole is aligned with the position (0,0) and the flow is indicated by the arrow from negative to positive on the "Flow Direction" axis. Figure 9.5 shows *Nu* beneath jet row one. The second maximum in *Nu* is readily apparent as the ring which encircles the central stagnation region. The circular nature of the heat transfer patterns shows that crossflow has little effect on the heat transfer distribution. The plate heat transfer coefficient increases with spanwise distance after 1*d*, as was shown in Figure 9.2. **Andrews et al.(1992)** and **Lucas et al. (1992)** identified a large recirculating region which surrounds the jet and that thermally couples the target plate to the impingement plate. This recirculation vortex significantly contributes to the plate heat transfer coefficient. The heat transfer distributions beneath the eighth jet row, in Figure 9.9, shows a markedly different structure. The area of enhancement brought about by the jet impingement is smaller than seen at jet row one as a result of the increased crossflow. There also is an increase in heat transfer in the channel due to the upstream flow being deflected between jets and accelerating with distance through the array. Jet row eight results exhibit a maximum in *Nu* at the stagnation point. Moving away from this point, the *Nu* distribution decreases in magnitude and develops a "tail" that is swept downstream between the jets. The jet effectiveness for jet row eight, Figure 9.10, is quite uniform away from the impingement region and

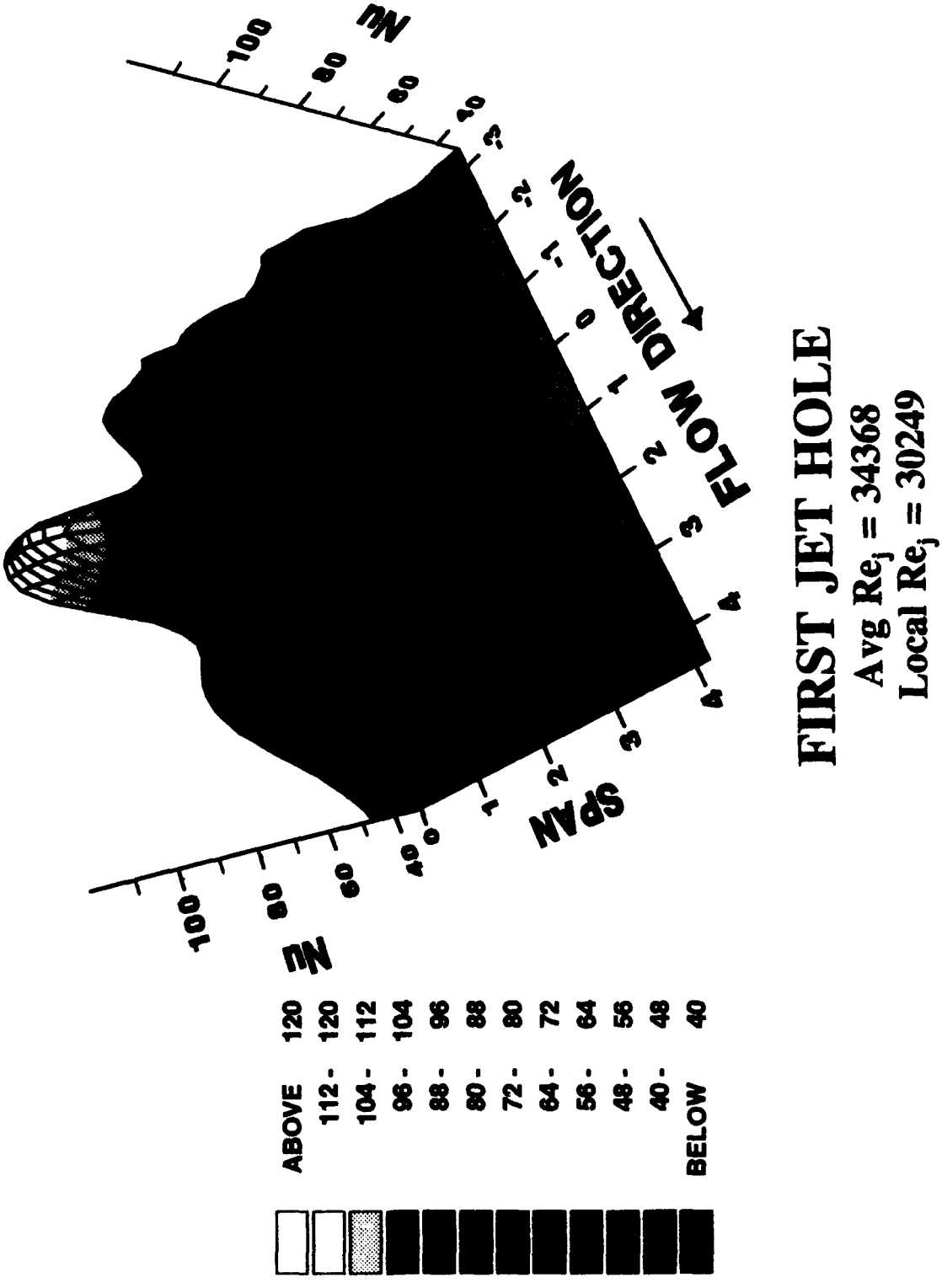

Figure 9.5 Nusselt number distribution at the first row of jets.

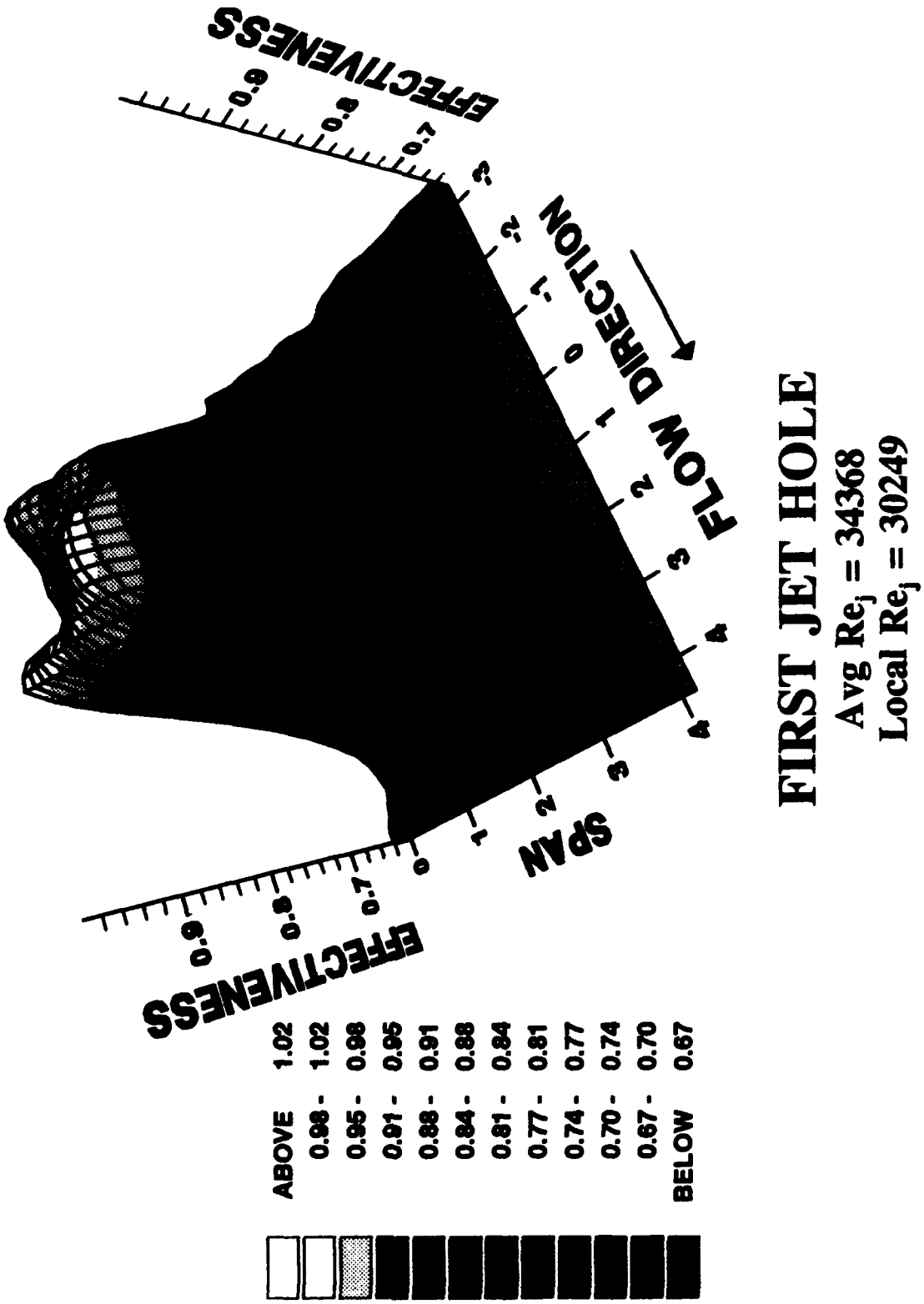

Figure 9.6 Jet effectiveness at the first row of jets.

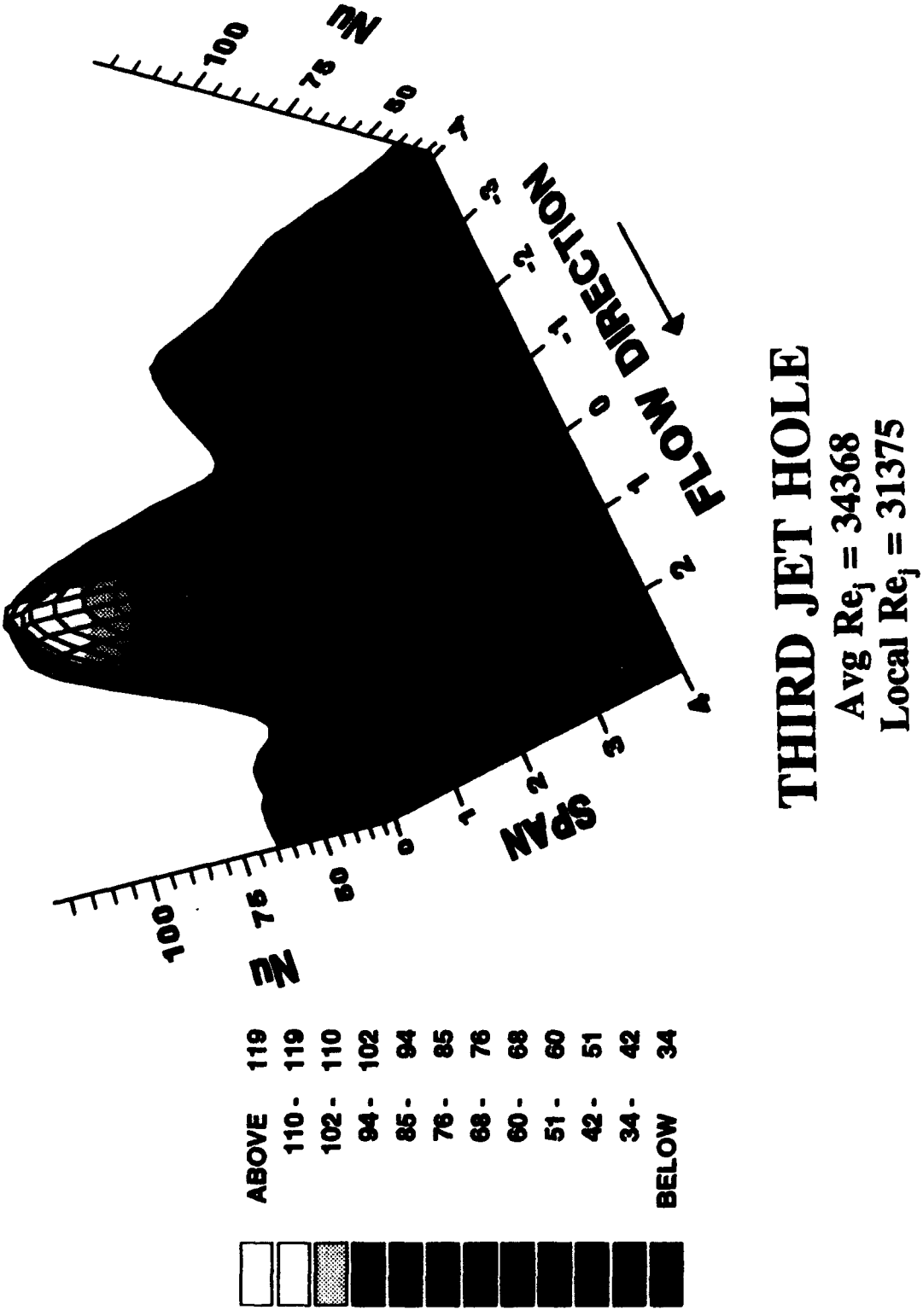

Figure 9.7 Nusselt number distributions at jet row three.

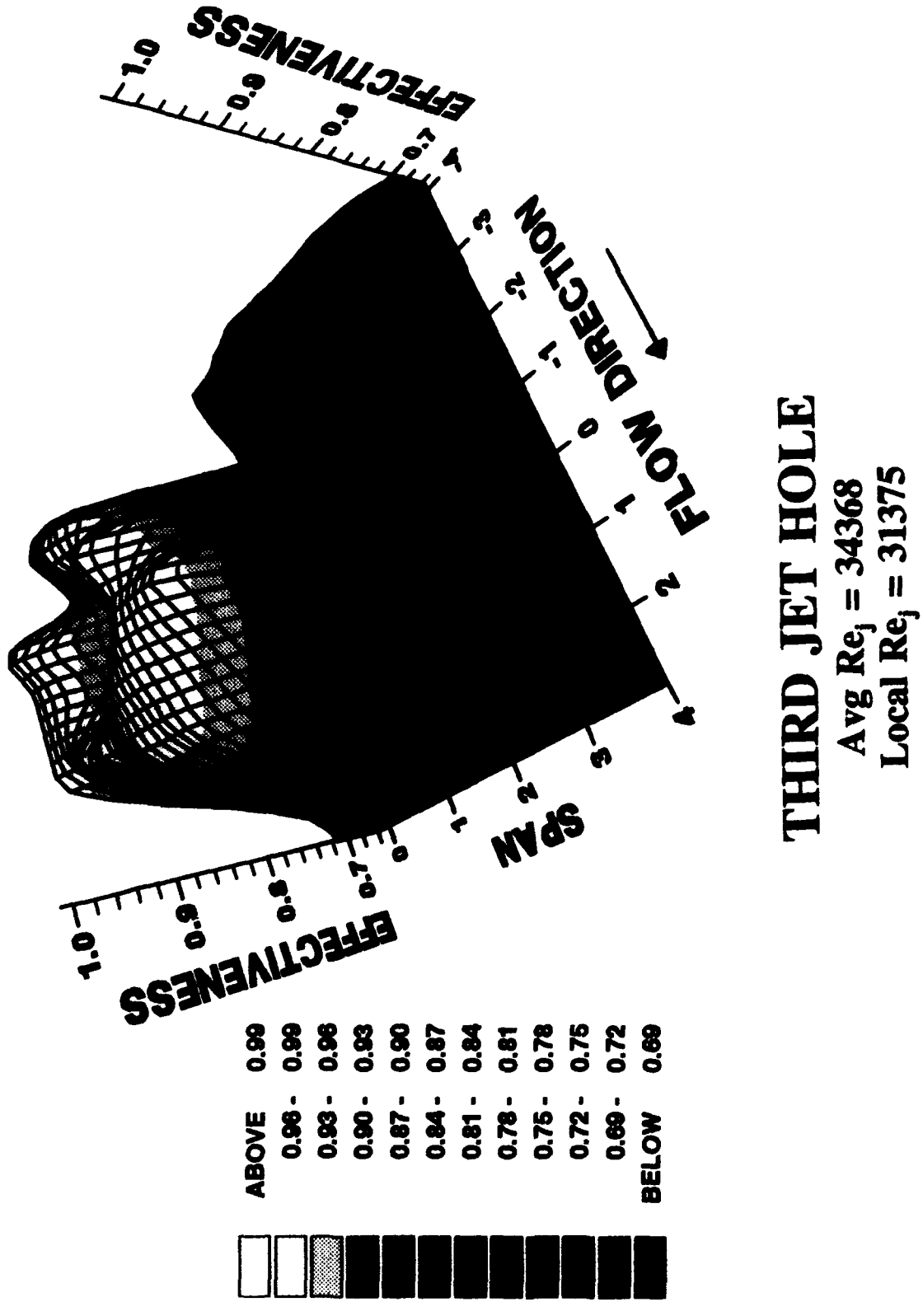

Figure 9.8 Jet effectiveness at jet row three.

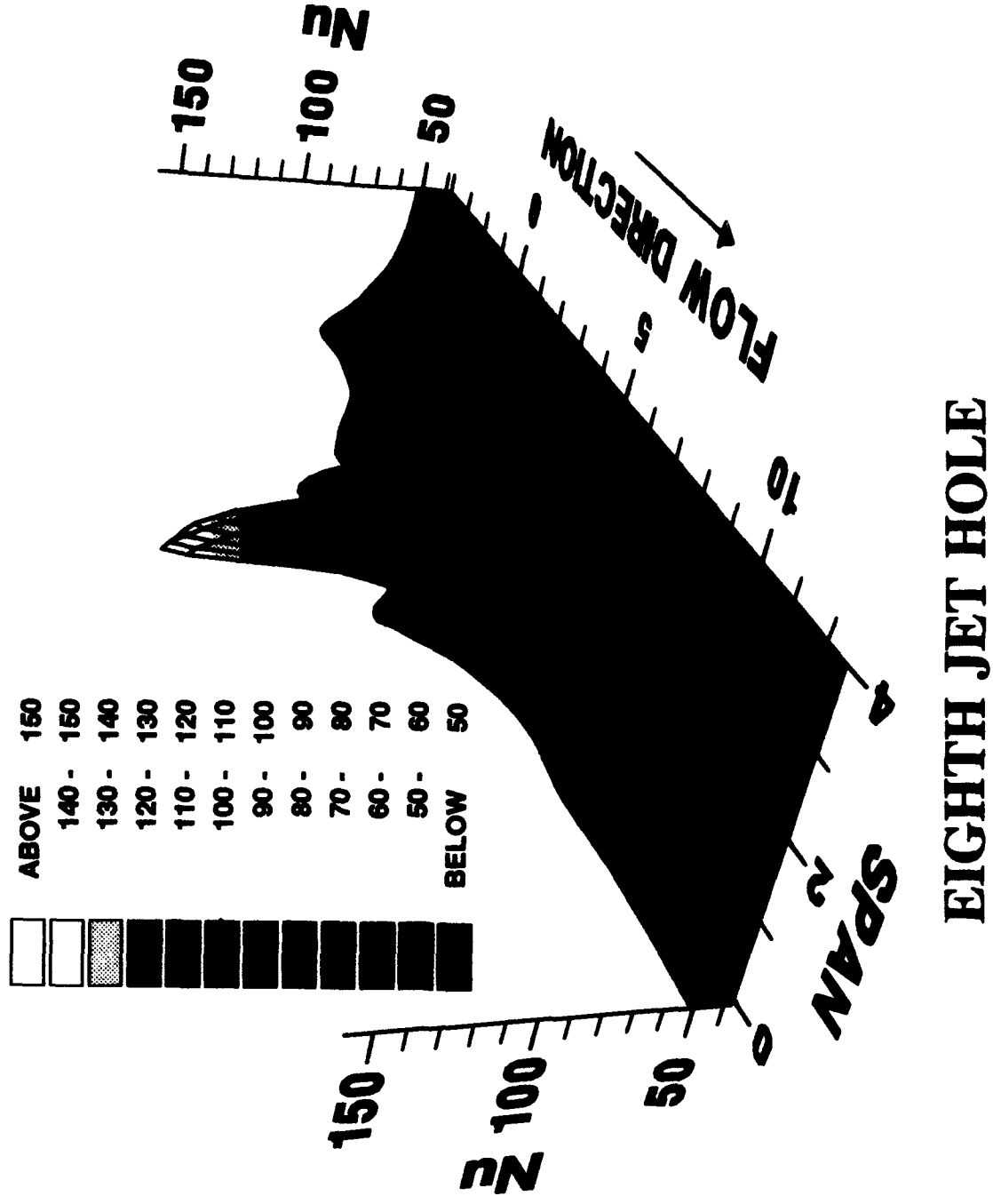

Figure 9.9 Nusselt number distributions at jet row eight.

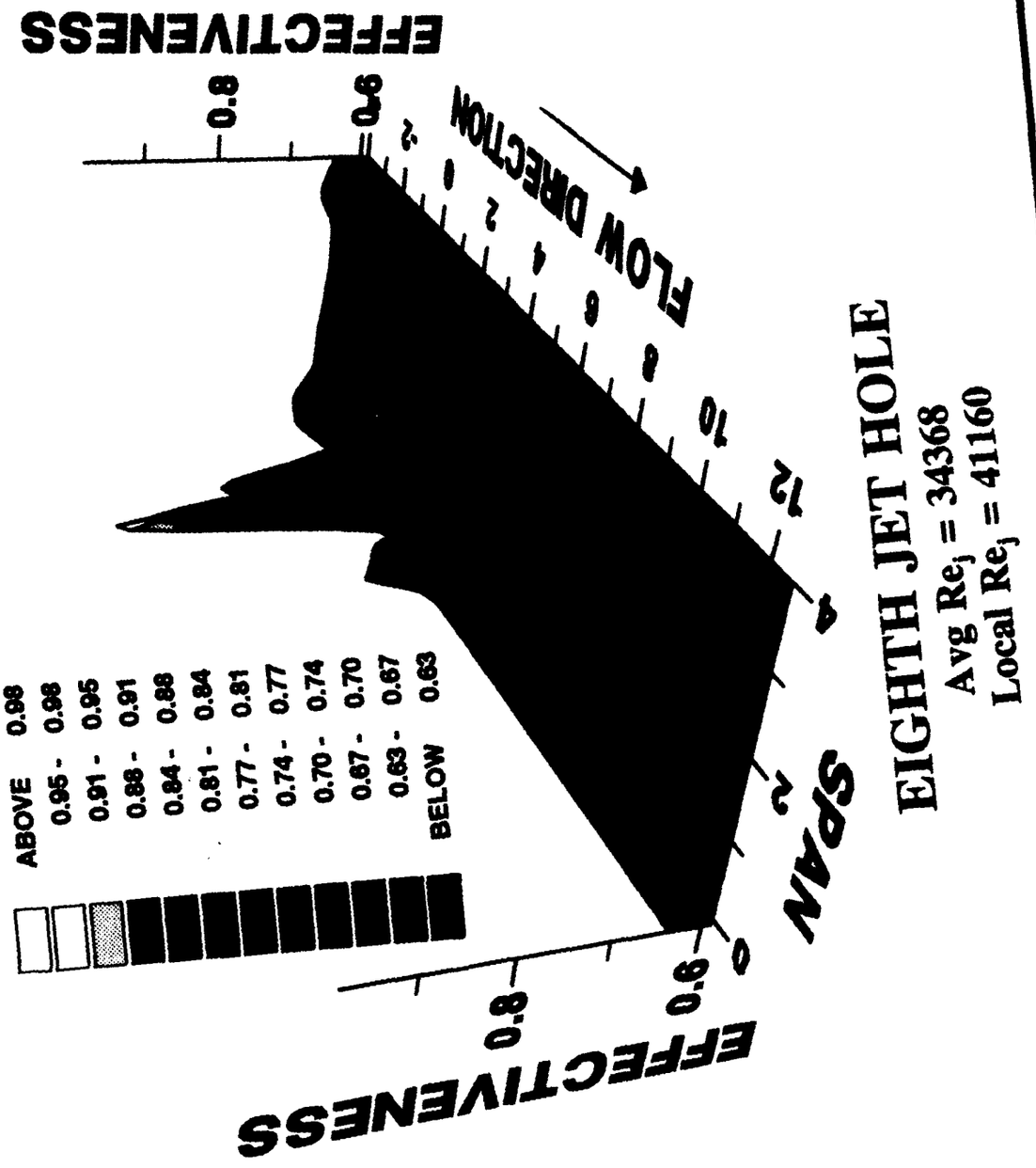

Figure 9.10 Jet effectiveness at jet row eight.

thus, indicates that the flow is very well mixed. Immediately downstream of the jet impingement point is another region of enhanced heat transfer which includes a peak located approximately one diameter downstream.

As previously discussed in Chapter 7, the stagnation point is not the position of peak local heat transfer for a $z/d = 2$ or less. Figure 9.11 shows radial profiles of the first jet row for a $z/d = 1$ and a local $Re_j = 18{,}000$. Moving radially outward from the stagnation point, Nu increases slightly to a peak value approximately $0.5d$ from the centre. The heat transfer then reaches a minimum value at approximately $1d$ and then rises to a second peak at $1.25\text{-}1.5d$ before dropping off to a lower channel value. **Goldstein and Timmers (1982)** observed this same structure using a steady state liquid crystal technique to qualitatively assess local heat transfer. They attribute this first increase in heat transfer at $0.5d$ to the high turbulence from the shear layer between the jet and surrounding air influencing the target plate surface flow. The implication is that the mixing-induced turbulence has not completely penetrated the potential core of the jet at this small plate spacing. **Pamandi and Belov (1980)** investigated theoretically the effect on heat transfer of the ring of high turbulence from the jet boundary shear layer. They computed a circle of elevated heat transfer at about $0.5d$ from the stagnation point for $z/d = 4$ for an unconfined , fully developed jet. The peak moves toward the jet centre as z/d is increased. Experimentally, the feature was not observed by the present study at $z/d = 4$. Figure 9.12 compares the present data with data from **Lucas et al. (1992)** and **Hollworth and Berry (1978)**. **Lucas et al.** data is from a single confined jet with similar geometry. The data was taken using steady state experimental technique with a thin liquid crystal coated heater pad.

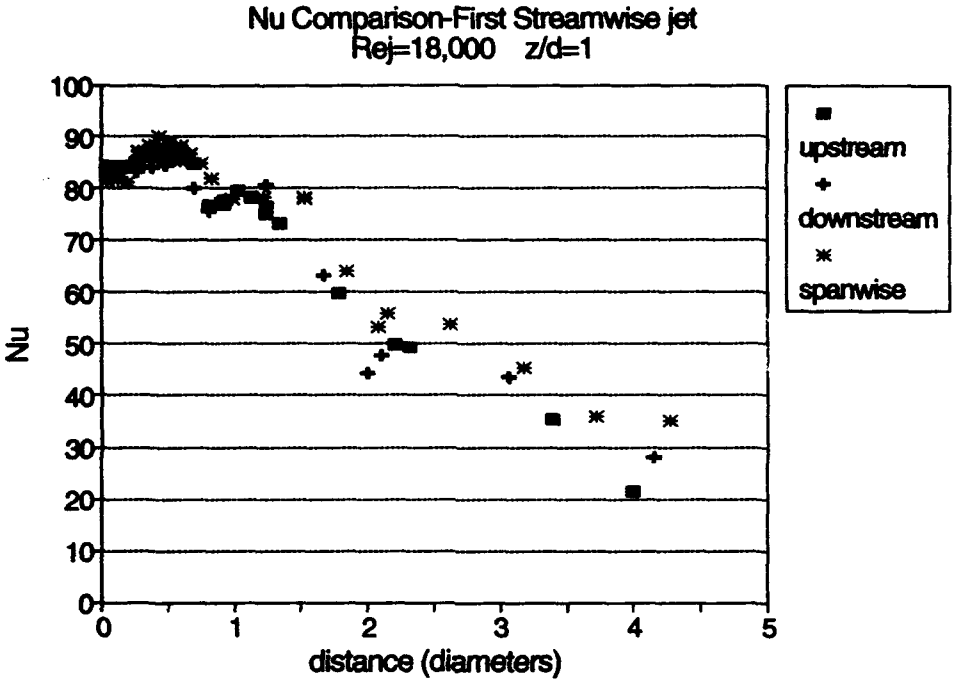

Figure 9.11 Radial distributions of Nusselt number at the first streamwise jet row (local Re_j = 18,000; z/d = 1).

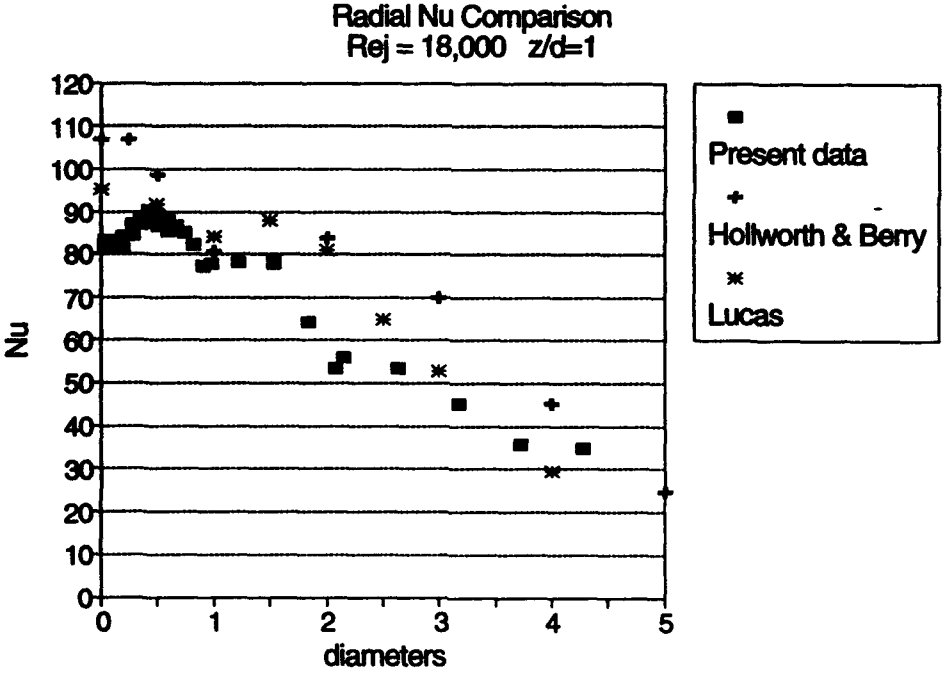

Figure 9.12 Comparison of radial distributions of Nusselt number for local Re_j = 18,000 and z/d = 1.

Hollworth and Berry used a steady state technique on a single confined jet with the same diameter as the present experiments and measured heat transfer to the target surface using a heat flux gauge with dimensions 1mm by 0.7mm. Their data is averaged over the surface of the gauge. Differences in stagnation point Nusselt number could be due to different initial plenum turbulence levels in their respective plenums, since none were reported.

Table 9.1 displays the percent increase in *Nu* at the 0.5*d* radial position when compared to the stagnation point *Nu* value. Comparison of stagnation point *Nu* with **Lucas et al.** in Figure 8.15 showed their stagnation point data to be slightly higher than the present study for very similar geometries. This difference in stagnation point

Table 9.1 Average increase in Nusselt number above stagnation point values for inline geometries near 0.5*d* locations from the impingement points.

Re_j Avg	*z/d*	% increase - avg
10,170	1	8.6
20,694	1	8.8
34,368	1	8.1
10,185	2	9.9
20,833	2	10.3
30,354	2	11.3
10,161	4	1.6
20,589	4	2.1
30,766	4	4.2

Nu is the same magnitude as the difference between the stagnation point and the first peak in heat transfer for the current set of experiments given in Table 9.1. The data in Table 9.1 are averaged over the eight jet rows and indicate encroachment of the jet by the crossflow in this 0.5*d* region increasing heat transfer. For $z/d = 1$, all tested average Re_j show a similar increase of about 8.5%. As the channel spacing increases to $z/d = 2$, the increase is slightly over 10% indicating the extra length allows more time for jet interaction with the channel air. The potential core still reaches the target surface maintaining the stagnation point dependence on local Re_j observed with the $z/d = 1$ data. The $z/d = 4$ data shows an increase of around 2%. In this case the extra mixing length makes the stagnation point *Nu* closer to this peak value. This first elevated *Nu* structure at 0.5*d* was not observed by **Lucas et al**. Perhaps their thin target surface heater was more influenced by lateral conduction and masked the variation in heat transfer over this small area. In addition, for the narrowband crystal used, the amount of temperature rise required to measure the difference in heat transfer in this region is within the one degree colour play used in their experiments. **Hollworth and Berry** single jet data does not show a strong peak at 0.5*d*. However, their experimental data supports the existence of this peak.

Local *Nu* and jet effectiveness values for the complete inline array are presented in Figures 9.13 to 9.24. For the inline array geometry and $z/d = 1$, Figure 9.13, one can see the increase in stagnation *Nu* with streamwise distance through the array. Figure 9.19 shows the stagnation *Nu* also increases as the average Re_j increases. What is most apparent at this z/d is the influence of crossflow on the target surface heat transfer. The first jet row heat transfer contours are nearly circular. As

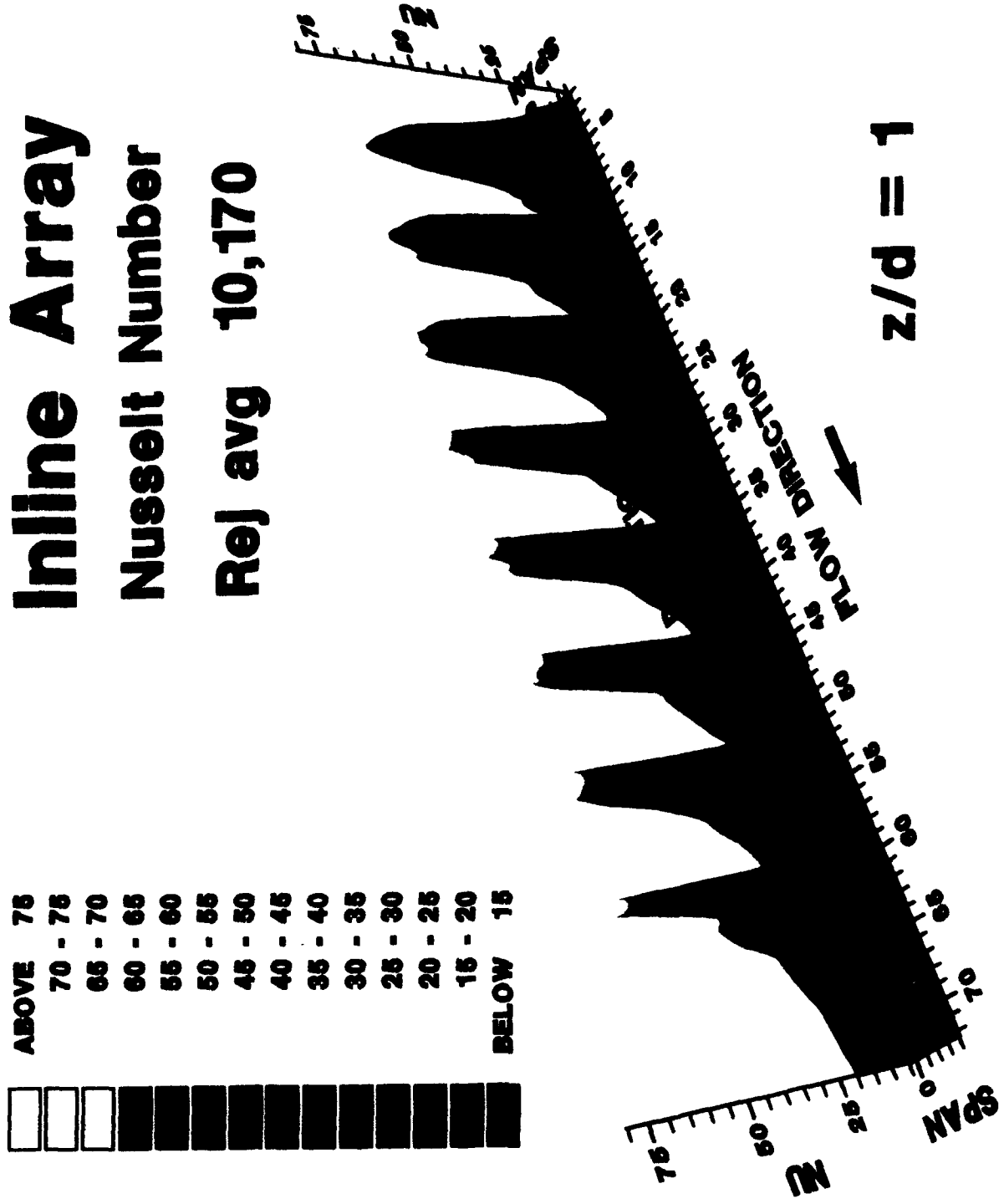

Figure 9.13 Inline array Nusselt number distributions at all locations for Re_j avg = 10,170 and z/d = 1.

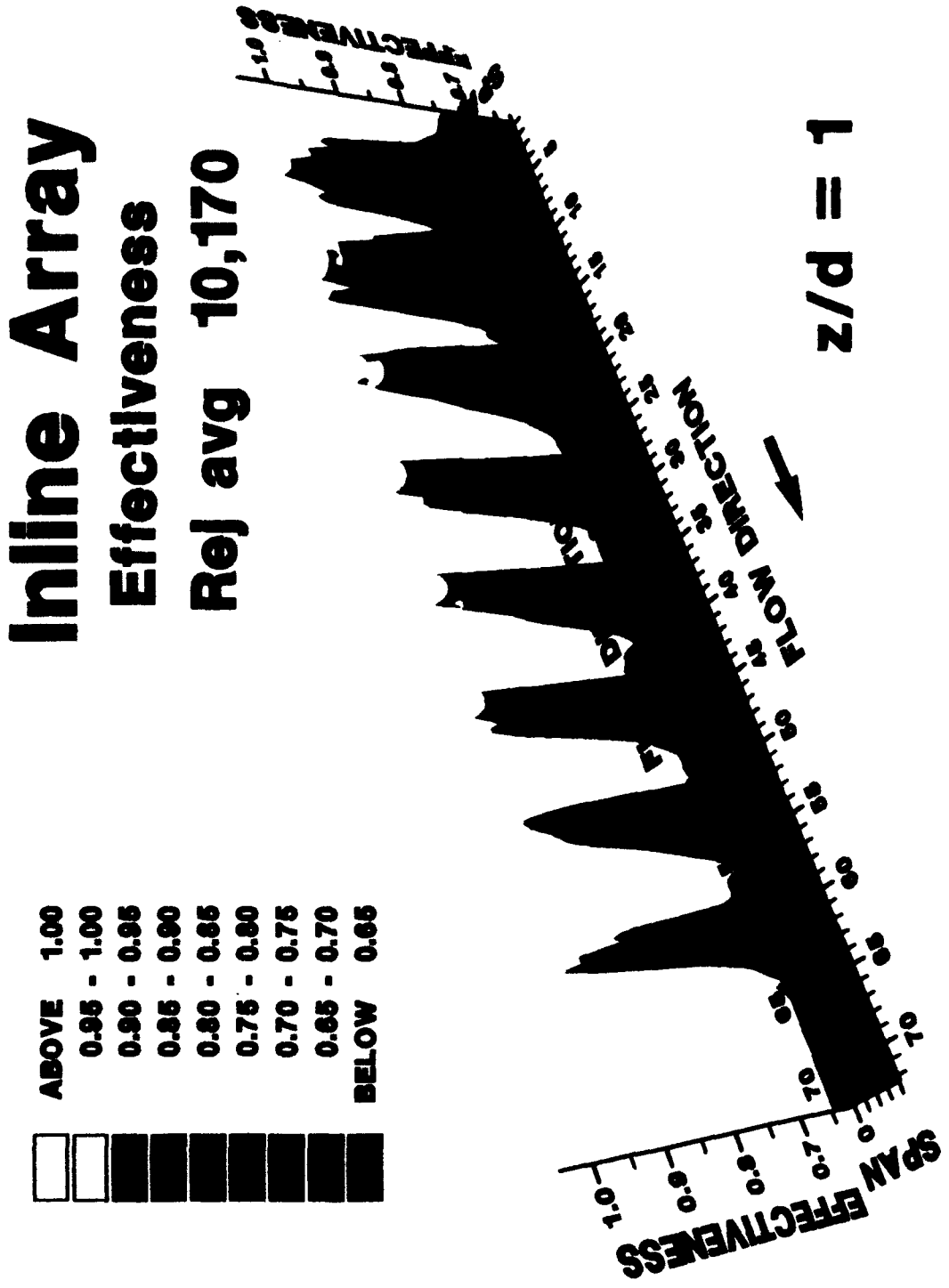

Figure 9.14 Inline array jet effectiveness at all locations for Re_j avg = 10,170 and z/d = 1.

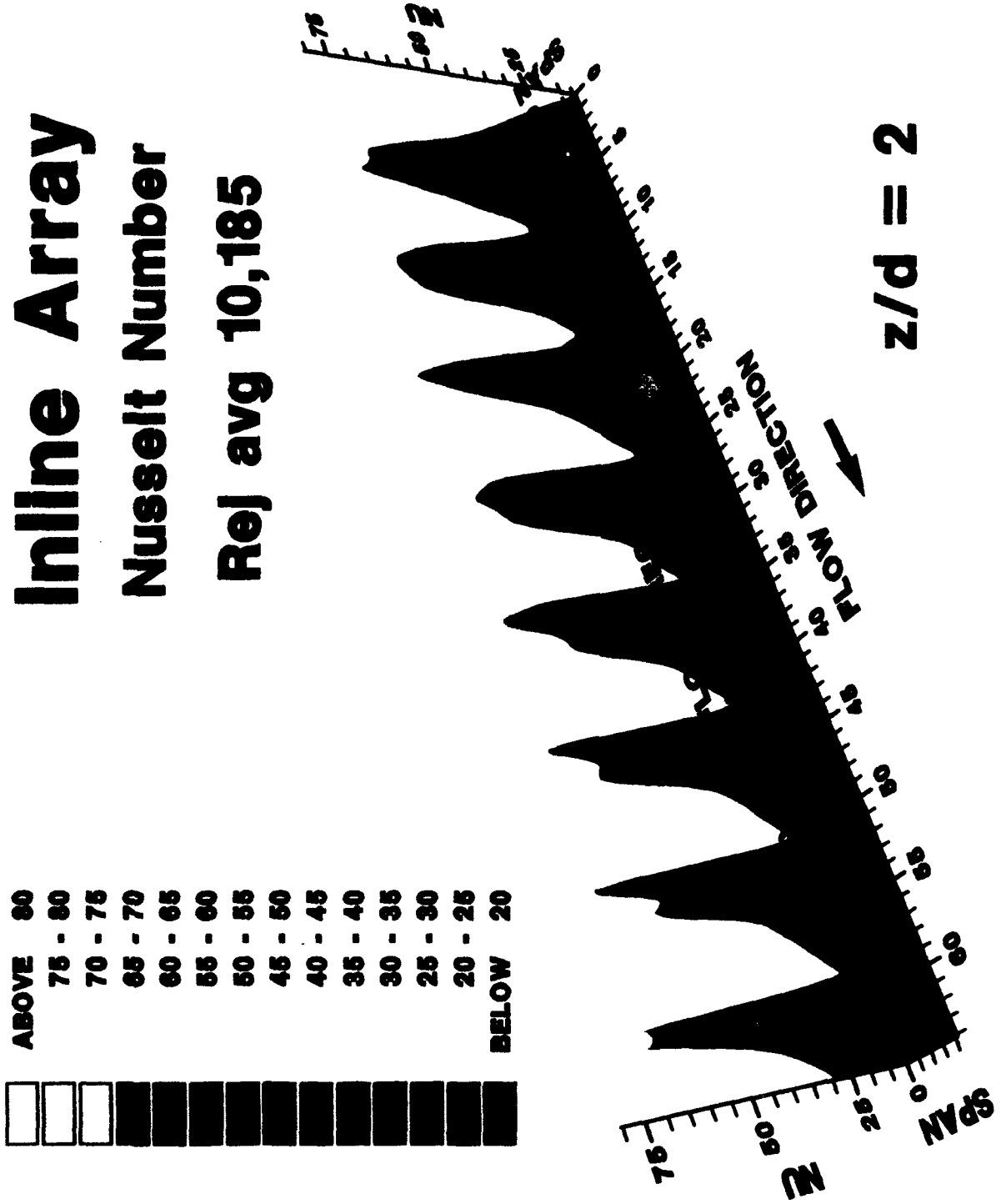

Figure 9.15 Inline array Nusselt number distributions at all locations for Re_j avg = 10,185 and z/d = 2.

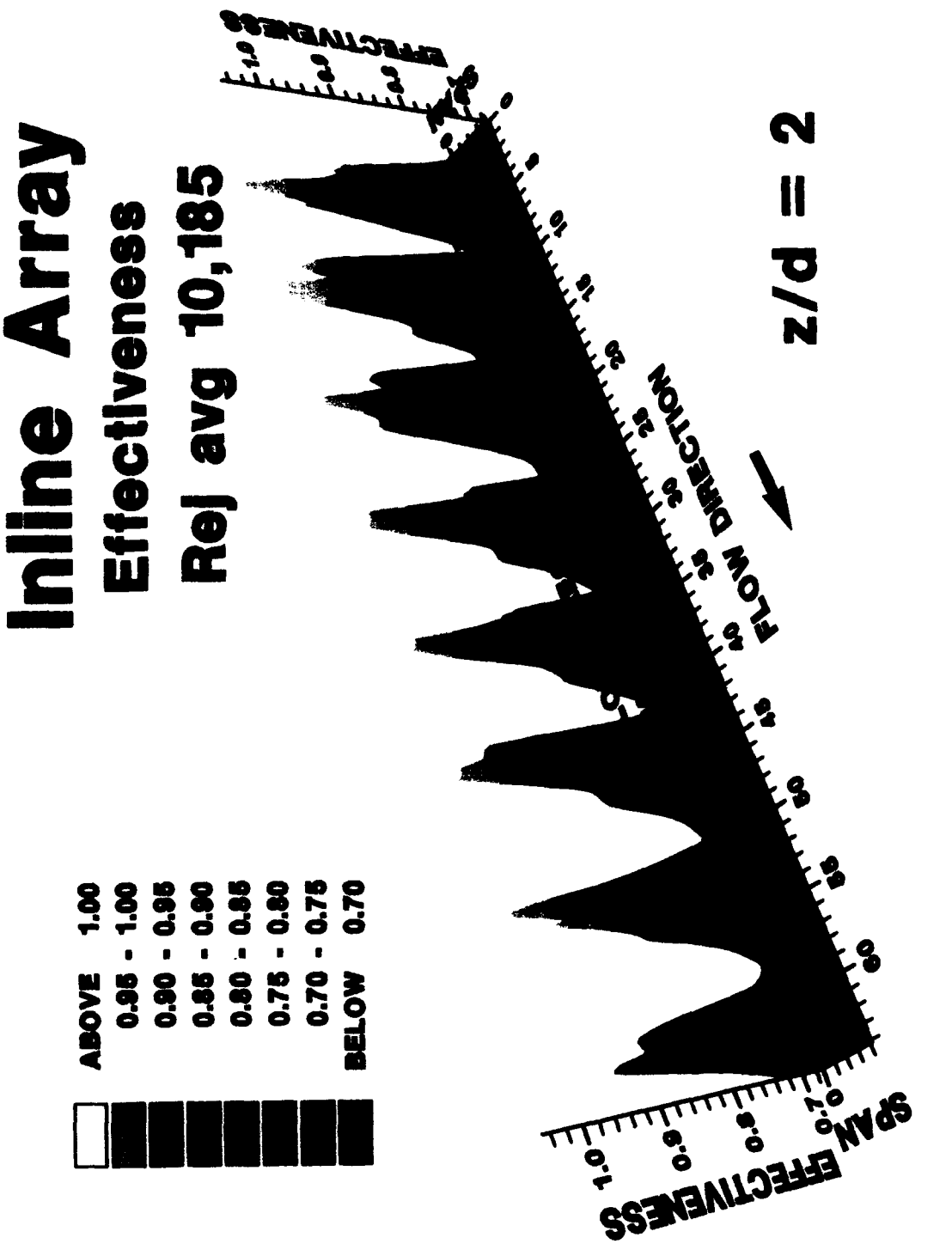

Figure 9.16 Inline array jet effectiveness at all locations for Re_j avg = 10,185 and z/d = 2.

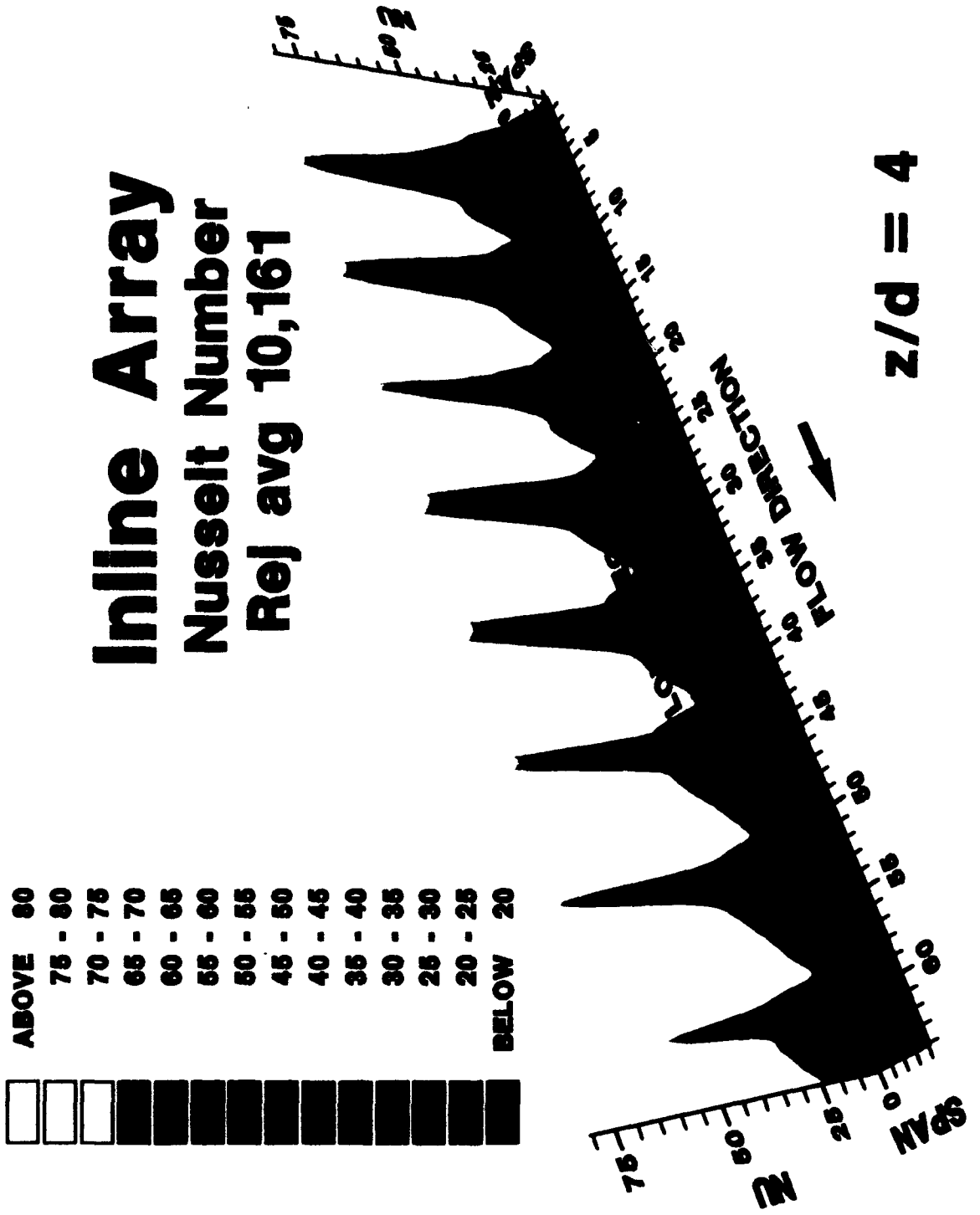

Figure 9.17 Inline array Nusselt number distributions at all locations for Re_j avg = 10,161 and z/d = 4.

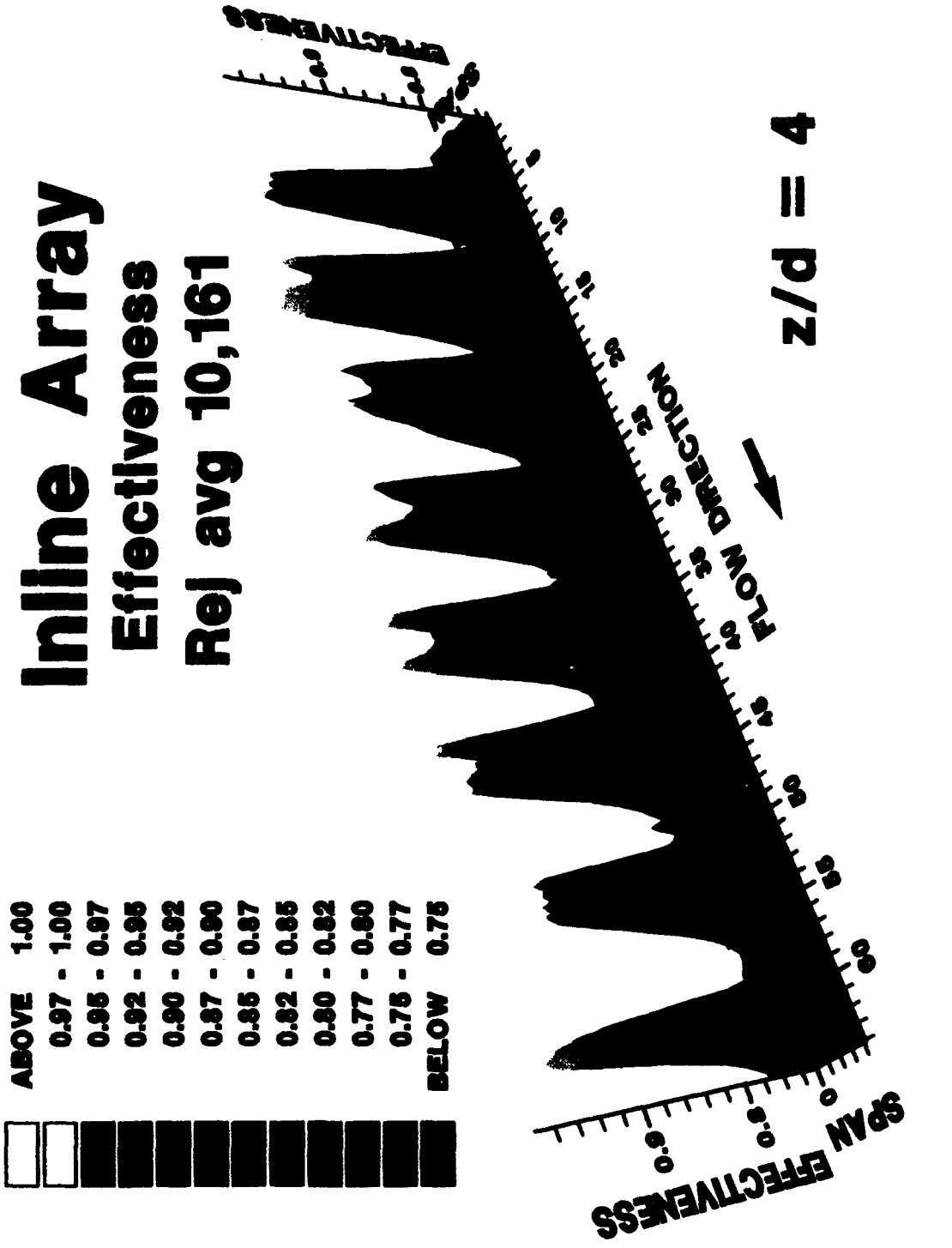

Figure 9.18 Inline array jet effectiveness at all locations for Re_j avg = 10,161 and z/d = 4.

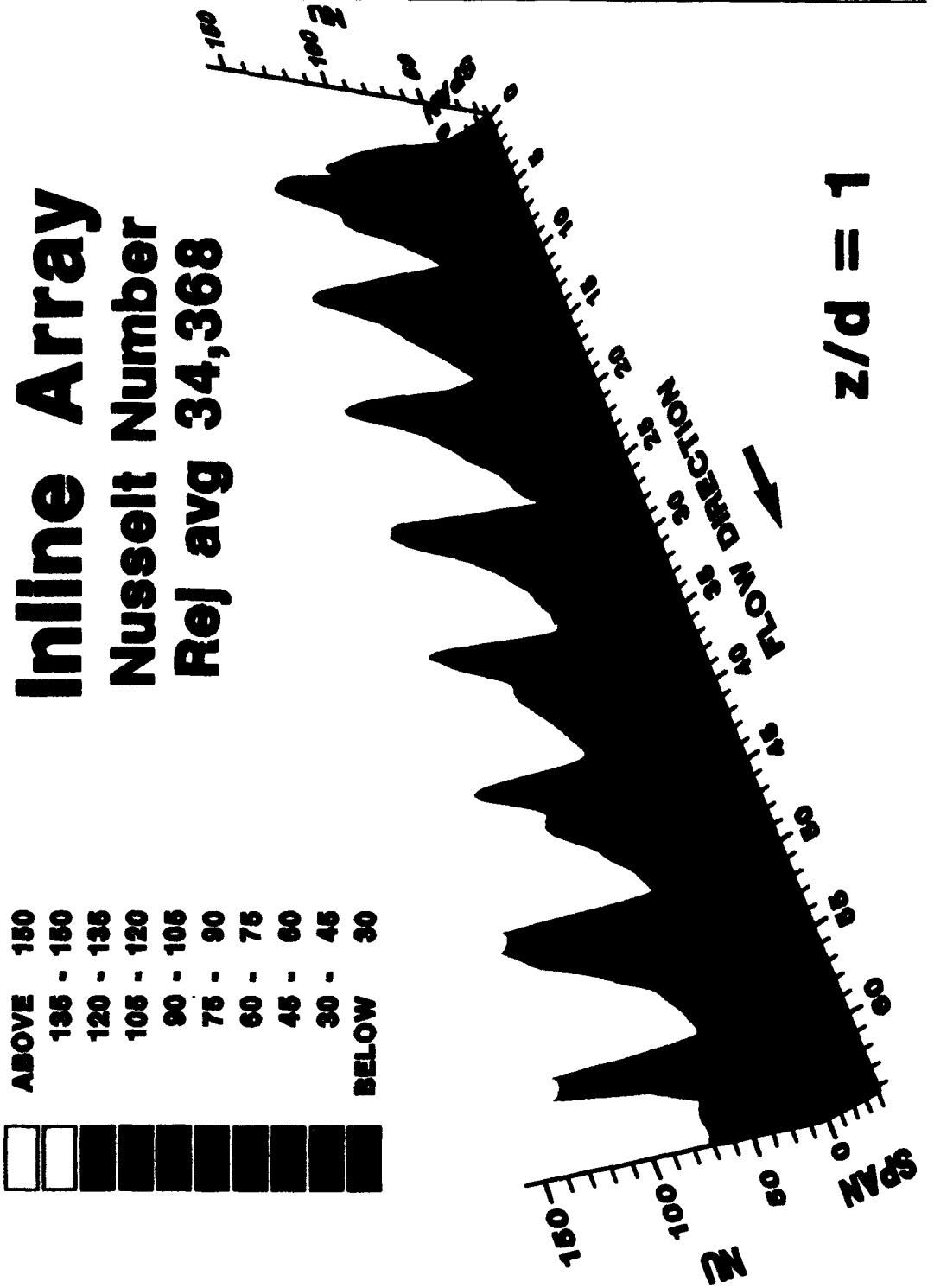

Figure 9.19 Inline array Nusselt number distribution at all locations for Re_j avg = 34,368 and z/d = 1.

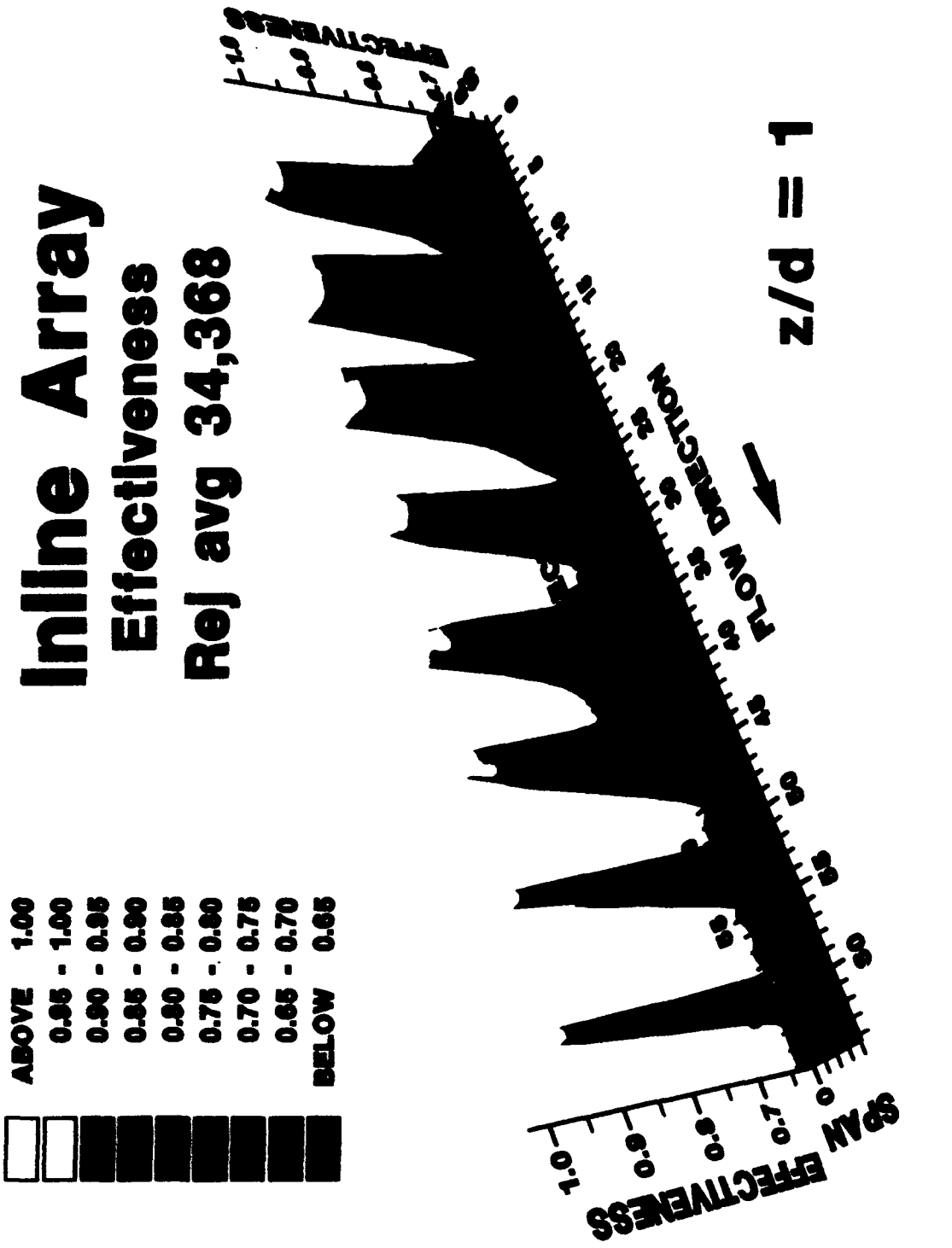

Figure 9.20 Inline array jet effectiveness at all locations for Re_j avg = 34,368 and z/d = 1.

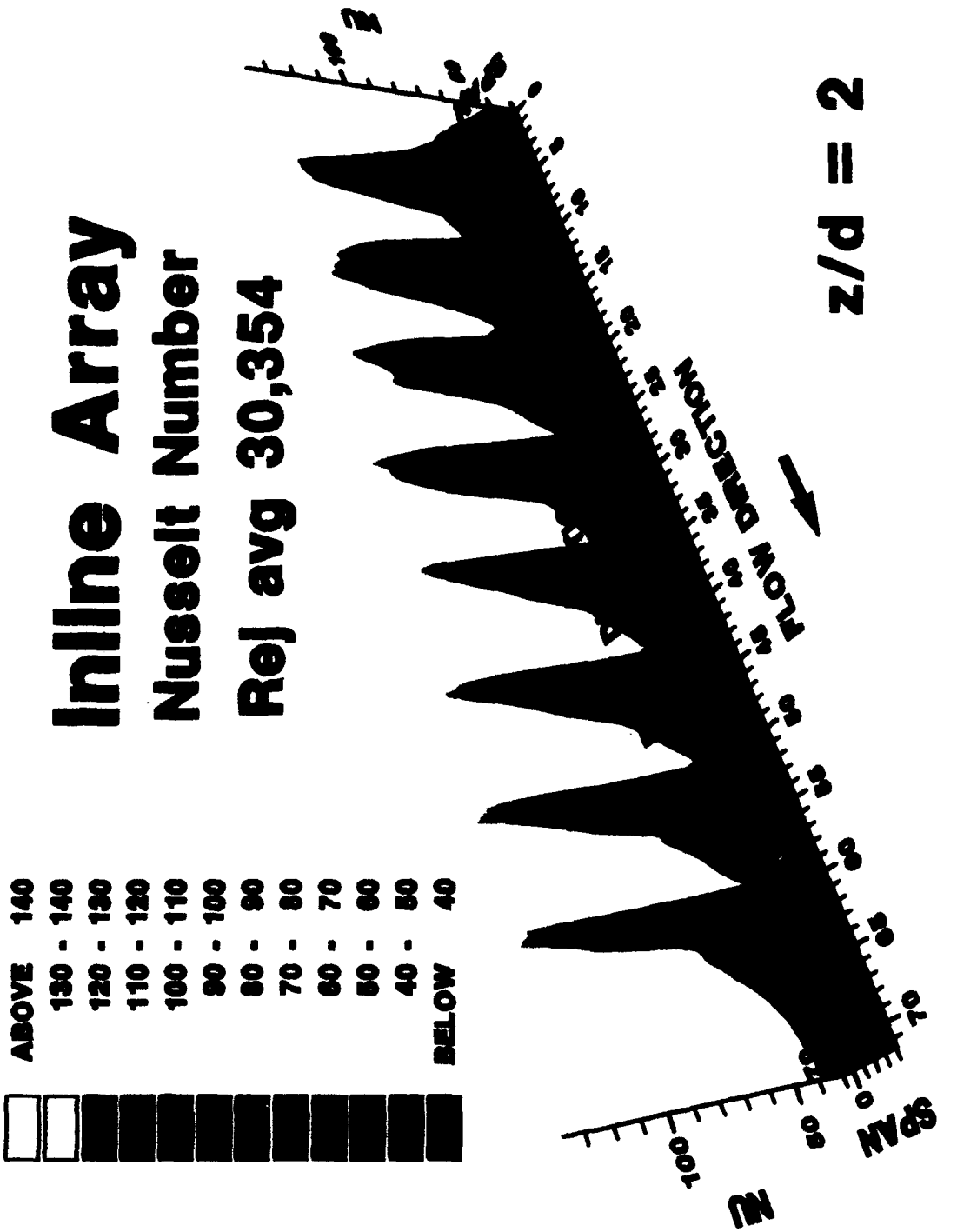

Figure 9.21 Inline array Nusselt number distributions at all locations for Re_j avg = 30,354 and z/d = 2.

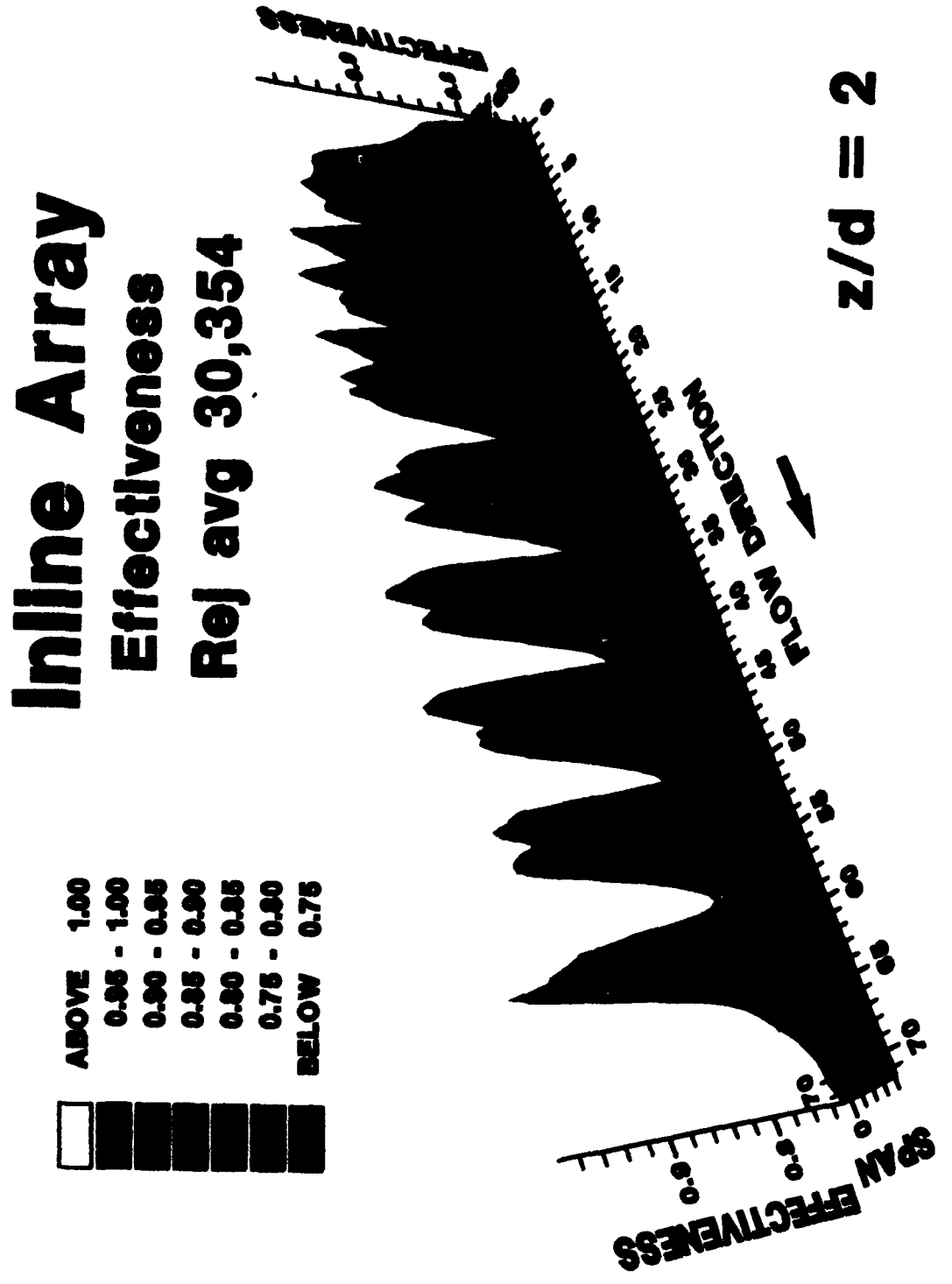

Figure 9.22 Inline array jet effectiveness at all locations for Re_j avg = 30,354 and z/d = 2.

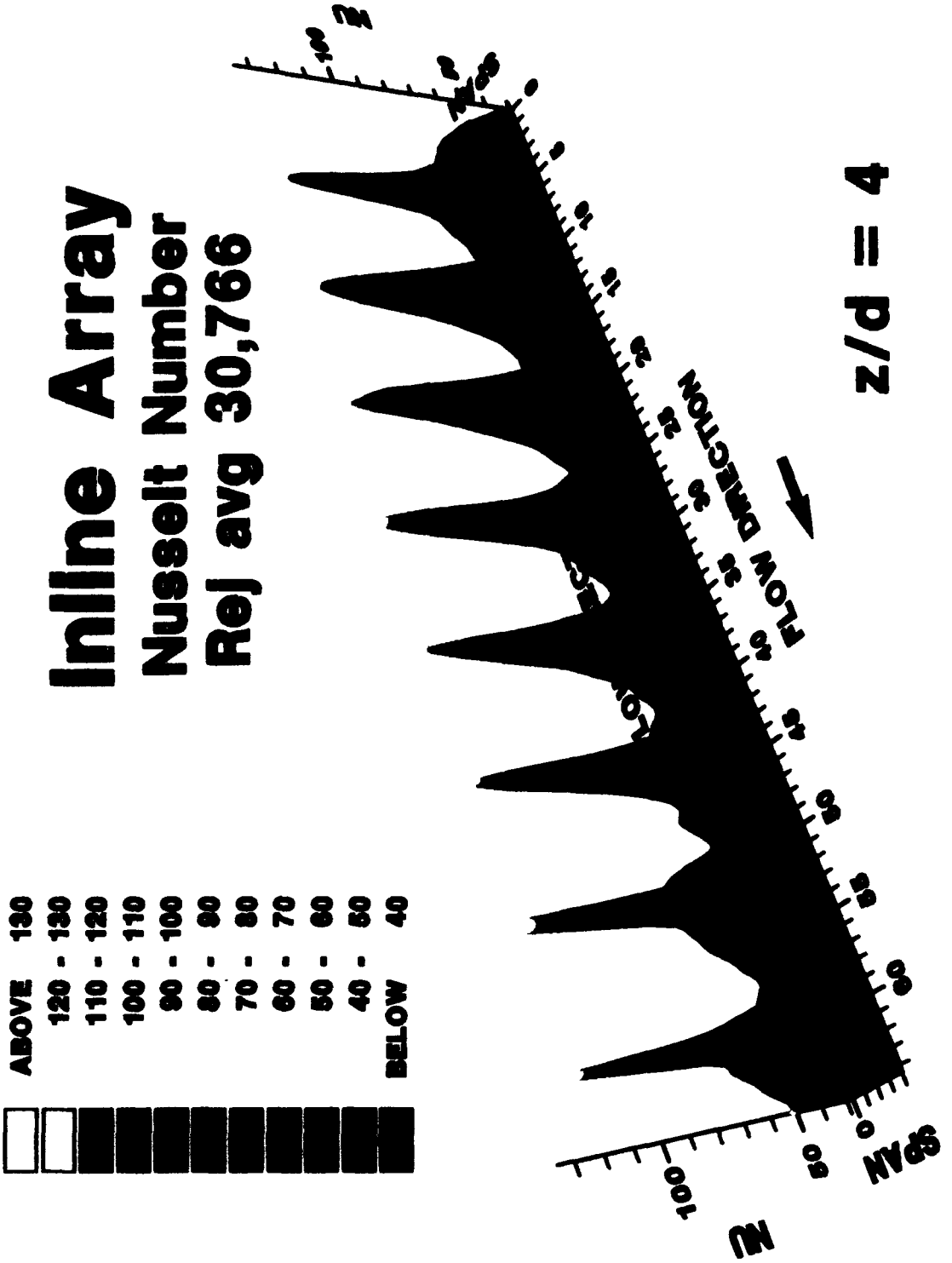

Figure 9.23 Inline array Nusselt number distributions at all locations for Re_j avg = 30,766 and z/d = 4.

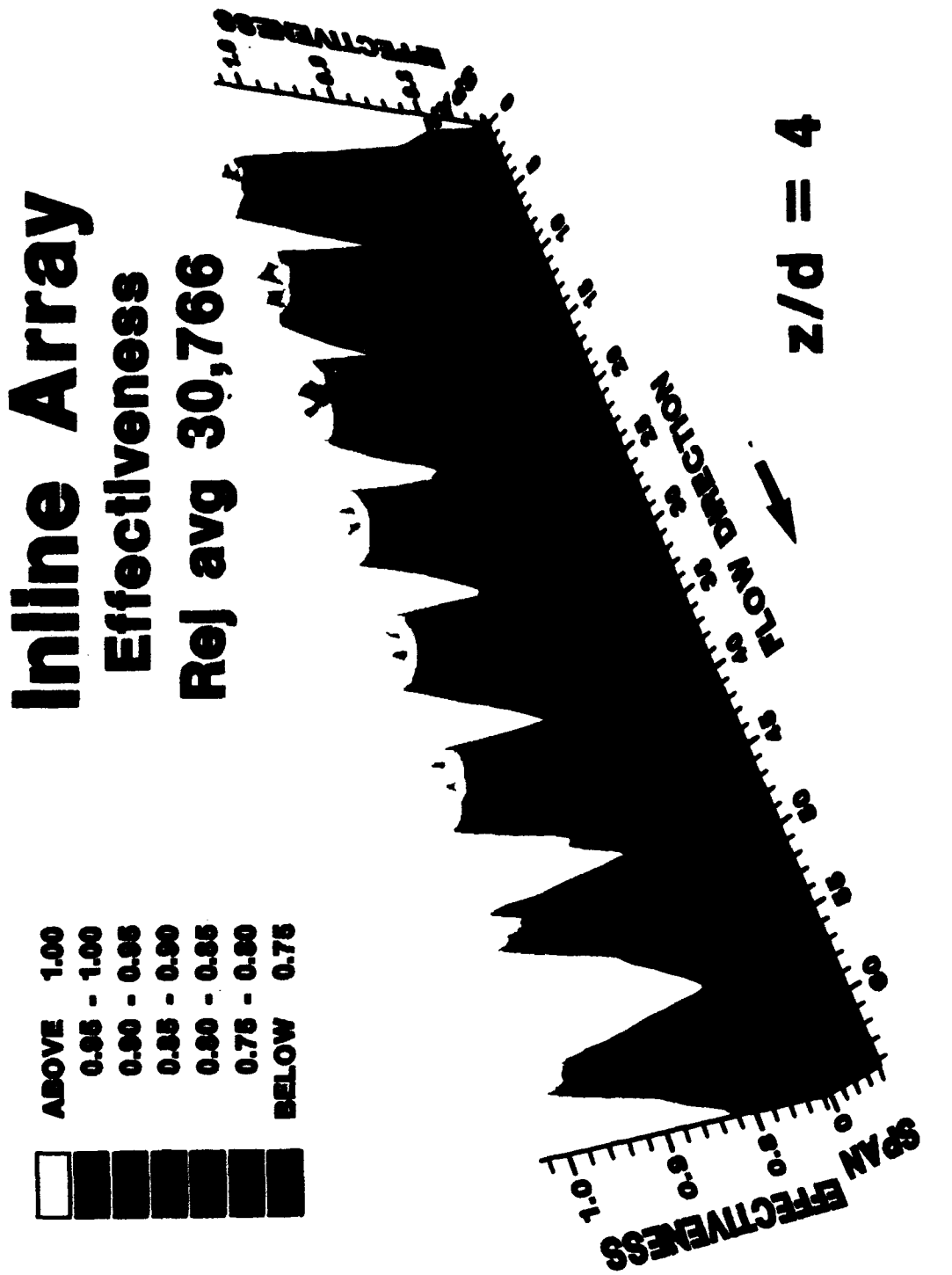

Figure 9.24 Inline array jet effectiveness at all locations for Re_j avg = 30,766 and z/d = 4.

crossflow develops, the jet influence is limited in both the upstream and spanwise directions. Increasing the z/d, the jet structure remains more circular throughout the array and at $z/d = 4$, Figures 9.17 and 9.23, little influence of crossflow is observed. Increasing the z/d shows the stagnation point Nu values to be more uniform. Once the data is in the form of a local area surface map, it can then be averaged over an area specific to a given jet location.

9.1.2 Average Value Data

Average values were determined by averaging local values over an area extending $4d$ from the jet centreline in the upstream, downstream and spanwise directions. It should be remembered that the hole spacing is $8d$. The plane of symmetry was through the jet hole centre in the streamwise direction. The advanced transient techniques developed for these experiments enabled not only the local Nu to be calculated but also the local T_{aw}. These local values were then used to determine average Nu and jet effectiveness. Controlling the impingement plate temperature, T_p, at approximately the initial target plate temperature for the duration of the test results in a local T_{aw} that ranges from T_{plen} in the stagnation region to a value between T_{plen} and T_p as one moves away from the jet impingement zone. Jet effectiveness is a measure of how this temperature variation occurs. Recirculation of hot jet gas couples the cool impingement plate to the target surface resulting in a T_{aw} lower than T_{plen}. In the experiments of all other reported work except **Lucas et al. (1992)**, T_p was allowed to float between T_{plen} and the target wall temperature and T_p is not reported.

Correlations from such data are only applicable to engines if the impingement plate thermal boundary conditions are representative of the engine. In situations where the impingement insert has strong thermal contact with the turbine blade, significant lateral conduction within the impingement insert changes its temperature and alters the thermal boundary conditions from the experimental ones. It is also likely that the plate temperature and thermal boundary conditions differ under engine transients. In engine operation, especially during the two situations mentioned, correlations that do not account for the impingement plate are suspect. The present experiments calculate T_{aw} for known plenum and plate temperatures. Most other experiments use a reference gas temperature, such as the plenum temperature, to define their heat transfer coefficients. Since the difference between the target wall temperature and the adiabatic wall temperature must be less than the difference between the plenum temperature and the target wall temperature, the data from the other reports would be correspondingly higher (depending on the plate temperature) if the data were based on T_{aw}. This emphasizes the need to consider all boundary conditions properly when comparing data. **Kim et al. (1993)** studied an unconfined impinging jet issuing from a pipe using a transient technique. They reported as much as 50% reduction in this temperature difference when using a local recovery temperature. The present experimental study is the first to provide data on the influence of the impingement plate temperature on the target surface for the more difficult conditions present in a confined jet array.

To compare the effect of plate spacing and Re_j on average Nu, data, presented in Figures 9.25 to 9.30, are shown as a function of average Re_j for the z/d values

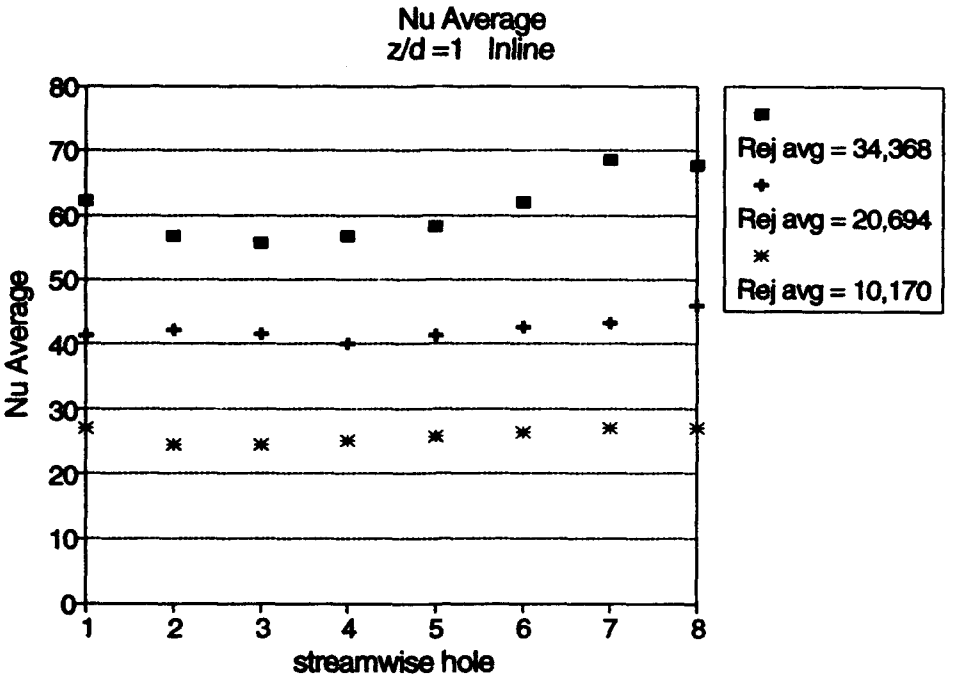

Figure 9.25 Average Nusselt number at streamwise jet locations for an inline array with $z/d = 1$.

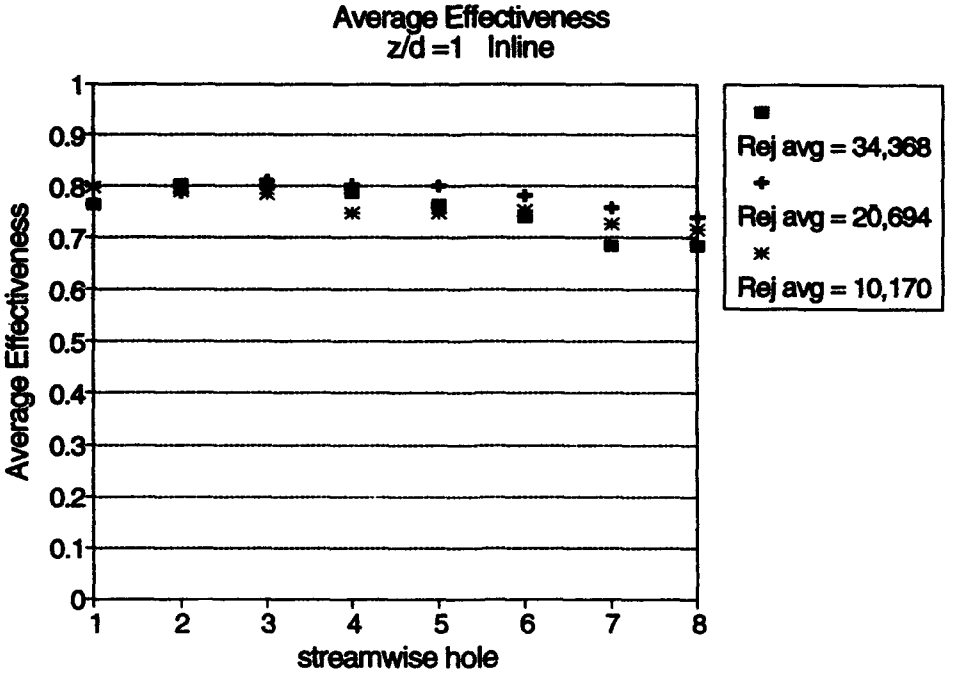

Figure 9.26 Average jet effectiveness at streamwise jet locations for an inline array with $z/d = 1$.

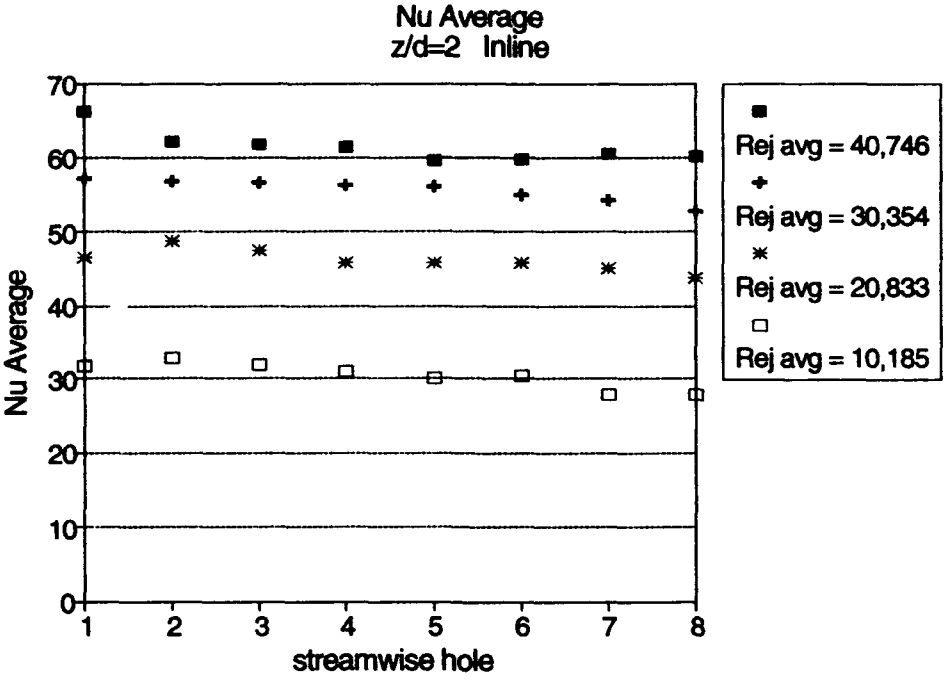

Figure 9.27 Average Nusselt Number at streamwise jet locations for an inline array with $z/d = 2$.

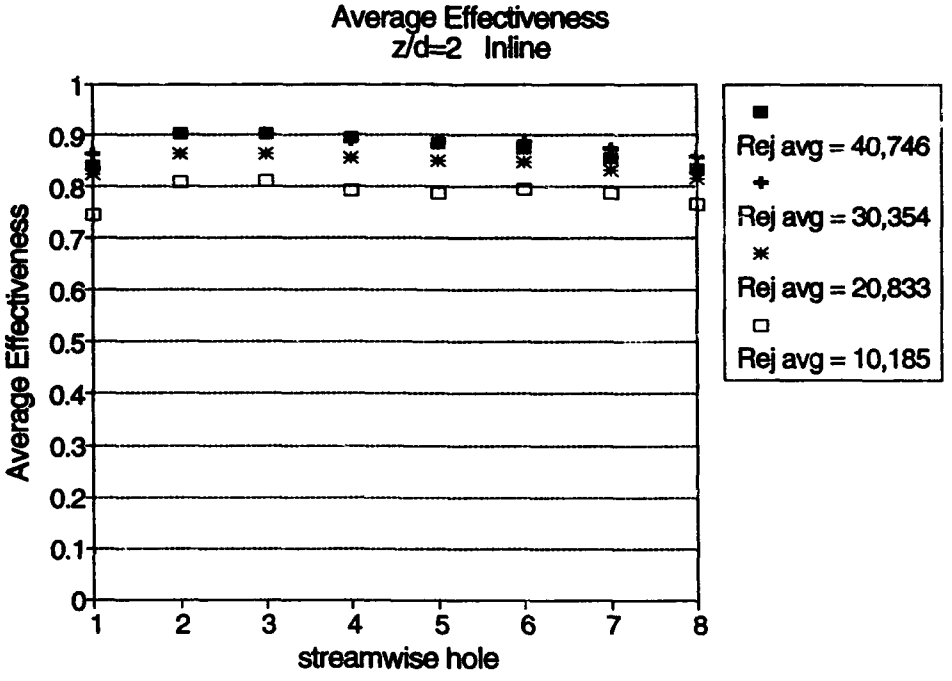

Figure 9.28 Average jet effectiveness at streamwise jet locations for an inline array with $z/d = 2$.

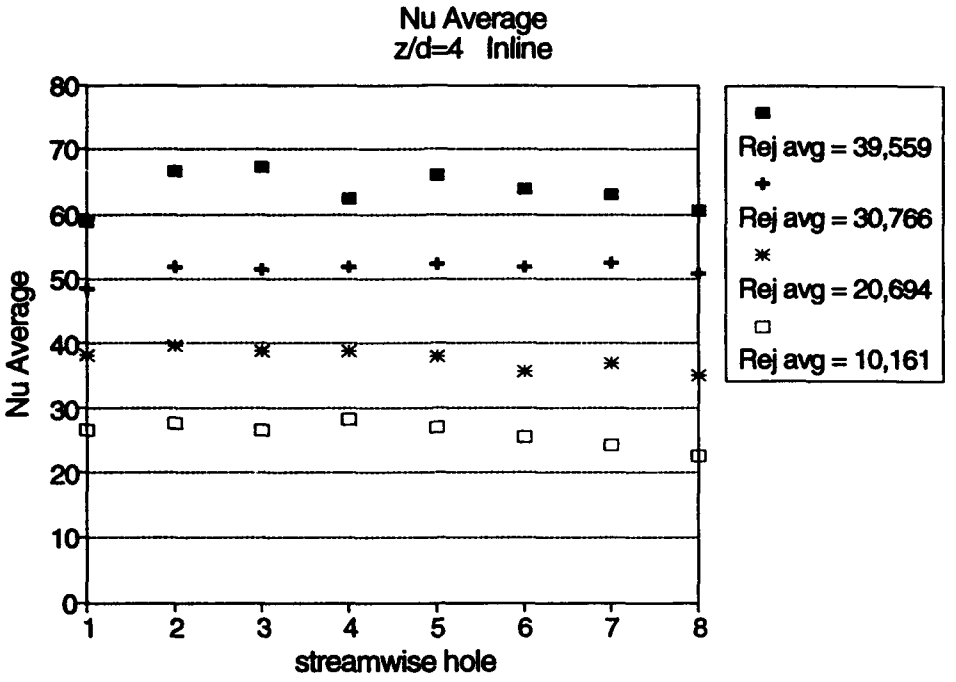

Figure 9.29 Average Nusselt number at streamwise jet locations for an inline array with $z/d = 4$.

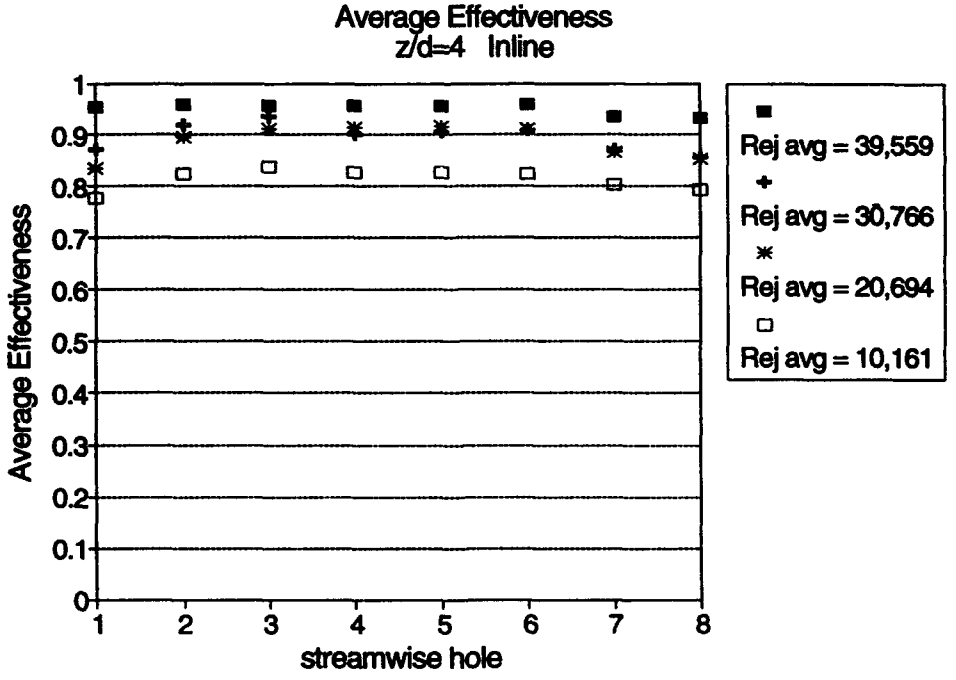

Figure 9.30 Average jet effectiveness at streamwise jet locations for an inline array with $z/d = 4$.

tested. The z/d = 1 results, shown in Figure 9.25, initially show a decrease in average *Nu* to jet row three or four. Increasing crossflow restricts the coverage of the impinging jet decreasing heat transfer values. After jet row three or four, the average *Nu* increases due to the accumulated crossflow accelerating between the jet rows and significantly contributing to the average *Nu* value near the exit to the array. This array exit *Nu* value is higher than the value found at the first jet row. The average jet effectiveness for a z/d = 1, in Figure 9.26, is essentially independent of Re_j except close to the exit from the array. Initially, a level of about 0.8 is achieved for the first three to four jet rows. After that position, the crossflow limits the jet effectiveness and it is seen to drop to a value of approximately 0.7. While the jet effectiveness is dropping, the average *Nu* in Figure 9.25 is increasing. This behaviour indicates crossflow, not jet impingement, is responsible for the increase in average *Nu* at the array exit. An increase in plate spacing to z/d = 2, Figure 9.27, increases the initial average *Nu* values above those of the z/d = 1 case. Since the influence of crossflow is less, the average *Nu* slightly decreases through the array. Jet effectiveness at z/d = 2 (see Figure 9.28) for an average Re_j of 10,185 remains at approximately 0.8, the same value as in the z/d = 1 case, and decreases less through the array because crossflow is not as strong. Increasing average Re_j from 10,185 increases jet effectiveness. A value of 0.9 is achieved for jet rows three to four and jet effectiveness decreases from this point more slowly than the z/d = 1 case. Jet effectiveness is essentially the same for average Re_j values above 10,185. Figure 9.29 shows that increasing z/d to 4 lowers the average *Nu* below the values for the z/d = 2 case. Crossflow influence is less than the z/d = 2 case but the average *Nu*

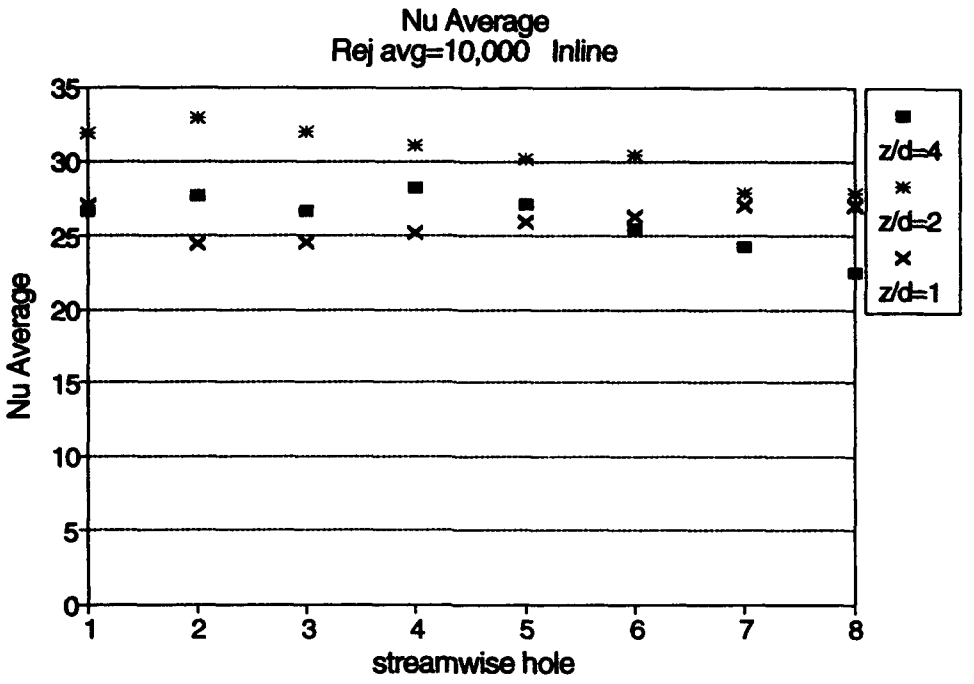

Figure 9.31 Inline - Average Nusselt number at jet locations for Re_j avg = 10,000 and z/d = 1, 2 and 4.

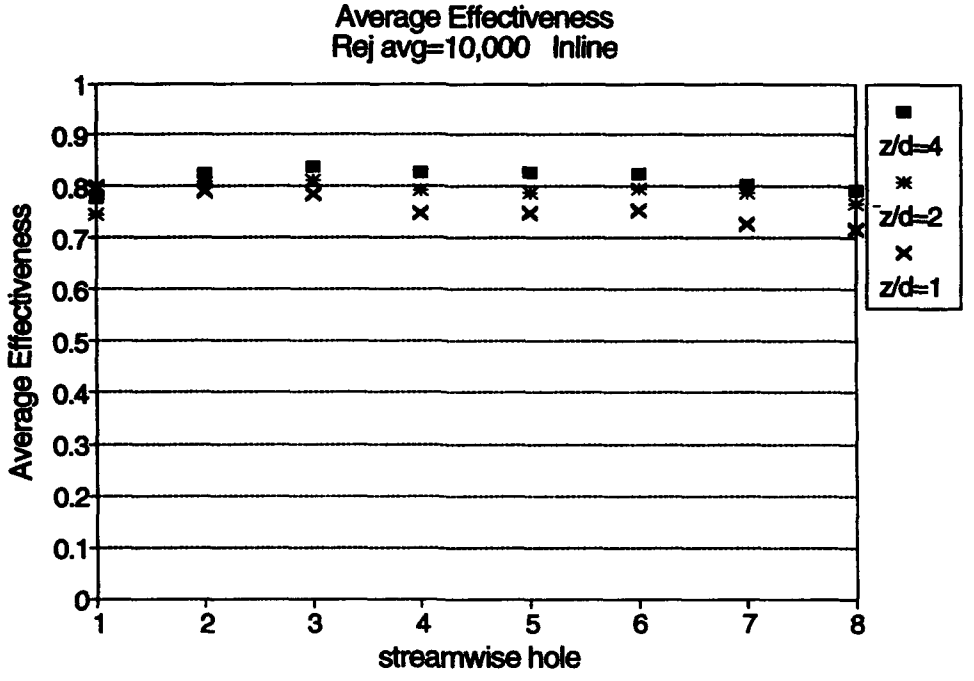

Figure 9.32 Inline - Average jet effectiveness for jet locations at Re_j avg = 10,000 and z/d = 1, 2 and 4.

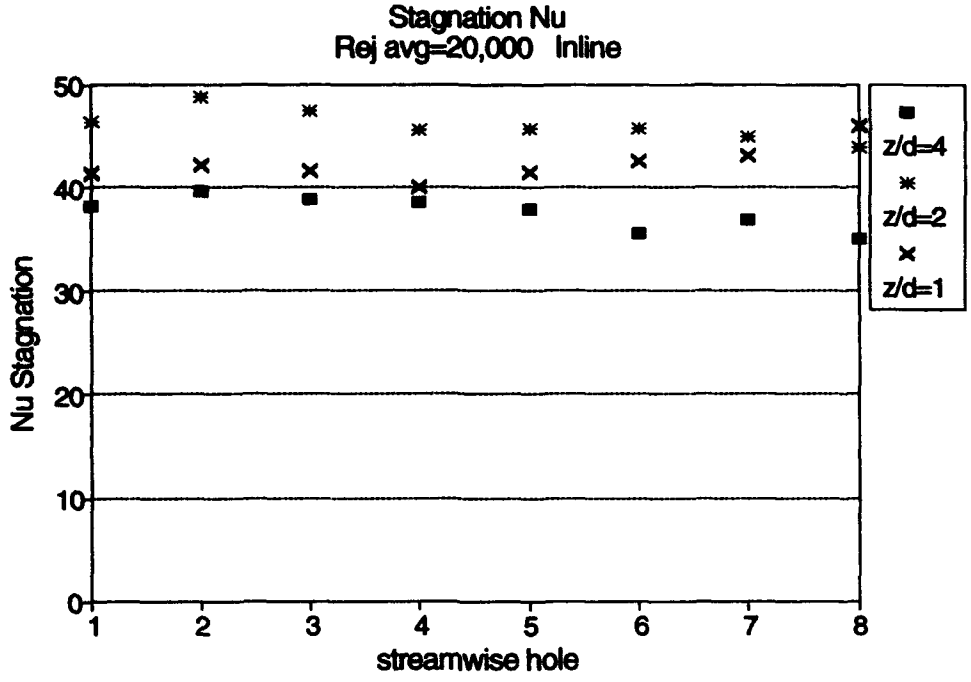

Figure 9.33 Inline - Average Nusselt number at jet locations for Re_j avg = 20,000 and z/d = 1, 2 and 4.

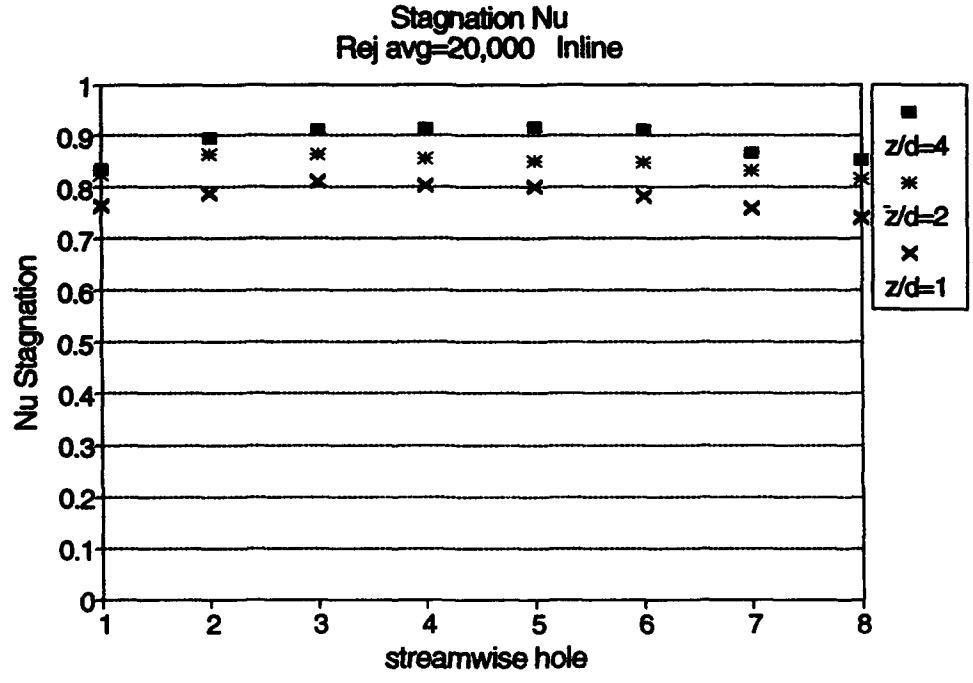

Figure 9.34 Inline - Average jet effectiveness at jet locations for Re_j avg = 20,000 and z/d = 1, 2 and 4.

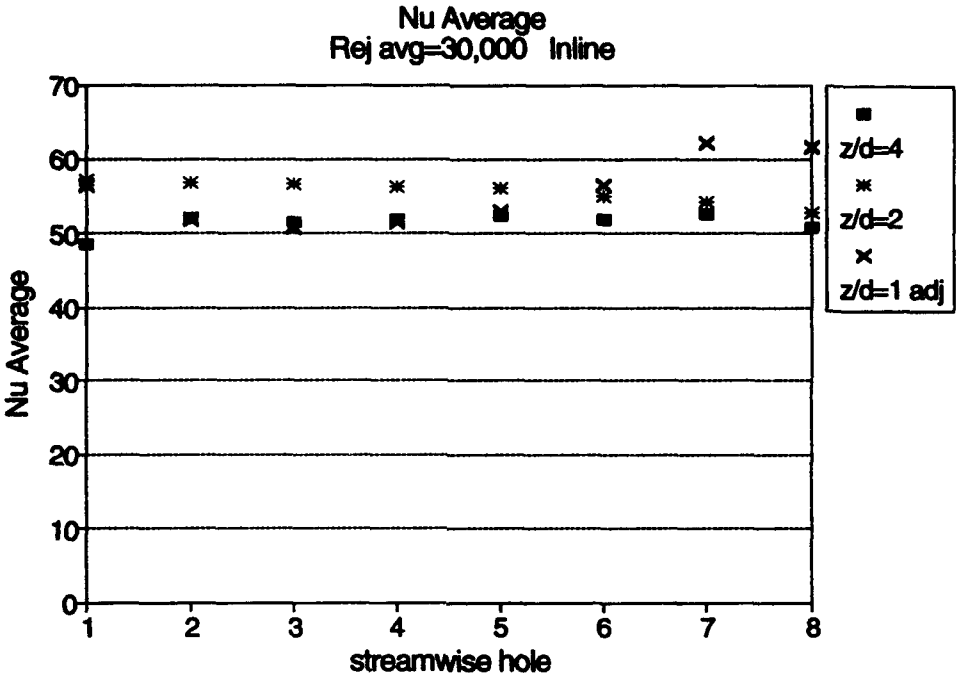

Figure 9.35 Inline - Average Nusselt number at jet locations for Re_j avg = 30,000 and z/d = 1, 2 and 4.

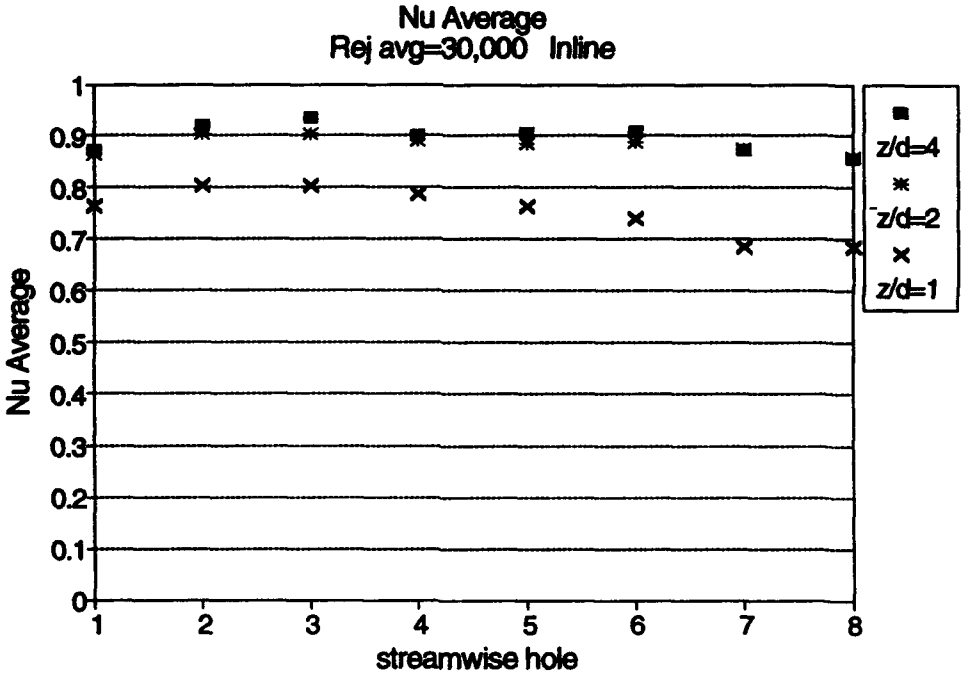

Figure 9.36 Inline - Average jet effectiveness at jet locations for Re_j avg = 30,000 and z/d = 1, 2 and 4.

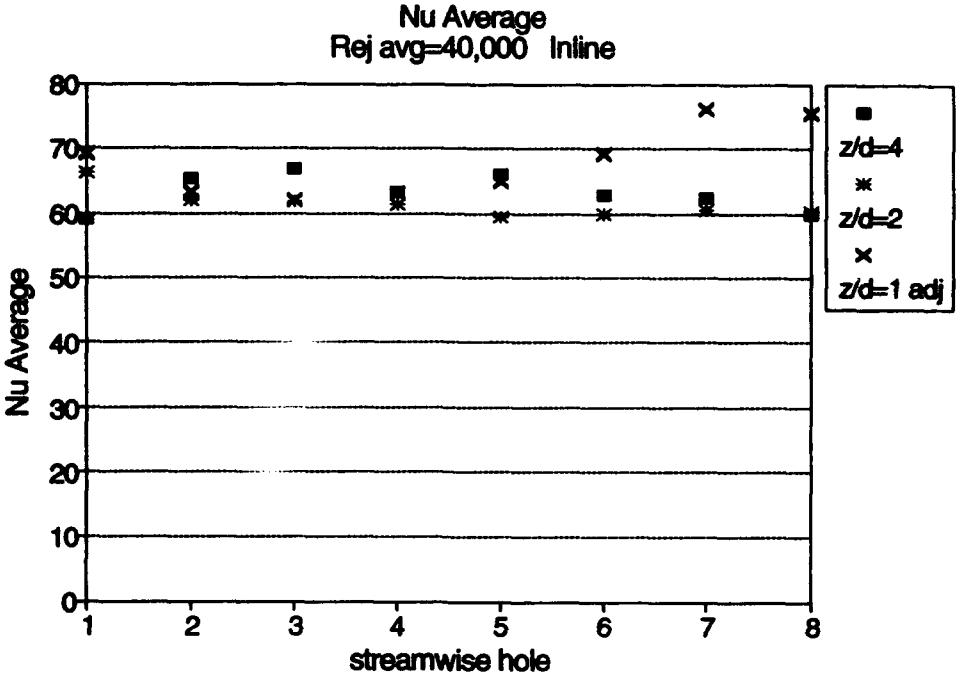

Figure 9.37 Inline - Average Nusselt number at jet locations for Re_j avg = 40,000 and z/d = 1, 2 and 4.

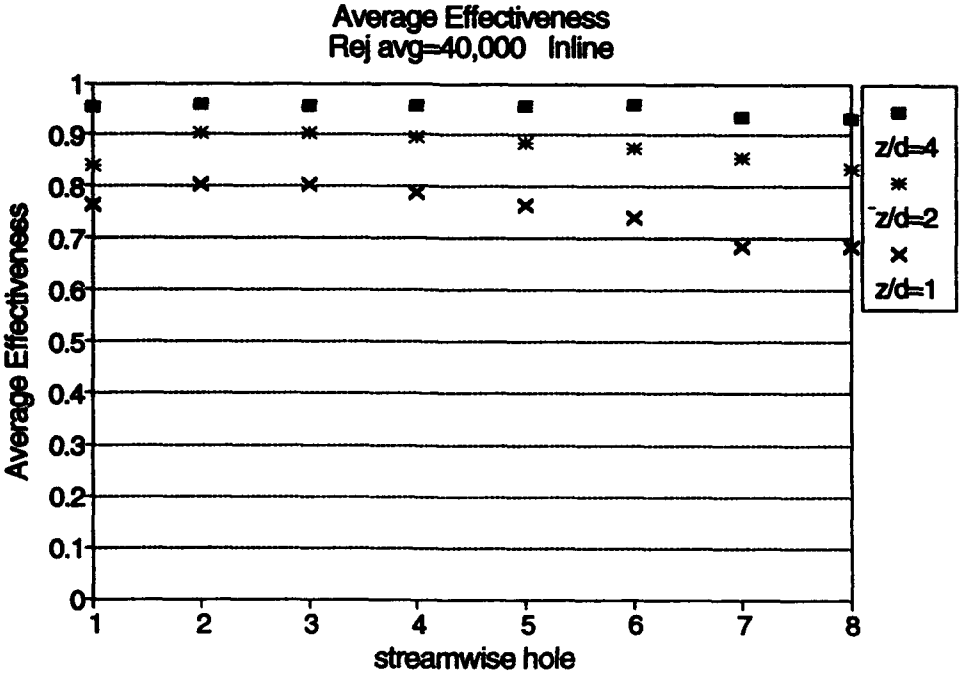

Figure 9.38 Inline - Average jet effectiveness at jet locations for Re_j avg = 40,000 and z/d = 1, 2 and 4.

essentially decreases with jet row through the array. Jet effectiveness, in Figure 9.30, increases with increasing average Re_j. All values are slightly higher than their z/d = 2 counterparts. Values for average Re_j of 20,694 and 30,766 are essentially equal at a value slightly above 0.9 early in the array. Through the array jet effectiveness decreases slightly.

An alternative form of presenting this average value data is shown in Figure 9.31 to 9.40. In these graphs average values are plotted as functions of jet hole position for different z/d over the range of average Re_j tested. The z/d = 1 and average Re_j = 34,368 test was scaled to appropriate values using a 0.7 power dependence for reasons discussed in Chapter 8. When considering average Nu, the z/d = 2 case results in higher values for all average Re_j tested with the exception of the highest Re_j. At the highest Re_j tested all values are approximately equal (Figure 9.37). Increasing z/d also increases jet effectiveness and decreases the influence of crossflow. Increasing z/d to 2 reduces the influence of crossflow at any jet row while not significantly diminishing the strength of the jet potential core, thus, the average Nu and jet effectiveness increase. Increasing z/d to 4 results in the jet mixing out more with associated lower values of average Nu in spite of a slight rise in jet effectiveness due to reduced crossflow.

Figures 9.39 and 9.40 compare present data with other data and correlations from the literature. The present values fall within the range of data listed. The **Andrews et al.** model was developed for a confined jet system with outflow freely discharging on all four sides (**Andrews et al. 1985**) as an average value least squares fit to experimental data. This model was later shown to exhibit good agreement with

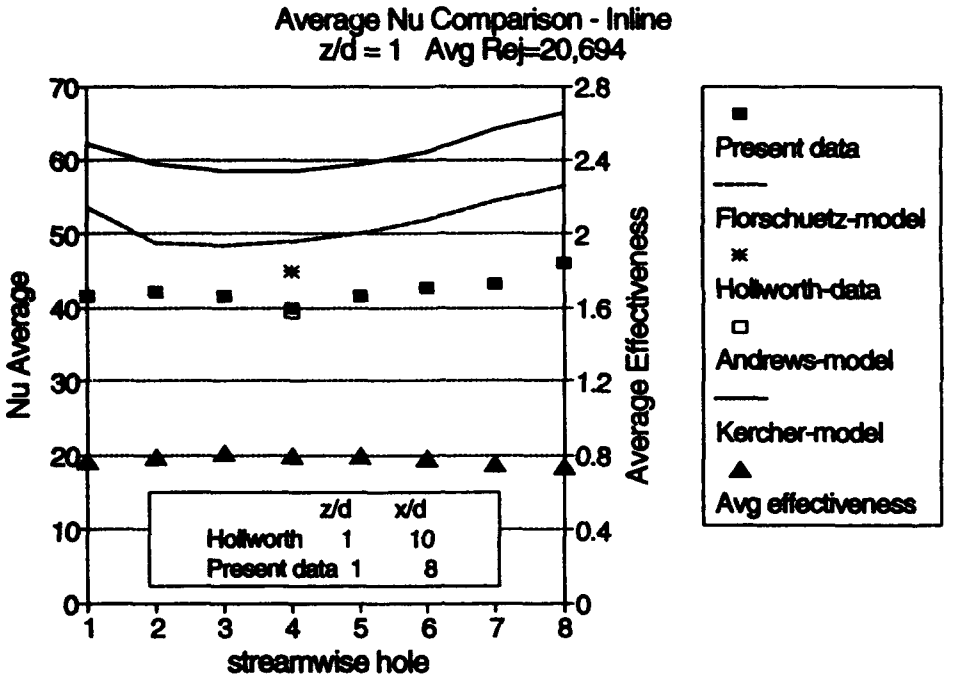

Figure 9.39 Comparison of average Nusselt number for an inline array (Re_j avg = 20,694; z/d = 1).

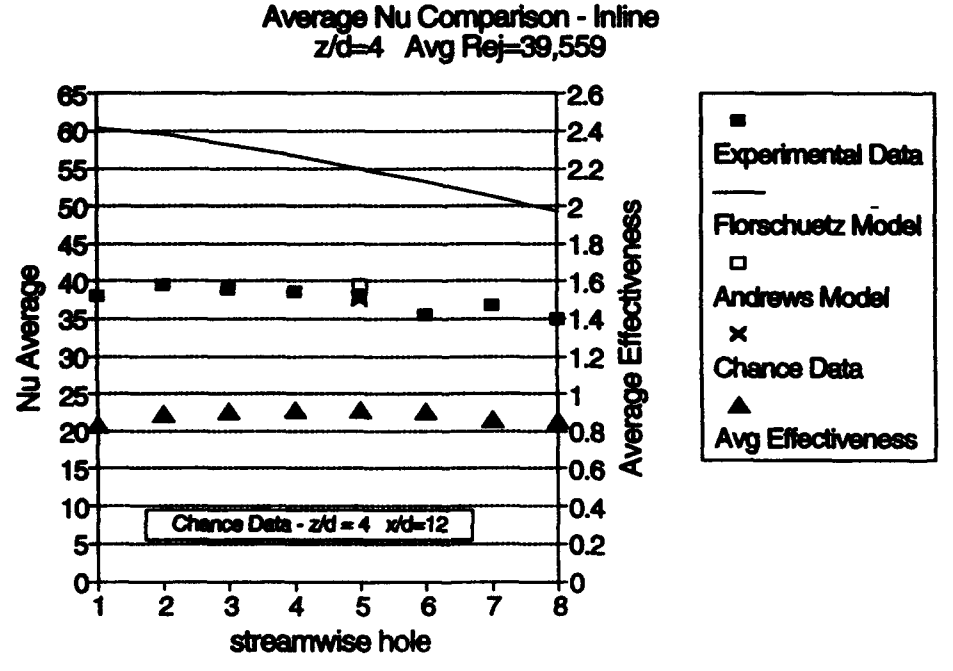

Figure 9.40 Comparison of average Nusselt number for an inline array (Re_j avg = 20,589; z/d = 4).

a confined jet system (**Andrews et al. 1986**) exiting in only one direction. The **Kercher and Tabakoff (1970)** model shows similar overall trends to the present data but the heat transfer levels are approximately 50% higher. The **Florschuetz et al. (1981)** model also tends to overpredict the present results but the trends are similar. The data point from **Hollworth and Berry (1978)** is an average value from a four sided free discharge rig similar to **Andrews et al.** Variations between experiments, such as impingement plate temperature, jet hole geometry, or initial jet turbulence level could significantly alter experimental results.

Of use to the engine designer are correlations of heat transfer for an array of impinging jets. Having detailed local values of heat transfer, it was decided to approach the development of a correlation in a different manner than previously done in the literature. Inspection of the local area maps for *Nu* led to the conclusion that two heat transfer areas could be defined, the first being the area of jet influence and the second being the area of crossflow influence, as was illustrated in Figure 3.3. The local distributions of *Nu* under an impinging jet, as shown in Figure 9.13, indicated the local jet heat transfer gradient was initially very large and then, at a recognizable position, the gradient decreased. This break point was found to correspond to a value equal to approximately 50% of the stagnation *Nu* and was taken as the defining parameter between jet and crossflow areas of influence. All *Nu* values above the 50% level were considered in the jet area of influence and all values below were considered in the crossflow area of influence. Local values were averaged over these areas of influence to produce a crossflow and jet average *Nu*. This process was repeated for each jet row. The local Re_j was used to correlate both the jet and crossflow *Nu*. For

the jet region, the choice was obvious, since the jet dominates the heat transfer process. For the crossflow region, initially it was thought to develop a dependence on a channel *Re* however, for the G_c/G_j values considered, the jet still dominates the channel flow. The trend was also found by **Florschuetz and Su (1985)**. Their data showed the *Nu* dependence on *Re* approaches a fully developed channel value for G_c/G_j values above 1.0 and 2.0, depending on *z/d*. Since crossflow has the strongest influence on the shape of the impingement zone, G_c/G_j was used as the correlating parameter for jet and crossflow areas. G_c/G_j for this application is defined as the average G_c/G_j between a location half a pitch upstream and half a pitch downstream of a particular jet row. This definition allows the jet flow expended upstream by the jet to be a crossflow influence on itself.

The data for *z/d* = 1 and average Re_j = 10,170 was analyzed and the following equation was developed for prediction of average *Nu* for a widely spaced inline array at *z/d* = 1.

$$\begin{aligned} Nu_{avg} &= Nu_{jet}\, A_{jet} + Nu_{crossflow}\, A_{crossflow} \\ &= (0.436\ Re_j^{0.52})\ (1-A_{crossflow}) \\ &\quad + (0.0141\ Re_j^{0.785})\left(0.895\left(\frac{G_c}{G_j}\right)^{0.0816}\right) \end{aligned} \tag{9.1}$$

Figure 9.41 shows the agreement of Equation 9.1 to the present data. Again, only the data for the lowest average Re_j tested was used to determine Equation 9.1. If one assumes, for a widely spaced jet array, the area of jet influence would be similar for other widely spaced array configurations, it would be possible to extrapolate this

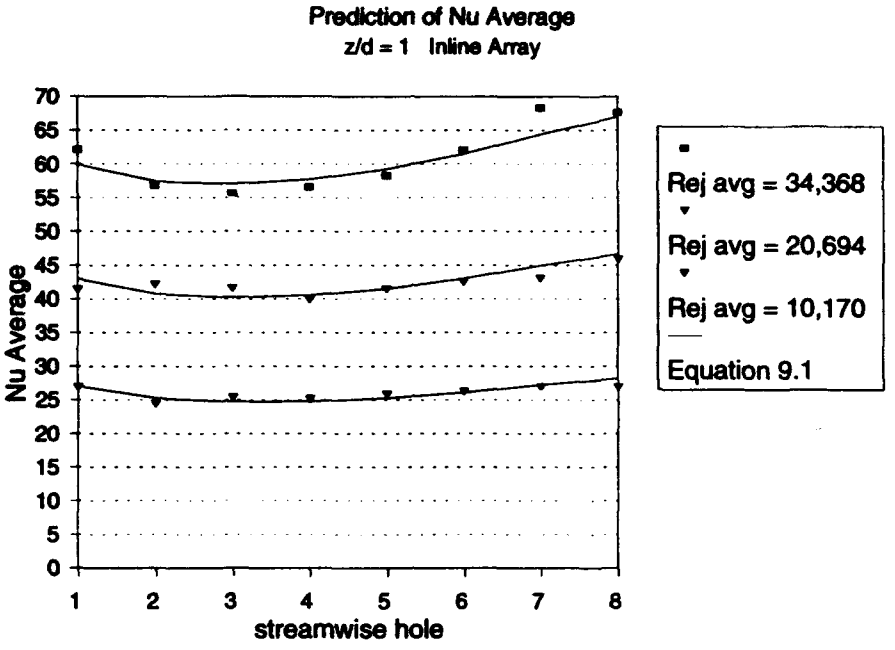

Figure 9.41 Prediction of average Nusselt number for all $z/d = 1$ inline arrays using Equation 9.1.

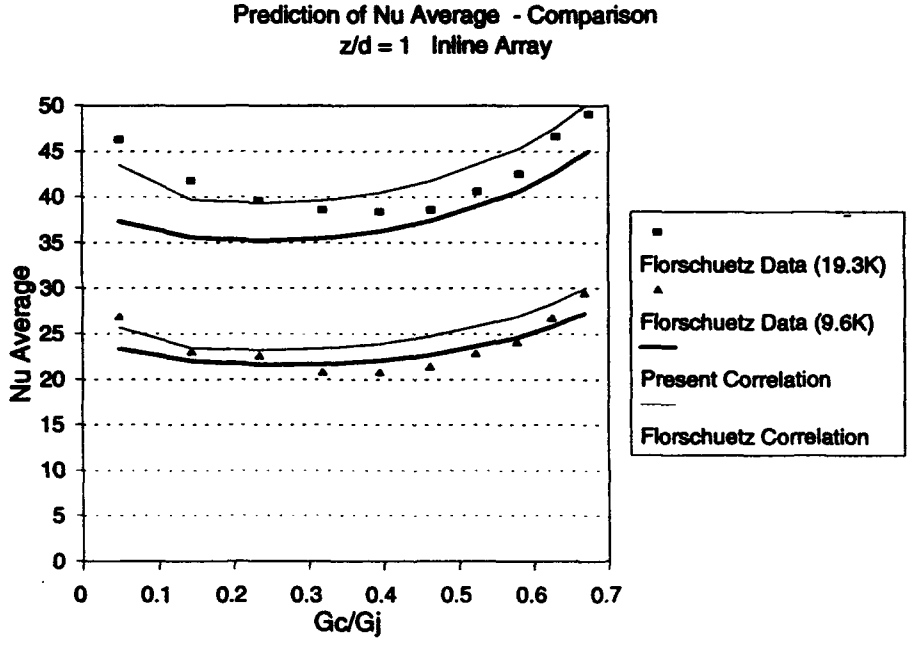

Figure 9.42 Comparison of average Nusselt number prediction to the data of **Florschuetz et al. (1980)** for an inline array with $z/d = 1$

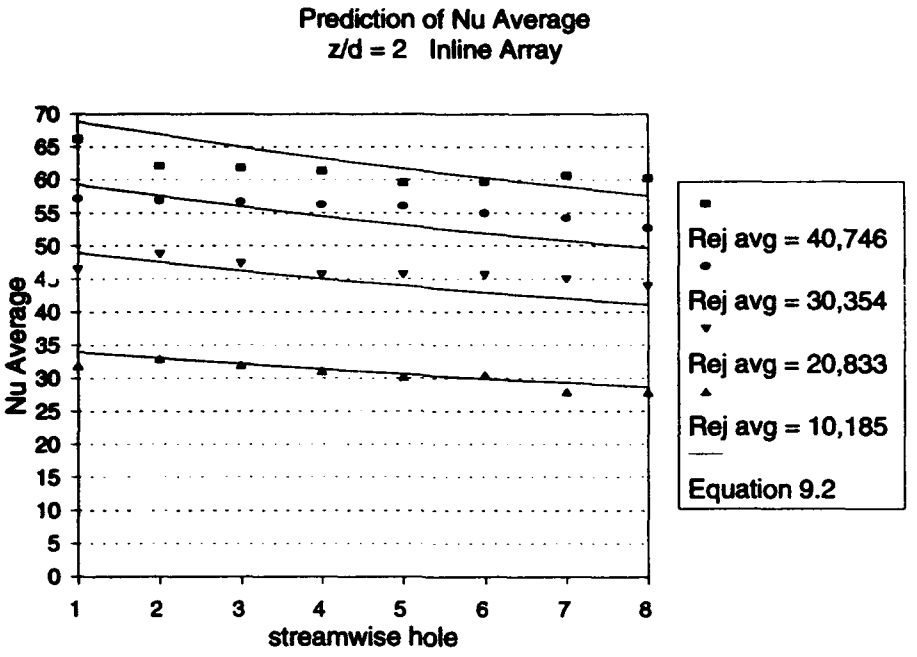

Figure 9.43 Prediction of average Nusselt number for all $z/d = 2$ inline arrays using Equation 9.2.

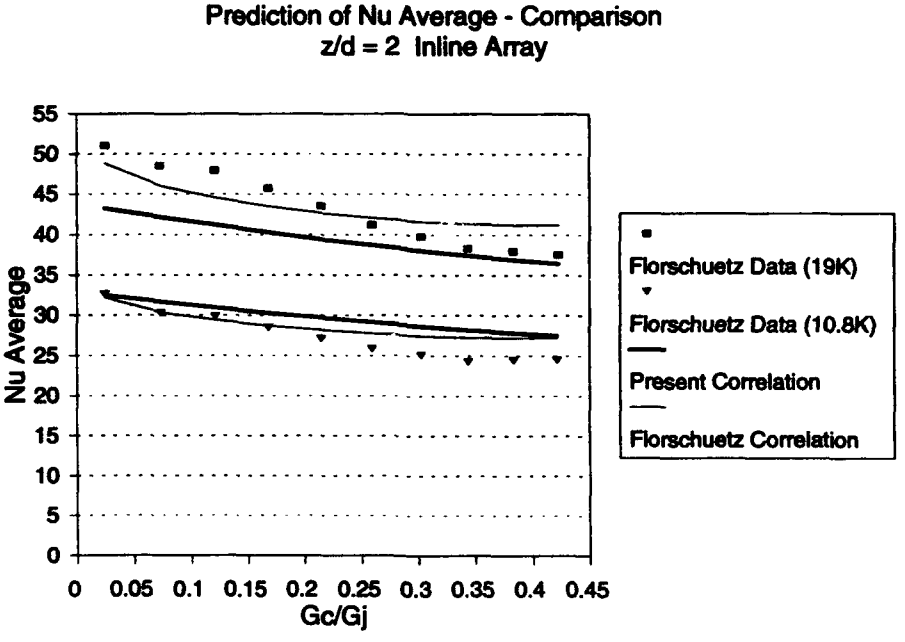

Figure 9.44 Comparison of average Nusselt number prediction to data from **Florschuetz et al. (1980)** for inline arrays with $z/d = 2$.

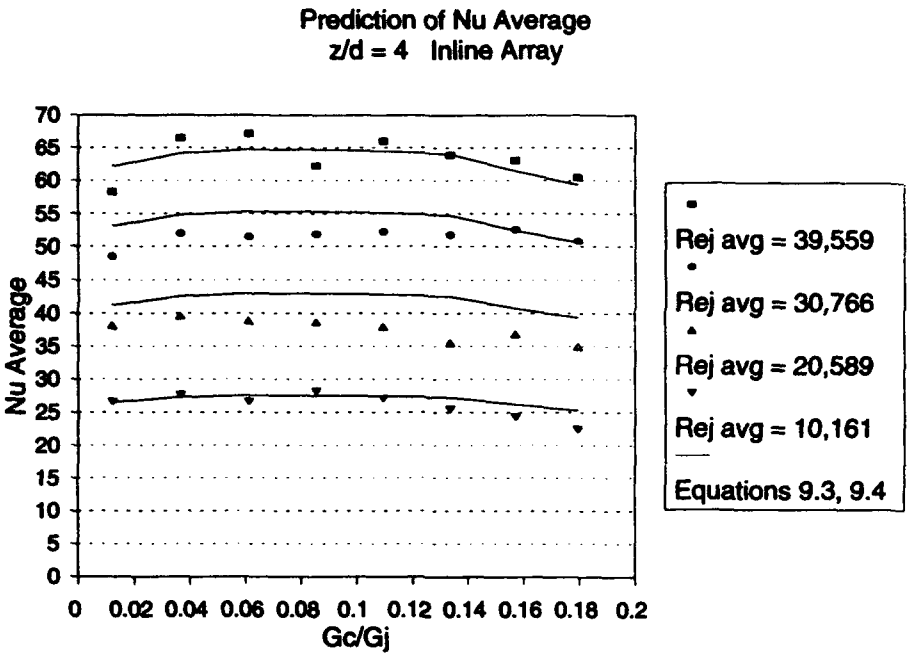

Figure 9.45 Prediction of average Nusselt number for all $z/d = 4$ inline arrays using Equations 9.3 and 9.4.

equation. This could be done by keeping the jet area of influence the same and increasing the crossflow area of influence appropriately. Values for jet and crossflow *Nu* would be sensibly the same. Figure 9.42 shows such an extrapolation to the data of **Florschuetz et al. (1980)**. They tested an array with a pitch of $.10d$ in the streamwise direction and $3d$ in the spanwise direction. As discussed in Section 9.1.2, data that does not account for the impingement plate temperature, such as **Florschuetz et al. (1980)**, would be correspondingly higher if the data were based on T_{aw}. The two methods of data collection are different however, the data trends and *Nu* levels are similar.

The present data for $z/d = 2$ and $Re_j = 10{,}185$ was used to produce Equation 9.2.

$$Nu_{avg} = (0.435\ Re_j^{0.515})\ (1-A_{crossflow}) + (0.233\ Re_j^{0.498})\left(0.551 + 0.781\left(\frac{G_c}{G_j}\right)\right) \quad (9.2)$$

The area dependence on G_c/G_j for this geometry is linear. Equation 9.2 is compared in Figure 9.43 to the current data with good agreement. An extrapolation to the **Florschuetz et al.** data is given in Figure 9.44. The agreement is also very good.

The $z/d = 4$ data was analyzed and found to contain two regions of interest. For $G_c/G_j < 0.12$ the average Nu increased and for $G_c/G_j > 0.12$ the average Nu decreased. Thus, the two regions were treated separately. The following correlation, using $Re_j = 10{,}161$ data only, predicted the experimental data for $G_c/G_j < 0.12$

$$Nu_{avg} = \left(75.823\left(\frac{G_c}{G_j}\right)^{0.117}\left(\frac{(Re_j)_{avg}}{10{,}161}\right)^{0.6}\right)(1-A_{crossflow}) + \left(26.157\left(\frac{G_c}{G_j}\right)^{0.0188}\left(\frac{(Re_j)_{avg}}{10{,}161}\right)^{0.6}\right)\left(0.881 + 0.438\left(\frac{G_c}{G_j}\right)\right) \quad (9.3)$$

and for $G_c/G_c > 0.12$

$$Nu_{avg} = \left(\left(85.949-232.081\frac{\frac{G_c}{G_j}}{\left(\frac{(Re_j)_{avg}}{10{,}161}\right)^{0.19}}\right)\left(\frac{(Re_j)_{avg}}{10{,}161}\right)^{0.6}\right)(1-A_{crossflow}) + \left(\left(30.4945-49.7615\frac{\frac{G_c}{G_j}}{\left(\frac{(Re_j)_{avg}}{10{,}161}\right)^{0.19}}\right)\left(\frac{(Re_j)_{avg}}{10{,}161}\right)^{0.6}\right)\left(0.8807+0.4381\frac{G_c}{G_j}\right) \quad (9.4)$$

The area relationship was again a linear dependence of G_c/G_j but, since the variation in *Nu* through the array is small, these values are scaled from the average Re_j = 10,161 case. Figure 9.45 shows the agreement of the data with Equations 9.3 and 9.4.

9.2 Staggered Array Data

9.2.1 Local Measurements

Staggered array local values of stagnation *Nu* and jet effectiveness are shown in Figures 9.46 to 9.53. At the first jet hole for all tests, the impingement zone is in fact circular showing little influence of crossflow at this location for the staggered array. Since the second jet row is offset half a pitch in the spanwise direction, all spent flow is channelled between adjacent jets and directed at the immediate downstream impingement area. A region of acceleration occurs between the jets which enhances heat transfer. Jets once again become limited in the upstream as well as the spanwise direction. For z/d = 1, Figures 9.46 and 9.48, local *Nu* increases in the channel as one moves through the array. This increase is not as pronounced as the inline case as the flow must change direction many times. A higher average Re_j causes an increase in *Nu*. Increasing z/d decreases the crossflow and causes the jets to be less distorted downstream.

9.2.2 Average Value Data

Average value data for the staggered array configuration is given in Figures

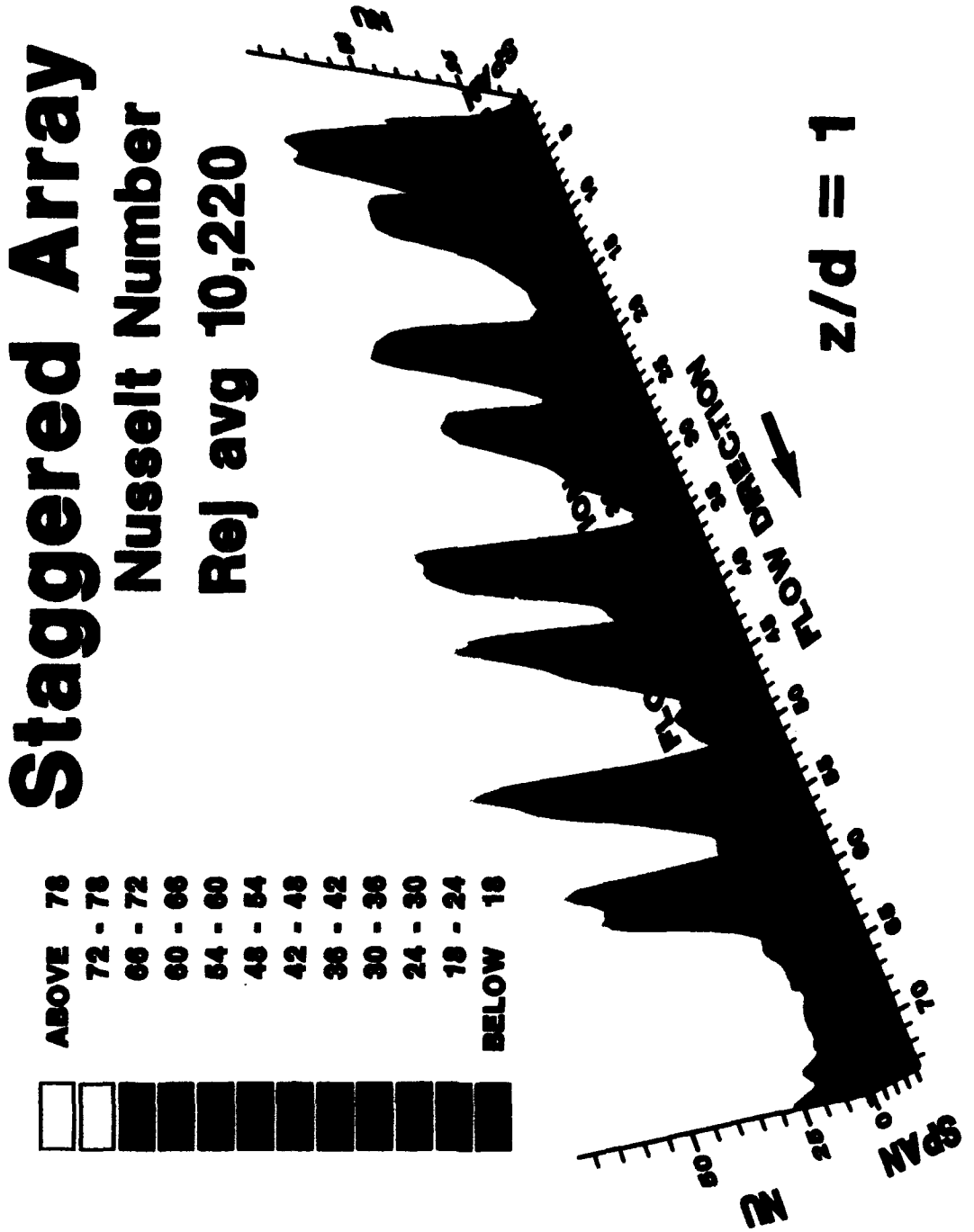

Figure 9.46 Staggered array Nusselt number distributions at all locations for Re_j avg = 10,220 and z/d = 1.

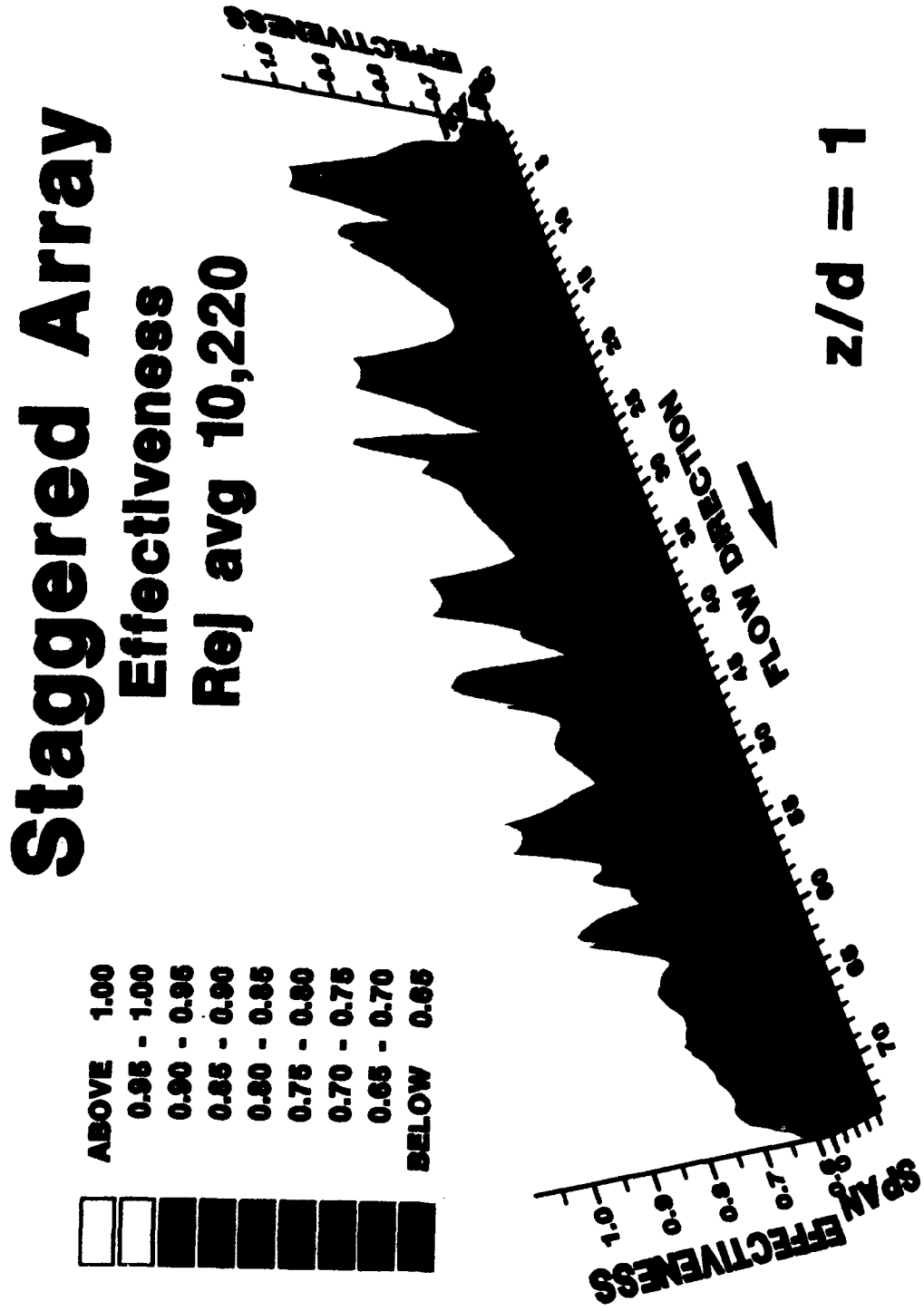

Figure 9.47 Staggered array jet effectiveness at all locations for Re_j avg = 10,220 and z/d = 1.

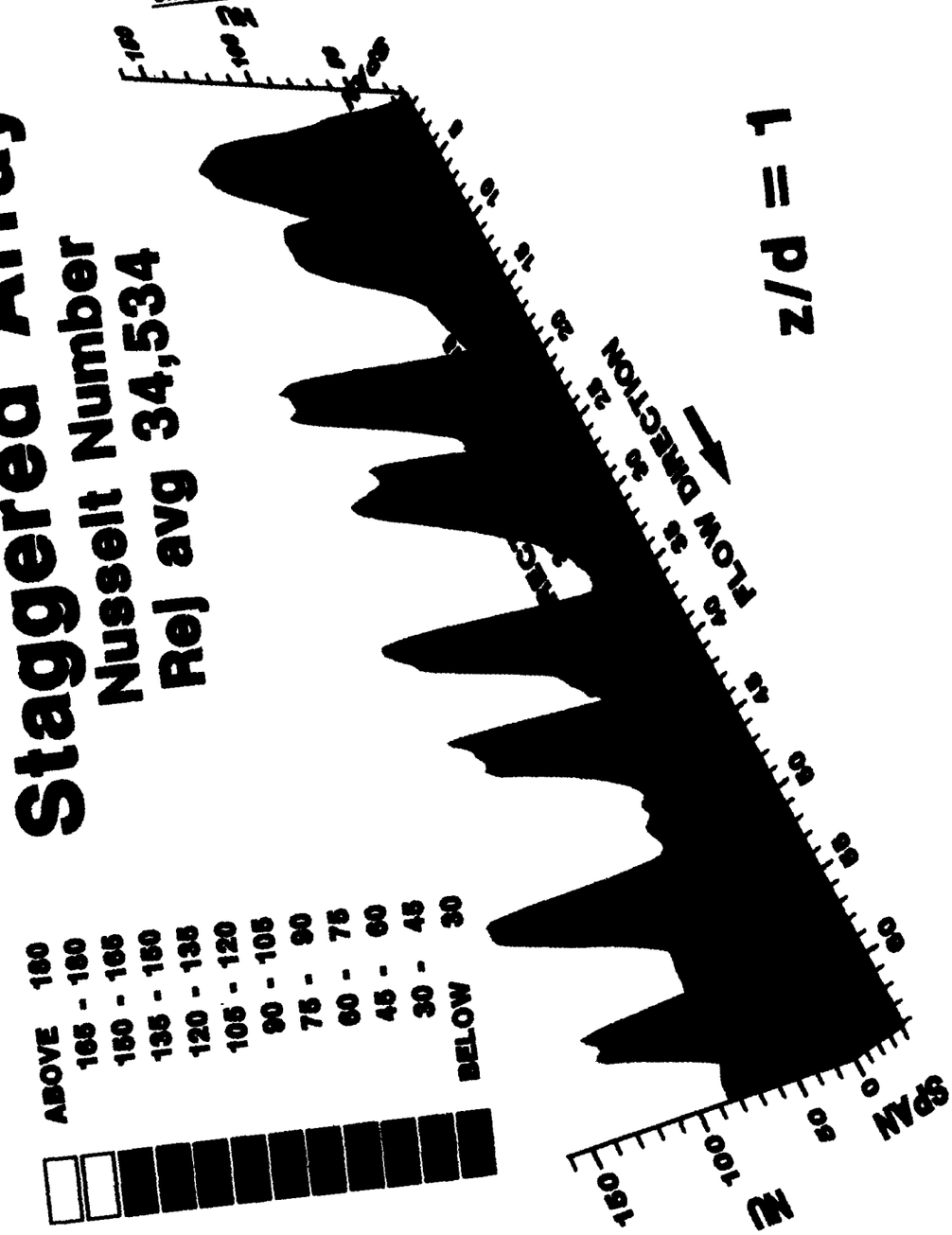

Figure 9.48 Staggered array Nusselt number distributions at all locations for Re_j avg = 34,534 and z/d = 1.

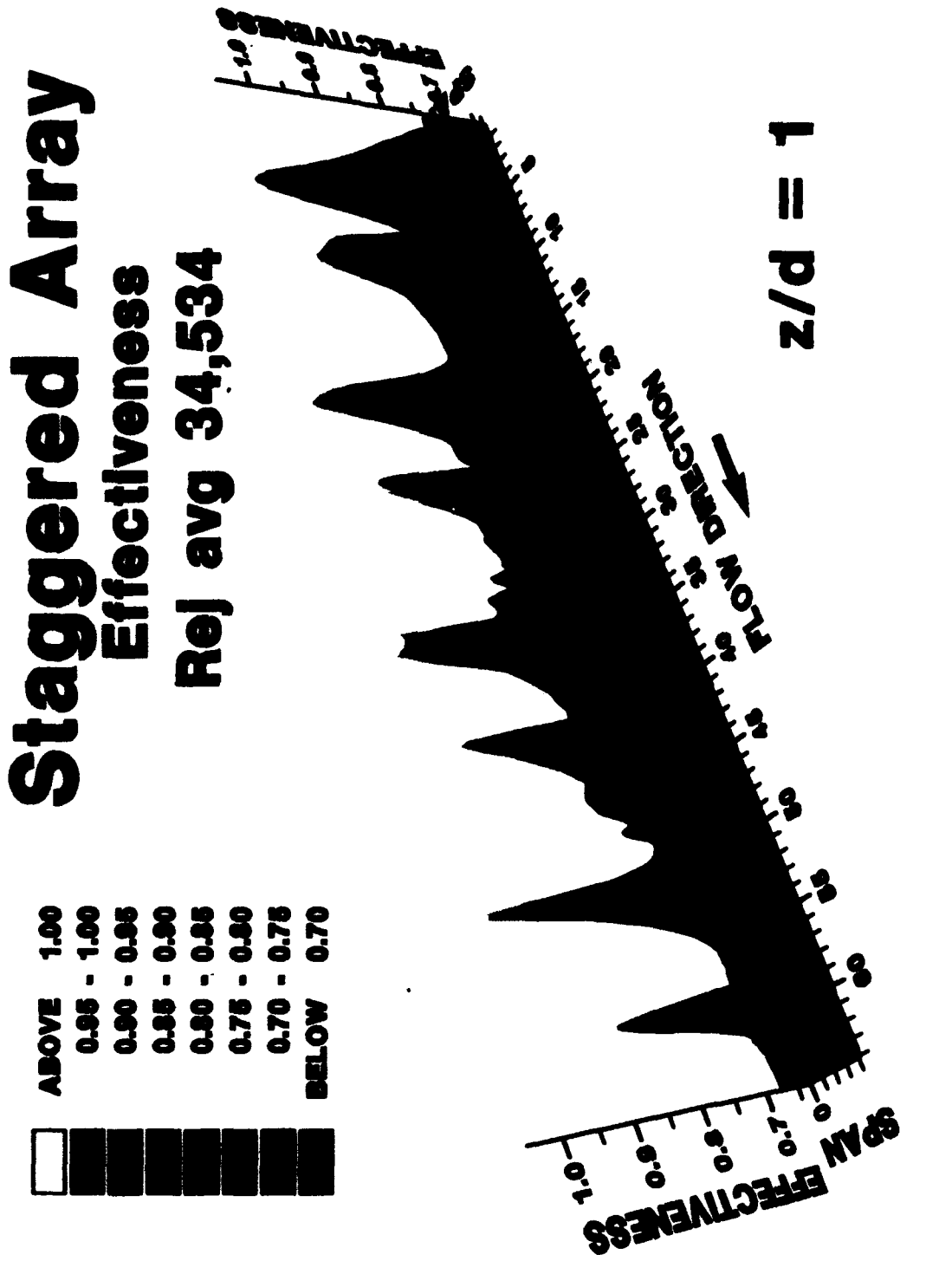

Figure 9.49 Staggered array jet effectiveness at all locations for Re_j avg = 34,534 and z/d = 1.

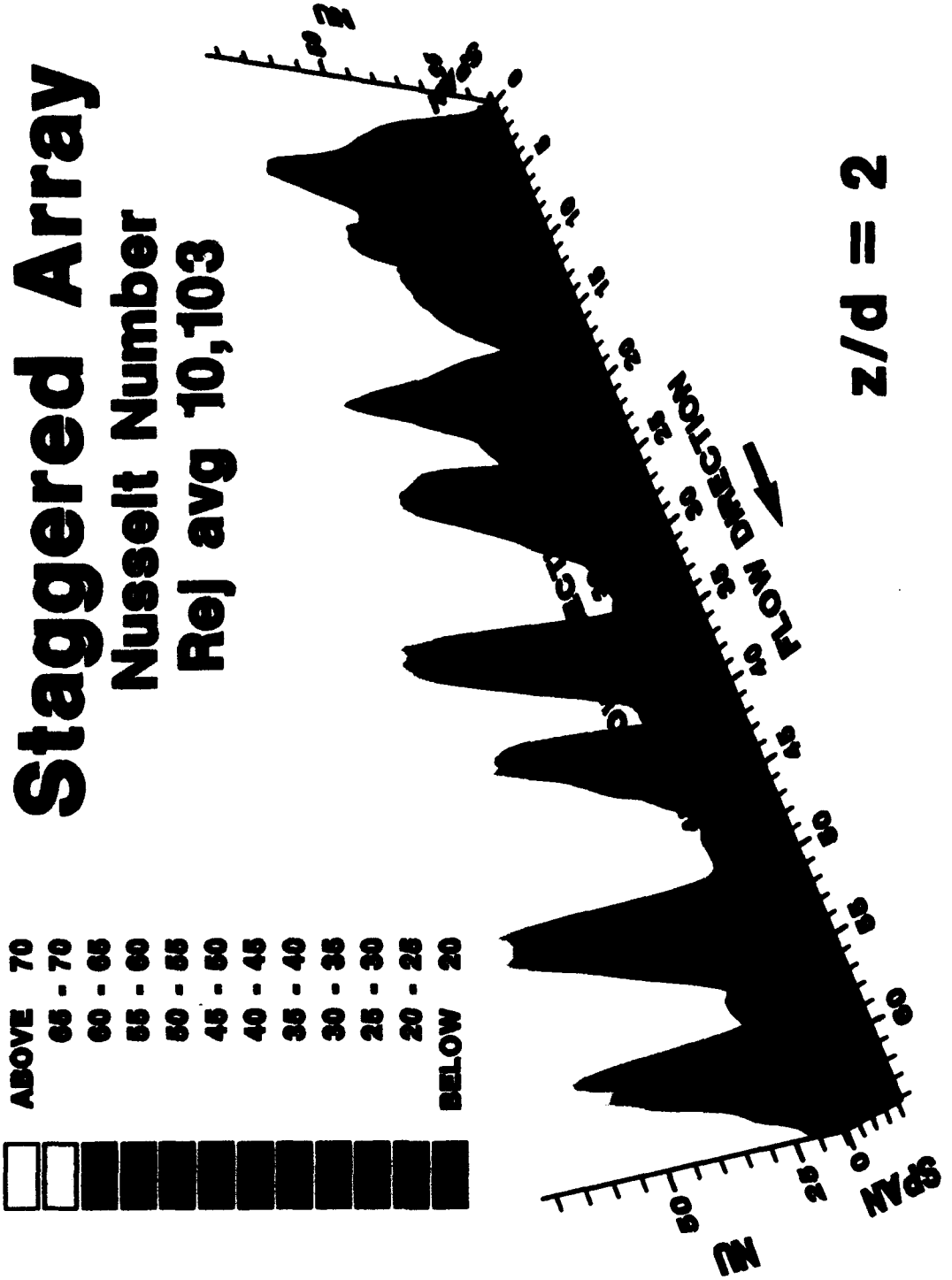

Figure 9.50 Staggered array Nusselt number distributions at all locations for Re_j avg = 10,103 and z/d = 2.

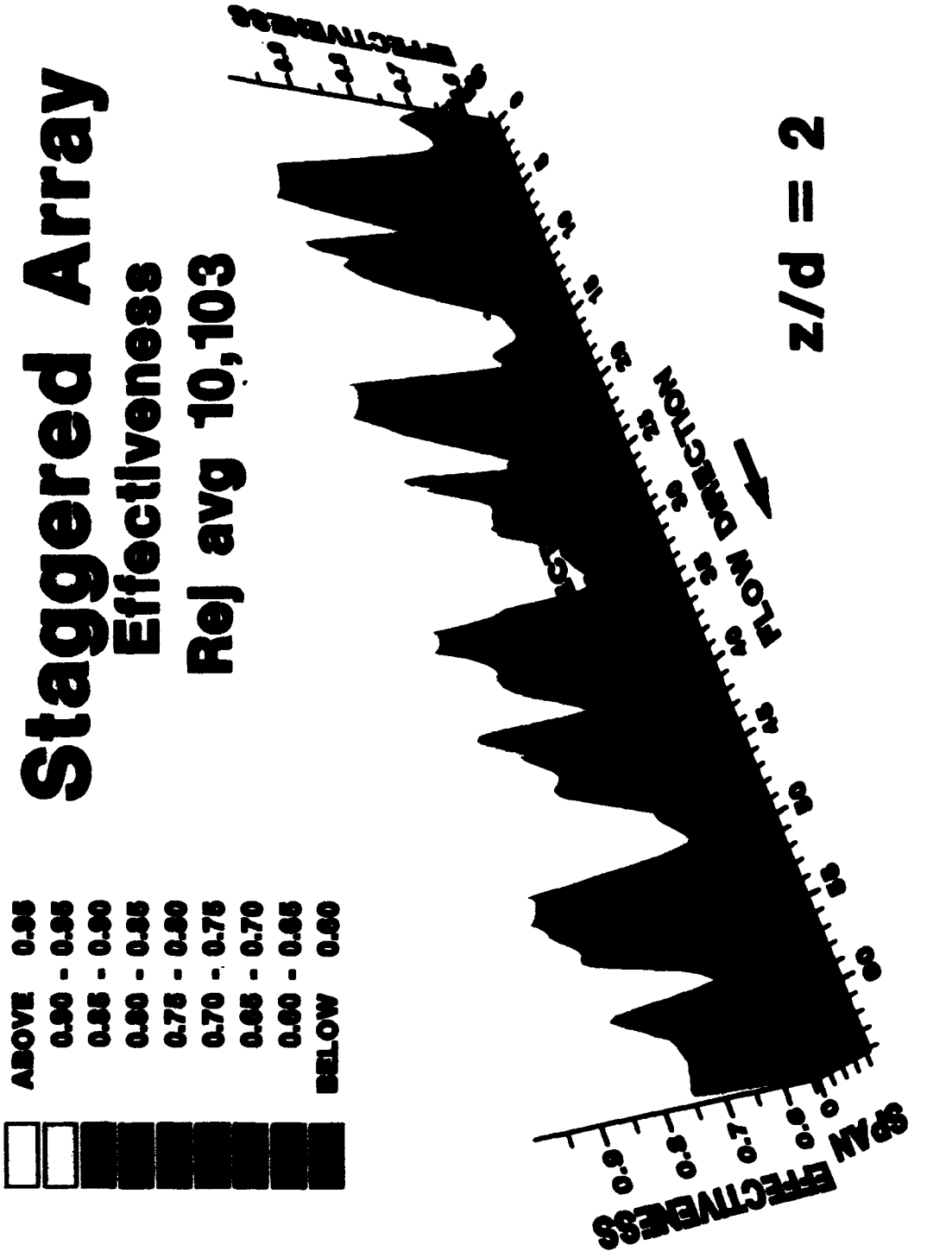

Figure 9.51 Staggered array jet effectiveness at all locations for Re_j avg = 10,103 and z/d = 2.

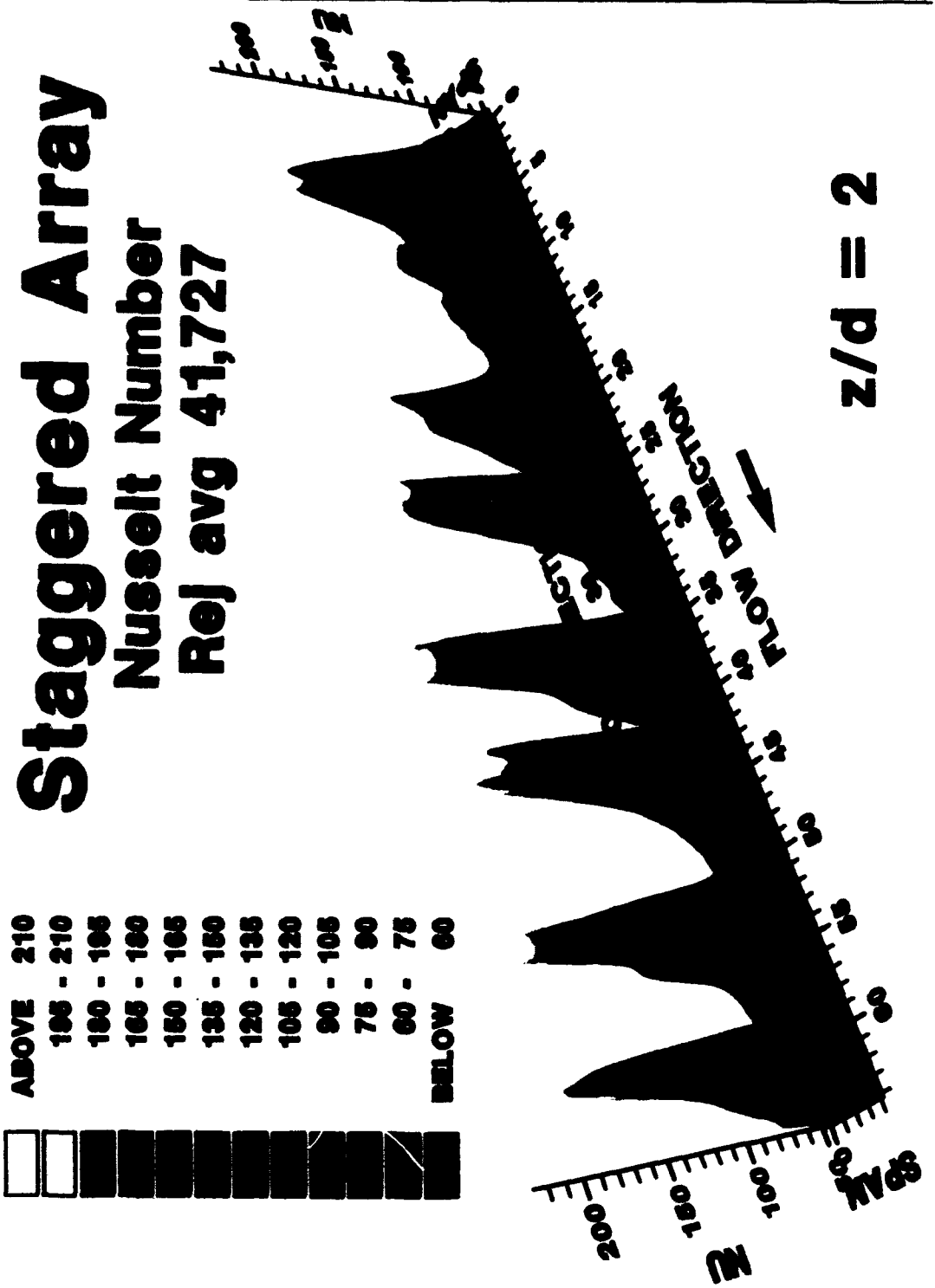

Figure 9.52 Staggered array Nusselt number distributions at all locations for Re_j avg = 41,727 and z/d = 2.

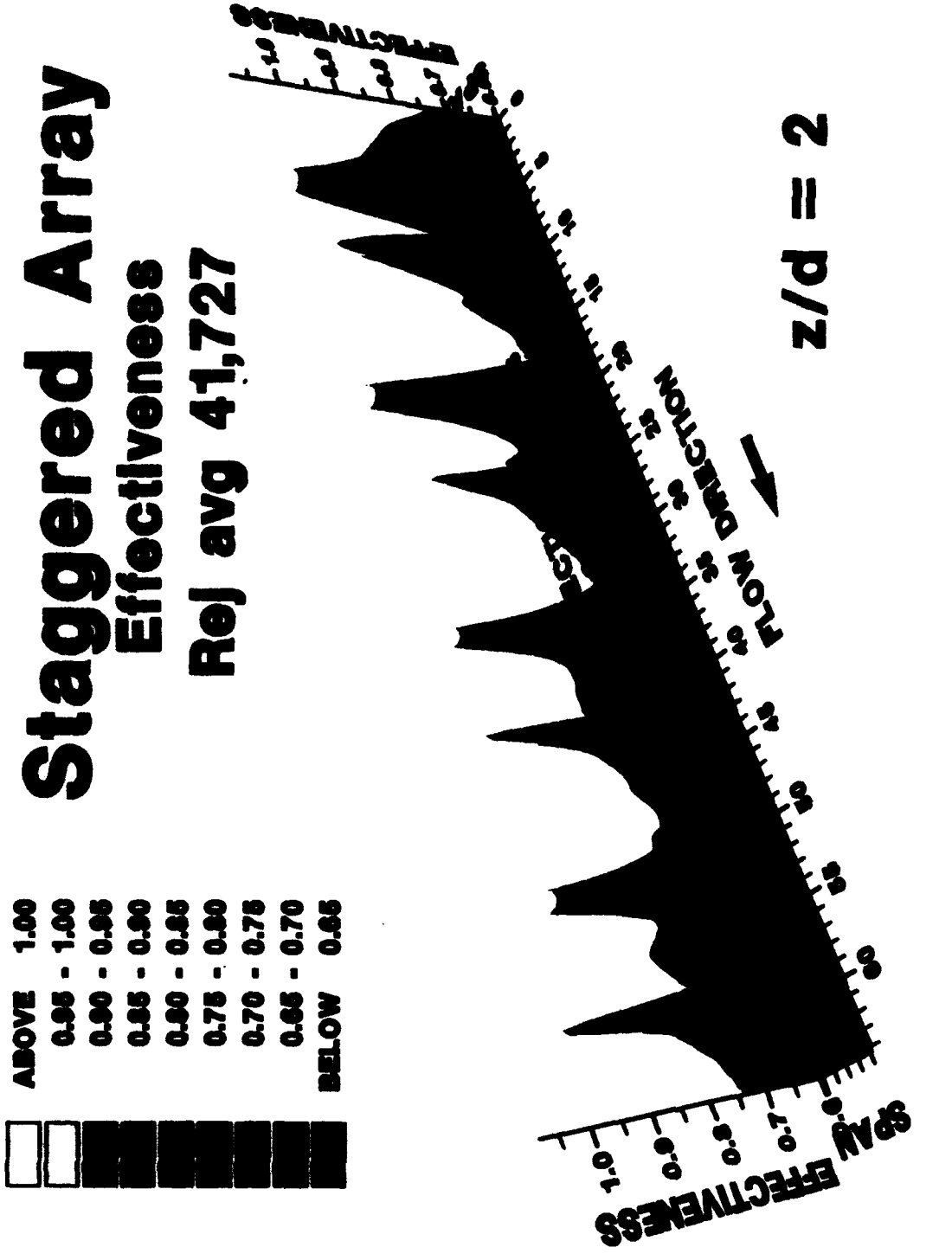

Figure 9.53 Staggered array jet effectiveness at all locations for Re_j avg = 41,727 and z/d = 2.

9.54 to 9.63. Figures 9.54 to 9.57 show average *Nu* and jet effectiveness as a function of average Re_j for the range of *z/d* tested. The average *Nu* for a *z/d* = 1, Figure 9.54, initially shows a decrease in heat transfer, similar to the inline *z/d* = 1 case, moving through the array to the fourth jet row. It then increases to a value equal to or greater than found at jet row one. Increasing average Re_j increases average *Nu* following a 0.7 power Re_j dependence for the first four streamwise jet rows and something closer to 0.8 for the last four streamwise jet holes. Jet effectiveness (Figure 9.55) for this configuration is essentially independent of average Re_j beginning at a value of 0.8 of the fourth jet row and then decreasing with array position due to crossflow. At *z/d* = 2 (Figure 9.56), the average *Nu* decreases slightly through the array showing a weaker influence of crossflow. Again average *Nu* scales with Re_j to the power of 0.7 initially. Jet effectiveness (Figure 9.57) starts at a value slightly lower than the *z/d* = 1 case and has a minimum at jet hole two. It then increases with distance through the array. Values of *Nu* for an average Re_j = 10,103 are slightly lower but all values are essentially the same in magnitude and form, having a minimum about 0.7 and increasing to 0.8 by the array exit. This would suggest less of an influence of the jet moving through the array similar to the *z/d* = 1 data at early streamwise locations in spite of a decrease in average heat transfer.

Figures 9.58 to 9.63 show average *Nu* and jet effectiveness as a function of *z/d* for the average Re_j tested. As in the inline case, the *z/d* = 2 data show a higher average *Nu* for a given average Re_j. The difference between the *z/d* = 2 and the *z/d* = 1 data is large initially and the two data lines gradually approach each other at the exit to the array. In all cases, jet effectiveness is initially lower for the *z/d* = 2 case

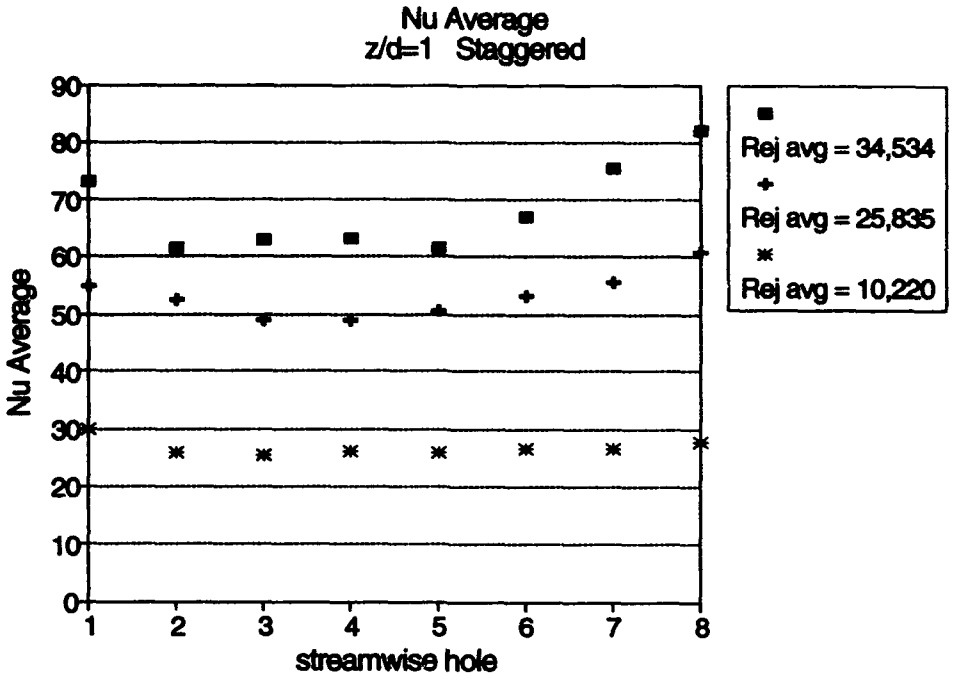

Figure 9.54 Average Nusselt number at streamwise jet locations for a staggered array at $z/d \approx 1$.

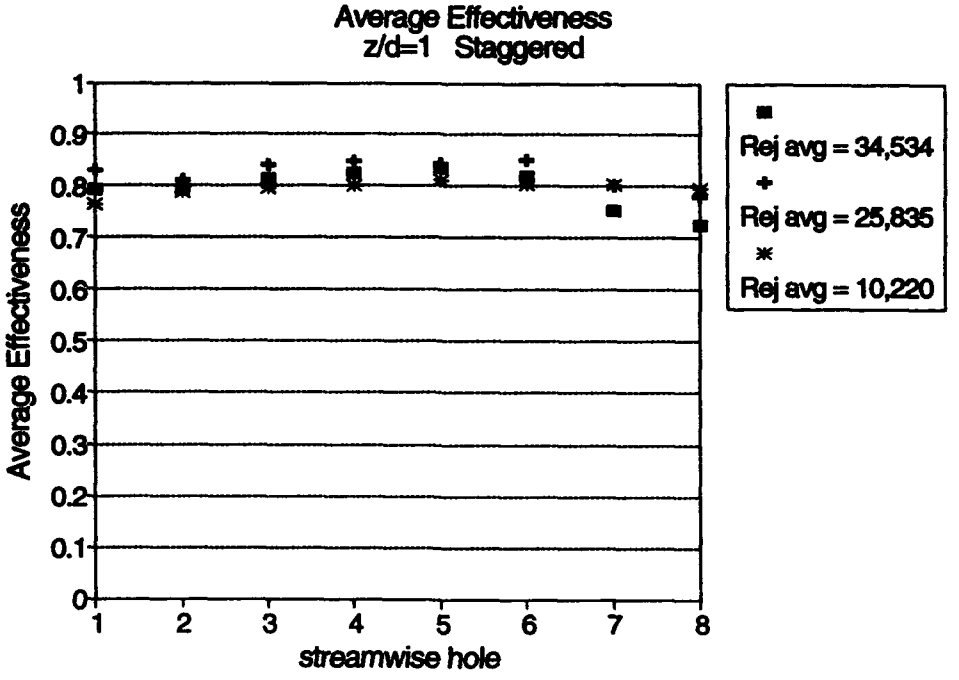

Figure 9.55 Average jet effectiveness at streamwise jet locations for a staggered array at $z/d = 1$.

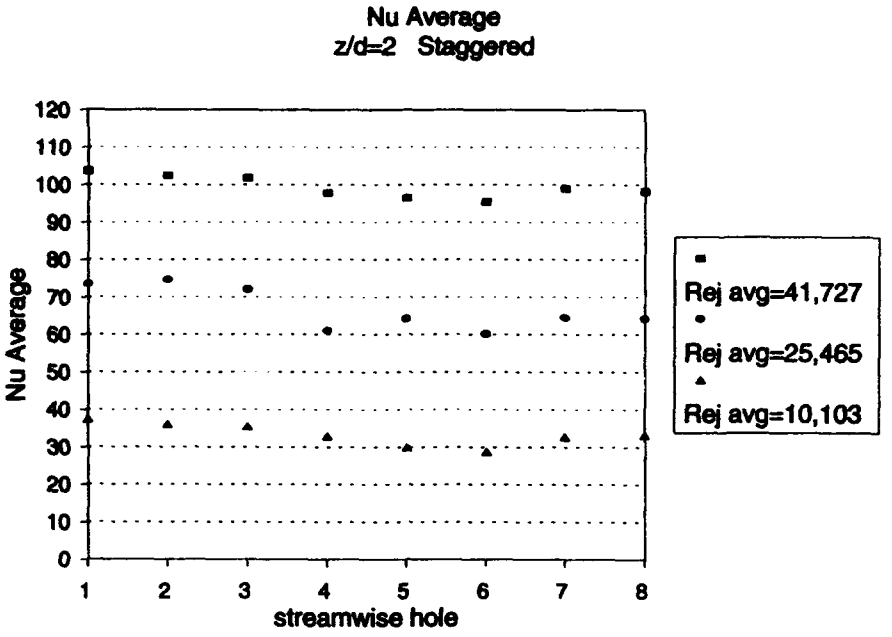

Figure 9.56 Average Nusselt number at streamwise jet locations for a staggered array with $z/d = 2$.

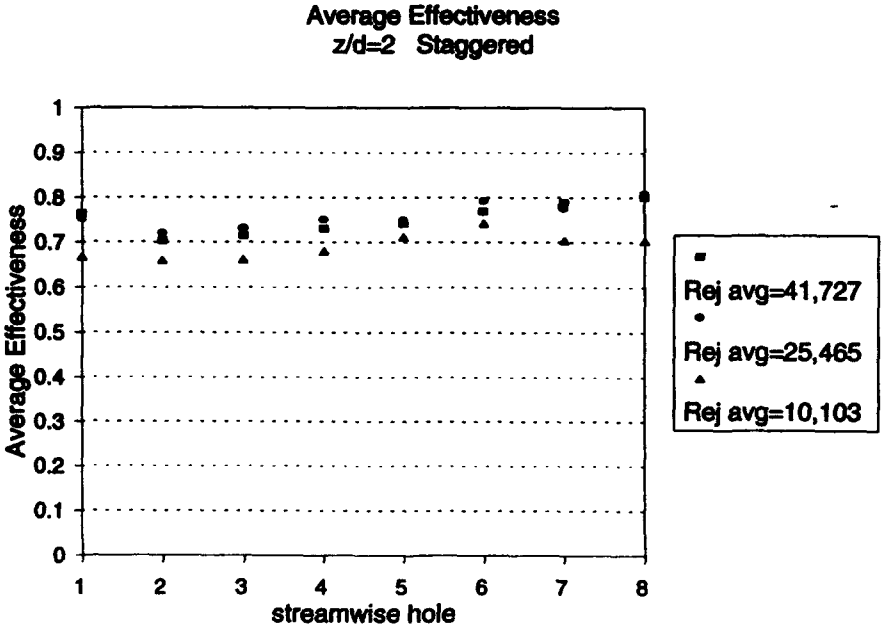

Figure 9.57 Average jet effectiveness at streamwise jet locations for a staggered array with $z/d = 2$.

with the two data lines gradually approach each other at the exit to the array. Figures 9.64 and 9.65 show comparisons with published data and correlations.

The same criteria as used in the inline case was used for determining the best fit to the staggered data. For the $z/d = 1$ case, analysis of the $Re_j = 10{,}220$ data led to the following equation.

$$Nu_{avg} = (0.00914\ Re_j^{0.934}) \left(0.168 \left(\frac{G_c}{G_j} \right)^{-0.348} \right) + (0.0447\ Re_j^{0.650}) \left(0.886 \left(\frac{G_c}{G_j} \right)^{0.154} \right) \tag{9.5}$$

A comparison with other $z/d = 1$ values for the range of Re_j tested is given in Figure 9.66 while a comparison with **Florschuetz et al. (1980)** is given in Figure 9.67. The extrapolation of the data to the **Florschuetz et al.** data is good.

The $z/d = 2$ and $Re_j = 10{,}103$ data was used to develop the following equation along the same guidelines previously discussed.

$$Nu = (0.0544\ Re_j^{0.737})(1 - A_{crossflow}) + (0.0332\ Re_j^{0.711}) \left(0.449 + 0.697 \left(\frac{G_c}{G_j} \right) \right) \tag{9.6}$$

The comparison of Equation 9.6 to the current data is shown in Figure 9.68 and the comparison with **Florschuetz et al. (1980)** is shown in Figure 9.69.

9.3 Comparison of Inline and Staggered Array Average Data

Figures 9.70 through 9.73 compare inline and staggered average Nu and jet effectiveness for the configurations and flow conditions tested. For $z/d = 1$ average

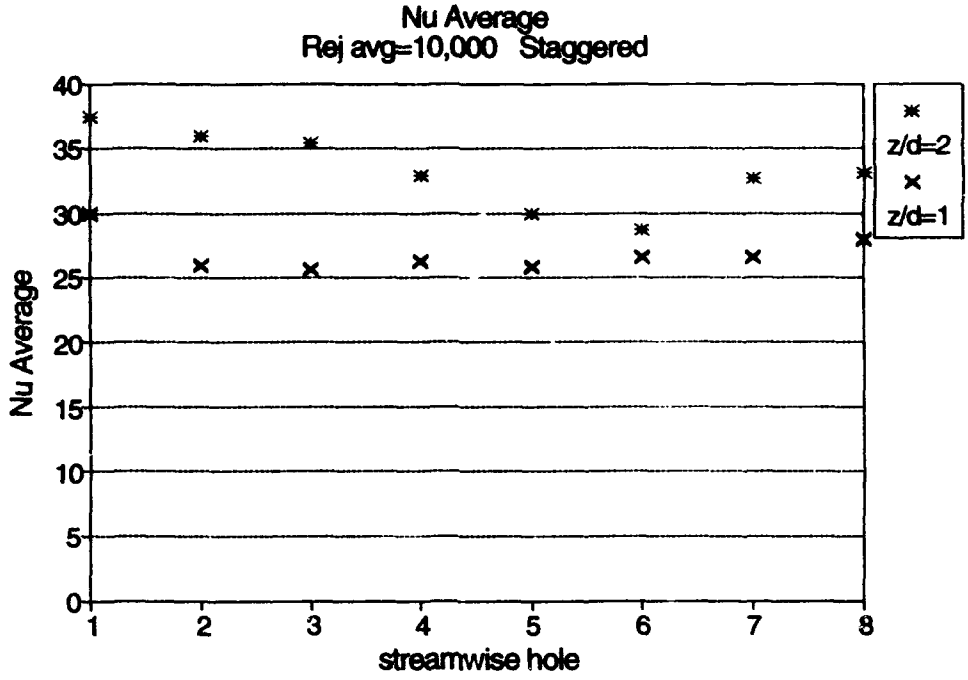

Figure 9.58 Average Nusselt number at streamwise jet locations for Re_j avg = 10,000 and z/d = 1 and 2.

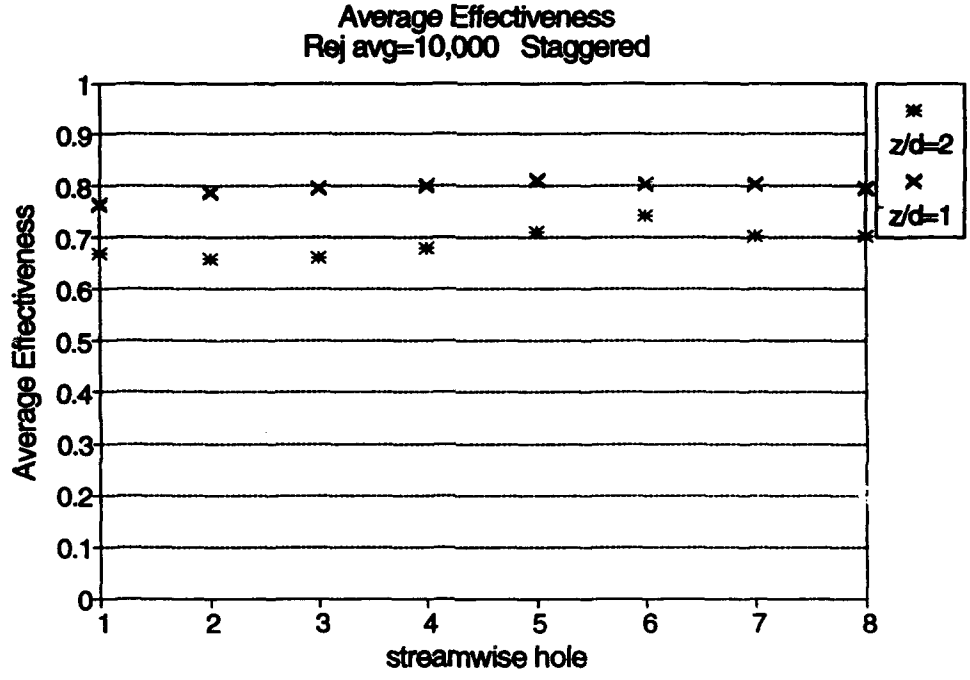

Figure 9.59 Average jet effectiveness for streamwise jet locations at Re_j avg = 10,000 and z/d = 1 and 2.

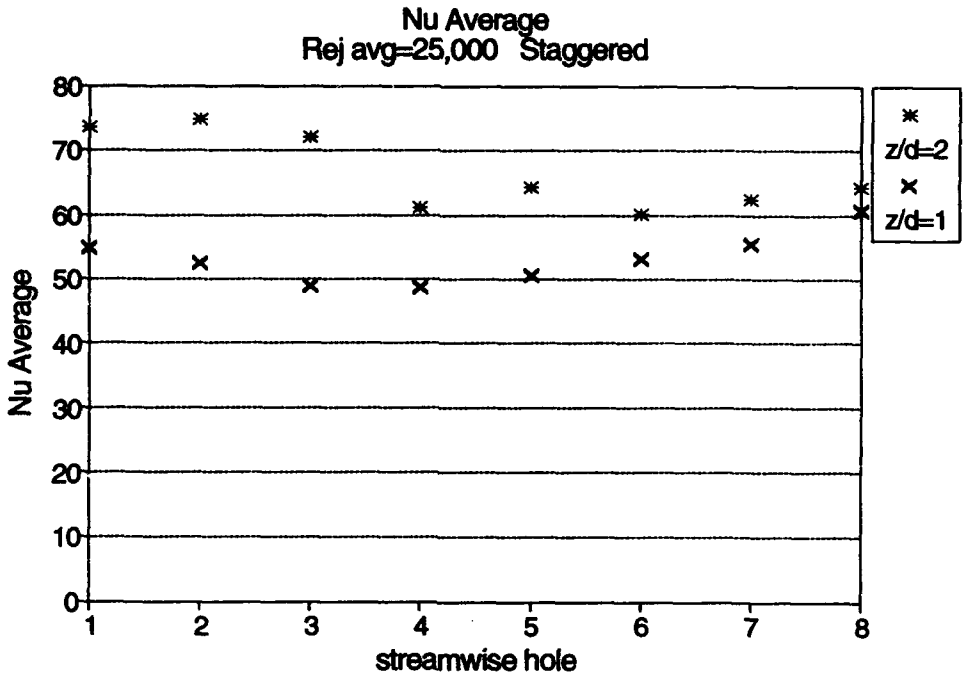

Figure 9.60 Average Nusselt number at streamwise jet locations for Re_j avg = 25,000 and z/d = 1 and 2.

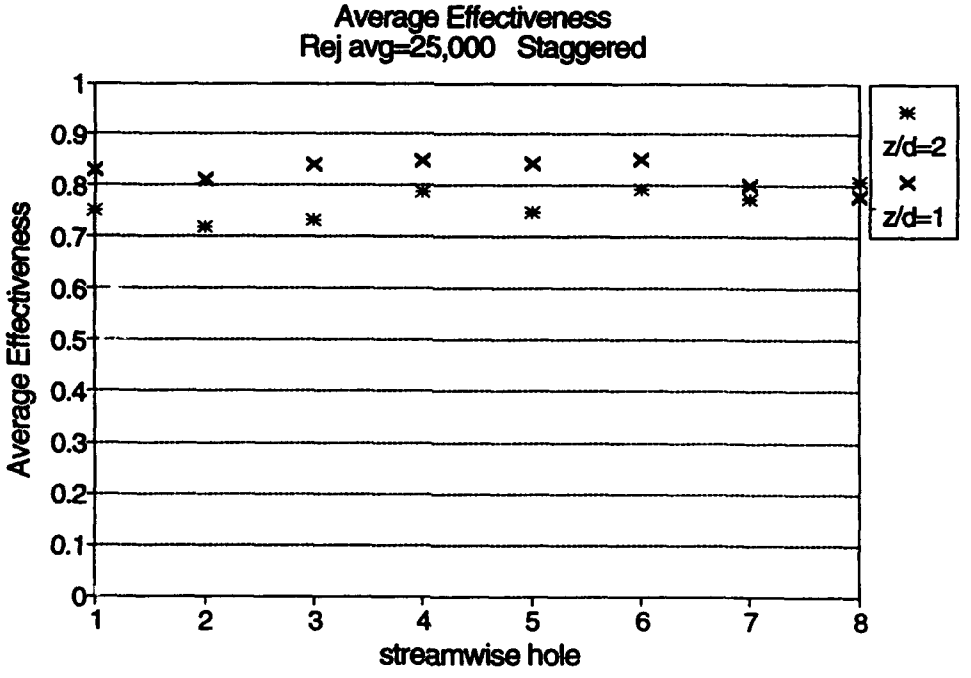

Figure 9.61 Average jet effectiveness for streamwise jet locations at Re_j avg = 25,000 and z/d = 1 and 2.

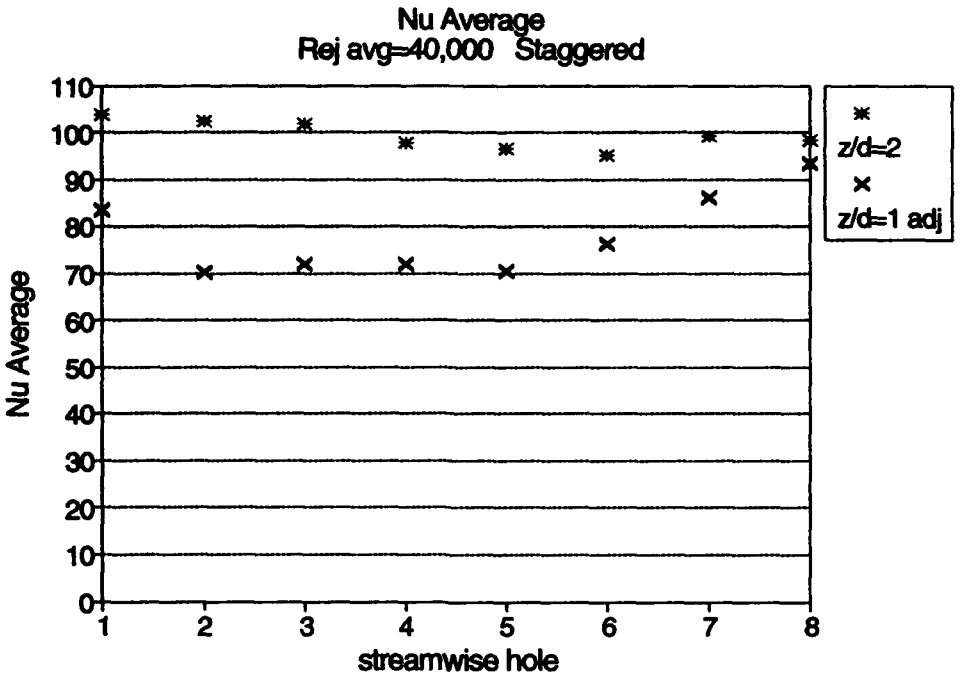

Figure 9.62 Average Nusselt number at streamwise jet locations for Re_j avg = 40,000 and z/d = 1 and 2.

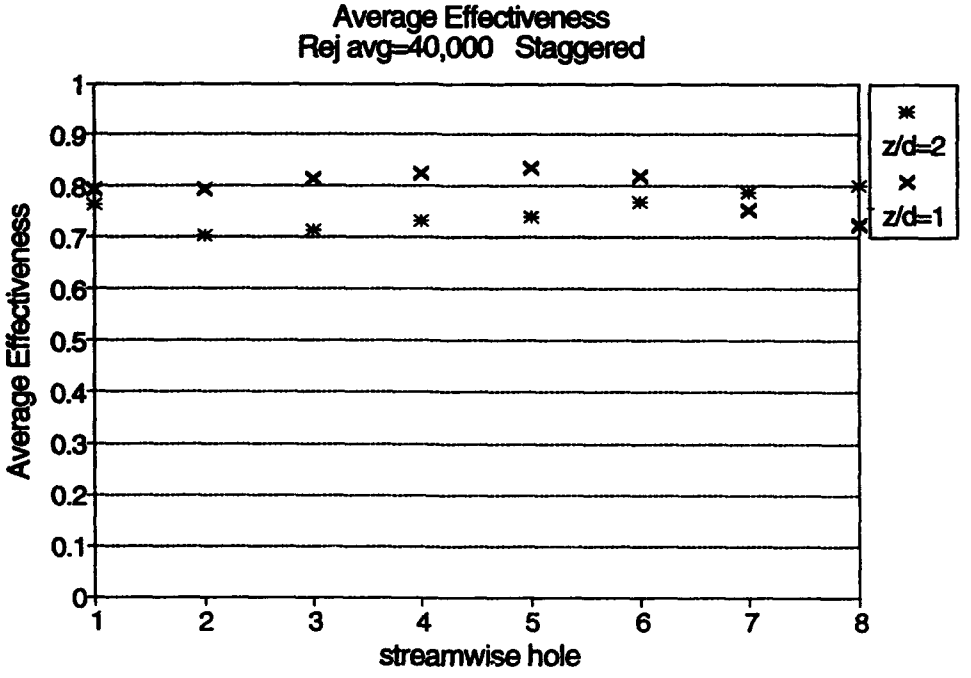

Figure 9.63 Average jet effectiveness at streamwise jet locations for Re_j avg = 40,000 and z/d = 1 and 2.

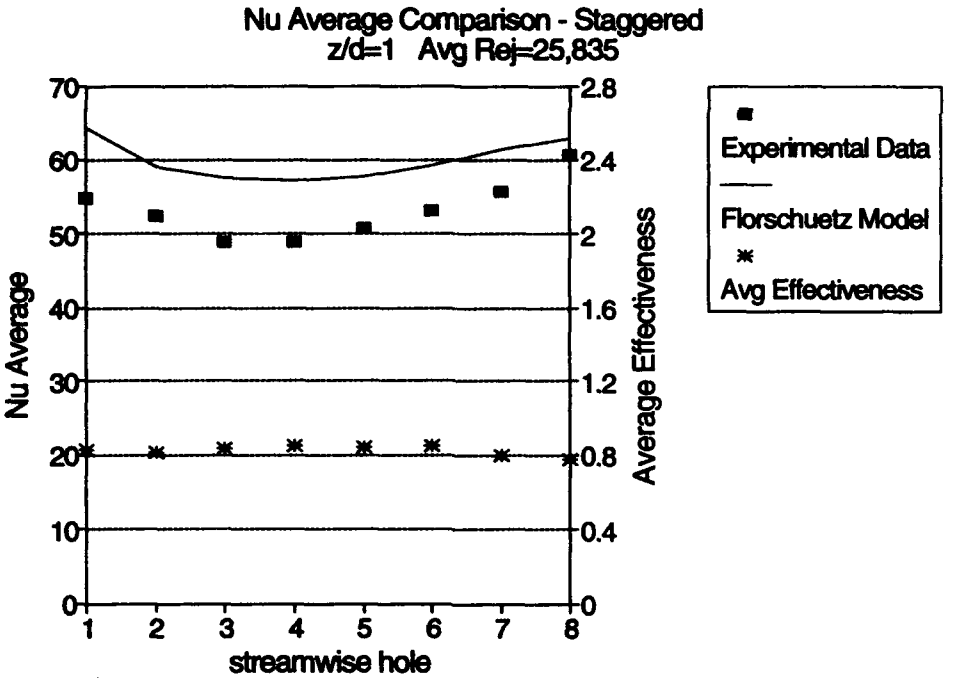

Figure 9.64 Comparison of average Nusselt number for a staggered array (Re_j avg = 25,835; z/d = 1).

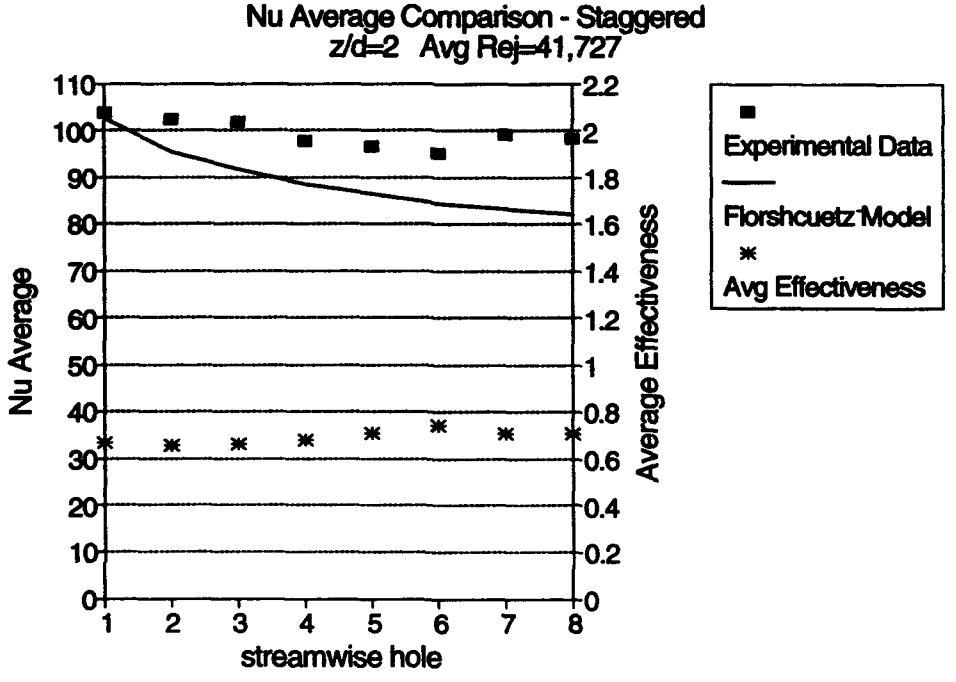

Figure 9.65 Comparison of average Nusselt number for a staggered array (Re_j avg = 41,727; z/d = 2).

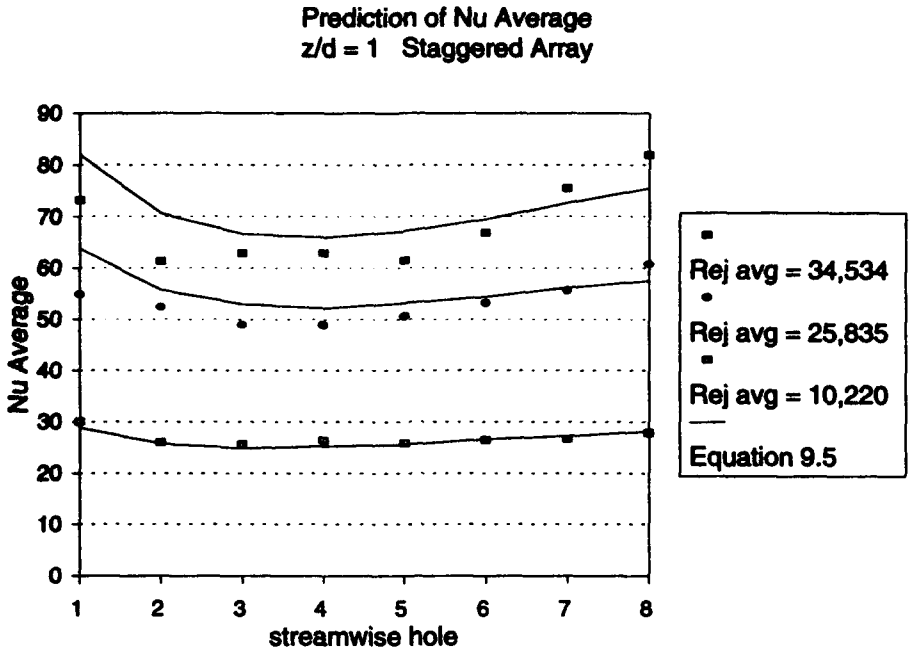

Figure 9.66 Prediction of average Nusselt number for all $z/d = 1$ staggered arrays using Equation 9.5.

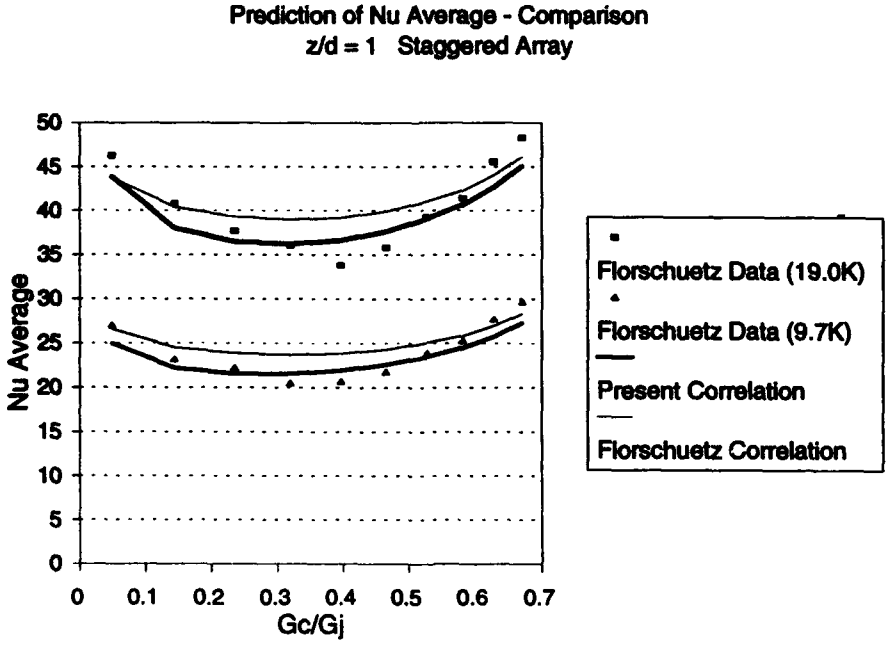

Figure 9.67 Comparison of prediction of average Nusselt number to data from **Florschuetz et al. (1980)** for a staggered array with $z/d = 1$.

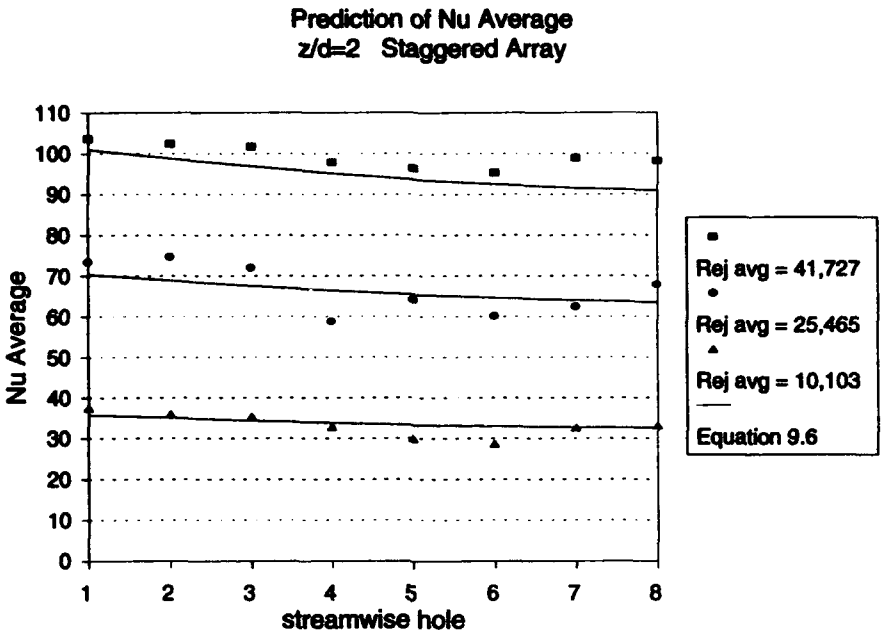

Figure 9.68 Prediction of average Nusselt number for all $z/d = 2$ staggered arrays using Equation 9.6.

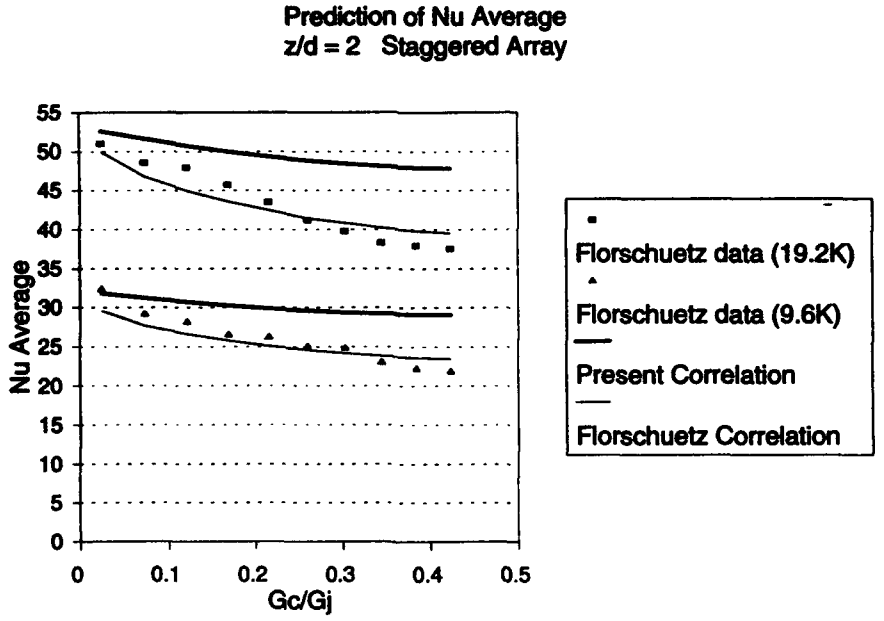

Figure 9.69 Comparison of prediction of average Nusselt number with data from **Florschuetz et al. (1980)** for a staggered array with $z/d = 2$.

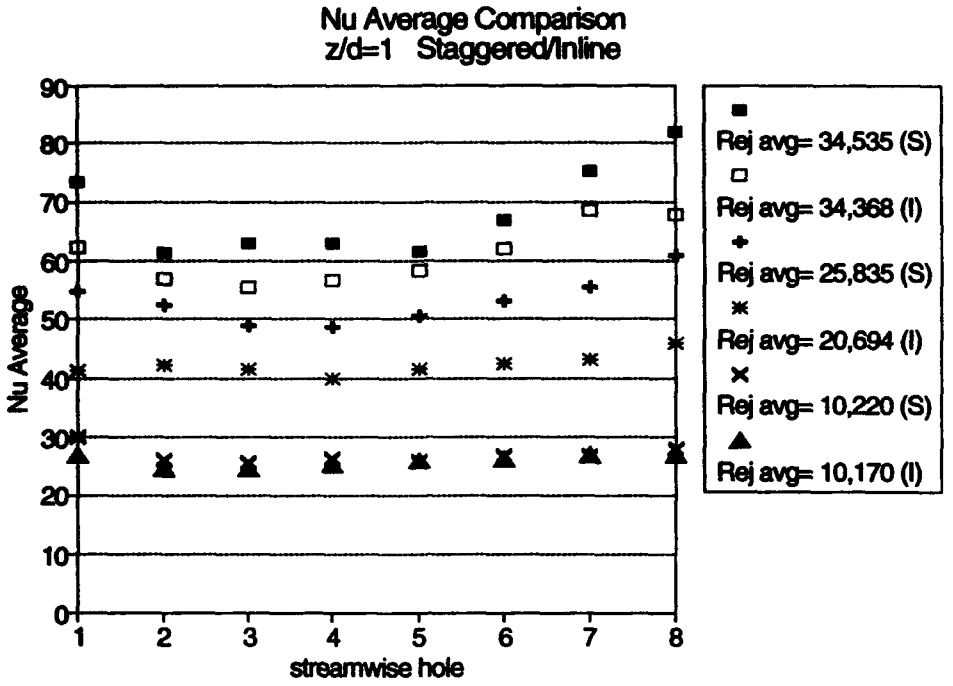

Figure 9.70 Comparison of average Nusselt number for staggered and inline arrays at $z/d = 1$.

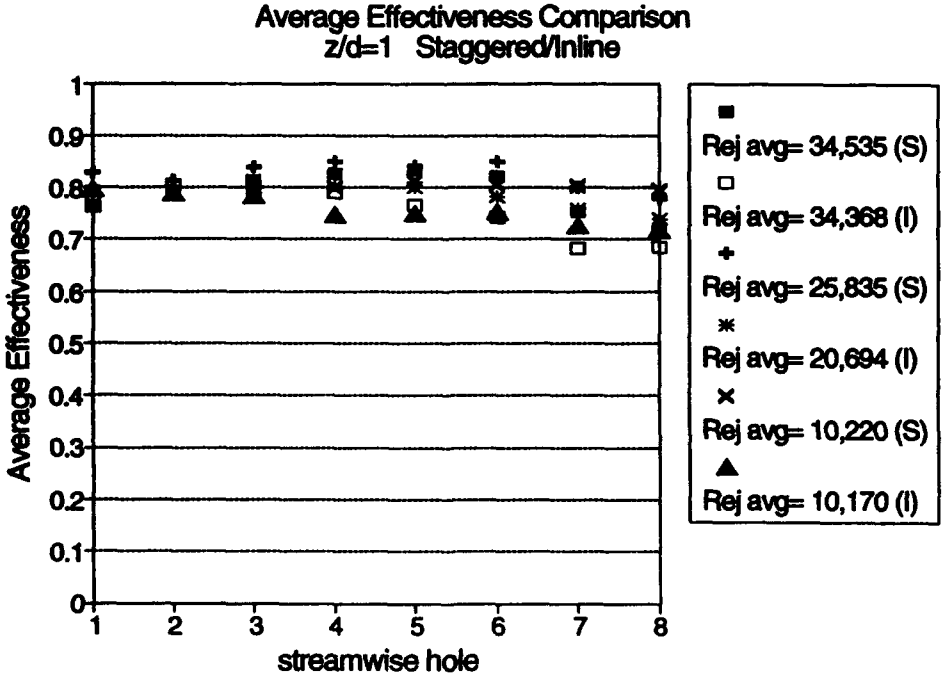

Figure 9.71 Comparison of average jet effectiveness for staggered and inline arrays at $z/d = 1$.

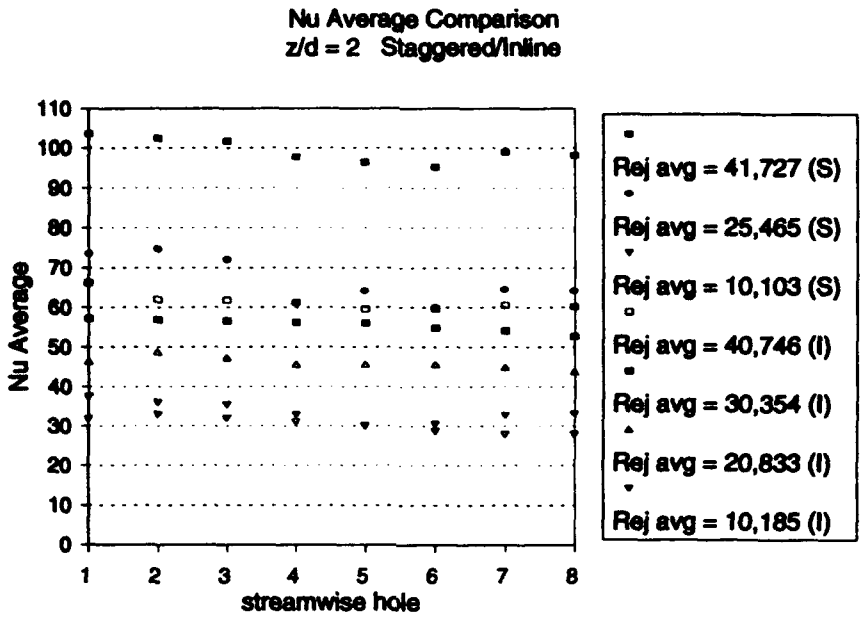

Figure 9.72 Comparison of average Nusselt number for staggered and inline arrays at $z/d = 2$.

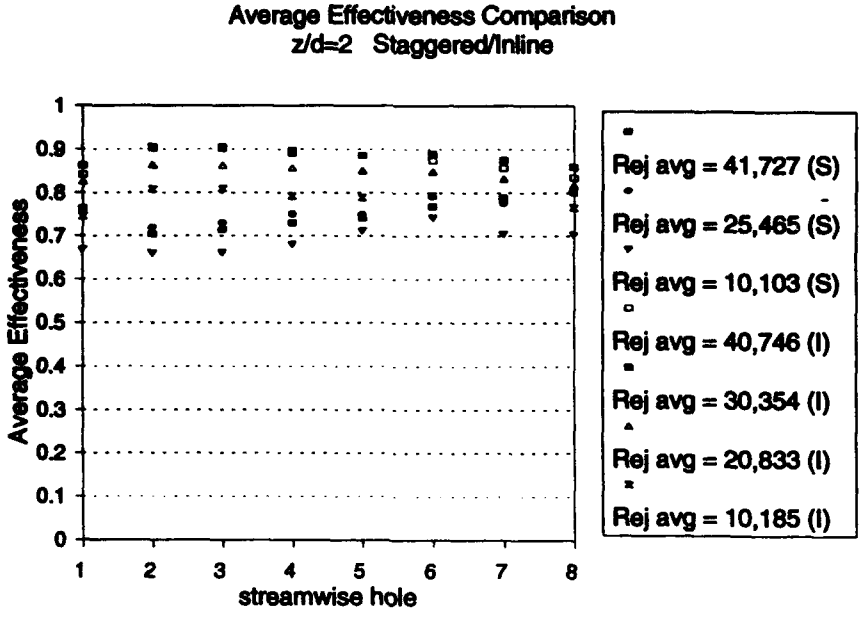

Figure 9.73 Comparison of average jet effectiveness for staggered and inline arrays at $z/d = 2$.

Nu values are higher for the staggered array for all flow conditions tested. Jet effectiveness starts with initially similar values with the staggered configuration being slightly higher on moving downstream through the array. For $z/d = 2$, average values of ***Nu*** are similar at low average Re_j with the difference increasing with increasing average Re_j. Correspondingly, jet effectiveness is lower for the inline case with the data approaching the same value at the array exit. The conclusion is for a given average Re_j choosing a z/d of 2 and staggered configuration would provide the greatest cooling value for the same amount of massflow.

CHAPTER 10 - CONCLUSIONS

This chapter summarizes the current work, highlighting some of the contributions to the understanding of arrays of impinging jets. The turbine blade designer will find the results of particular interest as both detailed distributions of heat transfer and average data are included. In addition, the transient techniques invented by the author to measure heat transfer coefficient and adiabatic wall temperature have far reaching applications to other experiments.

10.1 Contributions

For the first time, detailed measurements of heat transfer coefficient and adiabatic wall temperature have been determined under arrays of impinging jets. Also, the influence of the impingement plate on the cooling performance of arrays of jets has been quantified. The local adiabatic wall temperature follows naturally from the measurements as the driving temperature in the definition of heat transfer coefficient. This description of heat transfer to the target surface thus provides a much improved modelling of the process. Inspection of video tape colour change histories, discussed in Chapter 7, showed target surface heat transfer features which were quantified using the data reduction procedures outlined in Chapter 6. The surface features of a primary peak in heat transfer at $0.5d$ and a secondary peak between 1-$1.5d$ have been seen in jet arrays but previously had only been reported for isolated jets. The current experiments provide insight into the crossflow influence on the jet. This can significantly alter the jet structure at the target surface with corresponding changes in heat transfer. The detailed distribution of Nusselt number is important to the engine

designer and the current data constitutes a valuable resource. The local values are also able to be averaged providing data for comparison to other experiments. The conclusions from the present data are that, for a given air flow rate, of the configurations tested, a staggered configuration with a $z/d = 2$ provides not only the most uniform local heat transfer through the array, but a higher average Nu. The pressure drop through the $z/d = 2$ array is also less than for the $z/d = 1$ array.

Local stagnation point heat transfer under the arrays of jets has been investigated for the current sharp-edged jet hole configuration. Early in an array, the Nusselt number dependence on jet Reynolds number is 0.5, as one would expect in a laminar region. Examination of dust photographs along with target surface pressure information leads to the conclusion that the potential core strikes the target surface for the current type of jet holes up to a $z/d \approx 2$. This observation was also confirmed by observation of the video isotherms. Near the array exit, the Reynolds number dependence departs from the exponent of 0.5. Correlations are presented for stagnation point heat transfer for inline and staggered arrays with $z/d = 1$ or 2 which are valid when little or no crossflow is present.

The insight into flow structure is the basis for a series of average value correlations to predict the current data. By considering an area of influence of the jet and an area of influence of the crossflow, it is possible to determine average values over these areas and the variation of these parameters with crossflow. The analysis shows that use of the data for a low Re_j to build the correlations results in equations which apply to situations over the range of Re_j tested.

For the first time, the contribution of the impingement array plate on the heat transfer at the target surface has been measured. Recirculation regions present in the

arrays provide a mechanism which thermally couples the impingement plate to the target surface influencing the adiabatic wall temperature and hence local heat transfer. Throughout an array, the area influenced by the jet decreases and the contribution of the impingement plate becomes increasingly important to the overall heat transfer.

The development of the transient liquid crystal technique to encompass arrays of impinging jets demonstrates the versatility of the liquid crystal technique. Using at least two event times it is possible to determine both heat transfer and adiabatic wall temperature. A data processing procedure was developed using interactive spreadsheets and a graphics package which enabled detailed inspection of the detailed results found in this experiment possible. The peak intensity processing method is currently being used by other researchers. The hue temperature history method uses a unique regression routine which can automatically determine the adiabatic wall temperature and save processing time. This processing software developed by the author is also currently being used by other researchers. Not only did the author perfect the application of these processing methods, a careful comparison between stagnation point results obtained using both techniques has been made as reported in **Van Treuren at al. (1994)**. Wideband liquid crystal provides a nearly complete temperature history over the target surface which increases the accuracy of the data.

10.2 Recommendations for Future Work

The current work provides important insight into the thermal performance of arrays of widely spaced jets. It would be a natural extension of this work to analyze an array with closer jet hole spacing and compare the configurations. This could also

provide the basis for a correlation which could combine the two geometries and thus cover a wider range of engine representative situations. Also of interest would be the effect of initial crossflow on the jet array. Blade configurations exist where the leading edge impingement air flows back along the blade and causes a crossflow to be present at the beginning of an array of jets. It is suspected that this initial crossflow will decrease jet effectiveness and lower the heat transfer. With the current test facility it would also be possible to study the impinging jet array in conjunction with other turbine cooling methods, such as pedestals and film cooling holes, with the aim of optimizing such a configuration.

The current experiments with three different plate separations showed maximum heat transfer at a $z/d = 2$. The effect of plate spacing might be further investigated to determine whether the maximum in cooling performance occurs at a z/d between those tested.

LIST OF REFERENCES

1. Abdul Hussain, R. A. A., and Andrews, G. E., 1991, "Enhanced Full Coverage Impingement Heat Transfer with Obstacles in the Gap," *ASME Paper No. 91-GT-346.*

2. Abdul Hussain, R. A. A. and Andrews, G. E., 1990, "Full coverage Impingement Heat Transfer at High Temperatures," *ASME Paper No. 90-GT-228.*

3. AGARD Conference Proceedings 534, "Computational and Experimental Assessment of Jets in Crossflow," Papers presented and discussions recorded at the Fluid Dynamics Panel Symposium held in Winchester, United Kingdom From 19th-22nd April, 1993.

4. Andreopoulos, J., 1982, "Measurements in a Jet-Pipe Flow Issuing Perpendicularly Into a Cross Stream," *ASME Journal of Fluids Engineering*, Vol. 104, pp. 493-499.

5. Andrews, G. E., Gupta, M. L. and Mkpadi, M. C., 1984, "Combined Radiative and Convective Heat Transfer in an Enclosure," *1st UK National Conference on Heat Transfer (I.Chem.E.)*, Symp Series 86, pp. 979-988.

6. Andrews, G. E. and Hussain, C. I., 1984, "Impingement Cooling Using Large Arrays of Holes," *Proceedings 11th Annual Research Meeting (I.Chem.E.)*, pp. 86-91.

7. Andrews, G. E., Asere, A. A., Hussain, C. I., Mkpadi, M. C. and Nazadi, A., 1988, "Impingement/Effusion Cooling: Overall Wall Heat Transfer," *ASME Paper No. 88-GT-290.*

8. Andrews, G. E., Al Dabagh, A. M., Asere, A. A., Bazdidi-Tehrani, F., Mkpadi, M. C., and Nazari, A., 1992, "Impingement/Effusion Cooling," *AGARD CP-527*, Paper No. 30.

9. Andrews, G. E., Asere, A. A. and Mkpadi, M. C., 1984, "Transpiration and Full Coverage Discrete Hole Film Cooling," *11th Annual Research Meeting Proceedings (I.Chem.E)*, pp. 92-96.

10. Andrews, G. E. and Hussain, C. I., 1986, "Full Coverage Impingement Heat Transfer: The Influence of Channel Height," *8th International Heat Transfer Conference*, Hemisphere Pub. Corp., pp. 1205-1211.

11. Andrews, G. E. and Mkpadi, M. C., 1983, "Full coverage Discrete Hole Wall Cooling: Discharge Coefficients," *ASME Paper No. 83-GT-79.*

12. Andrews, G. E., Durance, J., Hussain, C. I. and Ojobor, S. N., 1987, "Full Coverage Impingement Heat Transfer: The Influence of the Number of Holes," *ASME Paper No. 87-GT-93.*

13. Andrews, G. E. and Hussain, C. I., 1987, "Full Coverage Impingement Heat Transfer: The Influence of Crossflow," *AIAA/SAE/ASME/ASEE 23rd Joint Propulsion Conference*, Paper No. AIAA-87-2010.

14. Andrews, G. E., Asere, A. A., Hussain, C. I. and Mkpadi, M. C., 1985, "Full Coverage Impingement Heat Transfer: The Variation in Pitch to Diameter Ratio at a Constant Gap," *AGARD Conference on Heat Transfer and Cooling in Gas Turbines*, CP390 Paper No. 26.

15. Andrews, G. E. and Hussain, C. I., 1984, "Full Coverage Impingement Heat Transfer: The Influence of Impingement Jet Size," *1st UK National Heat Transfer Conference (I.Chem.E)*, Symp. Series No. 86, pp. 1115-1124.

16. Baughn, J. W., and Shimizu, S., 1989, "Heat Transfer Measurements From a Surface with Uniform Heat Flux and an Impinging Jet," *ASME Journal of Heat Transfer*, Vol. 111, pp. 1096-1098.

17. Baughn, J. and Yan, X., 1991, "An Insertion Technique Using the Transient Method with Liquid Crystals for Heat Transfer Measurements in Ducts," *HTD Vol. 164*, The 28th National Heat Transfer Conference, ASME, Minneapolis, Minnesota, July 28-31, 1991.

18. Benedict, R. P., Wyler J. S., and Brandt, G. B., 1974, "The Effect of Edge Sharpness on the Discharge Coefficient of an Orifice," *ASME Paper No.* 74-WP/FM-4.

19. Bonett, P., 1989, "Applications of Liquid Crystals in Aerodynamic Testing," *D.Phil Thesis*, Department of Engineering Science, University of Oxford, England.

20. Borns, F. G., 1989, "Gas Turbine Engine Mechanical Design Considerations for Turbine Rotors," *Allied-Signal Aerospace Company Garrett Engine Division Presentation at the United States Air Force Academy.*

21. Bouchez, J. P. and Goldstein, R. J., 1975, "Impingement Cooling From A Circular Jet in a Cross Flow," *Int J Heat Mass Transfer*, Vol. 18, pp. 719-730.

22. Byerley, A. R., 1989, "Heat Transfer Near the Entrance to a Film Cooling Hole in a Gas Turbine Blade," *D.Phil Thesis*, Department of Engineering Science, University of Oxford, England.

23. Camci, C., Kim, K., and Hippensteele, S. A., 1992, "A New Hue Capturing Technique for the Quantitative Interpretation of Liquid Crystal Images Used

in Convective Heat Transfer Studies," *ASME Journal of Turbomachinery*, Vol. 114, pp 765-775.

24. Camci, C., and Kim, K., Hippensteele, S. A., and Poinsatte, P. E., 1993, "Evaluation of a Hue Capturing Based Transient Liquid Crystal Method for High Resolution Mapping of Convective Heat Transfer on Curved Surfaces," *ASME Journal of Heat Transfer*, Vol. 115, pp. 311-318.

25. Cataiano, G. D., Chang, K. S., and Mathis, J. A., 1989, "Investigation of Turbulent Jet Impingement in a Confined Crossflow," *AIAA Journal*, Vol. 27, No. 11, pp. 1530-1535.

26. Chance, J. L., 1974, "Experimental Investigation of Air Impingement Heat Transfer Under an Array of Round Jets," *Tappi*, Vol. 57, No. 6, pp. 108-112.

27. Chiu, S. H., Roth, K. R., Margason, R. J., and Tso, J., 1993, "A Numerical Investigation of a Subsonic Jet in a Crossflow," *AGARD CP-534*, Paper No. 22-1.

28. Claus, R. W., and Vanka, S. P., 1992, "Multigrid Calculation of a Jet in Crossflow," *AIAA Journal of Propulsion and Power*, Vol. 8, No. 2, pp. 425-431.

29. Clevenger, W. B., and Pickett, G. F., 1990, "Turbine Technology and Design," *Pratt & Whitney*, University of Tennessee Space Institute Short Course, April 23-27, 1990.

30. Collady, R. S., 1975, "Turbine Cooling," Turbine Design and Application, Vol 3, NASA SP-290.

31. Cooper, D., Jackson, D. C., Launder, B. E., and Liao, G. X., 1993, "Impinging Jet Studies for Turbulence Model Assessment-I. Flow-field Experiments," *Int. J. Heat Mass Transfer*, Vol. 36, No. 10, pp.2675-2684.

32. Cowie, W. D., "Engine Life Development Programs, ENSIP Damage Tolerant Designs," *United States Air Force Aeronautical Systems Division*, University of Tennesse Space Institute Short Course, April 23-27, 1990.

33. Crabb, D., Durao, D. F. G., and Whitelaw, J. H., 1981, "A Round Jet Normal to a Crossflow," *ASME Journal of Fluids Engineering*, Vol. 103, pp 142-153.

34. Craft, T. J., Grahm, L. J. W., and Launder, B. E., 1993, "Impinging Jet Studies For Turbulence Model Assessment-II. An Examination of the Performance of Four Turbulence Models," *Int. J. Heat Mass Transfer*, Vol. 36, No. 10, pp. 2685-2697.

35. Deckker, B. E. L. and Chang, V. F., 1965/66, "An Investigation of Steady

Compressible Flow Through Thick Orifices," *Proc. I. Mech. E.*, Vol. 180, Part 3J, pp. 312-323.

36. DeMeis, R., "Cutting with Sound," *Aerospace America*, Vol. 29, No. 9, pp. 64-65.

37. den Ouden, C., and Hoogendoorn, C. J., 1974, "Local Convective-Heat-Transfer Coefficients for Jets Impinging on a Plate: Experiments Using Liquid Crystal," *5th International Heat Transfer Conference.*

38. Dix, D. M. and Petty, J. S., 1990, "Aircraft Engine Technology Gets a Second Wind," *Aerospace America*, Vol. 28, No. 7, pp. 36-39.

39. Donaldson, C. D., Snedeker, R. S., and Margolis, D. P., 1971, "A Study of Free Jet Impingement. Part 2. Free Jet Turbulent Structure and Impingement Heat Transfer," *J. Fluid Mech.*, Vol. 45, Part 3, pp. 477-512.

40. Downs, S. J., and James, E. H., 1987, "Jet Impingement Heat Transfer - A Literature Survey," *National Heat Transfer Conference*, ASME Paper No. 87-HT-35.

41. Dunne, S. T., 1983, "A Study of Flow and Heat Transfer in Gas Turbine Blade Cooling Passages," *D.Phil Thesis*, Department of Engineering Science, University of Oxford, England.

42. Farina, D. J., Hacker, J. M., Moffat, R. J.,and Eaton, J. K., 1993, "Illuminant Invariant Calibration of Thermochromic Liquid Crystals," *ASME National Heat Transfer Conference,* Atlanta, GA, August 8-11.

43. Florscheutz, L. W., Metzger, D. E., Su, C. C., Isoda, Y. and Tseng, H. H., 1982, "Jet Array Impingement Flow Distributions and Heat Transfer Characteristics - Effects of Initial Crossflow and Nonuniform Array Geometry," *NASA Contractor Report 3630.*

44. Florscheutz, L. W., Metzger, D. E., and Truman, C. R., 1981, "Jet Array Impingement With Crossflow - Correlation of Streamwise Resolved Flow and Heat Transfer Distributions," *NASA Contractor Report 3373.*

45. Florschuetz, L. W. and Su, C. C., 1985, "Heat Transfer Characteristics Within an Array of Impinging Jets - Effects of Crossflow Temperature Relative to Jet Temperature," *NASA Contractor Report 3936.*

46. Florschuetz, L. W., Metzger, D. E., Takeuichi, D. I. and Berry, R. A., 1980, "Multiple Jet Impingement Heat Transfer Characteristic - Experimental Investigation of In-line and Staggered Arrays with Crossflow," *NASA Contractor Report 3217.*

47. Fox, M. D., Kurosaka, M., Hedges, L., and Hirano, K., 1993, "The Influence of Vortical Structures on the Thermal Fields of Jets," *J. Fluid Mech.*, Vol. 255, pp. 447-472.

48. Galant, S., and Martinez, G., 1982, "Cross Flow Influence Upon Impingement Convective Heat Transfer in Circular Arrays of Jets: A General Correlation," Seventh International Heat Transfer Conference, Vol. 3, pp 343-347.

49. Gardon, R. and Akfirat, J. C., 1965, "The Role of Turbulence in Determining the Heat-Transfer Characteristics of Impinging Jets," *Int J Heat Mass Transfer*, Vol. 8, pp. 1261-1272.

50. Gardon, R., and Akfirat, J. C., 1966, "Heat Transfer Characteristics of Impinging Two-Dimensional Air Jets," *ASME Journal of Heat Transfer*, pp. 101-108.

51. Gauntner, J. W., Gladden, H. J., Gauntner, D. J. and Yeh, F. C., 1974, "Crossflow Effects on Impingement Cooling of a Turbine Vane," *NASA TM X-3029.*

52. Goldstein, R. J. and Timmers, J. F., 1982, "Visualization of Heat Transfer From Arrays of Impinging Jets," *Int J. Heat Mass Transfer*, Vol. 25, No. 12, pp. 1857-1868.

53. Goldstein, R. J. and Franchett, M. E., 1988, "Heat Transfer From a Flat Surface to an Oblique Impinging Jet," *ASME Journal of Heat Transfer*, Vol. 110, pp. 84-90.

54. Goldstein, R. J., Sobolik, K. A. and Seol, W. S., 1990, "Effect of Entrainment on the Heat Transfer to a Heated Circular Air Jet Impinging on a Flat Surface," *ASME Journal of Heat Transfer*, Vol. 112, pp. 608-611.

55. Goldstein, R. J., Behabahani, A. I., and Heppelmann, K. K., 1986, "Streamwise Distribution of the Recovery Factor and the Local Heat Transfer Coefficient to an Impinging Circular Air Jet," *Int. J. Heat Mass Transfer*, Vol. 29., No. 8., pp. 1227-1235.

56. Goldstein, R. J. and Behbahani, A. I., 1982, "Impingement of a Circular Jet with and without Cross Flow," *Int. J. Heat Mass Transfer*, Vol. 25, No. 9, pp. 1377-1382.

57. Hay, N., Khaldi, A., and Lampard, D., 1987, "Effects of Crossflows on the Discharge Coefficients of Film Cooling Holes with Rounded Entries or Exits," *Proc. 2nd ASME-JSME Thermal Engineering Joint Conference*, Honolulu, HI, Vol. 3, pp. 369-374.

58. Hay, N., and Spencer, A., 1992, "Discharge Coefficients of Cooling Holes with

Radiused and Chamfered Inlets," *ASME Journal of Turbomachinery*, Vol. 114, pp. 701-706.

59. Hippensteele, S. A., Russell, L. M., and Stepka F. S., 1983, "Evaluation of a Method for Heat Transfer Measurements and Thermal Visualization Using a Composite of a Heater Element and Liquid Crystals," *ASME Journal of Turbomachinery*, Vol 105, pp. 184-189.

60. Ho, C., and Nosseir, N. S., 1981,"Dynamics of an Impinging jet. Part 1. The Feedback Phenomenon," *J. Fluid Mech.*, vol. 105, pp. 119-142.

61. Holland, M. J., and Thake, T. F., 1980, "Rotor Blade Cooling in High Pressure Turbines," *AIAA Journal of Aircraft*, Vol. 17, No. 6, pp. 412-418.

62. Hollworth, B. R., and Durbin, M., 1992, "Impingement Cooling of Electronics," *ASME Journal of Heat Transfer*, Vol. 114, pp. 607-613.

63. Hollworth, B. R., and Cole, G. H., 1987, "Heat Transfer to Arrays of Impinging Jets in a Crossflow," *ASME Journal of Turbomachinery*, Vol. 109, pp 564-571.

64. Hollworth, B. R., and Bowley, W. W., 1975,"Heat Transfer Characteristics of an Impinging Jet in a Crossflow," *ASME Paper No. 75-WA/HT-100.*

65. Hollworth, B. R., and Berry, R. D., 1978, "Heat Transfer From Arrays of Impinging Jets with Large Jet to Jet Spacing," *ASME Journal of Heat Transfer*, Vol. 100, pp. 352-357.

66. Huang, G. C., 1963, "Investigations of Heat-Transfer Coefficients for Air Flow Through Round Jets Impinging Normal to a Heat-Transfer Surface," *ASME Journal of Heat Transfer*, pp. 237-245.

67. Ireland, P. T., and Jones, T. V., 1985, "The Measurement of Local Heat Transfer Coefficient in Blade Cooling Geometries," *AGARD Conference on Heat Transfer and Cooling in Gas Turbines*, CP390 Paper No. 28.

68. Ireland, P. T., 1987, "Internal Cooling of Turbine Blades," *D.Phil Thesis*, Department of Engineering Science, University of Oxford, England.

69. Ireland, P. T. and Jones, T. V., 1987, "The Response time of a Surface Thermometer Employing Encapsulated Thermochromic Liquid Crystals," *J of Phys E: Sci Instrum 20.*

70. Ireland, P. T. and Jones, T. V., 1987, "Note on the Double Crystal Method of Measuring Heat Transfer Coefficient," *Oxford University Department of Engineering Science Report No. 1710/87.*

71. Jambunathan, K., Lai, E., Moss, M. A., and Button, B. L., 1992, "A Review of Heat Transfer Data for Single Circular Jet Impingement," *Int. J. Heat and Fluid Flow*, Vol. 13, No. 2, pp. 106-115.

72. Jones, T. V., 1991, "Definition of Heat Transfer Coefficients in the Turbine Situation," *IMechE Paper No. C423/046.*

73. Jones, T. V., and Hippensteele, S. A., 1987, "High-Resolution Heat Transfer Coefficient Maps Applicable to Compound Curve Surfaces Using Liquid Crystals In A Transient Wind Tunnel," *ASME Developments in Experimental Techniques in Heat Transfer and Combustion - HTD*, Vol. 71.

74. Kataoka, K., Mihata, I., Maruo, K., Suguro, M., and Chigusa, T., 1986, "Quasi-periodic Large-scale Structure Responsible for the Selective Enhancement of Impinging Jet Heat Transfer," Eighth International Heat Transfer Conference, Vol. 3, pp. 1193-1197.

75. Kays, W. M., and Crawford, M. E., Convective Heat and Mass Transfer, *McGraw-Hill Publishing Company*, Second Edition, New York, 1980.

76. Kercher, D. M., and Tabakoff, W., 1970, "Heat Transfer by a Square Array of Round Air Jets Impinging Perpendicular to a Flat Surface Including the Effect of Spent Air," *ASME Journal of Engineering for Power*, pp. 73-82.

77. Kim, S. W., and Benson, T. J., 1993, "Fluid Flow of a Row of Jets in Crossflow - A Numerical Study," *AIAA Journal*, Vol. 31, No. 5, pp. 806-811.

78. Kim, S. W., and Benson, T. J., 1992, "Calculation of a Circular Jet in Crossflow with a Multiple-Time-Scale Turbulence Model," *Int. J. Heat Mass Transfer*, Vol. 35 No. 10, pp. 2357-2365.

79. Kim, K., Wiedner, B., and Camci, C., 1993, "Fluid Dynamics and Convective Heat Transfer In Impinging Jets Through Implementation of a High Resolution Liquid Crystal Technique," *ISABE Paper No. 93-7077.*

80. Knowles, K., Bray, D., Bailey, P. J., and Curtis, P., 1991, "Impinging Jets in Cross-flow," *Aeronautical Journal*, pp. 47-56.

81. Koopman, R. N. and Sparrow, E. M., 1976, "Local and Average Transfer Coefficients Due to an Impinging Row of Jets," *Int. J. Heat Mass Transfer*, Vol. 19, pp. 673-683.

82. Li, L., Zhang, D., and Lin, J., 1988, "The Application of the Liquid Crystal Technique to the Experimental Modelling of Impingement Cooling," *2nd International Symposium on Heat Transfer*, Bejing, China.

83. Lichtarowicz, A., Duggins, R. K., and Markland, E., 1965, "Discharge

Coefficients for Incompressible Non-cavitating Flow Through Long Orifices," *Journal of Mechanical Engineering Science*, Vol. 7, Part 2, pp. 210-219.

84. Lucas, M. G., Ireland, P. T., Wang, Z., and Jones, T. V., 1992, "Fundamental Studies of Impingement Cooling Thermal Boundary Conditions," *AGARD CP-527*, Paper No. 14.

85. Ma, C.F., Gan, Y. P., Tian, Y. Q., and Lei, D. H., 1992, "Fundamental Research on Convective Heat Transfer in Electronic Cooling Technology," *Journal of Thermal Science*, Vol. 1, No. 1, pp. 30-40.

86. Martin, H., "Heat and Mass Transfer Between Impinging Gas Jets and Solid Surfaces," Advances in Heat and Mass Transfer Vol 13, *Academic Press*, pp. 1-60, 1977.

87. McGrehan, W. F., and Schotsch, M. J., 1988, "Flow Characteristics of Orifices with Rotation and Corner Radiusing," *ASME Journal of Turbomachinery*, Vol. 110, pp 231-217.

88. Metzger, D. E., 1985, "Cooling Techniques For Gas Turbine Airfoils - A Survey," *AGARD Conference on Heat Transfer and Cooling in Gas Turbines*, CP390 Paper No. 1.

89. Moffat, R. J., 1988, "Describing the Uncertainties in Experimental Results," *Experimental Thermal and Fluid Science*, Vol. 1, pp. 3-17.

90. Mudwar, I. and Wadsworth, D. C., 1991, "Critical Heat Flux From a Simulated Chip to a Confined Rectangular Impinging Jet of a Dielectric Liquid," *International Journal of Heat and Mass Transfer*, Vol. 34, No. 6, pp. 1465-1479.

91. Oates, G. C., 1985, Aerothermodynamics of Aircraft Engine Components, AIAA,Inc., New York.

92. Obot, N. T., Majumdar, A. S. and Douglas, W. J. M., 1979, "The Effect of Nozzle Geometry on Impingement Heat Transfer Under a Round Turbulent Jet," *ASME Paper No. 79-WA/HT-53.*

93. Obot, N. T., Douglas, W. J. M., and Mujumdar, A. S., 1982, "Effect of Semi-confinement on Impingement Heat Transfer," Seventh International Heat Transfer Conference, Vol. 3, pp. 395-400.

94. Obot, N. T., and Trabold, T. A., 1987, "Impingement Heat Transfer Within Arrays of Circular Jets: Part 1 - Effects of Minimum, Intermediate, and Complete Crossflow for Small and Large Spacings," *ASME Jour Heat Transfer*, Vol. 109, pp. 872-879.

95. Oldfield, M. L. G., Jones, T. V., and Schultz, D. L., 1978, "On-Line Computer for Transient Turbine Cascade Instrumentation," *IEEE Transactions on Aerospace and Electronic Systems*, Vol. AES-14, No. 5, pp. 738-749.

96. Pamadi, B. N., and Belov, I. A., 1980, "A Note on the Heat Transfer Characteristics of Circular Impinging Jet," *Int. J. Heat Mass Transfer*, Vol. 23, pp. 783-787.

97. Patankar, S. V., Basu, D. K., and Alpay, S. A., 1977, "Prediction of Three-Dimensional Velocity Field of a Deflected Turbulent Jet," *ASME Journal of Fluids Engineering*, Vol 99., pp. 758-762.

98. Petty, J. S. and Henderson, R. E., 1989, "The Coming Revolution in Turbine Engine Technology," *Presentation at the Propulsion Workshop*, United States Air Force Academy.

99. Popiel, Cz. O., and Bogusiawski, L., 1986, "Mass or Heat Transfer in Impinging Single, Round Jets Emitted By A Bell-shaped Nozzle and Sharp-Ended Orifice," Eighth International Heat Transfer Conference, Vol. 3, pp. 1187-1192.

100. Popiel, C. O., and Trass, O., 1982, "The Effect of Ordered Structure of Turbulence on Momentum, Heat and Mass Transfer of Impinging Round Jets," *Seventh International Heat Transfer Conference*, Vol. 3, pp. 141-146.

101. Popiel, C. O., and van der Meer, T. H., and Hoogendorn, C. J., 1980, "Convective Heat Transfer on a Plate in an Impinging Round Hot Gas Jet of Low Reynolds Number," *Int. J. Heat Mass Transfer.*, Vol. 23, pp. 1055-1068.

102. Saad, N. R., Mujumdar, A. S., Abdel Messeh, W. and Douglas, W. J. M., 1980, "Local Heat Transfer Characteristics for Staggered Arrays of Circular Impinging Jets with Cross Flow of Spent Air," *ASME Paper No. 80-HT-23.*

103. Saad, N. R., Polat, S., and Douglas, W. J. M., 1992, "Confined Multiple Impinging Slot Jets without Crossflow Effects," *Int. J. Heat and Fluid Flow*, Vol. 13, No. 1, pp. 2-14.

104. Scherer, V., Wittig, S., Morad, K. and Mikhael, N., 1991, "Jets in Crossflow: Effects of Hole Spacing to Diameter Ratio on the Spatial Distribution of Heat Transfer," *ASME Paper No. 91-GT-356.*

105. Schlichting, H., Boundary-Layer Theory, *McGraw-Hill Book Company*, Seventh Edition, New York, 1979.

106. Schultz, D. L., and Jones, T. V., 1973, "Heat-Transfer Measurements in Short-Duration Hypersonic Facilities," AGARD AG 165.

107. Sherif, S. A., and Pletcher, R. H., 1989, "Measurements of the Thermal Characteristics of Heated Turbulent Jets in Crossflow," *ASME Journal of Heat Transfer*, Vol. 111, pp. 897-903.

108. Sparrow, E. M., Goldstein, R. J., and Rouf, M. A., 1975, "Effect of Nozzle Surface Separation Distance on Impingement Heat Transfer for a Jet in Crossflow," *ASME Journal of Heat Transfer*, Vol. 97, pp. 528-533.

109. Stoy, R. L., and Ben-haim, Y., 1973, "Turbulent Jets in a Confined Crossflow," *ASME Journal of Fluids Engineering*, pp. 551-556.

110. Striegl, S. A., and Diller, T. E., 1984a, "The Effect of Entrainment Temperature on Jet Impingement Heat Transfer," *Journal of Heat Transfer*, Vol. 106, pp. 27-33.

111. Striegl, S. A., and Diller, T. E., 1984b, "An analysis of the Effect of Entrainment Temperature on Jet Impingement Heat Transfer," *Journal of Heat Transfer*, Vol. 106, pp. 804-810.

112. Van Treuren, K. W., Wang, Z., Ireland, P. T., and Jones, T. V., 1993,"Detailed Measurements of Local Heat Transfer Coefficient and Adiabatic Wall Temperature Beneath an Array of Impinging Jets," *ASME paper No. 93-GT-205.*

113. Van Treuren, K. W., Wang, Z., Ireland, P. T., Jones, T. V., and Kohler, S. T., 1994, "Local Heat Transfer Coefficient and Adiabatic Wall Temperature Measurements Beneath Arrays of Staggered and Inline Impinging Jets," *ASME paper No. 94-GT-181.*

114. Vedula, R. J., and Metzger, D. E., 1991, "A Method for the Simultaneous Determination of Local Effectiveness and Heat Transfer Distributions in Three-Temperature Convection Situations," *ASME Paper No. 91-GT-345.*

115. Wang, Z., 1991, "The Application of Thermochromic Liquid Crystals to Detailed Turbine Blade Cooling Measurements," *D.Phil Thesis*, Department of Engineering Science, University of Oxford, England.

116. Wang, Z., 1993, Private communication on unpublished work.

117. Wang, Z., Ireland, P. T., and Jones, T. V., 1993, "An Advanced Method of Processing Liquid Crystal Colour Change Images From Transient Heat Transfer Experiments Using an Intensity History Method," *ASME paper No. 93-GT-282.*

118. Wang, Z., Ireland, P. T., Jones, T. V., and Davenport, R., 1994, "A Colour Image Processing System for Transient Liquid Crystal Heat Transfer Experiments," *ASME paper No. 94-GT-290.*

119. Yan, X., Baughn, J. W., and Mesbah, M., 1992, "The Effect of Reynolds Number on the Heat Transfer Distribution From a Flat Plate to an Impinging Jet," *ASME Winter Annual Meeting*, Anaheim, CA.

120. Yeh, F. C., and Stepka, F. S., 1984, "Review and Status of Heat Transfer Technology for Internal Passages of Air-Cooled Turbine Blades," *NASA TP-2232*.

121. Young, W. C., Rorak's Formulas for Stress & Strains, *McGraw-Hill Book Company*, 6th Edition, 1989.